TOWARDS SEMICONDUCTOR-SUPERCONDUCTOR HYBRID QUANTUM CIRCUITS

Gatemon and Andreev Qubits based on InAs/Al, InAs/Nb and GaAs/InSb core/shell nanowires

Von der Fakultät für Mathematik, Informatik und Naturwissenschaften der RWTH Aachen University zur Erlangung des akademischen Grades eines Doktors der Naturwissenschaften genehmigte Dissertation

vorgelegt von

M. Sc. Patrick Zellekens
aus Düsseldorf, Deutschland

Berichter:
Ausserplanmäßiger Professor Dr. rer. nat. Thomas Schäpers
Universitätsprofessor Dr. rer. nat. Markus Morgenstern

Tag der mündlichen Prüfung: 22. 11. 2022

"Out of clutter, find Simplicity.
From discord, find Harmony.
In the middle of difficulty lies Opportunity."

Albert Einstein

Contents

Abstract/Zusammenfassung 1

Introduction/Outline 5

I Theory 9

1 Semiconductor nanowires 11

2 Quantum effects in low-dimensional systems 21

3 Mesoscopic Josephson junctions 29

4 Circuit quantum electrodynamics 49

5 Semiconductor-superconductor hybrid Qubits 57

II Towards low-loss quantum (control) circuits 67

1 Requirements 71

2 Fabrication of microwave quantum circuits 73

3 Superconducting quantum circuits 91

4 Optimization 99

III Experimental setups and techniques 117

1 Introduction 119

2 Qubit manipulation, readout and two-tone spectroscopy 123

IV Mesoscopic nanowire Josephson junctions 127

1 Introduction 129

2 Towards highly transparent nanowire Josephson junctions 133

3 Transport in shadow-mask defined nanowire Josephson junctions 145

V Qubits and microwave spectroscopy 155

1 Hybrid Qubits I: The Gatemon qubit 157

2 Hybrid Qubits II: The Andreev qubit 167

3 Spin-polarized Andreev bound states 175

VI Excitation-based phenomena 181

1 The Little-Parks effect 183

VII (Quantum) Transport in antimony-based core/shell nanowires 193

1 Introduction 195

2 Room temperature transport **197**

3 Electron interference and soi in GaAs/InSb core-shell nanowires **203**

Summary and Outlook **215**

Acknowledgements **221**

List of Publications **223**

Declaration/Eidesstattliche Erklärung **225**

VIII Appendix **227**

A Fabrication of superconducting microwave quantum circuits: Recipes **229**

Bibliography **233**

ABSTRACT

In this thesis, two different qubit concepts and their respective pre-stages are investigated. The Gatemon is a variant of the famous and well-studied Transmon. Both have in common that they rely on the macroscopic and collective excitation of an anharmonic LC circuit and are a very promising approach to realize scalable qubit systems. The Andreev qubit, on the other hand, is based on a single pair of Andreev bound states and the two-particle transitions associated with it.

Both mentioned systems have in common that they can be realized by means of semiconductor nanowires. Thus, the major part of this thesis is devoted to the characterization and subsequent optimization of nanowire-based devices treated with (high frequency) electromagnetic fields at ultralow and ambient temperatures. Using InAs/super-conductor core/shell nanowires that have been in-situ and epitaxially covered with a thin metal layer out of Al, Nb or other materials, mesoscopic Josephson junctions are fabricated and subsequently investigated by means of advanced experimental DC and AC techniques.

On the low frequency and DC side, we utilize **emission**, **SQUID**, **magnetoconductance** and **quantum dot** measurements to characterize the electronic properties of the fabricated devices including the hardness of the induced proximity gap, the interface transparency, the carrier concentration and the phase coherence length. In addition, we search for signatures of 4π-periodic supercurrent contributions. Here, a special focus is set on InAs/Al full shell nanowires [1] that, following theoretical predictions [2], can host pairs of Majorana fermions and, in combination with the **Little-Parks effect** [3], do not require a complicated *braiding* procedure to manipulate the state of the system.

The last part of the thesis is focused on flux- and gate-dependent measurements of Andreev qubits as well as the investigation of individual Andreev bound states by means of two-tone spectroscopy. The latter one reveals an unconventional state structure that is connected to the occurrence of single quasiparticle transitions caused by a Rashba-induced lifting of the spin degeneracy. This is one of the prerequisites for the realization of a helical gap and topologically-protected states. In addition, a nanowire-based 2D Gatemon was successfully realized. The analysis of the detuning-dependent Rabi oscillations exhibit a gate-tunable resonator-qubit coupling and reasonable large lifetimes of the two-level system $T_1 \approx 120\,\mathrm{ns}$.

ZUSAMMENFASSUNG

Innerhalb dieser Arbeit wurden zwei verschiedene Quanten-Bit-Strukturen [**Qubit**] untersucht. Das sogenannte **Gatemon** stellt dabei eine Alternative zu dem bereits im industriellen Einsatz befindlichen Transmon dar. Beide Systeme basieren auf der kollektiven Anregung eines anharmonischen LC-Oszillators, welcher sich aus einem supraleitenden Kondensator und einem Josephsonkontakt zusammensetzt. Der Vorteil liegt hier auf der robusten Kohärenz des makroskopischen Quantensystems. Letzteres geht dabei jedoch einher mit der Präsenz höherer Energiezustände, die eine Operation des Bauteils nur für bestimmte Konfigurationen, ausgedrückt durch die sogenannte *Anharmonizität*, erlauben. Im Gegensatz dazu positioniert sich das Andreev-Qubit, welches auf Zwei-Quasiteilchen-Übergangen zwischen mikroskopischen, räumlich lokalisierten Quantenzuständen, sogenannten Andreev-Zuständen, basiert.

Beide Qubit-Typen können mithilfe von Halbleiter-Nanodrähten hergestellt werden. Deswegen beschäftigte sich der Hauptteil dieser Arbeit mit der Prozessierung, Tieftemperatur- und Hochfrequenz-Charakterisierung, sowie der Optimierung von Josephsonkontakten auf Basis von Supraleiter-Halbleiter-Hybridstrukturen. Ein spezieller Fokus lag hier auf der DC- und AC-Vermessung von epitaktisch gewachsenen InAs-Nanodrähten, die unter Ultrahochvakuum- und *in situ*-Bedingungen mit einer dünnen supraleitenden Schicht aus Aluminium oder Niob bedeckt wurden. Die verwendeten Messmethoden umfassten die Durchführung von Emissions- und Shapiromessungen zur Analyse der Strom-Phasen-Beziehung, die Untersuchung des Bauteilverhaltens in schwachen und starken Magnetfeldern, sowie das Tunnelspektroskopie-gestützte Auslesen der induzierten Energielücke, der Grenzflächentransparenz, der Ladungsträgerkonzentration und der Phasenkohärenzlänge.

Ein besonderer Schwerpunkt wurde zusätzlich auf die Suche von 4-π-periodischen Anteilen im Suprastrom gelegt, welche als Signatur für die potentielle Existenz von topologisch geschützten Zuständen gelten. Als Plattform dienten hier InAs-Drähte, welche vollständig mit einer supraleitenden Aluminiumhülle umgeben sind [1]. Der in diesen Systemen auftretende *Little-Parks-Effekt* [3] kann, wie kürzlich stattgefundene theoretische Untersuchungen nahelegen [2], als Basis für die Erzeugung und Manipulation von Majorana-Fermionen dienen, welche derzeit als erfolgsversprechendster Ansatz für die Realisierung eines topologischen Quantencomputers gelten.

Den Abschluss der Arbeit bildet die Untersuchung der im Vorfeld erwähnten Gatemon- und Andreev-Qubit-Strukturen. Im Falle der Letztgenannten konnte erfolgreich den Übergang zwischen zwei Andre-ev-Zuständen mit einer durchschnittlichen Lebensdauer von 25 ns beobachtet werden. Mithilfe von magnetfeld- und gate-gestützter Zwei-Ton-Spektroskopie war es zusätzlich möglich, Nachweise für die Existenz von Ein-Quasipartikel-Übergängen zwischen spinpolarisierten Andreev-Zuständen zu beobachten. Letzteres lässt sich dabei auf die starke Spin-Bahn-Wechselwirkung innerhalb der InAs-Halbleiterstruktur zurückführen und gilt als Vorstufe für die Erzeugung einer *helikalen Energie-lücke*. Im Falle der zweidimensionalen, nanodraht-basierten Gatemon-Strukturen konnte erfolgreich der Nachweis für eine gatesteuerbare Kopplungsstärke zwischen Qubit und Mikrowellenresonator erbracht werden. Eine zusätzlich stattgefundene Analyse des Systems auf Basis von *Rabi-Oszillationen* zeigte durchschnittliche Lebensdauern des Zwei-Zustand-Systems von $T_1 \approx 120$ ns.

INTRODUCTION

Within the last decade, the hunt for larger and larger quantum systems that are suited to operate as a **quantum computer** has left the field of purely academic research and shifted into the focus of the big tech companies. In the following, major breakthroughs have been achieved, like the first 100-Qubit-system or the proof that a quantum computer can, indeed, outpace classical systems if it comes to optimization problems. However, all those systems, including the one used by **Google** to prove the **quantum supre-macy** [4], still fall under the more restricted, but less error-prone category of *adiabatic quantum systems* [5–8].

One of the most important benchmarking parameter of qubit systems is the **fidelity** F, which acts as a figure of merit for the likelihood of (uncorrectable) errors during the calculation or read-out operation that overshadow the clear distinction between ground and excited state [9–12]. After continuous research and optimization, state-of-the-art values for the error rate of single qubits are now on a level at which reasonable calculations are possible. However, when switching to entangled multi-qubit systems, the possible time for operations drops significantly and far below a level that is suitable for technical applications. Besides the option to use the less advanced path of the already mentioned adiabatic systems or *quantum annealer* to tackle this issue, it is also possibe to work on a more fundamental level by boosting the performance of the individual qubit.

In the last 15 years, the field of condensed matter physics was *hit* by to two major discoveries that both on their own can be considered as *fully disruptive*. In 2007, a group around Laurens Molenkamp at the university of Würzburg found the first experimental hints for the existence of a new state of matter in electronic systems, that, due to especially tailored band structures, only allow the transport of charge carriers in **edge states** [13]. Even though those so-called **topological insulators** have since then attracted great and growing interest on their own, they also demonstrated an actual realization of the concept of *topology* on a more general level. In 2012, the hunt for other (mesoscopic) system that can host *topologically protected gap states* reached a local peak when a team around Leo Kouwenhoven at the Technical University Delft found the first hint of a novel and exotic *quasi-particle* that exists outside of the conventional charge carrier continuum [14]. The **Majorana fermion**, also referred to as *Zero-order parafermion* [15, 16], has already been predicted theoretically in the late 30s of the last century and belongs to the class of *non-abelian anyons* [17]. These are a special family of particles which have the intriguing property that, if they undergo a sequence of *exchange operations*, the final state of the system is fully determined by the *sequential order* in which the sequence has been performed. This gives rise to a clear, *Bloch-like* state space that can be utilized for the realization of two level systems that are not affected by (most of the) disturbances and perturbations in solid state devices, which greatly enhances their fault-tolerance. However, the required coherent exchange of the *particle* and *anti-particle* component of a Majorana pair, the so-called **braiding** [18–20], has revealed itself to be a process of great complexity which, until now, has not been successfully achieved.

The findings of Molenkamp et al. and Kouwenhoven et al. have opened the door to a rich spectrum of different exotic systems, including but not restricted to *photonic anyons* [21, 22], *weyl semimetals* [23] or *transition metal dichalcogenides* [24]. However, the state-of-the-art solution for the realization and investigation of topological devices are **Josephson junctions**, consisting out of two superconducting contacts and a normal conducting weak link that is supposed to host *Majorana zero modes*. Several experiments have already shown transport features that can potentially be attributed to the existence of a topologically protected, anyonic state in the junction area. However, all those measurements, like the search for a *conductance anomaly* deep within the *superconducting gap* or the detection of periodicity changes in the *current-phase-relation* by means of the *AC Josephson effect*, have in common that they can only probe the **excitation spectrum** in a very limited and

indirect way which leaves room for a lot of other, more conventional explanations.

The presented project, as a joint collaboration between the group of Koji Ishibashi at the *Center of Emergent Matter Science* in the Tokyo branch of **RIKEN**, the group of Martin Weides at *Karlsruhe Institute of Technology* and the Peter-Grünberg-institute [PGI-9] at Forschungszentrum Jülich, aims at a multi-level approach to detect, analyze and manipulate two- and single-particle excitations in different kind of semiconductor-superconductor hybrid structures in order to realize Gatemon, Andreev and topological qubit structures. Here, a special focus is set on the optimization of the interface transparency between the superconducting electrodes and the semiconductor nanowire as well as the strength of the spin-orbit interaction. Additionally, various processing techniques are developed and optimized to fabricate low-loss superconducting microwave circuits that combine large quality factors with a well-controlled gate architecture and a magnetic field robustness far beyond the bulk critical field.

OUTLINE

The thesis is organized as follows:

- The first chapter covers the theoretical background of (mesoscopic) Josephson junctions and electron interference phenomena in low dimensional semiconductor nanostructures. Additionally, the basic principles of circuit quantum electrodynamics and extended microwave structures are presented including a special focus on network systems and the physics of coplanar waveguides. Lastly, the two qubit systems investigated within this thesis, i. e. the Gatemon and the Andreev qubit, are described.

- In the second chapter, a detailed description of all employed processing techniques and procedures for the fabrication of superconducting microwave circuits is provided by taking the example of so-called Andreev chips. Here, a special focus is set on the suppression of potential noise and loss sources like sidewalls at the metal structures or charge traps in the dielectric. Subsequently, more fundamental optimization approaches are presented including a precisely tailored flux management by means of antidots or the Flip-chip design based on sapphire substrates. Additionally, a new platform to perform both DC as well as AC measurements on nanowire Josephson junctions measurements is introduced. Using an on-chip bias tee, an extrinsic shunt resistor and a specially designed gate structure, it is possible to perform Shapiro-, emission-, magnetoconductance- and/or SQUID-measurements on the same chip without parasitic side effects like box modes or slotline modes. This allows to map the whole frequency-power parameter space.

- The experimental methods and measurement principles that have been used in this thesis are introduced in chapter 3.

- Chapter 4 is devoted towards the investigation of mesoscopic nanowire Josephson junctions. Here, a special focus is set on a comparison of devices with ex-situ contacts and hybrid structures for which the superconductor is deposited under ultrahigh vacuum conditions and in-situ. Typical characterization techniques are employed in order to extract values for the critical and excess current as well as the I_cR_N product. Additionally, more advanced methods using an extrinsic shunt resistor and an on-chip bias tee are presented. Doing so, it is possible to suppress phase noise, extract the real junction current and obtain information regarding high order multiple Andreev reflections. The occurrence of subharmonic Shapiro steps can be related to a strongly non-sinusoidal current-phase relationship caused by an ultrahigh interface transparency. The last part of the chapter provides an overview of tunnel spectroscopy and angle-dependent magnetoconductance measurements in self-defined InAs/Al half shell nanowire Josephson junctions, revealing the existence of Yu-Shiba-Rusinov states.

- The fifth chapter presents single- and two-tone spectroscopy measurements of Gatemon and Andreev qubits embedded in superconducting coplanar waveguide microwave circuits. A comparison between 3D and 2D Gatemons is provided in terms of electromagnetic field control. For the circuit-bound structures, typical characterization measurements are performed including the analysis of the single-tone response, gate-dependent dispersive readout and a controlled Rabi cycle in order to determine the lifetime of the qubit states. The second half of the chapter is devoted to mesoscopic qubits that are based on spatially localized states within the nanowire Josephon junction. Magnetic field and gate dependent single- and two-tone spectroscopy measurements of individual Andreev bound states are presented. Additionally, clear

signatures of a spin polarization in terms of single quasiparticle transitions are provided. Using an additional in-plane magnetic field, hints of an additional Zeeman-shift can be observed, which is one of the main requirements for the creation of a helical gap.

- The sixth chapter provides the first experimental investigation of an InAs/Al full shell nanowire Josephson junction that can host the Little-Parks effect. The latter is a recently proposed method to create and manipulate Majorana zero modes in a solid state system without the need for braiding. First a brief overview of the specific requirements and the chosen device geometry is given. Subsequently, the necessary calibration procedures in terms of the applied gate voltage and the in- and out-of-plane magnetic field are discussed. In the following, we provide evidence for the existence of conductance features in the device response that can not be explained in terms of conventional Andreev bound states or multiple Andreev reflections. In addition, both Shapiro and emission measurements are presented. The chapter concludes with the investigation of SQUID devices consisting of a full shell nanowire and another nanowire Josephson junction that is intentionally designed to exhibit a sinusoidal current-phase relation. Here, the angle-dependent interference pattern exhibits clear phase jumps in the order of π that can be potentially attributed to a change of the parity of the system.

- Chapter 7 concludes with the structural and electrical characterization of GaAs/InSb core/shell nanowires. By performing field-effect measurements, a shell thickness dependent switch from p-dominated to n-dominated behavior at ambient and cryogenic temperatures can be observed. The application of an out-of-plane magnetic field leads to the occurence of universal conductance fluctuations and a pronounced weak antilocalization feature. Both effects are analyzed to obtain information about characteristic parameter like the phase coherence length, the spin-orbit length and the mean free path. Using an in-plane field, Aharonov-Bohm-type flux periodic magnetocondutance oscillations can be observed. Here, an additional gate voltage leads to a splitting of the angular momentum states and a double peak feature in the Fourier spectrum, which is most likely caused by a strong spin-orbit interaction.

I

THEORY

1

SEMICONDUCTOR NANOWIRES

Semiconductor nanowires are one of the most prominent building blocks for novel electronic devices. The typical radial structure size of 100 nm or less sets them deep into the so-called *mesoscopic regime*, in which most of the device characteristics are fully determined by quantum mechanical effects and phenomena. Furthermore, by tailoring the *aspect ratio* of the nanowire, it is possible to (partially) suppress the motion of carriers into certain directions and therefore set the system into the one- two- or three-dimensional transport regime.

Within this project, the fabrication of devices was restricted to so-called **III/V** nano-wires, i.e. compound structures based on *Indium* [**In**], *Arsenic* [**As**], *Gallium* [**Ga**] and *Antimony* [**Sb**], with a special focus on *Indium arsenide* [**InAs**]. The latter was chosen due to its remarkable electronic properties in terms of the large *electron mobility* $\mu > 20000\,\mathrm{cm}^2/\mathrm{Vs}$ at cryogenic temperatures and $\mu > 4000\,\mathrm{cm}^2/\mathrm{Vs}$ at room temperature [25], the small *effective mass* $\mathrm{m}_0 = 0.023\,\mathrm{m}_e$ and the large spin-orbit parameters for the *Rashba effect* $\alpha = 6 \cdot 10^{-12}\,\mathrm{eVm}$ [26] and *Zeeman* effect $\mathrm{g}_{\mathrm{bulk}} > 13$ [27–29]. Additionally, InAs is much more stable than Sb-based materials with respect to typical process chemicals like the Aluminiun etchant *Transene D*, developers based on *Tetramethylammonium hydroxide* [**TMAH**] or *ion milling* prior to the contact deposition [30].

As most of the presented results in this Thesis aim towards the realization of semicon-ductor-superconductor hybrid structures, it is of significant importance that the used semiconductor is able to form high quality interfaces with common superconductors like Aluminium. Previous findings of [31–33] have already shown that InAs adopts well to Aluminium and Vanadium in terms of lattice mismatch and strain relaxation. Within this project, single crystalline and epitaxial Niobium films could be realized, too. All previously mentioned nanowire/superconductor core/shell systems can be grown in a half shell as well as a full shell geometry, as both of them originate from the same kind of growth procedure:

First, a p-doped silicon [**Si**] (100) wafer is cleaned by means of a wet chemical etch in a 3:1 mixture of *sulfuric acid*:*hydrogen peroxide* [**Piranha**] and 1% *hydrofluoric acid* [**HF**] in order to remove all organic contaminations and the native oxide. Subsequently, the substrate is cleaned in *deionized* [**DI**] water for 10 minutes, followed by another 1%HF dip for 10 minutes to remove the native oxide formed by the strongly oxidizing Piranha. The last step *hydroxylate* the Si surface, too, and therefore suppress any reoxidization for approx. 20 minutes. Within this given time frame, the substrate is loaded into an *oxidation furnace*. Here, a homogenous, 20 nm thick layer of *silicon dioxide* [$\mathbf{SiO_2}$] is grown in an ultrapure oxygen atmosphere, as depicted in Fig.1.1(a). However, it should be mentioned, that the exact growth rate of the oxide depends on various substrate parameters like the *doping level* and the *crystal orientation* and should therefore be checked by means of analysis techniques like *ellipsometry*.

The previously described oxide mask act as a capping layer for the crystalline silicon and suppress the formation of any *nuclei*. Thus, in order to facilitate the nanowire growth, the silicon surface has to be exposed again in certain, strongly spatially localized areas by means of a (resist) mask-assisted etching procedure. In order to achieve the required spatial resolution, *electron beam lithography* is used transfer the pattern into the resist. An optimal implementation of the etching step is crucial for the subsequent growth. Various previous works [34–37] have already shown that both the quality

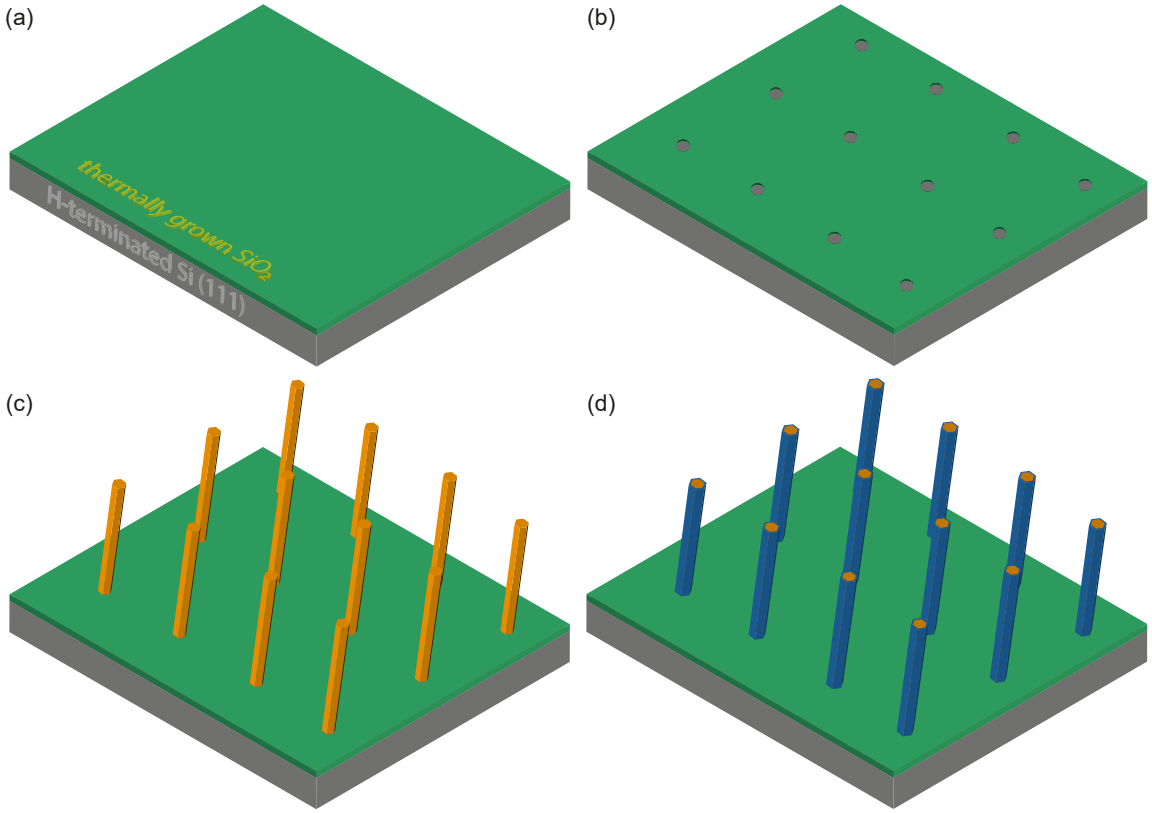

Figure 1.1 – *Schematic overview of the selective-area growth procedure for vertical InAs nanowires with superconductor shells. (a) Growth of a SiO_2 mask by means of thermal oxidization of the silicon (111) surface. (b) Wet chemical and dry etching-based opening of circular pores within the oxide mask. (c) Formation of the nanowires by self-catalyzed growth, originating from an oversaturated InAs droplet. (d) In-situ transfer of the substrate into the metal MBE and coverage of the nanowire surface with aluminium. Due to the rotation of the surface, the superconductor forms a full shell around the nanowire.*

and morphology of the nanowires are influenced by the *size* and *shape* of the pinholes as well as the *roughness* of the re-exposed silicon surface, as all of them alter the **contact angle** between the substrate and the growth nuclei. Here, a dry-etching approach based on *Fluoroform* [$\mathbf{CHF_3}$] was chosen, as it provides a precise control of the material removal due to the small etching rate of approx 0.1 nm/s. Thus, after a total etching time of 160 s at 20 °C and 50 sccm, large arrays of holes are formed within the oxide mask (cf. Fig.1.1(b)).

The growth of the nanowires is achieved by means of *molecular beam epitaxy* [**MBE**]. Here, a growth chamber, embedded in the so-called **Nanocluster**, is pumped down and kept at *ultra high vacuum* [**UHV**] conditions by means of a cryo pump, an ion getter pump and a nitrogen shield. The latter one is also used to thermally isolate the *effusion cells*, which act as sources for Indium and Gallium. Additionally, the chamber is equipped with *crackers* for Arsenic, Antimony and Tellurium, whereby the last one is used as a *dopant* for InAs. One of the biggest advantages of MBE is the comparably slow growth rate of approximately 1 μm/h, which enables a precise control of the thickness or - for this project - the length and diameter of the nanowires. Additionally, due to the high purity of the source materials, combined with the UHV conditions in the chamber, the semiconductor structures exhibit a much smaller *background doping* in comparison to other growth methods like *metal-organic vapor-phase epitaxy* [**MOVPE**]. While the specific MBE recipes are given in the theses of Torsten Rieger [38], Nicolas Güsken [32] and Pujitha Perla [39], at least a brief overview about the so-called *self-catalyzed* growth procedure, whose outcome is shown in Fig. 1.1(c), should be provided at this point:

- Cleaning of the substrate by means of a prebaking step
- Transfer of the growth substrate into the MBE chamber

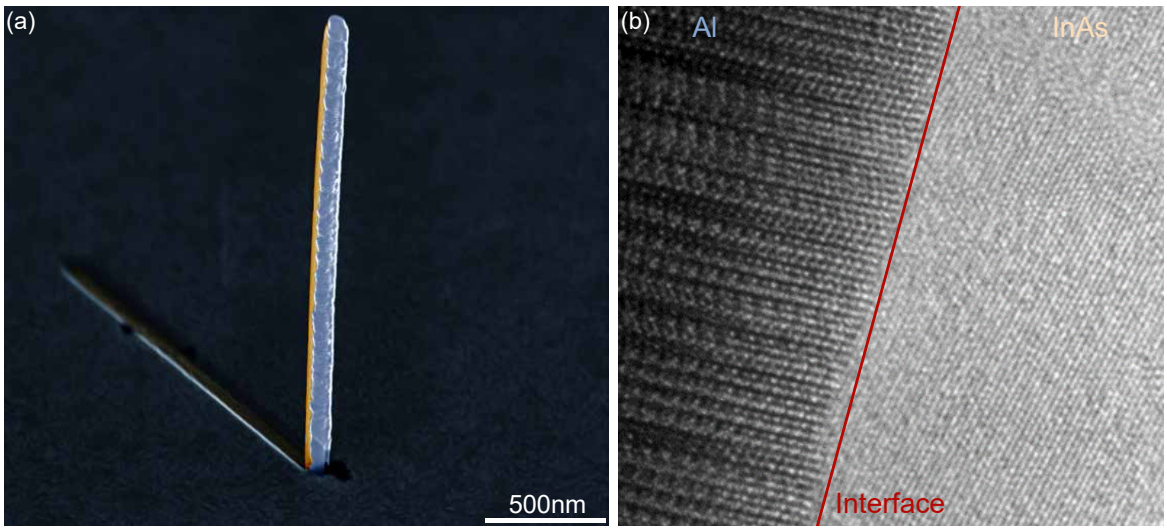

Figure 1.2 – *(a) False-colored SEM micrograph of an InAs/Al core/halfshell nanowire with a core diameter of 100 nm. The superconductor was in-situ deposited at -6 °C, resulting in a smooth and uniform metal layer. (b) TEM micrograph of a nanowire of the same growth run. It can be clearly seen, that the crystal lattice of the semiconductor is interspersed with multiple stacking faults. However, the interface between both materials as well as the aluminium itself are defect-free, which proofs the epitaxial and high quality growth of the superconductor.*

- Stabilizing of the Arsenic pressure
- Addition of Indium to start the actual growth
- Formation of InAs droplets inside of the holes
- Vertical nanowire growth due to oversaturation of the droplet
- Transfer into the preparation chamber
- Postbake in order to degas the Arsenic termination layer on the nanowire surface

Here, the final step is crucial for the subsequent deposition of the superconductor. In case of Aluminium, the outer monolayer of As would otherwise lead to the formation of *Aluminium arsenide* [**AlAs**], a wide gap semiconductor [E_g=2.12 eV] which would act as a tunnel barrier between the InAs and the Al.

Another specific issue of Al is the comparably large diffusion rate. If grown at room temperatures, the metal tends to form individual drops rather than a homogeneous, uniform epilayer. Thus, the whole system has to be cooled down to 0°C or below [31, 33]. However, during this thesis, it could be observed that the required temperature for layer growth also depends on the actual dimensions of the nanowire. In case of nanowires with a diameter of 110 nm or more, the Al tends to form a stable crystal at -6°C already. In contrast, if the radial extension of the nanowire is reduced, the temperature needs to be significantly lower. While a full understanding of the observed effect is still missing, the first simple explanation would be a correlation with the size dependency of the surface energy. In this model, the Al behaves like a water droplet on a plane that, in the case of a small drop size, has a quite large contact angle with respect to the material below it and, additionally, a much larger surface tension [40]. The latter one would then suppress the merging of multiple droplets into a closed layer.

However, if the temperature is low enough, the material forms an uniform, (almost) single crystalline layer on one side of the nanowire, i.e. three facets. Thus, these wires are usually refered to as **half shells**. Additionally, as one of the specialties of the *Nanocluster*, the growth substrate can also be rotated during the metal deposition. This results in a complete coverage of the nanowire, i.e. **full shells**, as depicted in Fig. 1.1(d). A typical example for a half shell nanowire as well as a corresponding picture of the lattice configuration, obtained by means of *transmission electron microscopy* [**TEM**], is given in Fig. 1.4 (b). It can be seen that, despite the large density of stacking faults in the nanowire,

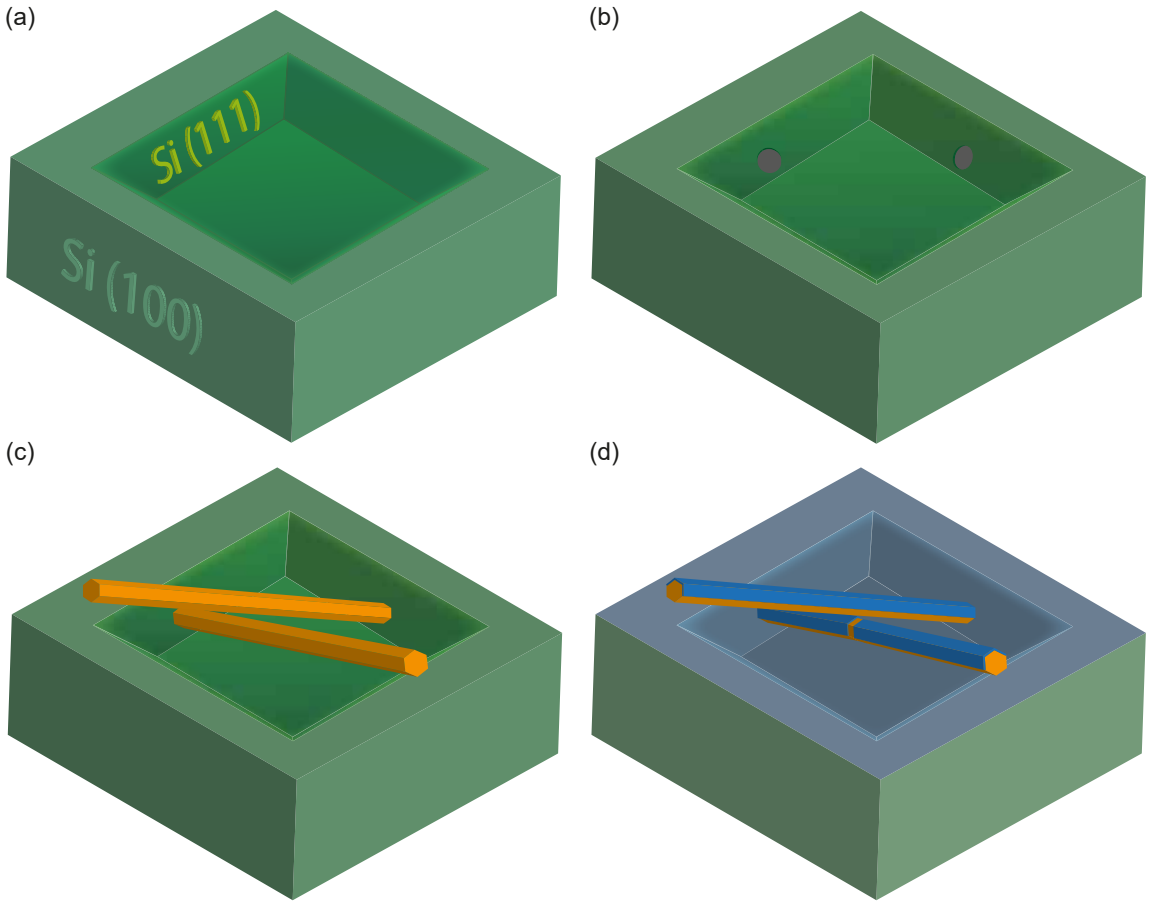

Figure 1.3 – *Schematic overview of the selective-area growth procedure for tilted InAs nanowires with superconductor shells and self-defined junctions. (a) TMAH-based etching of large rectangular holes into Si(100), revealing tilted Si(100) facet. Subsequent formation of the SiO_2 mask by means of thermal oxidization. (b) Wet chemical and dry etching-based opening of two circular pores within the oxide mask. The placement is thereby realized to be on adjacent facets, but with an offset in z-direction. (c) Formation of the nanowires due to self-catalyzed growth. The shadow nanowire grows above, but close to the junction nanowire in order to maintain well-defined metal contours on both sides of the junction. (d) In-situ transfer of the substrate into the metal MBE and coverage of the nanowire surface with aluminium. The shadow of the upper wire leaves a section of the lower wire uncovered, effectively forming a Josephson junction. The length of the junction is thereby roughly equal to the nanowire diameter.*

the interface between the InAs and the Al is completely defect-free and epitaxial. Besides the requirement of a homogeneous and defect-free coverage of the semiconductor with the superconductor, it is important, too, that the metal can be partially removed again in order to create the *weak link* of the Josephson junction. Experiments with various wet chemical and dry etching processes have shown that this can be rather difficult to achieve without degradation or destruction of the nanowire. The latter is especially true in the case of Niobium [41].

In order to overcome that issue, another growth approach has been developed by Pujitha Perla [39] within the timeframe of this project: By using a so-called **shadow mask approach**, the actual junction can be formed *in-situ* by means of another nanowire. This is different to other methods in which the uncovered section on the normal conducting element is formed with artificial mask structures out of oxides or nitrides[42–46]. One advantage of our approach is the significant reduction in complexity with respect to the total number of fabrication steps (cf. Fig. 1.3): By utilizing the same kind of oxide mask, the substrate is now further structurized. First, large squares are defined by means of electron beam lithography. Subsequently, the oxide layer within the squares is removed with a mixture of both dry and wet chemical etching. In the next step, a 1:3 mixture of TMAH:DI water at 80°C is used to etch 300 nm into the silicon substrate. Due to the much larger etching rate of Si (100) with respect to Si (111), one obtains a structure in the shape of a reversed, three-dimensional trapezium, with a tilt angle of 54.7° between the (100) plane and the (111) side facets [47–49]. After

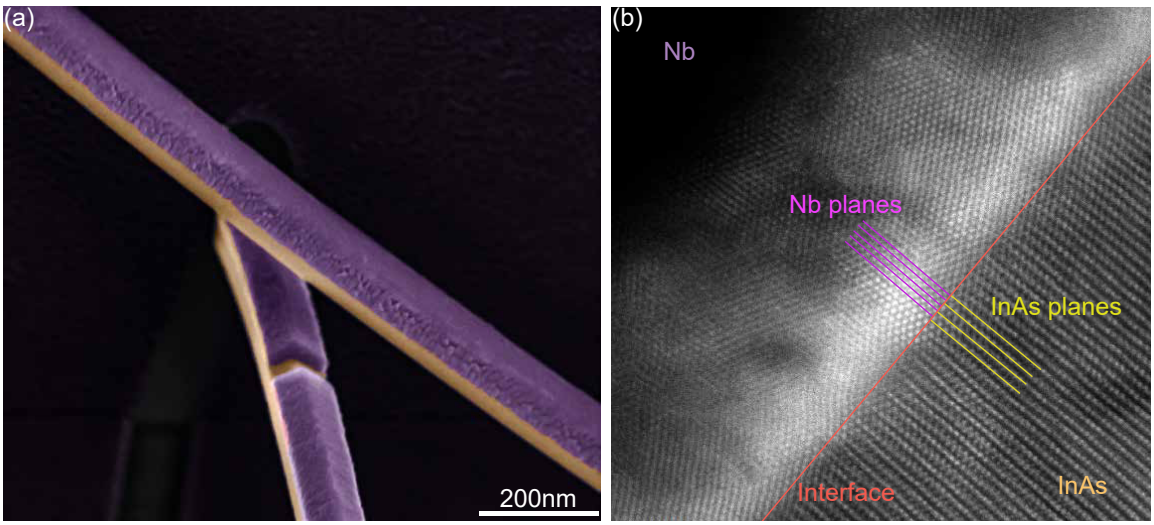

Figure 1.4 – *(a) False-colored SEM micrograph of an InAs/Nb core/halfshell nanowire with a self-defined junction and the corresponding mask nanowire above it. The superconductor is in-situ deposited at ambient temperatures, resulting in an uniform metal layer that smoothly follows the hexagonal shape of the InAs nanowire. The nanowire diameter is around 80 nm. (b) TEM micrograph of a nanowire of the same growth run. It can be clearly seen, that the crystal lattice of the semiconductor is interspersed with multiple stacking faults. However, the interface between both materials as well as the niobium itself are defect-free. The Nb adapts to the InAs underneath in a six planes Nb per four planes InAs arrangement. Images and data taken from [50].*

a subsequent re-oxidization step, shown in Fig. 1.3 (a), the actual growth spots have to be defined. By using EBL, two 80 nm wide holes on two adjecent sidefacets are defined. The three-dimensional alignment of the holes is thereby chosen in a way, that they form a angle of 90° in the xy-plane, with a small offset in z-direction. A subsequent etching step based on RIE and HF exposes the Si (111) planes inside of the holes, which can then be utilized for the actual nanowire growth, shown in Fig. 1.3 (b) and (c). For the final step, the growth substrate is transfered to the metal MBE. By setting the correct alignment between the upper nanowire that creates the *shadow* and the metal effusion cell, one achieves a well-defined junction on the lower nanowire, as depicted in Fig. 1.3 (d).

However, the previously described *self-defined* junctions do not only reduce the level of complexity for the fabrication. Even more important, at least with respect to transport measurements, is the direct relation between the achievable geometric channel length and the nanowire diameter. Most of the mesoscopic phenomena that have been studied within this thesis rely on quite specific junction properties, i.e. that the complete *supercurrent* is carried by a single **Andreev bound state**. Although a full theoretical description of the underlying effect and its impact on the junction dynamics is given at a later stage of this chapter, it should be at least mentioned at this point, that the so-called *single channel limit* just holds if (a) the coherence length of the superconductor is much larger than the effective length of the normal conducting segment and (b) there is only one accessible state in the nanowire. However, the latter one is directly related to the nanowire diameter due to one of the most intrigue properties of InAs and InSb: The intrinsic formation of a **accumulation layer** at the surface, caused by an effect which is normally referred to as *Fermi level pinning* and which is also the topic of the next section.

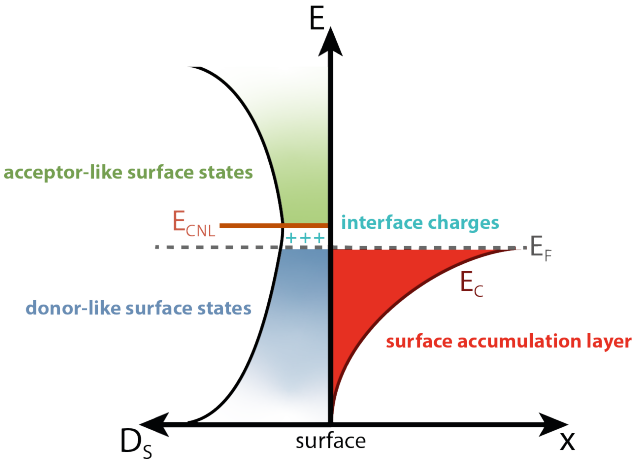

Figure 1.5 – *Schematic overview of the Fermi level pinning at the nanowire/vacuum interface. The unsaturated interface charges are compensated by means of an adjustment of the Fermi level with respect to the charge neutrality level at the surface. The result is an electron accumulation layer within the nanowire, which effectively forms a triangular potential well. The exact width of the shell determines thereby the number of states, as a stronger quantization leads to a larger level spacing and vice versa.*

1.1. SURFACE STATES AND FERMI LEVEL PINNING

One common method for the bandstructure determination of semiconductors is based on the *Kronig-Penney model* [51], which models a crystal as an infinitely long chain of one-dimensional square potentials. If combined with *Bloch's Theorem* [52], which describes a solution for the *Schrödinger equation* for a periodic lattice, one ends up in the *dispersion relation* E(k). However, due to its transcendental nature, there are some values of E for which no value of k exists that will satisfy the equation, ultimately leading to a certain energy range in which no states exist: The **band gap** E_g.

Obviously, this simple model only holds for the inner part of the crystal, the *bulk*. As soon as the underlying symmetry is broken, for example in the case of a cut through the lattice in terms of a *surface*, this leads to a perturbation of the local electrostatic environment and the emergence of **localized surface states** due to reconstruction and relaxation. The latter can be easily understood in terms of an imaginary wave vector ik, which results in an exponentially decaying wave for the Schrödinger equation. Even though this is an valid solution in general, it can not exist within the crystal. At the surface, on the other hand, this leads to a connection between the conduction E_c and valence band E_v, effectively bypassing the gap in the imaginary k-plane. Subsequently, there is as smooth transition between acceptor-like states and donor-like states, with the crossover point normally referred to as the **charge neutrality level** E_{cnl}. If the Fermi level lies above this energy, it quickly concentrates a lot of electrons there in real space. If it lies below, a lot of holes. Hence, for the semiconductor to be locally charge-neutral, the Fermi level must be permanently situated at this crossover point, i.e. it is *pinned*. However, as the absolute energetic position of the Fermi level has to be constant under equilibrium conditions, E_c and E_v are bend at the surface. In the case of InAs, E_{cnl} is located within the conduction band [53–55], which leads to a downward bending and the subsequent formation of an intrinsic **accumulation layer** [56–58], as depicted in Fig. 1.5.

The accumulation layer, as a triangular quantum well, gives rise to a built-in *two-dimensional electron gas* [**2DEG**], i.e. a highly conductive layer which usually extends up to 20 nm into the nanowire due to the comparably small number of screening charges [59]. This layer is the origin for most of the intrigue properties of InAs and, to a less extend, InSb. In contrast to other semiconductors like GaAs, which usually require a meticulously tailored procedure to form ohmic contacts, including some hardly controllable steps like *annealing* [60, 61], it is normally sufficient to remove the native oxide by means of *hydrogen cleaning* [58, 62], *sulfur passivation* [63, 64] or *ion milling* [65] to induce a barrier-free interface to metals like Ti, Cr, or Ni. Additionally, the steep slope of the conduction band further enhances the spin-orbit interaction in terms of the *Rashba effect*, which is one of the main ingredients for topological systems through the generation of a *helical gap*.

The restriction of the carrier transport to a thin layer close to the surface comes with some downsides. Most important is the relation between the localized surface states, also referred to as *Tamm states* [59, 66], and the chemical composition of the outer *termination layer*. In an ideal scenario, the whole nanowire is surrounded and somehow capped with a homogeneous, native oxide, which would restrict the origin of the surface states to *intrinsic and static* properties and effects like the

already mentioned relaxation and reconstruction. However, in a more realistic scenario, there are a lot of *extrinsic* sources, including defects and traps in the oxide itself as well as different adsorbate atoms [67]. All of them have in common that they alter the potential landscape at the surface in a much more *dynamic* way. This can give rise to the formation of small potential wells, i.e. *intrinsic quantum dots*, induce *charge reconfigurations* or just result in pronounced *gate instabilities*. All of these effects are highly detrimental for Josephson junctions, qubits and phase coherent transport phenomena in general [68]. Unfortunately, they are also tightly bound to the *aspect ratio*, causing them to be even more pronounced if the nanowire diameter gets further reduced. Thus, lots of work has been put into the question if there is a way to stabilize and/or tailor the potential landscape at the surface [55]. One possible solution is the global, controlled in-situ deposition of a dielectric layer by means of *atomic layer deposition* [**ALD**] right after the nanowire growth or the deposition of the superconductor shell, respectively. Another way is the direct modification of the band structure itself, by using a wide bandgap material like GaAs as a template and subsequently cover it with a narrow gap material like InAs or InSb. These so-called **core/shell nanowires** [69] are the topic of the following section.

I

1.2. CORE/SHELL NANOWIRES

Parts of this section, including figures and captions, have been already published by the author in [70] and [71]. All corresponding segments have been marked by using the phrase "...has been taken from..." and, in case of the main text, by changing the fontstyle to italic.

Starting with the first publication in 2012, the field of *topological states* in nanowires has grown exponentially in terms of experimental and theoretical efforts, all aiming towards the realization of so-called *Majorana zero modes* [**MZM**]. However, while a lot of findings showed possible indications or potential signatures of these intrinsically protected states, no clear evidence could be found so far. The main reason are the extremely strict requirements that are needed to push the electronic system of a device into the **topological phase space**. Besides the fact that properties like *ultrahigh interface transparencies* or *strong spin-orbit interaction* are hard to achieve in a reliable way, they usually create an environment in which more conventional effects, like Andreev bound states, are driven into extreme manifestations of themselves, too. Thus, it becomes nearly impossible to distinguish between the trivial and topologial regime without sophisticated experimental techniques like **braiding**.

One possible solution for the hybridization of Majorana fermion pairs is the combination of different phenomena, e.g. the **Little-Parks** and **Aharonov-Bohm** effects. Another possibility was recently suggested and aims on the extension of the topological phase space itself by utilizing nanowires that consists of an insulating, wide band gap core material and a highly conductive shell in order to enhance the spin-orbit interaction by means of band engineering [2] and the emergence of topological corner states [72–76].

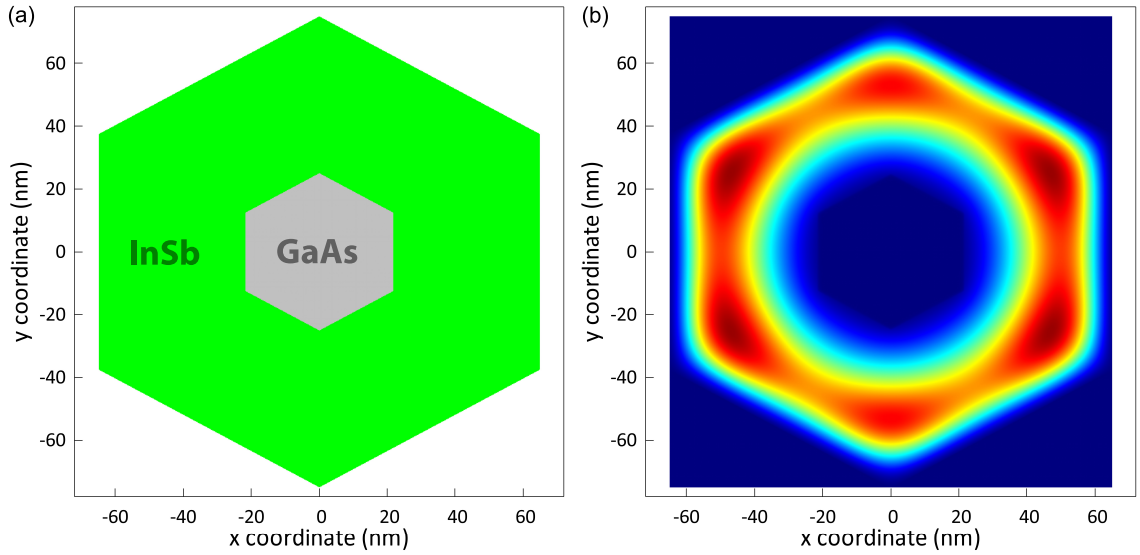

Figure 1.6 – *NextNano-based (see Refs. [77] and [78]) simulation of a typical GaAs/InSb core/shell nanowire with a core diameter of 40 nm and a shell thickness 45 nm. Based on the geometry shown in (a) and a grid width of 0.001 nm, one obtains a radial symmetric electron distribution, which is spatially localized at roughly 75% of the total shell thickness. Furthermore, following (b), there is a small but clearly obvious accumulation at the corners of the nanowire, even though it is not strong enough to create independent corner states. More information regarding the chosen simulation parameter are given in the main text.*

While the previously mentioned publication suggests to use a radial heterostructure based on a GaAs core and an InAs shell, no experimental signatures of spin-orbit interaction have been detected in phase-coherent transport [79–81], Hall effect measurements [79] or nanowire Josephson junctions based on this material combination [81, 82]. A full understanding of the underlying reason is still missing at the current state. However, the accepted theoretical picture is, that the *g-factor* is gradually suppressed for strong confinements due to the increased separation between electron and hole states [29]. In order to tackle this issue, a different material combination was chosen, eventually replacing InAs by InSb. The latter one provides a much larger bulk g-factor of 50, but comes with its

own challenges in terms of an increased lattice mismatch and a reduced mechanical and chemical resilience.

"Core-shell nanowires containing InSb suffer from the huge lattice mismatch to all other III-V semiconductors; the smallest between InSb and AlSb being still around 5.5 %. The lattice mismatch between GaAs and InSb is approximately 14%.[...] Band structure calculations of strained GaAs/InSb core-shell nanowires show significant changes in the band alignment as a function of the nanowire dimensions [83]. The possible alignments ranged from the conventional type I (straddling gap) to a type III (broken gap) band alignment. The latter is similar to the case of InAs/GaSb heterostructures, which results in a two dimensional topological insulator with dissipation-less edge states [84–86].[1]

However, under realistic experimental conditions, the required geometries can be not achieved. Especially the thickness of the InSb shell is a major issue, as everything below 16 nm results in a non-uniform, porous structure [71]. For thicknesses above this value, on the other hand, the nanowires can form stable heterostructures despite the huge lattice mismatch due to the formation of stacking faults.

Due to the basically strain-free configuration for transport channels that are not-too-close to the interface, the modeling of the structures becomes significantly easier. Figure 1.6 shows the probability distribution for a GaAs/InSb nanowire with a core radius of 20 nm and a shell thickness of 45 nm, respectively, resulting in a total diameter of 130 nm. The simulation was performed by means of the *contact block reduction* [**CBR**] [77] and *tight-binding* method within the *nextNano* software package [78] and assuming room temperature conditions and a carrier concentration of $n = 7 \cdot 10^{17}\,\mathrm{cm}^{-3}$. One can see, that the specific combination of an insulating core and a highly conductive shell ultimately results in a *ring*- or, in the case of a three-dimensional wire, *tubular-like* shape. The latter one is the main ingredient for various quantum phenomena, with the *Aharonov-Bohm effect* as the most intrigue one. Furthermore, the radial confinement leads to an additional quantization of the electronic system, adding so-called **angular momentum states** to the already present energy levels of the *2DEG*. Both topics will be further discussed in the next part of the theory chapter.

[1] paragraph taken from [71]

2

QUANTUM EFFECTS IN LOW-DIMENSIONAL SYSTEMS

2.1. ELECTRON INTERFERENCE EFFECTS

The earliest example of the real-world accessibility of a quantum mechanical phenome-non is the *double slit experiment*. Here, a photon, as the bosonic exchange particle of electromagnetism, is *pushed* into a regime in which it starts to exhibit its wave-like properties. By providing two different, but equally *favorable* paths, even a single photon starts to produce an interference pattern due to the temporary creation of two electromagnetic *partial waves*. This puts a spotlight on the potentially most striking feature of quantum mechanics: *Every path that can be taken will be taken*.

However, the previously described effect is not just restricted to photons or, in a more general way, bosons. In a properly designed sample, electrons can show a similar behavior, which is known as the *Aharonov-Bohm effect* [**AB**]. The key ingredient is the artificial creation of two possible paths, which enforces the virtual creation of electron partial waves, as shown in Fig. 2.1(a). For the optical variant of this two-path-system, i.e. the double slit experiment, the manipulation of the two partial waves is comparably simple and can be done by just changing the separation of both slits or the distance to the source or detector, respectively. For an electronic system, on the other hand, this is more complicated and eventually requires the application of an external magnetic or, in the case of the *Aharonov-Casher effect*, electrical field [87]. By doing so, it is possible to effectively alter the phase relation $\delta\varphi$ between both partial waves and therefore continously change the interference pattern between *constructive* and *destructive* and vice versa:

$$\delta\varphi = \Delta\Theta + \frac{e}{h}\oint \vec{A}\cdot \mathrm{d}\vec{s} = \Delta\Theta + 2\pi\frac{\Phi}{\Phi_0} \tag{2.1}$$

with $\vec{A} = \mathrm{rot}(\vec{B})$ as the vector potential, $\mathrm{d}\vec{s}$ as the full path and $\Delta\Theta$ as the initial phase relation. Assuming $\Delta\Theta = 0$, the system always interferes constructively if the ring-like system is penetrated by exactly $n = 0, 1, 2...$ **reduced flux quanta** $\Phi_0 = \frac{h}{e}$. The flux periodic nature of this effect leads to an additional oscillating conductance $\Delta G(\Phi)$ that superimposes the (ideally) field-independent background conductance G_o:

$$G = G_0 + \Delta G(\Phi) = G_0 + \cos\left(\Delta\Theta + 2\pi\frac{\Phi}{\Phi_0}\right). \tag{2.2}$$

However, this simple picture just holds under two conditions. Most importantly, the so-called **phase coherence length** l_φ needs to exceed at least some of the valid paths that can be taken by the electron partial waves. In an ideal system, this number is quite small, as the electron trajectories are just altered by boundary scattering at the borders of the ring structure. In a more realistic system, the traversing partial waves are also affected by impurities or lattice defects in the system. These *elastic* processes, caused by static scattering centers, do not only alter the absolute length scale over which the electron is affected by self-interference, i.e. l_φ. In addition, they will eventually change the exact shape of the wave trajectories and therefore the phase relation between both branches, as depicted

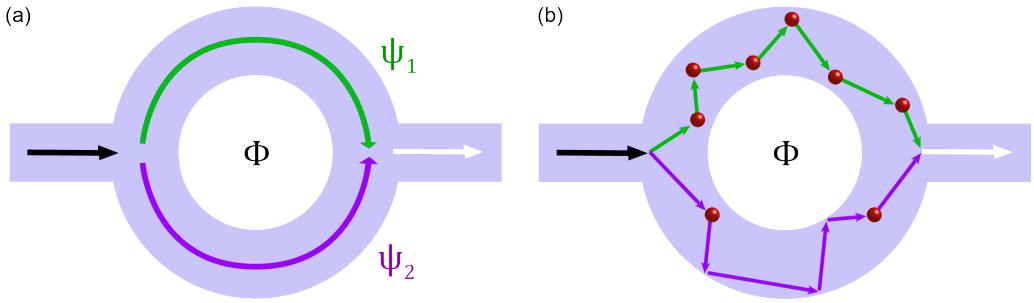

Figure 2.1 – *(a) The simplest realization of an Aharonov-Bohm system. Due to the inaccessible region in the middle of the ring, the incident electron splits into two partial waves with a fixed phase relation. For a finite magnetic flux* Φ*=B·A, the vector potential creates a phase difference between both branches, leading to a flux-dependent oscillation in the (magneto-)conductance with a period of one flux quantum* Φ_0*. (b) In real devices, the fully randomized distribution of scattering centers leads to an additional, constant phase offset even at zero magnetic field.*

in Fig. 2.1(b). Thus, in a real system, there is always an additional field-independent phase offset $\Delta\Theta$ between both partial waves, resulting in a more or less random conductance modulation ΔG at zero magnetic field.

It is also worth to mention, that a nanowire does clearly not fit into the classical design of an Aharonov-Bohm system. Here, the semi-classical electron trajectories are just bound to the ring-like structure, while for a nanowire, on the other hand, the extension in z-direction clearly surpass the ring area in the xy-plane. Thus, it is much more suitable to use a full quantum mechanical description based on the quantization of the **angular momentum**, resulting in the emergence of *l angular momentum states* for every single *n* state of the triangular quantum well (see section 1.1). Even though both pictures lead to the same oscillating, flux-periodic conductance, the latter one makes it much easier to introduce and describe more advanced phenomena like the influence of spin-orbit interaction and the *Zeeman effect* and the thereby caused splitting of the levels in energy and momentum. Both effects are described to a much broader extend within the experimental section VII, focusing on the phase-coherent transport in GaAs/InSb core/shell nanowires.

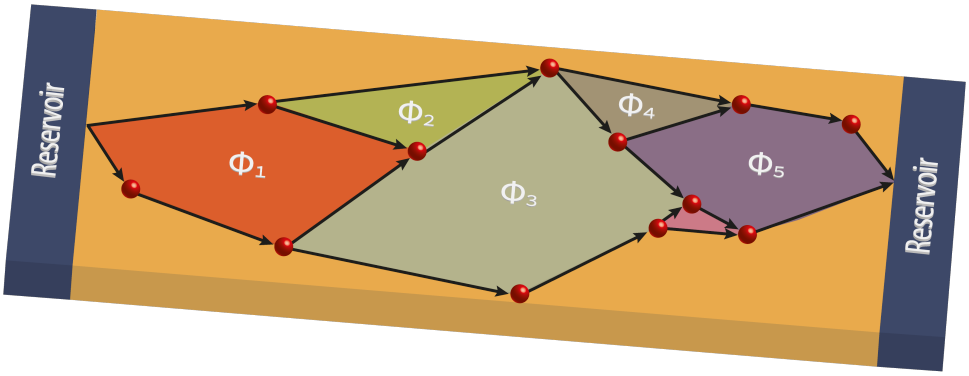

Figure 2.2 – *Multiple AB-ring-like scattering loops formed within a disordered two-dimensional layer, i.e. the top facet of a semiconductor nanowire. The electron partial waves that are propagating from the left reservoir to the right reservoir will accumulate different phase relations and flux periodicities, depending on the size of every individual loop. The signal at the right reservoir is the superposition of all individual oscillation pattern, resulting in a response that is unique for every sample.*

2.2. UNIVERSAL CONDUCTANCE FLUCTUATIONS

Even though the previously described, semiclassical picture of the Aharonov-Bohm effect in terms of traversing and interfering electron partial waves does not perform extremely well by including all semiconductor-specific quantum mechanical effects, it can still act as a good platform to describe other phenomena. Universal conductance fluctuations [**UCF**], as a superposition of multiple but not-too-many phase coherent scattering loops (i.e. small AB rings), are a transport feature which is unique for each mesoscopic system and therefore often referred to as the "footprint" of a sample. Although it is hard to directly compare the UCF patterns of multiple samples, the detailed analysis of there specific decay mechanisms under the influence of externally induced phase-breaking mechanisms, like an increase in temperature, can provide insights into characteristic parameters like the phase-coherence length l_φ or the mean free path l_e. Fig. 2.2 shows an exemplary loop structure within a two-dimensional transport layer, for example a single facet of a nanowire. At low temperatures, the resulting spectrum in Fig. 2.3 is a rich composition of both high- and low-frequency contributions, indicating the coexistence of coherent loops with various sizes and resulting in a modulation of the conductance:

$$\Delta G = \mathrm{rms}(G) = \sqrt{(G - \langle G \rangle)^2} \approx \frac{e^2}{h} \left(\frac{l_\varphi}{L} \right)^{\frac{3}{2}} . \tag{2.3}$$

Here, L corresponds to the channel length, which is usually given by the separation of the contacts.

However, if the temperature is increased, the rapidly oscillating components, which are related to larger loops, start to vanish. Based on that, it is possible to directly calculate the temperature-induced decrease of l_φ by means of the so-called **correlation field** B_c. It is generally obtained by the calculation of the field-dependent auto-correlation function of each single UCF trace

$$F(\Delta B) = \langle \Delta G(B + \Delta B) \cdot \Delta G(B) \rangle . \tag{2.4}$$

with itself and acts as a figure of merit for the maximum closed loop size in which the electron partial waves can coherently interfere, with

$$F(B_c) = \frac{1}{2} F(\Delta B). \tag{2.5}$$

Following the relation $\Phi = B_c \cdot A$, a larger correlation field is related to a smaller loop size and vice versa. The full theoretical framework, given by [88] separates the temperature-dependent decay of the UCF into three independent sections: Below a threshold temperature, $l_\varphi > w, L$, with w and L as the width of the channel and the contact separation, respectively. In this case, the maximum loop size is $A = L \cdot w$ and therefore not affected by changes in temperature. However, if the temperature increases above this value, l_φ becomes smaller than the larger one of the geometric dimensions, typically the contact separation L, and the transport channel splits into $N \cdot L / l_\varphi$ independent segments. Within this

regime, there is a direct correlation between the correlation field and the phase-coherence length:

$$B_c(l_\varphi) = \begin{cases} \frac{e}{h}\frac{\gamma}{L l_\varphi} & \text{for } w < L, \\ \frac{e}{h}\frac{\gamma}{w l_\varphi} & \text{for } w > L. \end{cases} \tag{2.6}$$

Here, γ = 0.42..1.3 [88–90] refers to an additional geometric correction factor, which takes into account that this model was initially devoloped for the characterization of two-dimensional samples. Although the phase coherence is maintained within each of the N sections, (parts of) the phase information are lost at the boundaries, ultimately leading to a significant and continuous damping of the fluctuation pattern in terms of both magnitude and possible frequency components. Finally, above a second threshold temperature, l_φ < w, L, which effectively suppresses the formation of coherent scattering loops, leading to a saturation of the correlation field and phase-coherence length, respectively.

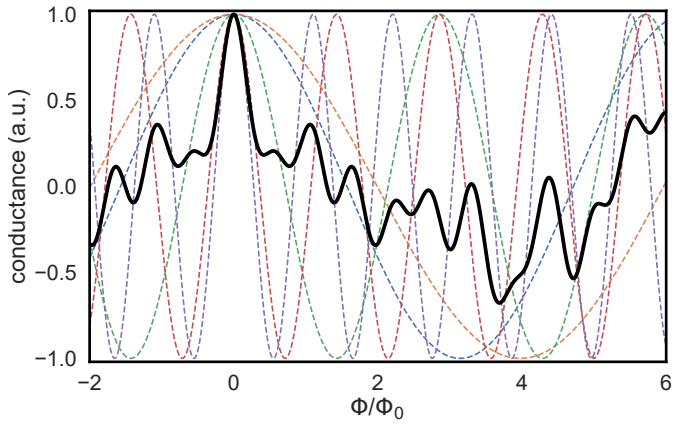

Figure 2.3 – *Simulated, exemplary magneto-conductance response of a disordered, two-dimensional sample with typical values for the phase coherence length and the mean free path. Due to the superposition of multiple Aharonov-Bohm-like periodic oscillations, one ends up with a seemingly random fluctuation pattern. If the degree of disorder and the corresponding number of coherent loops is too large, the measured signal will eventually evolve into the one of a classical device due to averaging effects.*

2.3. LOCALIZATION AND SPIN-ORBIT INTERACTION

Both the Aharonov-Bohm effect as well as universal conductance fluctuations originate from the combination of phase-coherent transport of multiple electron partial waves and more, for UCF, or less, for the AB effect, scattering events. However, for samples with a huge amount of disorder [91], it gets more and more likely to have a non-negligible amount of scattering paths that lead back to the point of origin, effectively blocking the partial waves from propagating through the sample along the extended states. This effect is tightly bound to the quantum mechanical nature of the electrons and therefore just occurs if the phase coherence length is sufficiently large thus that the carriers maintain there non-Markovian behavior, i.e. the dependency of the future evolution on the exact characteristics of the paths that have been taken. If the **localization length** l_{loc} exceeds the phase-coherence length l_φ, i.e. below the limit of the so-called *Anderson localization* [92], which can suppress the current flow through a sample completely, the correction to the conductance due to the *effectively* reduced numbers of charge carriers that are per time unit propagating through the sample is rather small, providing this effect its description as *weak localization* [**WL**].

A exemplary scattering center configuration is shown in Fig. 2.4. Here, the electron partial waves can propagate either clockwise or counter-clockwise around the artificially formed loop, which effectively connects the point of origin via back-scattering with itself. The enforced self-interference is either constructive, corresponding to a decrease in conductance, or, if one takes also the spin degree of freedom into account, destructive. The latter effect is thereby known as *weak antilocalization* [**WAL**] and will be discussed at a later stage.

In the case of a real sample with multiple scattering loops, one can write the total propagation probability [88] as

$$P(o,e) = |\sum_i A_i|^2 = \sum_i |A_i|^2 + \sum_{i\neq k} |A_i A_k^*|^2 . \tag{2.7}$$

Here, A_i refers to the probability along path i and o and e refers to the point of origin and the end point of the propagation, respectively. The first term $P_{class} = \sum_i |A_i|^2$ refers to the classical diffusion probability that is described within the *Drude model*. The second term $P_{qm} = \sum_{i\neq k} |A_i A_k^*|^2$, however, is of full quantum mechanical origin and thereby tightly bound to phase coherence. This provides also a way to quantitatively define the phase-coherence length as the maximum length scale that forms a closed loop and still produces a deviation from the classical conductance correction that is produced by P_{class}.

In the most simple picture, there are two different cases for the propagation of the electron partial waves: For adjacent start and end points o and e, all paths will have different phase relations, which ultimately cancels the quantum mechanical contribution due to averaging. However, if $o = e$, i.e. for perfect back-scattering along a closed loop, time reversal symmetry enforces the partial waves to accumulate the same *dynamic phase* and thereby to interfere constructively [93]. Thus, the quantum mechanical return probability is equal to twice the classical contribution $P_{class}(o \to e) = |A_{o\to e}|^2 + |A_{e\to o}|^2$. This results in a decreased chance for charge carriers to propagate through the sample and therefore induces an *increase* in resistance, as depicted in Fig. 2.4.

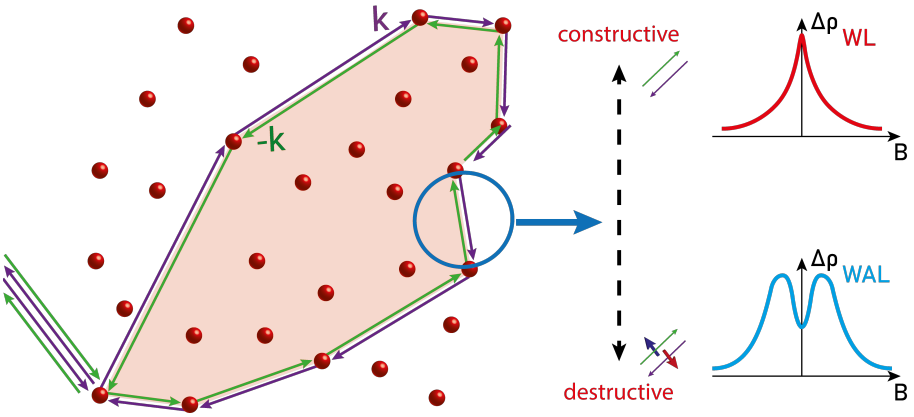

Figure 2.4 – *Schematic overview of two time-reversed electron trajectories in a closed quantum diffusive path. Since the lengths of the two paths are exactly equal, constructive interference always occurs at the endpoint of the two paths, resulting in* ***weak localization****. The latter is gradually destroyed if a magnetic field is applied perpendicular to the system. However, if the system features a significant degree of spin-orbit interaction in terms of the Rashba or Dresselhaus effect, the spin degree of freedom of the propagating electrons have to be taken into account. The corresponding precession of the spin, or, to be more precise, the non-commutativity of the spin rotation operators $AB \neq BA$ results in the* ***weak antilocalization*** *effect.*

While the full theoretical description of the conductance correction relies on a lot of sample specific parameters like the *dimensionality* or the *channel width* [88, 94, 95], it can be easily approximated for the special case of a quasi one-dimensional channel and a phase coherence length that surpasses the mean free path, i.e $l_\varphi \gg l_e$. In this case, which basically describes a typical semiconductor nanowire, the conductance correction is $\Delta G = e^2/h \cdot l_\varphi / L = G_o l_\varphi$. Here, G_o refers to the *conductance quantum* and L is the sample length. Thus, weak localization is most prominent in low-dimensional structures. Similar to the Ahanorov-Bohm effect and universal conductance fluctuations are the electron partial waves influenced by an applied magnetic field via the corresponding vector potential of the enclosed magnetic flux. This leads to the repeal of the time-reversal symmetry within the closed scattering loops and changes the formerly global constructive interference into one that is different for every individual ring-like structure. However, in contrast to UCF, the amount of scattering loops is so large, that the superposition of all different oscillatory contributions effectively suppresses the initial conductance correction. The exact decay behavior of the localization feature is thereby correlated with the phase-coherence length l_φ, the mean free path l_e,the sample dimensionality, channel width, the magnetic length $l_m = \sqrt{\hbar/eB}$ and the magnetic dephasing length l_B [88, 95]. The latter one also marks an upper boundary for the maximum loop size, as only those with $l_B^2 < D\tau_B$ can contribute to the weak localization effect [88], with τ_B as the magnetic dephasing time and D as the diffusion constant. In the case of diffusive nanowires, the magnetic field dependent decay of the conductance correction simplifies to an expontential decay e^{-t/τ_B} [94, 96], which is schematically depicted in Fig. 2.4.

The effective *trapping* of charge carriers in disordered, nano-sized structures due to (weak) localization is a fundamental effect that can be observed in a broad spectrum of materials and devices like topological insulator layers [99] and flakes [100], 2D materials like graphene [101] or semiconductor nanowires [102]. However, this picture falls too short for systems that have a significant interaction between the atoms of the crystal lattice and the propagating electrons, i.e. *spin-orbit interaction* [**SOI**] like the *Rashba effect* [103–105], i.e. a magnetic field due to a band-bending-related electric field and the *Dresselhaus effect* [106], that results from the crystal field in systems which lack inversion symmetry. In *topological insulators* [**TIs**] or semiconductor devices based on InAs or InSb, the spin component of the moving charge carriers can not be neglected anymore. in those systems, the electron spin is tightly bound to the motion of the carriers, resulting in an additional *precession movement* [107–109]. The change of the spin orientation can either happen while the electron is propagating between two scattering centers, that is referred to as the **D'Yanokov-Perel effect** [110], or during a single scattering event, i.e. the so-called **Elliot-Yafet mechanism**[111, 112]. Both phenomena have in common that they correlate the final spin orientation with the order in which the scattering events

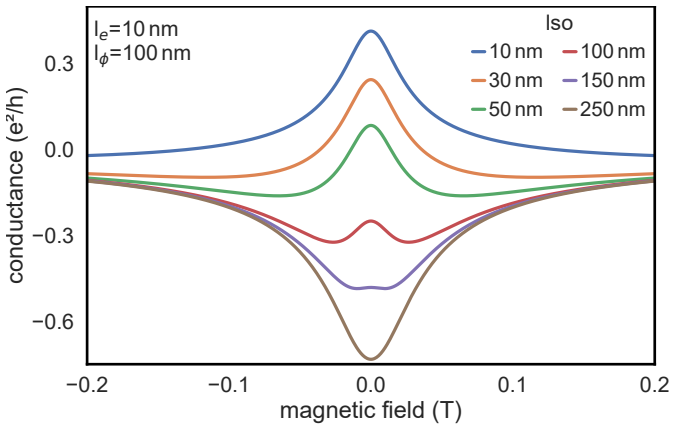

Figure 2.5 – *Simulations of the quantum mechanical conductance correction around zero magnetic field caused by the formation of closed-loop trajectories in a highly disordered sample. The calculations were performed by utilizing the theory frameworks presented in [95, 97, 98]. Assuming typical values for an GaAs/InSb core/shell nanowire, i.e. a mean free path $l_e = 10\,nm$ and a phase-coherence length $l_\varphi = 100\,nm$, one can see how the magnitude and sign of the conductance evolves for different values of the spin-orbit scattering length l_{SO}. For small values, the spin of the electron freely precess during its propagation, resulting in a conductance maximum due to antilocalization. If l_{SO} increases, the magnitude of the peak is gradually reduced until, at some point, it swaps its sign and turns into weak localization.*

have occurred. This effectively breaks the *time-reversal symmetry* of the system, as the two partial waves within a single scattering loop now provide different outcomes. In terms of a rotation matrix $\bar{R}$, one can now rewrite the two spin components as $\langle s_{\rightarrow}| = \bar{R}\,\langle s|$ for the clockwise $\langle s_{\leftarrow}| = \bar{R}^{-1}\,\langle s|$ for the counter-clockwise propagation. If one assumes again a large number of scattering loops with different sizes, the final spin states follow a statistical distribution [107], which ultimately changes the average phase relation from 0 to 2π. For fermions, this is equal to a sign reversal of the wave function and therefore a switch from *constructive* to *destructive* interference. Accordingly, the corresponding conductance correction changes from negative to positive, as shown in Fig. 2.4, providing this phenomena its name as *weak antilocalization* [**WAL**].

The analysis of the WAL feature can provide information about important device parameter like the phase coherence length l_φ or the exact strength of the spin-orbit interaction. Therefore, over the years, more and more sophisticated theoretical frameworks have been developed in order to improve the quality of fitting functions for the corresponding peak in conductance and its outskirts [113–116]. However, it should be mentioned, that up to the end of this project, there has been no *better* theoretical framework that could describe the exact mechanisms of SOI in GaAs/InSb as in InAs nanowires or other systems. Private correspondence with various theoretical physicists [117–119] have revealed, that the derivation of a full quantum mechanical model for this system is extremely complicated due to the involvement of multiple sub-bands, which effectively induces some additional *inter-band Rashba* and *inter-band Dresselhaus* contributions and dramatically increases the parameter space. Thus, within this project, the modeling of the WAL phenomenon was restricted to a much more simple approach [95, 97, 98], which basically just depends on the ratio between the *mean free path* l_e, the *phase coherence length* l_φ and the so-called *spin-orbit scattering length* l_{so}. Fig. 2.5 shows the shape and curvature of different magneto-conductance traces for various values for l_{so}, but constant l_e and l_φ. As can be seen, as long $l_{so} \leq l_\varphi$, one obtains a peak around zero magnetic field, indicating the presence of WAL. However, for $l_{so} \gg l_\varphi$, the conductance correction changes its sign, which corresponds to a transition to *weak localization*. The chosen model provides a reasonable description for the experimental findings in GaAs/InSb core/shell nanowires which are presented in chapter VII.

3

MESOSCOPIC JOSEPHSON JUNCTIONS

3.1. MACROSCOPIC JOSEPHSON JUNCTIONS AND CHARACTERISTIC PARAMETERS

Superconductivity, as the phase change of a normal conducting material into a dissipationless state due to the phonon-mediated, attractive interaction of electrons is one of the most striking phenomena in solid state physics. The newly formed, collective ground state of the system opens up a forbidden area in the density of states, in which no single particle levels are allowed. The total energy budget is thereby referred to as Δ, the so-called superconducting gap. Even though the transport below this energy value is not necessarily fully dissipationless, it is still dominated by the superconducting properties and all its unique side effects, like magnetic field screening, i.e. the Meißner-Ochsenfeld effect, and a huge set of possible exotic excitations. Above Δ, however, the so-called **Cooper pairs**, are destroyed, rendering the system back into the normal state.

After the initial theoretical description within the Bardeen-Cooper-Schrieffer (**BCS**) framework, subsequent progress has been made in terms of a broader understanding of superconductivity. The Ginzburg-Landau(**GL**) theory uses the Landau theory of second-order phase transitions to derive an additional classification system, which breaks down the whole set of existing superconductors into **type-I** and **type-II**, depending on their specific field-screening behavior. More importantly, they defined a macroscopic wavefunction $\Psi(\vec{r}) = \Psi \cdot \exp(i\phi)$ and a corresponding **complex order parameter field** $|\Psi|$, thus providing an combined description of the whole *Cooper pair condensate*.

Following basic quantum mechanics, the macroscopic wavefunction can *leak* into non-superconducting elements, i.e. extending the Cooper pair density across a barrier or interface within a certain length scale. This so-called **proximity effect** is schematically shown in Fig. 3.1 (a). Assuming that the whole semiconductor-normal conductor (**SN**) system is in the *dirty limit*, i.e. that the elastic mean free paths of both materials, l_S and l_N, are smaller than the other characteristic length scales, the coherence length can be written as

$$\xi_{S,N} = \sqrt{\frac{\hbar D_{S,N}}{2\pi k_B T_c}}. \tag{3.1}$$

Here, T_c refers to the critical temperature of the superconductor and $D_{S,N}$ are the diffusion constants of the superconductor and the normal conductor, respectively. Within these length scales, the density of states in the superconductor and normal conductor are *coupled* in the sense, that there is a finite, exponentially decaying Cooper pair density within the normal conductor. Concurrently, the order parameter of the superconductor becomes spatially varying towards the interface of both material, thus, the corresponding energy scale is reduced to an *effective gap* $\Delta_S(x)$ with respect to the bulk value Δ. This inverse proximity effect is especially important for superconductor-superconductor-normal conductor [SS$'$N] structures, in which the two superconductors have different gap sizes. However, in the case of a non-ideal interface, this effective gap is further reduced inside of the normal conductor. The so-called **induced proximity gap** Δ_p and the **interface transparency** T, as its corresponding figure of merit, is one of the most important properties of SN structures.

The previously described phenomena can be further extended if two SN stacks are combined i.e. by forming a *SNS sandwich*. In the case of a not-to-thick barrier, the two corresonding macroscopic

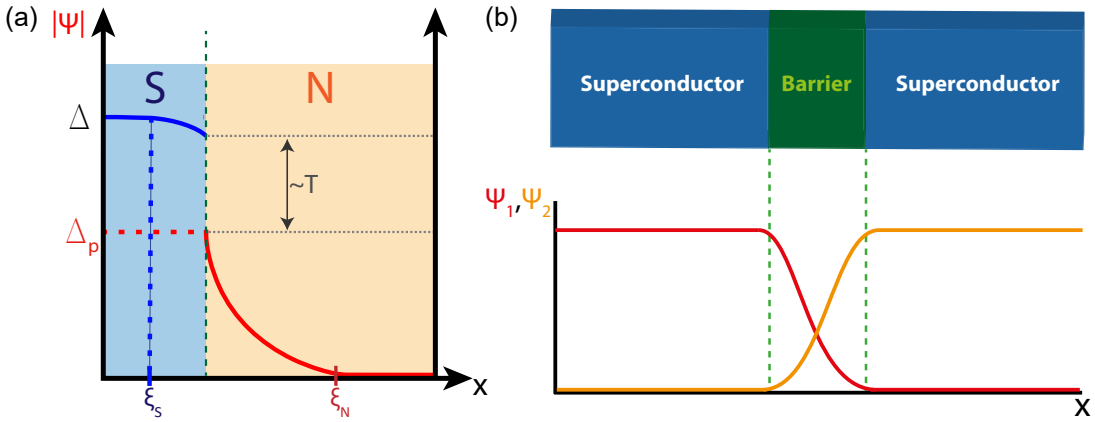

Figure 3.1 – *(a) Leakage of the macroscopic wavefunction into a non-superconducting element, e.g. an insulating barrier, over the length scale ξ_N (bright red), the so-called* ***coherence length****. Depending on the coupling transparency T, the surface value of the superconducting gap, Δ_s, is reduced to an* ***induced proximity gap*** *Δ_p. Concurrently, the order parameter $|\Psi|$ inside of the superconductor is altered over the length scale ξ_S (dark blue), leading to a spatial variation of the gap with respect to the undisturbed bulk value. (b) Schematics of a Josephson junction based on a SNS sandwich structure. In the case of a short channel length L and high interface transparencies T_1, T_2, the two macroscopic wavefunctions can leak into the normal conducting region. The overlap of both contributions leads to an induced superconducting channel and a finite tunnel probability of Cooper pairs.*

wavefunctions $\Psi_1(\vec{r})$ and $\Psi_2(\vec{r})$ can overlap within the normal conducting region and, depending on the **phase difference** $\delta = \phi_1 - \phi_2$, form an *artificial* superconducting channel, through which Cooper pairs can be transferred from one electrode to the other by means of **tunneling**. This is shown in Fig. 3.1 (b). The relevant criteria is the ratio of the channel length L with respect to both coherence lengths $\xi_{S,1}$ and $\xi_{S,2}$, respectively, and therefore the interface transparencies T_1 and T_2. The resulting device, a so-called **Josephson junction**, derives all of its properties, i.e. the effective current flow, the voltage drop and its response to electromagnetic fields, from the phase difference δ. Thus, it is an example for a full *macroscopic quantum system*, which shows an *intrinsic Aharonov-Bohm-type behavior*, as the current flow can be externally controlled by means of a phase-tuning.

The theoretical description of a Josephson junction is based on a set of formulas, the so-called **Josephson equations**, of which the first one is the **current-phase relationship** or **DC Josephson effect**

$$I_s(\delta) = I_c \sin(\delta). \tag{3.2}$$

Here, I_c refers to the *maximum supercurrent* of the device, which is, following the *Ambegao-kar-Baratoff relation* [120], directly proportional to the superconducting gap at T = 0 K and the **normal state resistance** R_N

$$I_c = \frac{\pi \Delta^2}{4 e R_N T_c}. \tag{3.3}$$

However, for real systems, the maximum supercurrent is further influenced by other parameters, e.g. the density of states within the superconductor and normal conductor, the interface transparency or the junction type, i.e. if it has to be considered as *ballistic* or *diffusive* [121].

Figure 3.2 gives an example for a typical IV curve of a Josephson junction. One of the most remarkable features is the existence of a finite current flow without any voltage drop, the so-called **zero voltage state**. However, it should be stressed, that this phenomena just refers to the energy contribution, which is externally accessable. Internally, the current flow is associated with a change in the *total free energy*, i.e. $dF = dF_1 - dF_2 = I(V_1 - V_2)dt$ [122]. By applying the already introduced theoretical framework for Josephson junctions, this thermodynamic-based argument can be translated into a phase-dependent *inner energy*

$$U(\delta) = E_J(1 - \cos(\delta)) \tag{3.4}$$

with the **Josephson energy**

$$E_J = \frac{\Phi_0 I_c}{2\pi}. \tag{3.5}$$

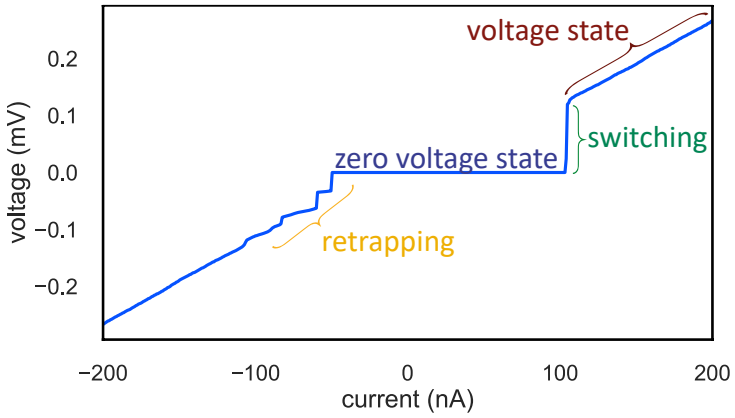

Figure 3.2 – *Exemplary measurement of a nanowire Josephson junction coupled to a transmission line. For currents below the critical current I_c of the junction, the device exhibits a plateau-like section that corresponds to the zero voltage state. Above I_c, the system switches into the voltage state and the transport becomes dissipative, effectively mimicking the response of a purely ohmic device. The corresponding current value in the forward direction, the so-called switching current (positive branch), is thereby usually larger than its counterpart in the backward direction, i.e. the retrapping current I_r. The step-like features in the negative branch are thereby related to the absorption of self-emitted photons caused by the AC Josephson effect*

If the phase across the junction is changed, the corresponding change in energy is

$$U(\delta_1) - U(\delta_1 + \Delta\delta) = E_J(\cos(\delta) - \cos(\delta_1 + \Delta\delta)) \tag{3.6}$$

which, for small $\Delta\delta$, can be Taylor-expanded to

$$dU(\delta) = \frac{E_J \sin(\delta)}{I_c \cos(\delta)} dI = \frac{L_J}{cos(\delta)} I_c dI = L_t(\delta) I_c dI \tag{3.7}$$

with the **Josephson inductance**

$$L_J = \frac{\Phi_0}{2\pi I_c}. \tag{3.8}$$

The latter one, which is often referred to as **kinetic inductance**, is one of the most important properties for qubit applications and superconducting circuits. It is tightly bound to the motion of Cooper pairs, or, to be more specific, to their inertial mass and therefore to the specific superconducting material. While this will be further discussed in the section focusing on the Gatemon qubit and the implementation of microwave circuits, at this point, it should just be stressed that L_J is a **nonlinear inductance**, which does not rely on any magnetic field rather than the **absolute value of the critical current** I_c.

If the applied signal exceeds the maximum current of the junction, i.e. the critical current I_c, the Cooper pairs break down into electron- and hole-like quasiparticles, which renders the transport back into the dissipative regime. Thus, the device suddenly switches into the so-called **voltage state**. However, while both the zero voltage state as well as the dissipative region can be explained within the already introduced theoretical framework, there are additional features which need some deeper insights into the *dynamics* of Josephson junction.

For the measurement shown in Fig. 3.2, the sweep direction was set from negative to positive. It can be seen, that the measurement shows a pronounced asymmetry in the sense, that for the positive branch there is a clear and direct jump from the zero to the dissipative state at $I = I_c$. However, for the negative branch, the transition between both regimes starts at a slightly smaller I_c. Additionally, in contrast to the positive region, it takes place in intermediate steps. This effect is referred to as **retrapping** and is, together with the small variation in the positive and negative I_c, a signature of the underlying complex electronic composition of a Josephson junction. To be more precise, an individual junction does not only consists of a single inductance rather than of a parallel circuit of a resistive, capacitive and inductive component, which is theoretically treated within the so-called *resistively and capacitively shunted junction* (**RCSJ**) model proposed by Stewart and McCumber [123, 124].

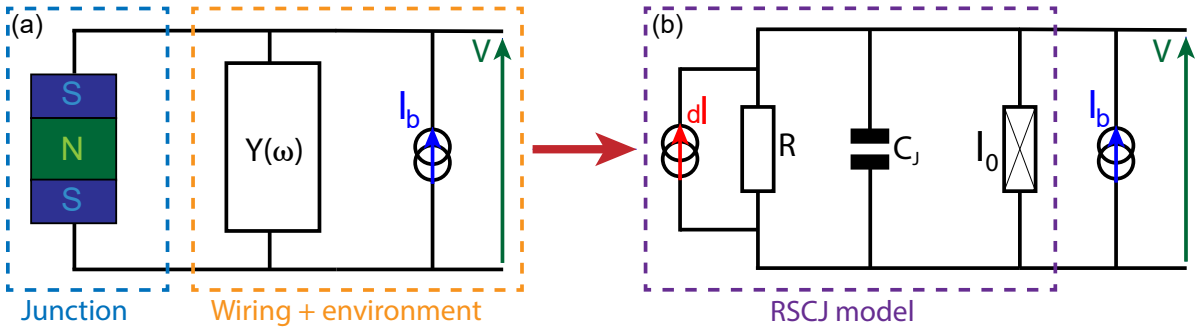

Figure 3.3 – *(a) Schematic model of a Josephson junction embedded in an electromagnetic environment, modeled by the admittance $Y(\omega)$. The device is supplied with a bias current I_b. (b) Equivalent circuit of the same device in terms of the **RCSJ model**. The latter consists out of a pure Josephson element that is shunted by the Josephson capacitance C_J and an intrinsic shunt resistor R. Even though the former is of purely ohmic nature, the finite temperature T of the system induces current fluctuations of the order δI, which are represented as an additional noise source in parallel to the device.*

The schematic structure of a Josephson junction coupled to an electromagnetic environment is shown in Fig. 3.3. The latter one is thereby modeled by means of a dynamic perturbation $Y(\omega)$, which combines all resistive, capacitive and inductive contributions of the leads and the wiring, the bias current I_b and the corresponding voltage drop V. This system can be transposed into a parallel circuit of a pure Josephson inductance, defined by the unperturbated critical current I_0, a shunt capacitor C_J and an *internal* shunt resistor R. The latter one is affected by fluctuations in the population of states, i.e. an effective *electron temperature* which is usually larger than the temperature of the surrounding system. This **Johnson-Nyquist**-type electronic perturbations lead ultimately to fluctuations of the applied current, represented by the parasitic and noisy current source dI parallel to the shunt resistor.

By combining the Josephson relations with the Kirchhoff law for the circuit shown in Fig. 3.3, one obtains

$$\frac{2e}{\hbar}V = \frac{\partial\delta}{\partial t} \tag{3.9}$$

and

$$C_J\left(\frac{2e}{\hbar}\right)^2\frac{\partial^2\delta}{\partial t^2} + \frac{1}{R}\left(\frac{\hbar}{2e}\right)^2\frac{\partial\delta}{\partial t} + E_J[\sin(\delta) - s] = \frac{\hbar}{2e}\delta I \tag{3.10}$$

with $s = \frac{I_B}{I_0}$ as the so-called *reduced bias current*. These equations are similar to the motion of a particle with a finite mass that is moving down a tilted chain of potential wells [125, 126]. The exact mechanical and electrical analogies are given in Table 3.1.

Property	**Circuit picture**	**Particle picture**
position	δ	x
mass	$C_J\frac{\hbar^2}{4e^2}$	m
damping	$\frac{1}{RC_J}$	D
velocity	$V\frac{2e}{\hbar}$	v
noise factor	$\frac{\hbar}{2e}dI$	ξ
potential shape	$U(\delta,s) = -E_J[\cos(\delta) + s\delta]$	$U(x,s) - E_J[\cos(x) + sx]$
correlation	$\langle dI(t)dI(t')\rangle = \frac{2k_BT}{R}d(t'-t)$	$\langle\xi(t)\xi(t')\rangle = \frac{2mD}{(t'-t)}$

Table 3.1 – *Overview of the parameter within the RCSJ model and their mechanical analogues.*

Here, the potential is of special interest, as it describes a **washboard-like** energy landscape (see Fig. 3.4 (a)). The *inner energy* U is thereby equal to the Josephson energy E_J, which was introduced in Eq. 3.5 and is modified by the phase difference across the junction δ and the ratio between critical

current I_c and the externally *applied* bias current I_b. Based on the ratio of both current, i.e. s. one can define two different transport regimes of a Josephson junction

- For $0 \leq s \ll 1$, i.e as long as $I_b \ll I_c$, the particle becomes fully trapped in one of the potential wells, effectively suppressing any possible *motion*. This situation is the *DC Josephson effect* (see Eq. 3.2), in which a constant phase results in the supercurrent branch of the *zero voltage state*.
- As soon as the bias current surpasses the critical current of the junction, i.e. $s > 1$ and $I_b > I_c$, the junction **switches** into the so-called *running state*. Here, the propagation of the particle is not longer affected by the underlying shape of the potential, as the induced tilt is much larger than the height difference between adjacent wells. Thus, the phase starts to continuously evolve in time, which corresponds to a finite voltage drop.

Even though this naive picture is suitable to describe the basic characteristics of a Josephson junction, e.g. how the system converts an external voltage drop into an internally stored energy, it is not sufficient to describe a realistic system. Most important is the *stochastic nature* of the switching current. The already introduced current fluctuations dI, which originate from various perturbation channels like thermal photons or parasitic high-frequency contributions, induce some additional *phase noise* $d\delta$ on top of the time-dependent phase difference δ. Therefore, the particle starts to oscillate in the corresponding energy minimum of the potential well, effectively shifting the whole system into a **metastable state** with a finite probability for the particle to *escape* out of the well even deep inside of the zero-voltage state. Sticking again to the picture of the washboard potential, one can now use two parameters to model the escape chance and rate.

In order to simplify the system, one can use the *relative barrier height*

$$\delta U(s) = E_J \left[2\sqrt{1-s^2} - s\,(\pi - 2\arcsin(s)) \right] \tag{3.11}$$

rather than the exact shape of the tilted energy landscape. Here, a large barrier leads to a small escape rate and vice versa. Additionally, the current noise dI effectively acts as a small *AC signal*, which leads to a coherent oscillation of the particle even in the minimum of a potential well. The characteristic frequency of those oscillations is the *plasma angular frequency*

$$\omega_p(s) = w_{p,0} \left(1 - s^2\right)^{1/4}, \tag{3.12}$$

with

$$\omega_{p,0} = \frac{1}{\sqrt{L_J C_J}} \tag{3.13}$$

as the bare plasma frequency. Both parameters together give rise to a third case within the model of the tilted washboard potential: The so-called **phase diffusion** or **retrapping** regime. If one assumes an extremely tilted potential, as shown in Fig. 3.4 (b), and therefore a small barrier height, the noise-induced particle oscillations can be so strong that they ultimately *push* the particle out of the minimum. The resulting motion is referred to as *phase diffusion*, as it is just driven by the shape of the underlying potential and typically correlated with a extremely small phase velocity. The latter one is also the reason why the particle eventually gets stuck again in a energy minimum - i.e. *retrapped* - until the next diffusive motion sets in. The outcome is a set of step-like features on the return branch rather than a sudden voltage jump, as already shown in Fig. 3.2. However, a comparable behavior can also occur in forward direction, i.e. for an increased bias current. Here, the combination of a small barrier and (large) phase fluctuations can alter the maximum current up to which the junction can maintain a dissipationless current flow, effectively changing the switching current to a more-or-less *stochastic* variable. This effect is usually tackled experimentally by measuring *switching statistics*, which is exemplary depicted in Fig. 3.5(b). One can see, that I_c follows an almost normal-distributed behavior, with a clear maximum at 18.9 nA and a variation width of approximately 5 %.

The exact current-voltage characteristics of a Josephson junction, as a dynamic process, relies on the *internal damping behavior*. Within the *RCSJ model*, one usually separates into **underdamped**,

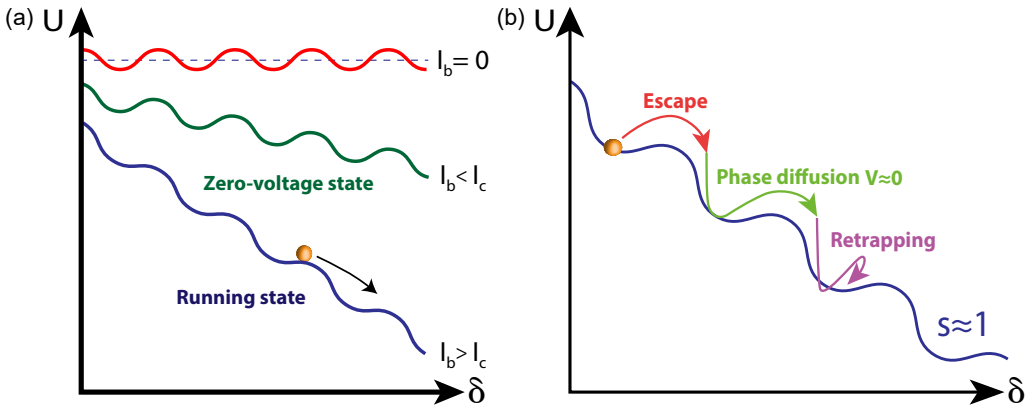

Figure 3.4 – *(a) Tilted washboard potential of a Josephson junction associated to the dynamics of the phase in absence of thermal fluctuations . For s< 1, i.e. bias currents that are smaller than the critical current of the device, the potential presents wells with a large barrier height which will eventually trap the particle in one of the local minima. This corresponds to the* ***zero-voltage-state*** *s=0. For s≥ 1, on the other hand, the wells effectively disappear and the particle can freely run down the washboard potential, resulting in the dissipative* ***voltage state****. (b)Tilted washboard potential of an overdamped Josephson junction. The green arrow indicates the effect of phase diffusion, usually caused by thermal activation, while the purple one corresponds to the recapturing process of the fictitious particle.*

overdamped and **normal** junctions. The exact distinction is thereby given by the so-called **Steward-McCumber parameter**

$$\beta_c = \frac{\omega_c^2}{\omega_{p,0}^2} = \frac{\omega_c}{\omega_{RC}} = \frac{2e}{\hbar} I_c R^2 C_J \quad (3.14)$$

with

$$\omega_{RC} = \frac{1}{RC_J} \quad (3.15)$$

as the **damping rate** and

$$\omega_c = \frac{R}{L_J} = \frac{2e}{\hbar} V = \frac{2\pi}{\Phi_0} V \quad (3.16)$$

as the **relaxation rate** of the system, with $\Phi_0 = \frac{2e}{\hbar}$ as the *reduced flux quantum*[1]. Accordingly, one can define a **quality factor** for the system, which connects the decay of the oscillation amplitude with the oscillation period:

$$Q = \frac{RC_J}{\sqrt{L_J C_J}} = \sqrt{\beta_c} \quad (3.17)$$

Based on that, the system can now be clearly separated into the already mentioned categories:

$\beta \ll 1$ Small capacitance or small resistance ⇒ **Overdamped**

$\beta \gg 1$ Large capacitance or large resistance ⇒ **Underdamped**

In the case of semiconductor nanowires, the formed junction usually resides at the border between the *normal* and *underdamped* regime due to the comparably large normal state resistance [127, 128]. This has important consequences if it comes to measurements that fully rely on dynamic processes in the junction, e.g. single state transitions in a qubit and their corresponding decoherence rate, due to the possibility of additional phase jumps of (fractions of) π. In order to further analyze the internal relation between the *phase evolution* and *Cooper pair transport*, i.e. the current-phase-relation, one typically uses *AC-driven* measurements based on the **(inverse) Shapiro effect** or so-called *superconducting quantum interference devices* [**SQUIDs**]. Both concepts are further discussed in the subsequent sections.

[1] In a superconducting system, the transport is carried out by Cooper pairs, i.e. two coupled electrons. Thus, a reduced flux quantum is equal to **half** a flux quantum of the Aharonov-Bohm effect or other electron interference phenomena

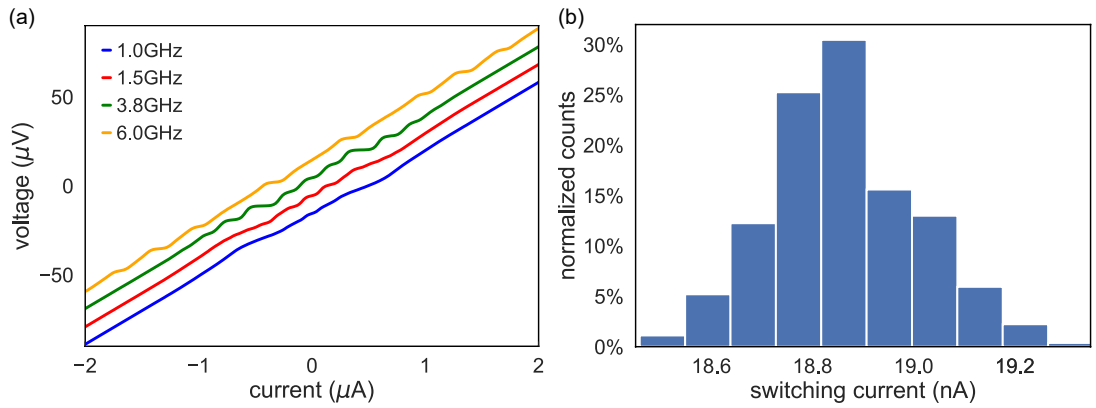

Figure 3.5 – *(a)Integer Shapiro steps in the current-voltage characteristics of an InAs/Al nanowire Josephson junction for different frequencies and a constant microwave power of -10dBm. One can see how the separation between adjacent steps becomes larger and larger if the frequency is increased.(b) Switching statistics for an InAs/Al fullshell nanowire Josephson junction based on a set of 1000 individual measurements.*

3.1.1. SHUNTED JOSEPHSON JUNCTIONS

The most important outcomes of the last section are the facts, that (a) in a Josephson junction $I = f(\delta)$, i.e. the **first Josephson equation**, and (b) the dynamic behavior can be described in terms of the **tilted washboard potential**. If one extends the picture of the latter one, it is easily understandable, that a sufficient *tilt* of the underlying potential landscape always results in a *time-dependent evolution of the phase*. In electronics, a potential difference is equal to a *voltage drop*, which ultimately leads to the *second Josephson equation* [122] or **voltage-phase relation**:

$$\frac{\partial \delta}{\partial t} = \frac{2\pi}{\Phi_0} V. \tag{3.18}$$

Combining both equations, one can see that the switching current I_s of a SNS device is oscillating with the so-called **Josephson frequency** f_J

$$I_s = I_c \sin(\delta(t)) = I_c \sin\left(\frac{2\pi}{\Phi_0} V t\right) = I_c \sin\left(2\pi f_J t\right). \tag{3.19}$$

The latter is a fundamental property of every Josephson junction, with the **constant frequency-voltage relation**

$$\frac{f_J}{V} \approx 0.484 \frac{\text{GHz}}{\mu\text{V}} \tag{3.20}$$

This has important consequences. If the junction is exposed to an additional *AC driving source* with a fixed frequency, like an *antenna* as a dedicated photon source,

$$V(t) = V_{dc} + V_{ac} \cos(\omega_{ac} t) \tag{3.21}$$

the *internal* RLC circuit starts to oscillate. Re-evaluating the voltage-phase relation, one obtains now

$$\delta(t) = \delta_0 + \frac{2\pi}{\Phi_0} V_{dc} t + \frac{2\pi}{\Phi_0} \frac{V_{ac}}{\omega_{ac}} \sin(\omega_{ac} t) \tag{3.22}$$

Here, δ_0 refers to an *initial phase offset*, which is important for so-called π- or ϕ_0-junctions [129–131]. In combination with the current-phase relation, the final junction response takes the form

$$I_s(t) = I_c \sin\left(\delta_0 + \frac{2\pi}{\Phi_0} V_{dc} t + \frac{2\pi}{\Phi_0} \frac{V_{ac}}{\omega_{ac}} \sin(\omega_{ac} t)\right) \tag{3.23}$$

which is a *superposition* of the constant frequency $\omega_{dc} = \frac{2\pi}{\Phi_0} V_{dc}$ and an additional, sinusoidal phase evolution component. Even though the external driving source and the Josephson junction are thereby nominally *desynchronized*, one can always find a certain ω_{ac} that, and its multiples n, can couple to the constant junction frequency ω_{dc}. The resulting *coherent resonance* is referred to as **phase locking** and gives rise to the so-called **Shapiro effect** [132]. Here, one can distinguish two different current responses:

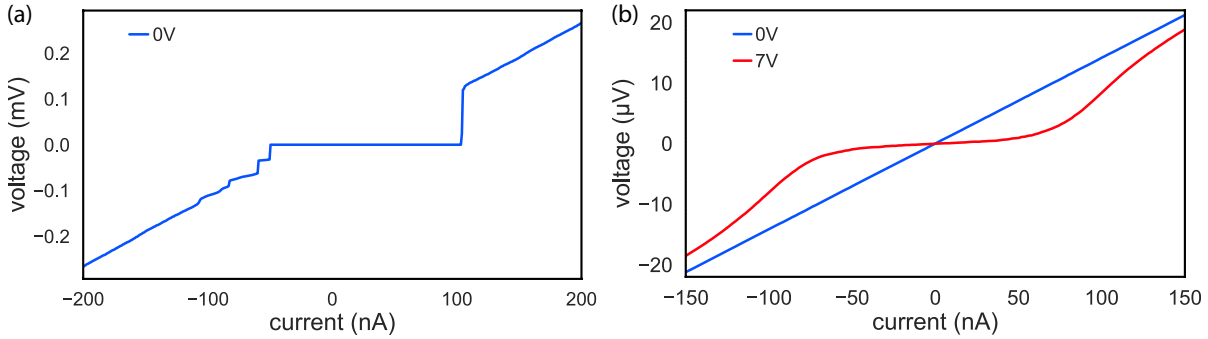

Figure 3.6 – *Comparison of the current-voltage characteristics of a nanowire Josephson junction without (a) and with (b) an external shunt resistor. The curve in (a) shows a pronounced switching event, that bypasses a comparably large voltage range of roughly 150 µeV. In terms of emission or Shapiro measurements, this would correspond to a frequency range of 10th of GHz that would not be experimentally accessible. (b) If a shunt resistor R is used, on the other hand, the voltage drop increases gradually. If the device can also be pushed into pinch-off, one can use the residual IV curve (blue) to extract the exact value of R. The latter information can then be used to correct the respond of the actual Josephson junction for phase fluctuations and effectively reveal the real current flow through the junction, which contains information about the onset of MAR events, the junction capacitance etc.*

$nV_{ac} \doteq V_{dc}$ The junction is in resonance with the external drive. In the picture of the tilted washboard potential, this is equal to the case in which the induced *up-and-down movement* of the particle within a single potential well is synchronized with the periodic de- and increase of the tilt of the energy landscape. Subsequently, and similar to an increase of the oscillation amplitude for a swing, the particle gains more and more *height* until it ultimately *jumps* into an adjacent (or n-sections afield) potential well. This temporary switches the junction into the running state, inducing a sudden voltage *jump*.

$nV_{ac} \neq V_{dc}$ In this case, the oscillatory component $\frac{V_{ac}}{R_N}\cos(\omega_{ac}t)$ of the current vanishes due to averaging, forcing all the carrier transport to be taken by the *dissipative normal current* $\frac{V_{dc}}{R_N}$.

Both regimes together are exemplary shown in Fig. 3.5 (a) for an InAs/Al in-situ fabricated nanowire Josephson junction at various AC signals with different frequencies but the same microwave power. One can easily see, that the current-voltage characteristic [**IVC**] now mostly mimics the one of a conventional ohmic system with superimposed, equidistant *constant-voltage-plateaus*. The latter are the already mentioned **Shapiro steps**. The step width in energy - and thereby the periodicity - directly follows from the second Josephson equation.

Due to its direct connection to the underlying *current-phase relation*, the measurement of frequency- and power-dependent Shapiro patterns has evolved into one of the state-of-the-art tools to analyze Josephson junctions. For example, a lot of theories have been build (and partially experimentally proven) around the concept of detecting *topological quasiparticles* by means of the search for either **missing** or **fractional Shapiro steps** that are caused by the 4π-periodicity [133, 134]. However, this connection to the CPR is also its major downside. Due to the measurement principle, i.e. the irradiation of high-frequency photons, the device always resides within a quasi-metastable regime, which makes it extremely sensitive to changes in the environment (both the internal damping as well as the *admittance* of the measurement equipment). Additionally, deviations from the underlying sinusoidal behavior can induce higher-order effects like *subharmonic Shapiro steps* [135–138] (see experimental section). A more suitable approach is the measurement of the *inverse Shapiro effect*, also called **emission**, in which the junction is driven by a constant DC voltage and one tries to detect the **emitted photon** with the corresponding *Josephson frequency* f_J by means of a transmission line setup and an *amplifier* [139]. Here, the relevant time scales caused by the measurement setup are usually much longer than the internal relaxation times of the charge carrier system and therefore less sensitive to noise.

Both measurements, i.e. *Shapiro* and *emission*, have in common, that the observable energy range is usually limited by the *switching* of the device. An extreme example is shown in Fig. 3.6(a).

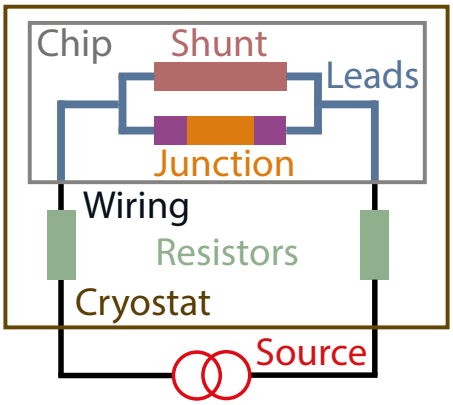

Figure 3.7 – *Schematic overview of a shunted Josephson junction and the corresponding connection to the environment. In order to remove the majority of the noise, the lines inside of the cryostat are filtered by means of two large, equally dimensioned resistors. Additionally, there is an on-chip shunt resistor in close proximity to the junction. The resistive element, interconnected in parallel to the device, is typically fabricated out of a thin film of metal (t<20 nm) with a known resistance per square. The separation between the resistor and the junction is thereby chosen in the way that it is close enough to remove most of the charge fluctuations and phase noise (causing the **overheating** effect) in the leads to the device, but also in a sufficient distance that does not allow the formation of a new noise source due to local heating caused by the dissipation in the normal metal.*

Here, the energy difference between the zero voltage state and the onset of the running state in the positive branch is 120 μeV, which corresponds to a frequency window of roughly 60 GHz that is not accessible during the measurement. This issue can become even worse if one takes into account the previously mentioned stochastic distribution of the switching current, which adds additional phase noise to the system. One way to tackle this is the inclusion of an additional, external *admittance* $\Gamma(\omega)$ by means of a **shunt resistor** connected in parallel and in close proximity to the junction. An exemplary measurement setup is shown in Fig. 3.7. Here, the shunt resistor is directly fabricated on the device chip, while additional, highly resistive filters are embedded into the wiring of the cryostat. Figure 3.6(b) shows the IVC of an InAs/Al in-situ nanowire Josephson junction for two different gate voltages. At $V_g = 7V$, the device is in the multi-channel-regime, with a clearly pronounced zero voltage state. However, instead of a sudden *jump*, the junction now changes continuously into the dissipative state, which makes the whole energy range accessible. The small, but clearly visible backwards bending of the curve is thereby probably related to an *overheating effect* of the electronic system [131] caused by shot noise or other disturbances within the junction. If the gate voltage is decreased, the semiconductor nanowire eventually switches into **pinch-off**. In this case, the only remaining signal is the ohmic response of the normal conducting shunt resistor (blue curve in Fig. 3.6(b)). The calculated, effective resistance value can then be used to *re-calibrate* the junction response. By doing so, one can extract the *pure critical current* of the Josephson junction itself, which is normally overshadowed by parasitic effects like overheating or phase noise.

Previous works on *break junctions* (see Refs. [136, 140]) have shown, that it is also possible to get information about the internal state structure of the Josephson junction by using the theoretical frameworks of Ivanchenko-Zil'berman [141] and Ambegaokar-Halperin-Kurkijärvi [142**?** , 143]. This is especially important for low-dimensional structures like nanowires. Here, it is possible to not only measure in the conventional Josephson junction regime, which can be well-described by a macroscopic, continuous *Cooper pair condensate*, but also operate on the level of single states. This **mesoscopic** regime and the underlying excitations, so-called *Andreev bound states* [**ABS**], are the topic of the next section.

3.2. (MULTIPLE) ANDREEV REFLECTIONS AND BOUND STATES

In the previous section, the key concepts of Josephson junctions have been introduced. Here, a nominally normal conducting section between two Cooper pair reservoirs can host an superconducting transport channel, if the corresponding **coherence length** of the two contacts is large enough to induce an overlap of the two pair wave functions. This macroscopic picture is sufficient to describe phenomena like Shapiro steps, the emission of single photons with well-defined energies or the emergence of a pseudo-Aharonov-Bohm effect in *SQUID* structures. However, it falls way too short if it comes to one- or two-dimensional systems with a small number of channels and a strong confinement in one or multiple directions like a nanowire. In this case, one has to consider that the observable superconductivity in the semiconductor is just an *induced* bypass caused by the adjacent leads rather than a true dissipation-less Cooper pair system. Thus, one can no longer neglect the spatial-dependency of the **pairing potential**, i.e. the amount of energy the coupled electron pairs gain due to the condensation in the common ground state compared with the energy that is needed to overcome the Coulomb repulsion. This can be easily understood if one considers a single *SN-interface*, as depicted in Fig. 3.8 (a). Here, the normal conducting element is modeled by the most simple system, i.e. a metal, in which all states below the Fermi level E_F are empty and all above E_F are occupied. On the left hand side is the superconductor, in which the transport is carried by Cooper pairs. The transition into the bosonic state is thereby achieved via the coupling of electrons with opposite spin and momentum. This requirement puts a strong restriction on the way of how both particle reservoirs can interact with each other, especially if it comes to the injection of a single electron from the normal conductor to the superconductor.

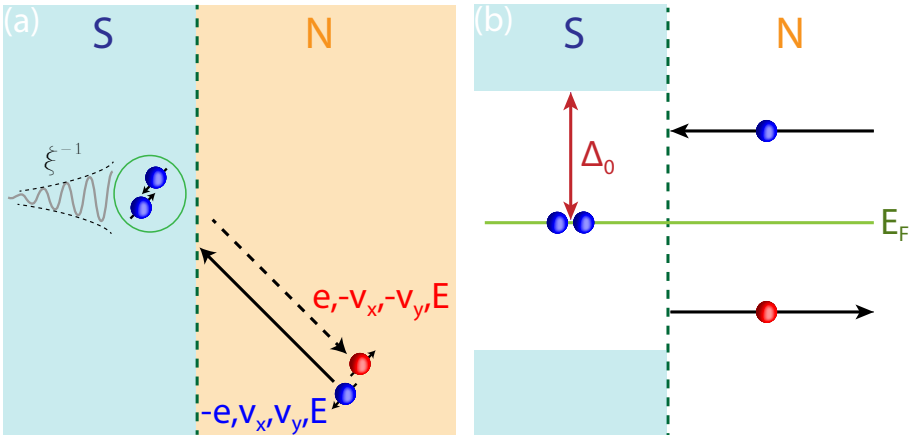

Figure 3.8 – *Schematic representation of the Andreev reflection process in the (a) real space scattering picture and (b) excitation and energy space. The discontinuity in the order parameter at the superconductor-normal conductor border behaves like a potential barrier. However, in contrast to an insulator-normal conductor (**IN**) interface, which only exhibits specular reflection events, the pairing interaction in the superconductor induces a new type of scattering mechanism. The so-called **Andreev reflection** allows the transformation of a spin-down electron (blue) into a spin-up hole (red). When the energy of the incident propagating states in the normal region is smaller than , the newly formed Cooper pair decays within the superconductor on a length scale ξ^{-1} .*

In the most simple case, the fermion just undergoes a conventional *specular reflection*, i.e. a back-scattering at the interface with spin and energy conversion but an inversion of the momentum. However, due to the **pairing interaction**, which can be formally derived from the **Bogoliubov-de Gennes** framework [144, 145], the incident electron can also couple to an *electron-like* excitation within the superconductor and thereby form an additional Cooper pair if its energy is *smaller* than the **superconducting gap** Δ. In order to maintain the number of charges in the complete system, the latter *reacts* to that with the creation of a hole in the normal conductor with opposite spin and momentum as the incident electron, but the same energy. This seemingly conversion of an incident electron into an outgoing hole is called *retro-reflection* or **Andreev reflection** and describes the **elementary excitations** of a *SN stack* [146–148]. An important result of this picture, the so-called *Andreev approximation* of the *Bogoliubov-de Gennes* equations [149], can be used to find an analytical expression for

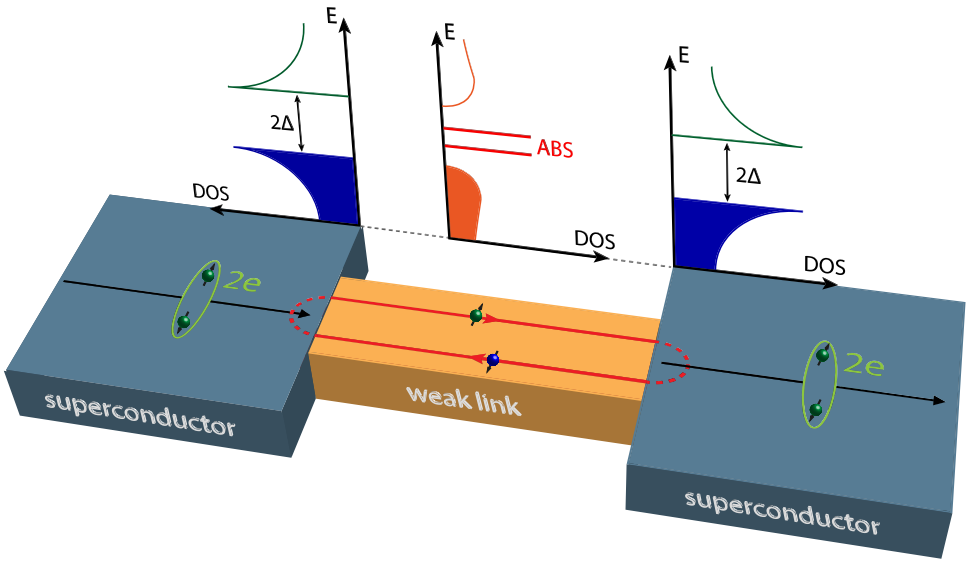

Figure 3.9 – *Sketch of a low-dimensional, mesoscopic SNS junction formed by a ballistic semiconductor nanowire sandwiched between two superconducting contacts. Repetitive Andreev reflection events at the left and right SN interfaces result in the formation of spatially localized, coherent bound states with energies E_A smaller than the superconducting gap Δ.*

the **coherence length** ξ by calculating the probability for the transformation of an spin-up electron into an spin-down hole:

$$P(E,\delta) = \frac{e^{-i\delta}}{\Delta} \begin{cases} E - sgn(E)\sqrt{E^2-\Delta^2} & E > \Delta, \\ E - i\sqrt{\Delta^2 - E^2} & E < \Delta \end{cases} \tag{3.24}$$

Here, as long as the energy of the electron is smaller than the superconducting gap, it will always undergo an Andreev reflection process at the interface. Strikingly, there is still a finite chance for Andreev reflection even if the energy is already larger than Δ [149]. However, the complex phase of the probability amplitude is energy-dependent, too, and already reaches its saturation values φ and $(\varphi + \pi)$ at $-E < \Delta$ and $E > \Delta$, respectively [148]. The result of the *Andreev approximation* is now, that the wave vector of the incident electron becomes complex as long as $E < \Delta$, i.e. $k_e = k_F + i\kappa$, with k_F as the Fermi wave vector. Thus, the resulting wave function is evanescent within the superconductor. For $E = 0$, the maximum decay length is equal to the **superconducting coherence length**

$$\xi = \frac{\hbar v_F}{\Delta} = \frac{2\mu}{\Delta k_F}, \tag{3.25}$$

with μ as the *chemical potential* of the system. The Andreev reflection mechanism is the key concept which universally explains the mesoscopic Josephson effect [150–152]. This becomes immediately obvious if one considers a real device geometry, consisting out of two superconducting electrodes with a phase difference δ and a normal conducting segment in between that acts as a coherent link [153], as depicted in Fig. 3.9. The whole setup can be, in a, extremely simplified description, reduced to a connection of two mirrors in which an electron is retro-reflected as a hole which is retro-reflected as an electron and so on. The result is a **spatially localized** and **coherent** *standing wave*. The first property is thereby in direct contradiction to the conventional Cooper pair states inside of an homogenous superconductor. Due to the **phase twist** across the *weak link* and the resulting inhomogeneity [153], the system can now maintain *single-particle* states within the superconducting gap, so-called *Andreev bound states* [**ABS**]. Here, every **channel**, in terms of the *Landauer-Büttiker formalism* [154, 155], can host a **pair** of *ABS* [156] and is described by a specific **transmission probability** τ_i. Due to the fact that the Andreev reflection mechanism does not mix up different conduction channels, one can now simplify the system to the so-called **single channel limit**, which is of particular interest for the later on described *Andreev qubit* or *topological systems* [157, 158]. In this case, the

dispersion relation of the two bound states just follows

$$E_A(\tau,\delta) = \Delta\sqrt{1-\tau\sin^2\frac{\delta}{2}}, \tag{3.26}$$

with τ as the so-called **transparency**. If one considers, that the phase δ evolves periodically between 0 and 2π and that the superconducting gap Δ is (in good approximation) a material constant, it becomes immediately obvious that the whole system is determined over the fact of how *efficient* electrons can be transferred between the weak link and the surrounding electrodes. Thus, a major part of this project deals with methods to optimize the coupling between the superconductor and the semiconductor nanowire.

Fig. 3.10 (a) provides an overview of the change in the dispersion relation for a pair of bound states with different transparencies [156]. The dark red curve with $\tau = 1$ corresponds to the ideal case of a perfectly transmitting, i.e. **ballistic**, system. Here, both states *merge* at $\delta = \pi$. Even though hardly experimentally accessible, this is the point at which one could potentially open-up a *topological mini-gap*. The latter is the the main requirement for the formation of **Parafermions**. Left and right of this *phase sweet spot*, the bound state energy changes continuously until they couple to the **quasiparticle continuum** at $\delta = 0$ and $\delta = 2\pi$, respectively. If the transparency gets worse and worse, the minimum/maximum energy of the ABS becomes smaller than Δ and a gap starts to open, with a minimum width of $2\Delta\sqrt{1-\tau}$. In contrast to the *propagating* and *delocalized* continuum states, the bound states can only exist inside of the weak link and decay within the superconducting electrodes over a characteristic length scale

$$l_D = \frac{\xi}{\sqrt{\tau}\sin\frac{\delta}{2}}, \tag{3.27}$$

with ξ as the coherence length of the superconductor. For $\delta = 0$ and $\delta = 2\pi$, the decay length *diverges* and the states become effectively *delocalized* and merge with the continuum.

Following this picture, it is easy to understand why most of the described experiments within this project can not be done in a conventional **tunnel junction**. Here, the transparency is always $\tau = 0$, which means that even though there are still Andreev reflection processes, no accessible bound states can be formed anymore due to the strong, *disruptive* coupling to the dissipative *quasiparticle continuum*. However, there are *some* systems, which only work if the transparency is *not-too-perfect*. The reason is the alteration of the **current-phase relation**, visible in Fig. 3.10 (b) [159]. By revisiting the already introduced *first Josephson equation*, which just depicts the special case of $\tau = 0$, one obtains the more general form [151]

$$I_{ABS}(\delta,\tau) = \frac{\Delta}{4\Phi_0}\frac{\tau\sin\delta}{\sqrt{1-\sin^2\frac{\delta}{2}}}, \tag{3.28}$$

with Φ_0 as the *reduced magnetic flux quantum*. Here, for the extreme case of an ballistic junction $\tau = 1$, the CPR effectively becomes a *sign* function, with a sudden reversal of the current at $\delta = \pi$. In this case, the total current of the junction starts to increase *step-wise* with the number of individual bound states N [160, 161]:

$$I_c = N\frac{\Delta}{\hbar}. \tag{3.29}$$

For smaller transparencies, one obtains a *distorted* or *skewed* sine function and the more general expression for the current per channel maximum current per channel of

$$I_{ch}(\tau) = \frac{\Delta}{2\Phi_0}\left(1-\sqrt{1-\tau}\right). \tag{3.30}$$

As a consequence, and easily understandable in terms of a *Fourier transformation*, the system now hosts **higher harmonics**, which manifest themselves in CPR-sensitive measurements like Shapiro steps [162] or the readout signal of *Squids* [128]. However, if it comes to qubit applications like *Transmons* or *Gatemons*, this *non-sinusoidal* behavior can be highly contradictive due to major changes in the resulting potential structure and **anharmonicity** [163]. More details are given in the corresponding section (5.1).

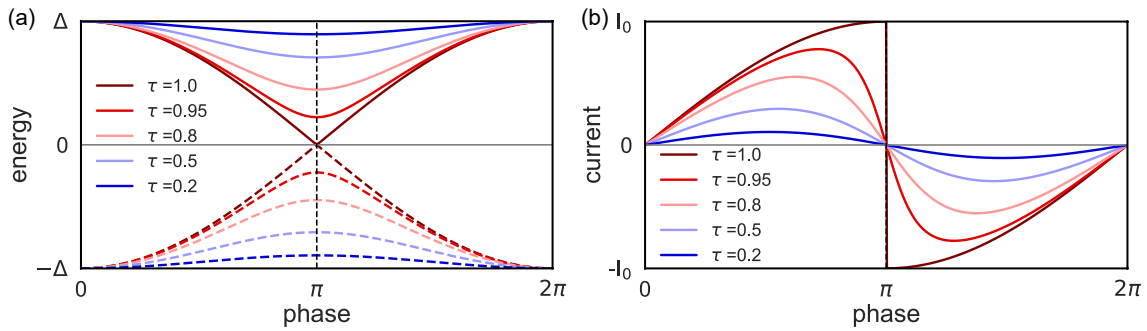

Figure 3.10 – *Theoretical dispersion relation (a) and current-phase relationship (b) of a mesoscopic Josephson junction at zero temperature for different transparencies and a single channel. For $\tau = 1$, the CPR takes the form of a signum function. For smaller values of τ, the curve gradually evolves into the typical sinusoidal shape of a tunnel junction.*

3.2.1. MULTIPLE ANDREEV REFLECTIONS

In experiments, the Josephson junction is usually treated by an applied bias voltage. In this case, the whole system moves out of the already described **equilibrium** solution. Thus, together with the oscillating supercurrent, the device can also maintain a dissipative dc current even for energies below the superconducting gap. The corresponding effect is known as *multiple Andreev reflections* [**MAR**] and was first described in a semiclassical approach and later on in a full quantum mechanical framework [164]. In the most simple picture, shown in Fig.3.11, charge carriers within the *weak link* lose or gain energy, respectively, while they are propagating through the channel. To be more precise, and in the case of a single carrier, one can think about a hole-like quasiparticle that enters the weak link of the SNS stack at the interface of the lower band of the left superconductor and the normal conductor. Subsequently, it is *transformed* into an electron that accumulates energy during its propagation through the channel. Eventually, it reaches the opposing superconducting electrode and undergoes another Andreev reflection, effectively creating a Cooper pair within the superconductor and a left moving hole in the normal conductor.The whole process continues until the generated particle within the weak link reaches the upper band of the left or right superconductor. Here, every **even**, i.e. $2 \cdot n$, process is connected with the destruction of a Cooper pair. For the odd processes $2 \cdot n + 1$, on the other hand, one ends up with a Cooper pair, a *charge transfer* of ne and a corresponding, composite current flow from left to right. In the most simple case, i.e. for $n = 1$, the MAR process is just the transfer of a single quasiparticle and therefore equal to the special case of a tunnel junction.

As already discussed, this process can even continue for energies above the superconducting gap even though it is not accessible for transport anymore. If one neglects the quasiparticle continuum and just restricts the valid energy range to $\pm\Delta$, the *lowest possible* MAR process for a given bias voltage is simply

$$n(V) = \frac{2\Delta}{eV}. \tag{3.31}$$

In the previously described picture, the order of the reflection process does not have a real experimental meaning. However, this changes if one reconsiders the fact that the probability for **every** Andreev reflection at the left and right interface is tightly bound to the *transparency* τ. Thus, if one assumes n reflections, the *total intensity* of the resulting MAR signal scales with τ^n. In real devices, $\tau < 1$, which means that the major part of the current is carried by the lowest order process given by Eq. 3.31. This holds even in the case of *multiple channels* due to the **coherent** nature of the MAR process, which does not allow *inter-channel transitions*. Therefore, the total current scales with

$$I_{tot} \propto \sum_i \tau_i^n. \tag{3.32}$$

This makes it immediately obvious why this effect can be neglected in the case of a tunnel junction $\tau \ll 1$. In the case of a mesoscopic and shunted junction (see section 3.1.1), on the other hand, one can use the extracted *real junction current* together with the already introduced framework of Ivanchenko-Zil'berman [141] to calculate the transparency of *every individual channel* τ_i. However,

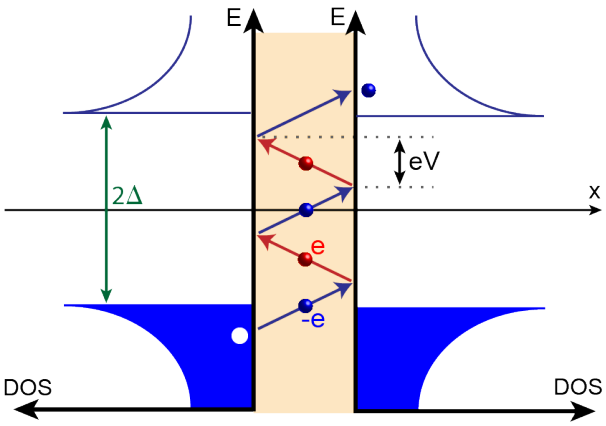

Figure 3.11 – *Multiple Andreev reflection process of odd-order in a mesoscopic Josephson junction, resulting in the transformation of a hole-like quasiparticle in the left lead into an electron-like particle in the right contact. Here, the chemical potential of both reservoirs is kept at the same level, while the dissipative voltage gain is determined by the kinetic energy that the charge carrier accumulate through the electrical field across the channel.*

for the special case of small bias voltages, i.e. when the time-evolution of the Andreev bound states is almost neglectable, the MAR process can be better described in terms of **Landau-Zener transitions**. These are of special importance as they correspond to the main decay channel for the Andreev qubit (see Sec. 5.2) or two-tone spectroscopy measurements. On the other hand, under the correct circumstances, they can open up a topological minigap by effectively creating a 4π-contribution.

3.3. S-QD-S JUNCTIONS AND SHIBA STATES

Every superconductor-normal conductor-superconductor structure can act as a Josephson junction. However, based on the quality of the coupling between all three components, the general characteristics can be fairly different from the behavior that was first described via the two Josephson equations. In the most extreme case, i.e. for ultra-high transparencies, the relation between current and phase can completely lose its famous sinusoidal shape and turn into a sign function. In the previous section, a special focus was set on both SN borders and the resulting Andreev reflection processes, while the normal conductor itself just took the role of a transmitting channel. This picture fails if the normal conductor becomes more and more *non-classical*, e.g. with a significant *spin-orbit interaction* or, more importantly, with a strong confinement that reduces the effective **dimensionality** of the system. In the case of a semiconductor nanowire, this can even extent up to the transformation into the *zero-dimensional* state, a so-called *quantum dot* [**QD**]. The latter can either intrinsically emerge due to surface potential fluctuations or be formed in a controlled fashion by means of a locally applied gate voltage.

If one neglects the outer superconducting electrodes, one can model a single quantum dot within a nanowire as a charge island that is tunnel-coupled to adjacent electron reservoirs. This approach is known as the *constant interaction model* [66, 165]. In order to simplify the system, both coupling factors to the source and drain leads, Γ_S and Γ_D, are assumed to be equal. The combined coupling strength $\Gamma = \Gamma_S + \Gamma_D$ is thereby a figure of merit for both the energy width of the single levels as well as for the corresponding electron lifetime. Within this picture, the QD can be quantitatively described with two different energy contributions. The first of them can be easily understood in terms of the **Coulomb repulsion** between the *trapped* electrons, which also provides the name for the related effect on the charge carrier transport: **Coulomb blockade**. Here, all electron transfers through the charge island are completely suppressed as long as the chemical potential of a quantum dot state, typically referred to as μ_N does not overlap with the chemical potentials of the source and drain leads μ_S and μ_D, respectively. The latter can be experimentally achieved by two different means, shown in Fig. 3.12 (a). In the uppermost picture, there is no valid state within the energy window given by the two outer charge carrier reservoirs. However, if one applies an external gate voltage, one can energetically shift the position of μ_N and thereby open up a transport channel through the quantum dot. A similar effect can be enforced by the energetic displacement of the source and drain contact μ_S and μ_D, i.e a bias voltage, which increases the valid energy window in which electrons can flow through the structure. If the bias voltage is large enough, it is also possible that multiple quantum dot levels can participate in the transport. The separation of adjacent level is thereby given by the amount of energy that is needed to overcome the Coulomb repulsion and *charge* the island with another electron. Accordingly, it is called **charging energy** E_C [166] and can be calculated by combining all charge contributions

$$E_c(N) = \frac{e^2 N^2}{2C_\Xi} + eN\left(\frac{Q_G}{C_\Xi} + \sum_{i=1}\frac{C_i V_i}{C_\Xi}\right). \tag{3.33}$$

Here, N corresponds to the number of electrons on the charge island, C_Ξ refers to the total capacitance of the system, Q_G to the total number of charges on the gate electrode and $C_i V_i$ combines the individual number of charges and the applied voltages for source, drain and gate contact, respectively. However, due to the quantum mechanical nature of the system, there is an additional energy that originates from the strong spatial confinement. The so-called **single particle energy** ε_N [167] is thereby equal to the increase of the inner energy $U(N)$ of the system if another electron is added to the dot and, in the most simple case of a radial symmetric charge island, given by

$$\varepsilon_N(N+1) = U(N+1) - U(N) = \frac{\hbar^2}{2m^* r^2}(2N+1). \tag{3.34}$$

One of the most striking features of a quantum dot is the complete suppression of any charge carrier transport as long as there is no valid state within the energy window given by the chemical

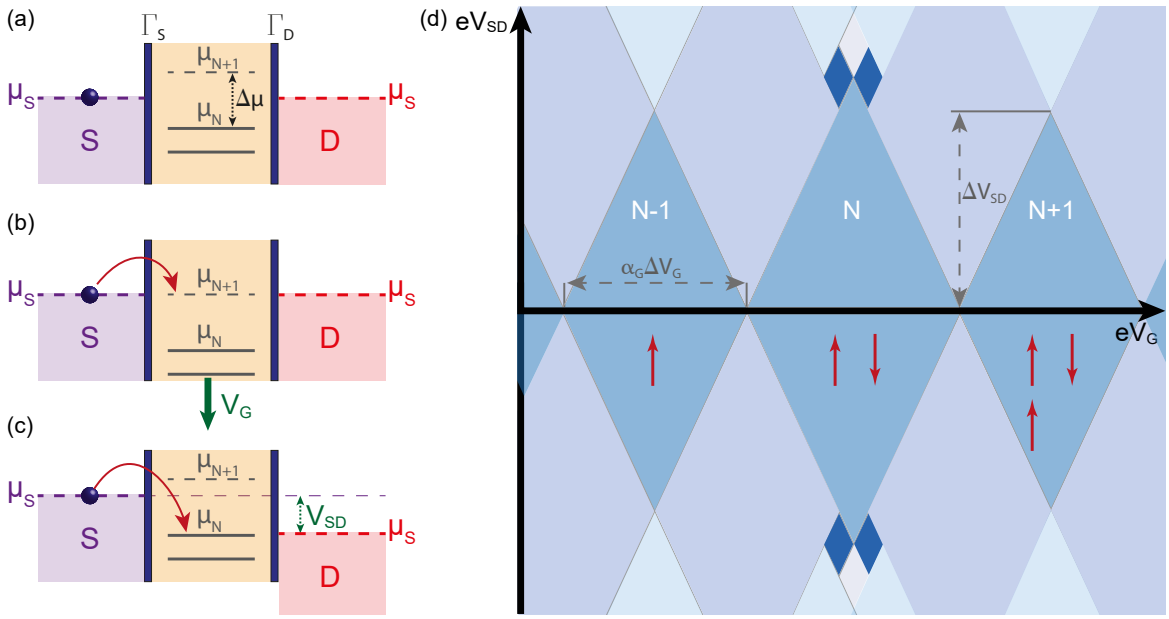

Figure 3.12 – *(a),(b),(c) Schematic model of a quantum dot in the energy picture. Here,[**S**] and [**D**] correspond to the source and drain contact, respectively. (a) If there is no valid state in the energy window given by the chemical potentials of the source and drain leads μ_S and μ_D, respectively, the charge carrier transport is completely suppressed. (b) The current flow can be restored if quantum dot level is energetically shifted between μ_S and μ_D by means of an applied gate voltage. (c) Additionally, it is possible to apply a bias voltage and thereby broaden the valid energy window. (d) Summary of the three different cases in terms of a **stability diagram**. The dark blue Coulomb diamonds correspond to V_{SD}-V_g combinations that lead to Coulomb blockade. The number of possible electrons N in the dot is given for each individual diamond. The white area on the central axis corresponds to the case of a fully depleted dot. The brighter areas at finite bias voltages, however, represent situations in which a current can flow through the structure.*

potential of the source and drain leads μ_S and μ_D. As already mentioned, the latter requirement can be overcome both with the enforcement of a misalignment of μ_S and μ_D as well as by an electrostatic shift of the quantum dot states by means of an applied gate voltage. Thus, if one maps out a quantum dot structure experimentally, the response in both source-drain voltage V_{SD} as well as gate voltage V_G direction show characteristic, *plateau-like* sections with zero conductance. The combination of both parameters results in the most prominent feature of zero-dimensional transport: **Coulomb diamonds**. Fig. 3.12 (b) shows an exemplary sketch of a so-called *stability diagram*. Here, the *rhombus-like* sections along the gate axis correspond to sections with no valid quantum dot state and therefore no charge carrier transport. Whenever the gate voltage hits exactly the energy value between two diamonds, the system reacts with a sudden *conductance spike*, a so-called **Coulomb resonance**. For T=0 K, this feature follows the shape of a δ-function, while finite system and electron temperatures lead to a broadening and a transformation into a *peak-like* feature [66, 166]. The size of the diamonds depends thereby on the occupation of the corresponding quantum dot state. For *odd configurations*[2], the amount of energy that is needed to add another electron is significantly smaller than for *even* situations. Additionally, by measuring the maximum width and height of the diamonds, one can directly determine the required bias voltage V_{SD} as the gate voltage V_G. However, for the latter, there is usually a more-or-less large mismatch between the externally applied value and the effective level shift within the quantum dot. The figure of merit for the *efficiency* of this shift is the so-called *coupling factor* or **lever arm**

$$\alpha = \frac{\Delta V_{SD}}{2\Delta V_G} = \frac{C_G}{C_\Xi}, \tag{3.35}$$

with C_G as the capacitance of the connection to the gate electrode. Depending on the type of gate connection (bottom gate, plunger gate, side gate, backgate...), the quality of the dielectric (air, SiO_2, high-k) and the cleanliness of the nanowire surface (unpassivated, capped, cleaned with sulphur),

[2] Odd refers to the case of 1 + 2·n particles in the dot.

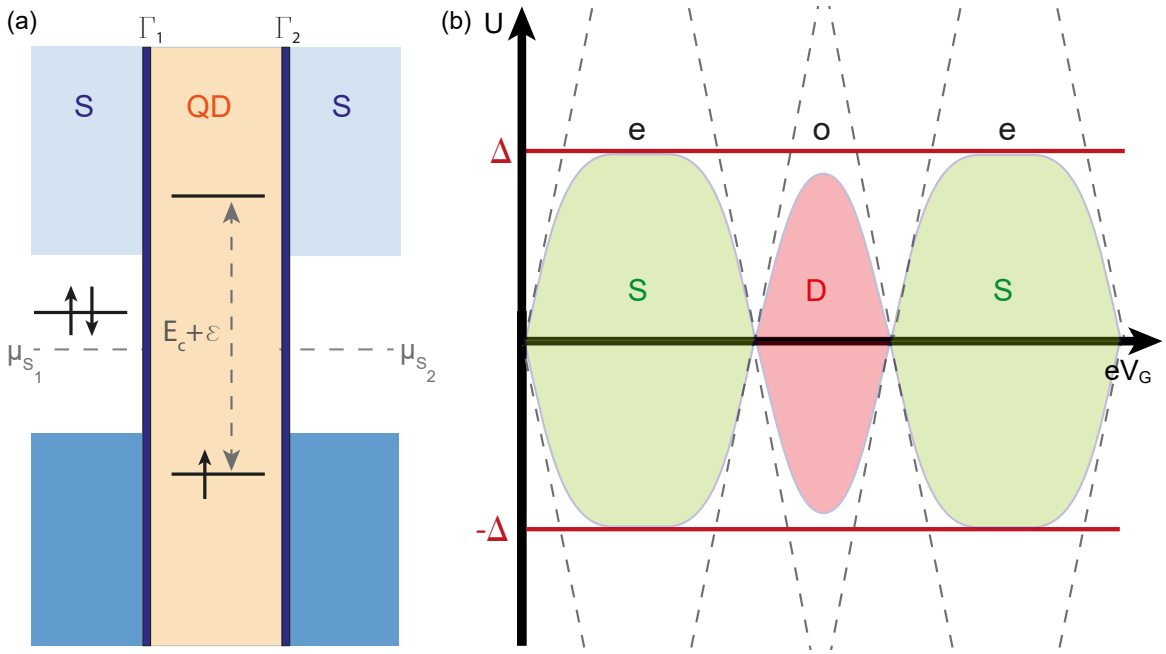

Figure 3.13 – *(a) Schematic of a quantum dot sandwiched between two equal superconductors. The energy levels in the quantum dot are represented with their characteristic energy scales: the charging energy E_c, the coupling strengths between the dot and the left and right reservoir Γ_1 and Γ_2, respectively, and the electrostatic shift of the energy levels ϵ. (b) Excitation spectrum of a single quantum-dot tunnel-coupled to two superconducting leads. In the uncoupled case, the superconductor would exhibit conductance peaks at its gap edge while the quantum dot limits the transport in terms of the formation of Coulomb diamonds (dashed lines). For strong coupling, on the other hand, a* ***hybridized*** *S-QD-S system with occupation-dependent ground states is formed. From left to right: Empty dot singlet [**S**], single occupied doublet [**D**], double occupied singlet [**S**]. Here, the border of the colored areas marks the shape of the measured sub-gap resonance. Due to the* ***phase twist*** *at the e-o-boundaries, the system performs a* 0-π ***quantum phase transition***.

α can range from 1/10 down to 1/1000, i.e. a level shift of 1 meV corresponds to 10 mV or 1 V, respectively [168–170]. If the source and drain contacts are replaced by superconducting electrodes, things become much more complicated. Superconductivity, on one hand, is based on the formation of a common ground state due to the condensation of coupled electrons into bosonic Cooper pairs. Thus, it privileges the simultaneous tunneling of two electron with opposite magnetic moment, i.e. zero net spin. The latter can just happen for *even* quantum dot states, i.e. **spin singlets**. However, the additional *Coulomb repulsion* within the dot enforces a sequential *one-by-one* filling, which leads to a stabilization of both the *even* as well as the *odd* states. The exact outcome of this competition depends on the four relevant energies of the system:

- The induced proximity gap Δ_p. For reasons of simplification, it will be assumed that the interface is perfect, i.e. $\Delta_p = \Delta$
- The coupling strength between the superconducting electrodes and the quantum dot $\Gamma_L + \Gamma_R \equiv \Gamma$
- The charging energy of the quantum dot E_c
- The energy position of the individual quantum dot level with respect to the Fermi energy of the superconductor ϵ

Here, as long as $\Delta > E_c$, the system is dominated by the superconductor and the current flow through the structure is carried by proximity-induced Andreev bound states, utilizing a new superposition state of the $|n=0\rangle$ and $|n=2\rangle$ quantum dot level. This can be understood in terms of an *effective* suppression of all quasiparticle transport (if one assumes $\Delta \to \infty$), which results in a hybridization of the QD with the Cooper pairs of the superconductor.

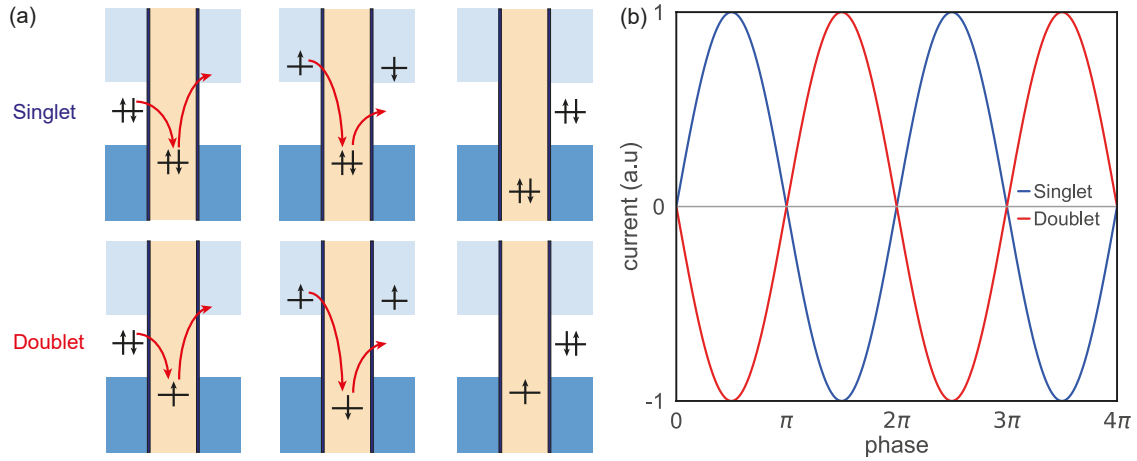

Figure 3.14 – *(a) Schematic overview of the relevant (co)-tunneling processes for even (top) and odd (bottom) occupation of the quantum dot for the most simple case of a single spin-degenerate level. For a fully (un-)occupied level and a net spin S = 0 on the dot, the charge transfer can be seen as a sequence of four coherent tunneling events. Most importantly, the order of spins of the annihilated and newly formed Cooper pair is the same. This results in a conventional or 0-type current–phase relation. For an odd number of confined electrons and a net spin S = 1/2, on the other hand, the spin ordering is reversed, effectively resulting in a phase offset of π. Thus, the change of the dot occupation by one electron induces a reversal of the supercurrent. (b) Simulated flux-dependent response of a S-QD-S structure embedded in a SQUID loop. The phase sensitivity makes it possible to directly distinguish between even (blue) and odd (red) occupation of the dot.*

However, for the opposite case, i.e. if $\Delta < E_c$, the system is dominated by the quantum dot. This gives rise to so-called *Yu-Shiba-Rusinov* [**YSR**] states [171–173] (cf. Fig. 3.13(a)). The latter are mediated by magnetic exchange coupling of unpaired spins in the quantum dot and quasi-particles of the superconducting leads, effectively leading to a **singlet state** that moves deeper and deeper into the superconducting gap if the coupling strength is increased. The underlying mechanism was first developed for single magnetic impurities coupled to superconductors and shares a lot of similarities with the *Kondo effect* [174, 175]. In the same spirit, one can say that the superconductor **screens** the unpaired spin in the quantum dot by means of a quasi-particle originating from its bulk. It should be mentioned, that ABS and YSR states share a lot of similarities as the both correspond to the binding of an additional quasi-particle to the local, unpaired spin. However, for the YSR state the QP mainly resides within the superconductor, while for the ABS it is bound to the normal conducting segment, in this case the quantum dot, due to the hybridization of the 0 and 2 electron states.

Fig. 3.13(b) shows the gate- and bias-dependent conductance map, i.e. a stability diagram, of such a S-QD-S system. It can be seen that the resulting states for *even* occupation, which are given by the outlines of the bright green areas, are confined between the gap edges of the superconductor and the borders of the Coulomb diamonds of the quantum dot. The sub-gap states within the odd diamond, on the other hand, do not extend up to Δ. The exact energy separation between this newly formed *doublet ground state* and Δ can be thereby calculated within the *Anderson model* by utilizing the coupling strength Γ. This crossover from *even* to *odd*, and therefore *doublett* to *singlet* configuration is of special interest as it marks the point at which the formerly 0-junction undergoes a **quantum phase transition** [176–179] into a so-called π-junction [180–182]. In order to understand this process and the resulting consequences on the device behavior, one should (again) revisit the Josephson equations. The non-dissipative supercurrent across a SNS junction is driven by the phase gradient and follows the current-phase relation $I_s = I_c \sin\delta$. However, there is another solution for the system with a reversed current direction:

$$I_s = I_c \sin(\delta + \pi) = -I_c \sin(\delta) \tag{3.36}$$

The latter describes the already mentioned π-junction. Both the 0 and π-junction share a lot of similarities like the suppression of the supercurrent *if* the phase difference is zero. However, it was shown, that for a π-junction the $\delta = 0$ configuration is *unstable* due to the location of the energy minimum at π. This is the reason why the 0-π-transition is assumed to be a real phase change of the system rather

than just a simple sign change of the supercurrent. One important consequence of this behavior is the fact, that even the lowest energy state of a superconducting loop with an embedded π-junction carries a non-vanishing, circulating supercurrent and a corresponding finite magnetic field. Qualitatively, and with focus on the discussed S-QD-S system, one can understand both types of junctions in terms of **higher-order co-tunneling processes**, as shown in Fig. 3.14(a).

Even N The transfer of a Cooper pair can be splitted into a four-step process. First, a $\downarrow$-electron tunnels out of the quantum dot into the quasi-particle continuum of the right superconducting lead. Here, it creates a virtual excitation. Additionally, the quantum dot is driven into a virtual, high-energy excited state. Subsequently, a Cooper pair in the left lead is broken apart, creating a $\uparrow$-QP excitation and a $\downarrow$-electron that tunnels into the quantum dot. Now, the initial $\uparrow$-electron inside the QD state tunnels out and forms a Cooper pair with the initial $\downarrow$ in the right lead. Finally, the $\uparrow$ from the left lead tunnels in, which eliminates the excited state and pushes the quantum dot back into its initial configuration. As long as the whole process is faster than $\frac{\hbar}{E_c}$, it can be assumed as coherent and does not violate energy conservation. Additionally, in some kind of *handwaving argument*, it is then easily understandable that even though the transfer of the singlet state from the left lead $|\Psi\rangle_l = (|\uparrow\downarrow\rangle - |\downarrow\uparrow\rangle)$ to the right lead $|\Psi\rangle_r = (|\uparrow\downarrow\rangle - |\downarrow\uparrow\rangle)$ is a change of the spatial location of the Cooper pair, it is not connected with a **phase change**. Thus, the system behaves as a 0-junction.

Odd N In this case, the process is slightly more complicated. First, the $\uparrow$-electron tunnels out of the dot into the right superconducting lead and forms a quasi-particle excitation. In the following, a $\downarrow$ from the left lead tunnels in, occupies the quantum dot and state and decreases its energy. Finally, the same spin tunnels out from the dot and recombines into a Cooper pair in the right lead. The remaining $\uparrow$ on the left lead then moves into the quantum dot, effectively driving it back into its starting configuration. However, even though the final state of the quantum dot is the same as the initial one, the spin ordering of the Cooper pair in the right lead is **reversed**, i.e. $|\Psi\rangle_r = (|\downarrow\uparrow\rangle - |\uparrow\downarrow\rangle) = e^{i\pi}|\Psi\rangle_l$. Thus, the whole system undergoes a phase shift of π, that translates into a reversal of the supercurrent.

The experimental realization of π-junctions has attracted considerable interest over the last couple of years due to theoretical predictions pointing towards a "simpler" realization of *Majorana zero modes*. However, together with the rising number of different experiments on S-Ferromagnet-S juctions [183–185], SQUIDs with *d-wave*-superconduc-tors [186, 187], and carbon nanotubes [182], the initial definition of **YSR** states has become more and more detailed and separated and now also includes different cases for non-neglectable *Kondo temperatures* [188–190], weak, strong and intermediate coupling factors Γ [191, 192] and even systems with *Dirac-type* dispersion relations like (twisted bilayer) graphene [193–195] or topological insulators. Here, the theoretical description was restricted to the most simple - and original - picture of a competition betwen supercon-ductor-centered and QD-localized Andreev bound states. A more in-detail description focused on superconductor-semiconductor hybrid structures is given in the experimental section 3.

4

CIRCUIT QUANTUM ELECTRODYNAMICS

The fundamental prerequisite for information processing is the existence of two *entities* which are fully distinguishable and can therefore be mapped into a *two-state representation*. The most simple ways to realize such a system in physics are either a spin 1/2-system, as the most nonlinear system, or a harmonic oscillator, the upmost linear entity, which both host single or multiple two-level systems (in the following referred to as a **TLS**) with defined transition energies. Consequently, each atom can, technically speaking, act as a *encoding container* for a single *bit*. Despite the dominance of quantum mechanics on meso- and microscopic scales, this analogy can be further pursued to the methods how such basic information container can be manipulated: If the external driving force is not strong enough, the system remains in the energetically favourable position, the so-called **ground state** $|g\rangle$. However, if there is too much power involved, the system just *breaks* and, ultimately, lose its capability to store information forever. So, applying the right amount of energy is a key ingredient to push the TLS into the so-called **excited state** $|e\rangle$. However, while this requirement can be comparably easy fulfilled for a classical switch, things are much more complicated as soon as it comes to an atom as a purely quantum mechanical entity. Here, the driving power has to be realized by quantized electromagnetic modes, usually *photons*, and can be described within the framework of a relativistic quantum field theory. However, in free space, the interaction with single photons just leads to neglectably small perturbations of the atomic energy spectrum due to the relatively weak coupling. In order to observe the true dynamics of the interaction between coherently coupled quanta of light and matter, it is necessary to enhance the vacuum fluctuations of a single optical mode in order to outperform all other environmental influences which could disturb the state of the atom. This can be achieved by, for example, trapping both a photon and an atom inside of a cavity with a high *quality factor Q*, i.e. with a neglectable *photon leakage rate* κ. As soon as the so-called **coupling factor g** exceeds both κ as well as the decay rate of the TLS γ, the whole system is in the so-called **strong coupling regime**. The physical description of such a strongly coupled *atom-photon system* gave birth to a completely new disciplince, the field of *cavity quantum electrodynamics* (**cQED**), with the *Tavis-Cummings model* as the underlying theory to describe interactions between an arbitrary number of atoms and a microwave photon field with multiple modes. However, for reasons of simplicity, this thesis limits itself to the special case of a single atom coupled to a single resonant mode, which reduces the degree of complexity to the search for a proper interaction term: The **Jaynes-Cummings Hamiltonian** $\mathcal{H}_{jc}$.

4.1. THE JAYNES-CUMMINGS MODEL

The full quantum mechanical description of an coherently coupled atom-cavity-system consists out of five different contributions:

$$\mathcal{H}_{acs} = \mathcal{H}_a + \mathcal{H}_p + \mathcal{H}_\kappa + \mathcal{H}_\gamma + \mathcal{H}_{int}. \tag{4.1}$$

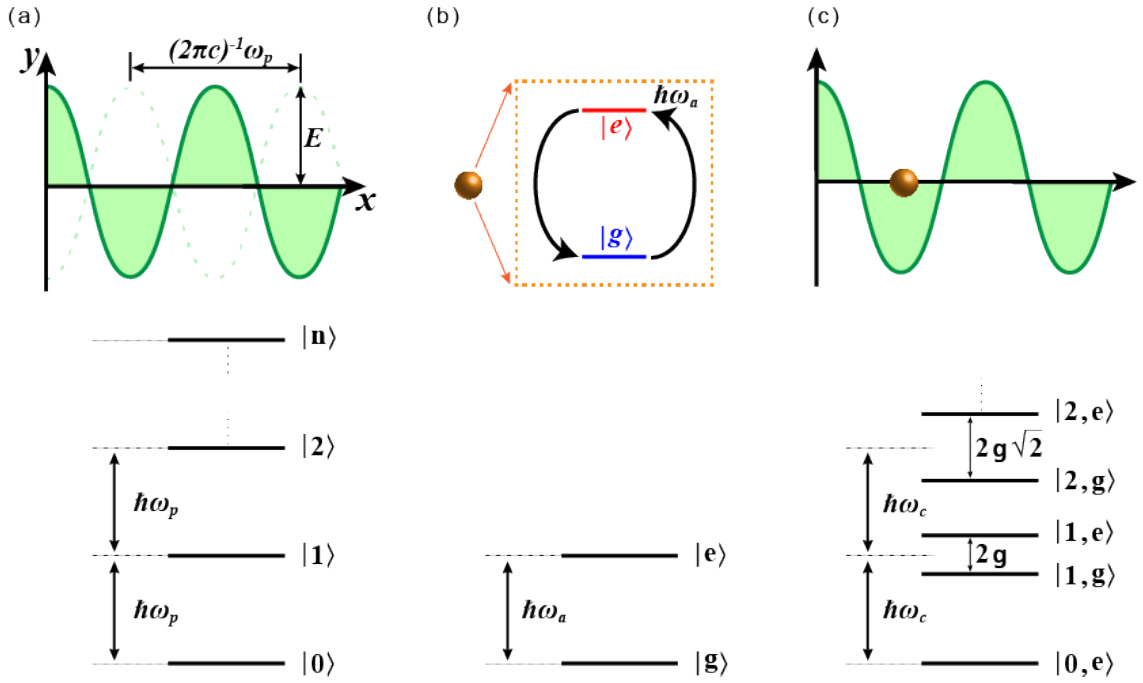

Figure 4.1 – *Schematics of the atom-photon coupling in terms of the Jaynes-Cummings model. (a) The oscillating electromagnetic field inside of a cavity exhibits a harmonic energy ladder where the individual steps correspond to the number of excitations, i.e.* ***photons****. (b) In the same spirit, a single atom is described as a two-level system consisting out of a ground and excited states $|g\rangle$ and $|e\rangle$, repectively, and a well-defined transition energy. (c) A strong, resonant* ***dipole coupling*** *between the atom and the cavity results in the formation of so-called* ***dressed states*** *and the Jaynes-Cummings ladder.*

Here, $\mathscr{H}_a$ is an isomorphic representation of a spin-1/2 system trapped in a magnetic field (Fig.4.1(b)) and can therefore be written in terms of the Pauli spin-matrix σ_z and the transition frequency ω_a

$$\mathscr{H}_a = \frac{\hbar}{2}\sigma_z\omega_a, \tag{4.2}$$

while the microwave photon field inside of the cavity takes the usual form of a harmonic oscillator, forming a evenly spaced energy ladder in which the individual levels represent the number of excitations (Fig.4.1(a)):

$$\mathscr{H}_p = \hbar\omega_p\left(aa^\dagger + \frac{1}{2}\right). \tag{4.3}$$

The bosonic ladder operators a and $a^\dagger$ are thereby comparable to the classical field amplitudes and, if combined, build up the photon number operator $n = aa^\dagger$.
The two contributions $\mathscr{H}_\kappa$ and $\mathscr{H}_\gamma$ act as container for any perturbations which could disturb the photonic or atomic system, respectively, and are quantitatively described by the cavity photon leakage rate κ and the spontaneous decay rate of the TLS γ. For reasons of simplicity, all potential loss channels are neglected, i.e. the properties of the coupled system are only determined by the interaction term

$$\mathscr{H}_{int} = \vec{d}\cdot\vec{E} = d\left(\sigma+\sigma^\dagger\right)E_x\left(a+a^\dagger\right). \tag{4.4}$$

Here, $\vec{d}$ describes the dipole moment of the atom, $\vec{E}$ the field distribution of the single optical mode and $\sigma,\sigma^\dagger$ are the fermionic creation and annihilation operators. With the full definition of the photon-atom coupling strength for a given cavity volume V_c

$$g = \sqrt{\frac{\omega_p d^2}{2\hbar V_c \epsilon_0}} \tag{4.5}$$

the interaction term can be rewritten as

$$\mathscr{H}_{int} = \hbar g\left(\sigma+\sigma^\dagger\right)\left(a+a^\dagger\right) = \hbar g\left(\sigma a^\dagger + \sigma^\dagger a + \sigma a + \sigma^\dagger a^\dagger\right) \tag{4.6}$$

However, by taking a closer look onto the different photon-atom ladder operations, it is obvious that there are some obstacles which render this description into an unphysical regime by violating the particle number conservation: While the first two terms describe the excitation/relaxation of the atom by the absorption/emission of a single bosonic mode, the latter two belong to an excitation-driven emission and an absorption followed by relaxation, respectively. In order to deal with this issue, the so-called *rotating wave approximation* [**RWA**] has been developed [196–198]. The latter is based on the *transformation* of the coupling Hamiltonian from the Schrödinger picture to the interaction space by representing the particle ladder operators in terms of time-varying amplitudes which oscillate with the photonic and atomic excitation frequencies, respectively:

$$\mathscr{H}_{int} = \hbar g \left(\overline{\sigma a}^{\dagger} e^{i(w_p - w_a)t} + \overline{\sigma}^{\dagger} \overline{a} e^{i(w_a - w_p)t} + \overline{\sigma a} e^{i(w_p + w_a)t} + \overline{\sigma}^{\dagger} \overline{a}^{\dagger} e^{i(w_p + w_a)t} \right) \tag{4.7}$$

For the assumption that the atom-photon system is close to resonance, i.e. for a **detuning** $\Delta = \omega_a - \omega_p \approx 0$, the last two contributions are almost double the transition frequency of the atom and will therefore quickly average to 0. This leads to the final representation of the coherently coupled system, the Jaynes-Cummings Hamiltonian

$$\mathscr{H}_{jc} = \frac{\hbar}{2} \sigma_z \omega_a + \hbar \omega_p \left(a a^{\dagger} + \frac{1}{2} \right) + \hbar g \left(\sigma a^{\dagger} + \sigma^{\dagger} a \right). \tag{4.8}$$

and the corresponding eigenstates, the so-called *dressed states*

$$|1n\rangle = (|n, e\rangle + |n+1, g\rangle)/\sqrt{2} \tag{4.9}$$

$$|2n\rangle = (|n, e\rangle - |n+1, g\rangle)/\sqrt{2}, \tag{4.10}$$

with the eigenenergies

$$E_{1n,2n} = \hbar \left(n + \frac{1}{2} \right) \omega_r \mp \hbar g \sqrt{n+1}. \tag{4.11}$$

Fig. 4.1 gives a complete overview about the interaction process: By coupling the bosonic excitations of the cavity (a) to the pseuso-spin-1/2-system of the atom(b), the formerly degenerated, bare states of the atom split and transform into the new eigenstates of the strongly coupled atom-cavity system (c), which is also known as the *(AC) Stark effect*. The separation is thereby proportional to the coupling strength g and the number of bosonic excitations n. One of the striking results of the Jaynes-Cummings framework is, that even without a *real* photon in the cavity, i.e. for $n = 0$, there is an interaction due to the coupling of the dipole moment of the atom to the root-mean-square amplitude of the vacuum field. Thus, as long as the atom was initially in the excited state, it undergoes an alternating process of emission and absorption, referred to as **Rabi flopping**, in which it coherently exchanges a photon with the cavity. The rate in which the atom either absorbs or emits a photon, i.e. the change of the occupation probability from 0 to 1 and vice versa, is called the **vacuum Rabi frequency** Ω_0.

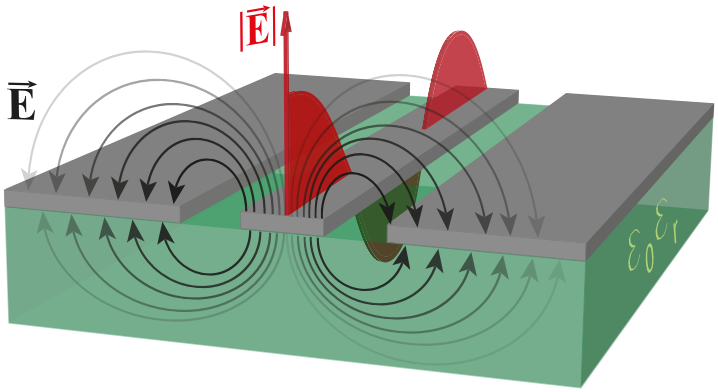

Figure 4.2 – *Schematic overview of a transmission line in coplanar waveguide-geometry on top of a dielectric substrate. For a broad range of frequencies, the dominant and confined mode is of TEM-nature, i.e. the distribution of the magnetic field is the same as for the depicted electric field. The field lines of the latter are distributed between the dielectric underneath and the air-layer, which is a source for radiation losses, above the structure. One important optimization criterica is therefore the maximization of the electric field that goes through the substrate into the ground plane by means of a proper tuning of the effective permittivity.*

4.2. CIRCUIT IMPLEMENTATION: THE COPLANAR WAVEGUIDE

In order to control an actual qubit - or any other realization of a one or few mode system - it is necessary to precisely tailor the excitation dynamics in terms of pulse length, number of photons, photon energy and so on. In solid state physics, this is often achieved by means of a so-called *coplanar waveguide* [**CPW**] [199, 200] made out of superconducting materials. The latter acts both as an extended cavity as well as, if well-designed, a protection for the actual device. It should be mentioned that besides the CPW geometry there are a lot of other implementations like microstrip lines, striplines, lumped element resonators etc. Even though all of them require much less effort in fabrication, like, in the case of a microstrip line, the lack of a dedicated ground plane in exchange of the simple metalization of the substrate backplane, they also provide less control about the electromagnetic field distribution.Thus, it becomes much harder to build more complex circuits that consists out of multiple Qubits or, like in the case of the Gatemon and Andreev Qubit, require the (local) application of additional electric and magnetic fields in terms of gate and flux control. In the same spirit, one can say that coplanar waveguides act as pipes to guide and **confine** the electromagnetic waves and thereby reduce losses and **crosstalk** for electromagnetic waves up to the mid-Gigahertz range.

Fig. 4.2 provides an overview of the schematic layout and field distribution within a so-called **transmission line**. The latter is the fundamental building block of all microwave designs used in this thesis, including *feedlines*, *resonator* and *gate pulse lines*. It consists out of a central conductor, surrounded by two *ground planes* [**GND**] in close proximity. The gap between the central line and GND is thereby chosen in a way that the major part of the field lines is concentrated in the dielectric underneath, reducing the raditation losses to air and also minimizing the dispersion of the propagating wave. Another advantage of the design is the fact, that the primary or **coplanar mode** of the system is, up to large frequencies and without a *cut-off point*, of **(quasi) transverse electromagnetic** [**TEM**] nature, i.e. $E_z = H_z = 0$. The limitation *quasi* thereby points towards the fact that the *magnetic field* is **elliptically polarized**, which drives the system more and more into a *transverse electric* behavior for higher frequencies, i.e. $H_z \neq 0$ but those are usually far above typical operation points. Last but not least, if it comes to the experimental realization, the system can be easily designed in a way that the *effective dielectric constant*[1] reaches its threshold value for comparably small thicknesses. Additionally, the achieved *impedance value* is (in good approximation for typical, commercial available substrates independent from the substrate thickness. All things together minimize the span-width of fabrication-related parameter fluctuations and therefore make it easier to achieve reproducible and well-controlled *quantum control circuits*. In contrast to other works, the spatial extension of the circuit elements used in this thesis, which can be in the order of a few millimeter and

[1] Will be further discussed in the corresponding section of the *Fabrication* chapter.

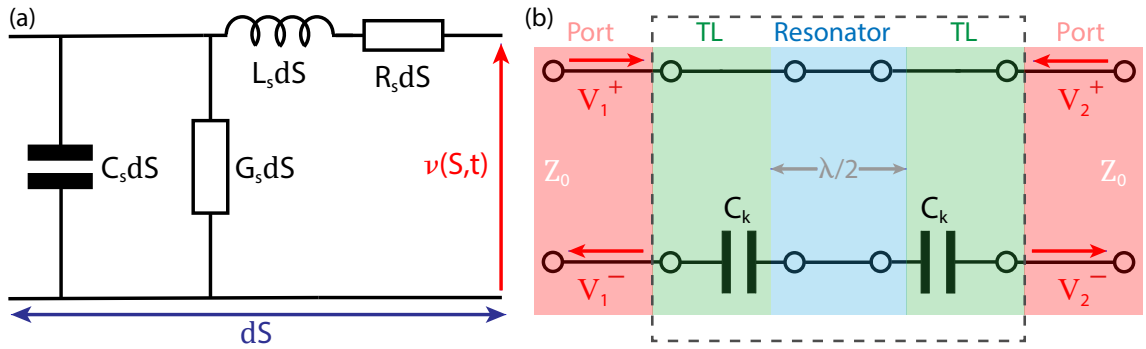

Figure 4.3 – *(a) Distributed element model of a transmission line of the length dS with all revelant electrical components. The latter are described in terms of there specific properties per unit length. (b) Voltage-based network model of a λ/2 CPW-resonator. The latter is capacitively coupled to a* ***two-port*** *transmission line with the characteristic impedance Z_0. Here, the TL is characterized by four* ***S parameter*** *that are equal to the individual ratios between incident, transmitted and reflected signals.*

therefore much larger than the typical threshold criteria of $\lambda/20$, does not allow to use the more simple *lumped element picture* [201, 202]. That makes it rather complicated to model the whole system as an equivalent circuit of discrete elements. However, it is still possible to use the lumped element theory on infinitesimally small fractions dS of the line S, ending up with the equivalent circuit in Fig. 4.3 (a). Here, R_s corresponds to the distributed resistance of the transmission line (Ω/m), i.e. the non-phase-active contribution. Accordingly, L_s and C_s summarize all *inductive* (self-inductance, the induced field around the wire etc.) and *capacitive* parts per unit length. The latter is thereby modeled as a **shunt capacitor** to ground, with a corresponding *conductive bypass* G_s that is determined by the dielectric between the central conductor and the two GND planes. All four parameters are also known as **primary line constants**.

The actual current flow and voltage drop across the transmission line follow a pair of *linear differential equations*, the so-called **Telegraph equations** [203–205], which describe the *time-* and *distance-dependent* signal propagation along a transmission line in terms of the *Maxwell equations* of a **distributed-element-system** [206, 207]:

$$\frac{\partial V(S,t)}{\partial S} = -R_S I(S,t) - L_S \frac{\partial I(S,t)}{\partial t}, \tag{4.12}$$

and

$$\frac{\partial I(S,t)}{\partial S} = -G_S V(S,t) - C_S \frac{\partial I(S,t)}{\partial t}, \tag{4.13}$$

with the *second order form* in the frequency domain

$$\frac{\partial^2 V(S)}{\partial S^2} = \gamma^2 V(S), \tag{4.14}$$

$$\frac{\partial^2 I(S)}{\partial S^2} = \gamma^2 I(S), \tag{4.15}$$

and with

$$\gamma = \alpha + i\beta = \sqrt{(R_S + i\omega L_S)(G_S + i\omega C_S)} \tag{4.16}$$

as the **complex propagation constant**. This, together with the *attenuation factor* α and the *phase constant* β forms the **secondary line constants**. The important result of Eq. 4.15 is, that the signal on the transmission line consists out of a superposition of two, exponentially decaying plane waves, which are traveling with the same propagation speed in forward and backward direction. Thus, in a more technical picture, there is always a **reflected signal** that interferes with the original signal.

The determination of the various individual transmission line parameters can be rather complicated experimentally or with simulation approaches. Thus, a single, externally accessible design

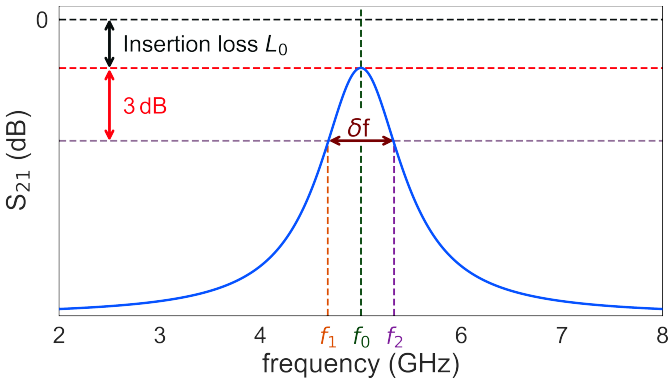

Figure 4.4 – *Qualitative transmission through a resonator in transmission [S_{21}] direction with respect to the external frequency and with a fixed insertion loss L_0. Close to the resonance frequency f_0, the system changes into a state of **collective excitation**, which effectively shrinks down the system into a pseudo-lumped element behavior. The shape of the resonance then follows a Lorentz function, with the full width at half maximum frequency defined as the point of 3 dB signal loss.*

parameter was developed that fully characterizes the behavior of every CPW-based element with respect to the internal wave propagation as well as for connections to other microwave-related systems. Therefore, a major part of this thesis aims on the optimization of the so-called **characteristic impedance** [208, 209]

$$Z_0 = \sqrt{\left(\frac{R_S + i\omega L_S}{G_S + i\omega C_S}\right)} \tag{4.17}$$

Based on *technical conventions* [210, 211], its value for most of the commercially available signal generators, cables etc. is typically set to $Z_0 = 50\Omega$. If one designs a microwave circuit, it is of special importance to maintain this value across all photon-transmitting components in order to avoid *reflections*. Otherwise, the thereby formed **standing waves** can increase up to such extend that they completely suppress any signal propagation. Quantitatively, the relevant design parameter for all internal and external connections is the **reflection coefficient**

$$\Gamma = \frac{Z_L - Z_0}{Z_L + Z_0}, \tag{4.18}$$

which is, for a perfect **impedance match**, equal to zero. Here, the *loaded impedance* Z_L combines both the actual connection to the next element as well as the impedance of the connected element itself.[2] In most arrangements, however, there is also a (small) *reflected* wave. Thus, the actual measured impedance differs from the theoretical value with respect to the distance s from the loaded impedance Z_L:

$$Z_{in}(s) = \frac{V(s)}{I(s)} = Z_0 \frac{1 + \Gamma e^{-2\gamma s}}{1 - \Gamma e^{-2\gamma s}} = Z_0 \frac{Z_L + Z_0 \tanh(\gamma s)}{Z_0 + Z_L \tanh(\gamma s)}, \tag{4.19}$$

with Z_{in} as the effective **input impedance**.

So far, the description was just focused on a single transmission line without any real environment. In the case of a real circuit, however, one has to deal with multiple microwave-transmitting component. A typical layout usually consists out of a central transmission line - a **feedline** - that is connected to both the external input and output **port**. This is then *capacitively* coupled to one or more **resonators**, all with there individual **resonance frequency**

$$f_0 = \frac{1}{2\pi\sqrt{LC}}. \tag{4.20}$$

Here, L and C refer to the total inductance and capacitance, i.e. the combination of the already introduced properties *primary line constants* with the actual line geometry. Close to f_0, the resonator starts to behave like a **lumped element** with the *Lorentz*-like transmission function shown in Fig. 4.4:

$$T(f) = \frac{L_0}{(f - f_0)^2 + \frac{1}{4}\Delta f^2}. \tag{4.21}$$

[2] Interestingly, both for the case of an *open connection* $Z_L \longrightarrow \infty$ as well as for a *short circuit* $Z_L = 0$, $\Gamma = 1$ i.e. complete reflection. Thus, one refers to both cases as *perfect discontinuities*.

Here, Δf corresponds to the *full peak width at half maximum* [**FWHM**] and L_0 is the insertion loss of the system with respect to the transmitted signal S_{21}. In order to understand the latter, one has to take a brief look into the **network theory** [212, 213].

At higher frequencies, the description of a propagating signal in terms of *voltages* and *currents*, as shown in Fig. 4.3(b), becomes more and more complicated. Therefore, on usually starts to describe with *power waves* and a set of so-called **complex S parameters** [214, 215] which contain the real and imaginary parts of *magnitude* and *phase*. Thus, they allow to quantify how much *energy* is transferred through a system - usually displayed in **dB** - rather than trying to determine the individual potential differences or charge carrier motions. Thus, it is not longer necessary to know the exact realization of a network. Instead, one just measures the input and output signal and uses this information to model and optimize the system. Here, a single **port** always refers to a set of two lines at the terminal. Therefore, if one now considers an *incident wave* that propagates towards the left-hand side *input line* a_1 of a **two-port network**, one ends up with a set of *four* S parameter. In the same picture, a part of the wave is reflected out of the *outpot line* b_1 of the same port, while most of it is transmitted and leaves the system through the *output line* b_2 of the second port. The *input line* of the second port is here $a_2 = 0$. This rather long description can be simplified in terms of a **scattering matrix**:

$$\begin{pmatrix} b_1 \\ b_2 \end{pmatrix} = \begin{pmatrix} S_{11} & S_{12} \\ S_{21} & S_{22} \end{pmatrix} \times \begin{pmatrix} a_1 \\ a_2 \end{pmatrix}. \tag{4.22}$$

Here, $S_{21} = \frac{b_2}{a_1}$, i.e. the ratio between the *transmitted signal* at **port 2** and the *incident signal* at **port 1**. Thus, the off-diagonal parameter S_{21} and S_{12} act as **transmission coefficients**, while S_{11} and S_{22} are those for **reflection** [216]. Generally speaking, the second index always refers to the port that is excited.

Even though the *S parameter* can be used to describe a whole microwave circuit network or individual components, they are not really suited to *benchmark* it due to their dependency on the frequency, the load impedance and so on. If one wants to do so, the usual figure of merit is the so-called **quality factor**:

$$Q = \frac{\text{total amount of stored energy}}{\text{energy loss per second}} = \frac{f_0}{\Delta f}. \tag{4.23}$$

However, in the case of a real microwave circuit, the effective quality factor is determined by a broad set of internal and external properties, e.g. dielectric losses caused by parasitic TLS in the substrate and the superconductor itself, resistive losses due to *quasi-particle poisoning* at finite temperatures or external radiation losses due to thermal photons coming from the fridge components. Therefore, one usually characterizes the energy decay rate of the system by means of three individual parameters:

Q_i The **internal Q factor** tries to quantify the quality of the system for the case of no external influences or couplings. Consequently, it acts as a figure of merit for the *used superconductor* (crystallinity, the density of surface states, material defects during the growth....) and the *applied fabrication processes* (edge losses, etch-induced defects, residual resist...). It should always be as large as possible due to its back-action on all other circuit components, including the qubit, and the fact that it usually corresponds to the largest volume of the sample. In the case of a $\lambda/2$ resonator, like it is used for the capacitively coupled Gatemons within this thesis (cf. Sec. 1), close to its resonance, one finds

$$\frac{1}{Q_i} = \sum_i \frac{\pi}{2\alpha_i L}, \tag{4.24}$$

with L as the total length of the resonator and α_i as the **attenuation constant** for every individual loss channel. Typical state-of-the-art values for Q_i are in the range of $500000 - 1000000$, depending on the chosen superconductor, the substrate and the used process steps [217–219].

Q_c The **external** or **coupling Q factor** determines the efficiency of the photon-transfer between the *source*, usually realized by means of a **feedline**, and a **resonator**. It is usually controlled by

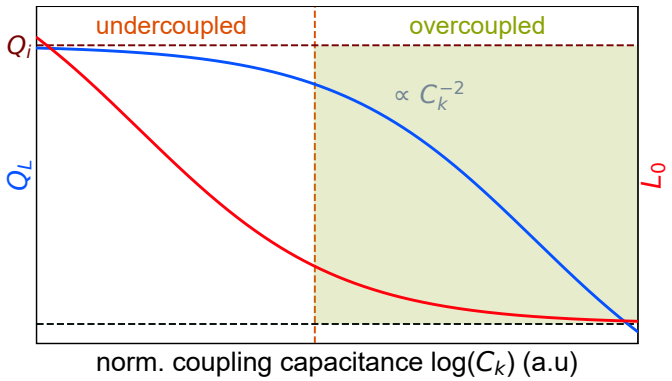

Figure 4.5 – *The loaded quality factor and insertion loss in the different coupling regimes. The dashed lines are the asymptotes for the different coupling regimes.*

means of a properly designed **coupling capacitor** C_k and directly influences the lifetime of the photons on the resonator. Assuming a large enough Q_i, Q_c is usually set to comparably small values for qubit measurements. The obvious reason is the fact, that the successful measurement of **Rabi oscillations** requires the full elimination of the initial *excitation pulse* first. For spectroscopy measurements, on the other hand, Q_c is usually in the same order as Q_i in order to maximize the lifetime of the *probe photon*.

Q_L The so-called **loaded Q factor** is related to the connection between a resonator, as a photon-transmitting component, and an *active element* that can absorb and emit photons, like a **qubit**. It strongly depends on the kind of coupling, i.e. *inductive* for $\lambda/4$ or *capacitive* for $\lambda/2$, the separation in y (the actual gap between both structures) and x direction (the mismatch between the field maximum and the dipole). It is the only parameter that is directly accessible in the experiment.

In a complete system, the three quality factors are thereby related as

$$\frac{1}{Q_L} = \frac{1}{Q_i} + \frac{1}{Q_c}, \tag{4.25}$$

with Q_c as the only *independent* and *fully tunable* loss mechanism.

As already mentioned, the behavior of a microwave circuit including a *feedline*, a *resonator* and an *active element* in terms of energy and photon transfer fully depends on the ratio between the three quality factors. Here, three different regimes can be defined, which are exemplary and qualitatively shown in Fig. 4.5. The point of *maximum energy transfer*, the so-called **critical coupling**, thereby refers to the condition $Q_i = Q_c$. For $Q_i \ll Q_c$, the system is **undercoupled** and the loaded quality factor just depends on the intrinsic quality of the system, i.e. Q_i. Additionally, in this regime, Q_L is also almost indepedent from the *coupling capacitor* C_k, which is beneficial for the design of the circuit. In the opposite case, i.e. $Q_i \gg Q_c$ and **strong coupling**, the total quality and energy dissipation of the system is controlled by the coupling between the resonator and the feedline. Here, $Q_L \propto 1/\sqrt{(C_k)}$ and a precise tailoring of the coupling capacitor becomes necessary. It should be pointed out, that even though the above analyzed mechanisms are summarized as *losses*, an external coupling is always necessary to read out the resonator and thereby get information about the state of the *active element*.

After this discussion about the different ways to control, manipulate and readout a Qubit-like structure, the next chapter is now focused on two actual realizations of those underlying principles: The **Gatemon** [220], as a capacitively coupled device based on a macroscopic supercurrent, and the mesoscopic **Andreev Qubit** [157], which is based on the *inductive coupling* to single *Andreev bound states*.

5

SEMICONDUCTOR-SUPERCONDUCTOR HYBRID QUBITS

Currently, the field of solid-state qubits is divided into two independent sections: On one hand, there are the well-established **superconducting qubits**, like the Fluxon, which provide stable and long-living quantum states due to the build-in coherence of the Coo-per pair condensate. Here, the underlying principle is always related to the *critical current* of a Josephson junction and the collective excitation of an macroscopic and distributed circuit. On the other hand, there are the semiconductor-based systems, where the two-level system is realized on the level of single electrons by means of strong confinement, i.e. quantum dots, and spin-orbit interaction.

Over the last couple of years, a growing number of **hybrid systems** were proposed, all of them aiming to combine the main advantages of both approaches, i.e. robustness, small footprints and electrical tunability. One of them is the **Gatemon** qubit, which adapts the main principle of the most promising superconducting qubit, the **Transmon**, and combines it with a semiconductor nanowire or a semimetal in order to replace the required magnetic field generating circuity with a single gate electrode. However, the main control parameter is still a *bulk property*, the **kinetic inductance**. Accordingly, the goal is to realize a normal Josephson junction with a huge number of channels within the weak link and a sinusoidal current-phase relation. In contrast to that is the **Andreev qubit**, which was already proposed more than two decades ago and now finally gets closer and closer to the actual technical realization [157, 221]. Here, the two-level system is realized on the most fundamentally excitation level in terms of a *single Andreev bound state*.

Both approaches, the Gatemon and the Andreev qubit, are the topic of the following chapter.

5.1. TUNING THE CRITICAL CURRENT : TRANS- AND GATEMONS

The transmon qubit has been described historically as an special case of the earliest realization of a superconducting qubit, the *Cooper pair box* [**CPB**] [222, 223]. The latter consists out of a Josephson junction that is *capacitively* coupled to a massive gate electrode and a superconducting, as depicted in Fig. 5.1. Here, a superconducting charge island is formed between the gate capacitor and the Josephson junction. The degree of freedom of the device is the number of Cooper pairs on the island n_g. Thus, it is the prototype of a **charge qubit**, in which the so-called *offset charge* is used to control the *coupling* and interaction with the environment.

The two systems, i.e. the Transmon and the CPB, are qualitatively identical and differ just in the size of their characteristic energy scales. The first of them is the **charging energy** E_c, which was already introduced within the discussion of *quantum dots* (see Sec. 3.3), and acts as a figure of merit for the amount of energy that is required to place a single charge e on the island:

$$E_c = \frac{e^2}{2C_\Xi}. \tag{5.1}$$

Here, $C_\Xi = C_g + C_J$, with C_g as the gate capacitance and C_J the self-capacitance of the Josephson junction. Based on the design, C_Ξ takes rather small values, which results in a large charging energy and therefore a transport behavior that is based on the transfer of *single electrons or Cooper pairs*, i.e. the **Coulomb blockade regime**.

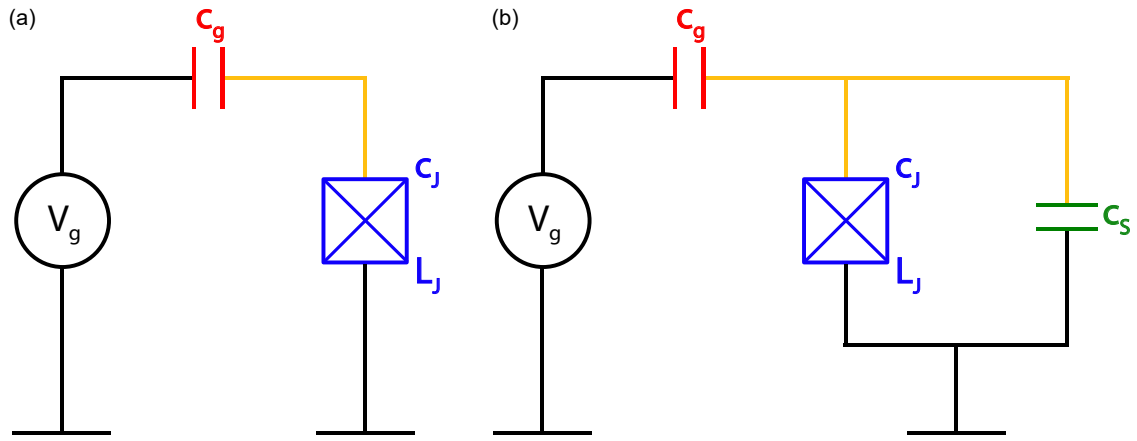

Figure 5.1 – *(a) Equivalent circuit of the Cooper pair box. A Josephson junction with intrinsic capacitance C_J the kinetic inductance L_J is capacitively coupled to a gate voltage V_G by means of a capacitor C_G. The orange area corresponds to the **superconducting charge island**. (b) Circuit scheme of the Transmon qubit. The additional, large shunt capacitance C_s makes it insensitive to charge noise and reduces the contribution of the charging energy E_C.*

The second contribution is the amount of energy that is necessary to induce a phase change of 2π between the charge island and the connected superconducting. It is given by the **Josephson coupling energy**

$$E_J = \frac{\Phi_0 I_c}{2\pi} = L_J I_c^2 \tag{5.2}$$

and thereby directly determined by the critical current of the junction. It should be pointed out that this relation is generally defined under the assumption that system is or *behaves* like a **tunnel junction**, i.e. with a **sinusoidal current-phase relationship**. For real CPB devices, however, $E_J << E_c$. The latter, and especially the weak coupling to its environment, is the reason why there are distinct levels in the charge qubit that can be described in terms of the macroscopic state $|n\rangle$ by utilizing the number operator $n^\dagger$. The former counts the number of additional Cooper pairs on the island with respect to the offset charge n_g. The two relevant energy levels of the qubit, i.e. ground and first excited state, can then be expressed with two adjacent Cooper pair number states $|n\rangle$ and $|n+1\rangle$.

If one now tries to write down the total energy of the system, consisting out of the electrostatic energy stored in the combined *capacitor* C_Ξ and the magnetic energy stored within the non-linear

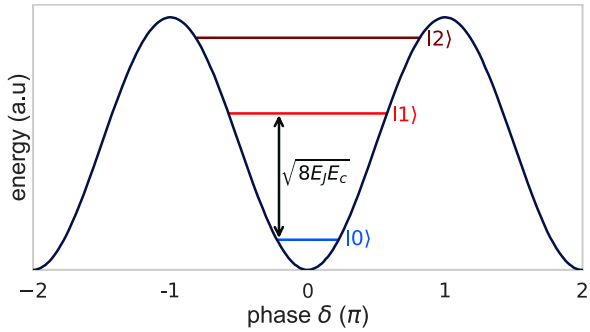

Figure 5.2 – *Cosine potential of the transmon qubit plotted versus the phase difference across the Josephson junction. The intrinsic anharmonicity results in the formation of a non-uniform level spacing and thus different transition energies.*

inductance of the Josephson junction, one ends up with the **Hamiltonian**:

$$\hat{H} = 4E_C\left(n^\dagger - n_g\right)^2 - E_J\cos(\hat{\delta}). \tag{5.3}$$

The operator $n^\dagger$ corresponds to the number of Cooper pairs that are transferred to the island, n_g is the number of *excess charges* and $\hat{\delta}$ is the phase difference across the Josephson junction. The former is thereby promoted to a quantum mechanical operator, too. However, one of the advantages of the system, namely the comparably simple tuning of the **transition energy** E_{01} by means of the number of charges, is also its major drawback. This becomes immediately obvious if one considers the dispersion relation of the system, shown in Fig. 5.3. Here, the two top most images correspond to the case $E_J/E_c \leq 1$, which makes the system operate as a charge qubit. The plot on the left hand side shows the different energy level in dependency of the *excess charge* n_G and with respect to the minimum value of E_0. In order to use the $|0\rangle \rightarrow |1\rangle$ transition as the actual qubit TLS, a proper *sweet spot* has to be picked. To be more specific, it should be equal to the point of **maximum anharmonicity** α, i.e. where $E_{12} \gg E_{01}$. For the given system, this is always the case if the charge island is occupied by an even amount of Cooper pairs plus a single electron, i.e.

$$n_G = 1/2 \cdot i \text{ for } i = ...\text{-}3, \text{-}1, 1, 3, ... \tag{5.4}$$

Thus, those half-integer points represent the *logical qubit states*. If the system moves away from the working point by adding another single electron, the transition energies immediately swap in magnitude, i.e. $E_{12} \ll E_{01}$. For even smaller values of E_c, the upper level are degenerated, which destroys the anharmonicity in total. In this case, the qubit state collapses and all stored information is lost. This makes the system extremely sensitive to any kind of charge noise and therefore, due to the resulting **short coherence times**, basically unusable for any real-world application. One way to tackle this issue is the reduction of the charging energy by means of an alteration of the total capacitance of the system. If one increases the latter, the two characteristic energies of the system swap in magnitude, i.e. $E_J/E_c > 1$. A proper way to do this is the inclusion of an additional, large capacitor in parallel to the Josephson junction, as depicted in Fig. 5.1 (b). This newly added capacitive element also provides the name for the resulting structure, i.e. the *transmission line shunted plasma oscillation qubit* or **Transmon**.

The major drawback of the CPB, as a charge qubit, is its sensitivity to noise plus the required *charge bias* to fix the system at the half-integer points for the *excess charge* n_G. However, if one increases E_J or decreases E_C, respectively, the dispersion of the levels flattens (see Fig. 5.3 (a),(c),(e)) until, at some point, the Josephson junction within the circuit becomes the dominating element, effectively pushing the whole system into the **phase regime**. The resulting **cosine potential**, already introduced with Eq. 5.3 is shown in Fig. 5.2. Here, the two lowest levels correspond to the actual *qubit states* $|0\rangle$ and $|1\rangle$. They are separated by the **plasma frequency** of the junction (see Sec. 3.1)

$$\hbar\omega_p = \sqrt{8E_JE_c}, \tag{5.5}$$

which accounts for the description as *plasma oscillation qubit*. However, if one compares the **relative anharmonicity** α_r of the system, depicted in Fig. 5.3 (b),(d),(f)) for different E_J/E_C ratios, it

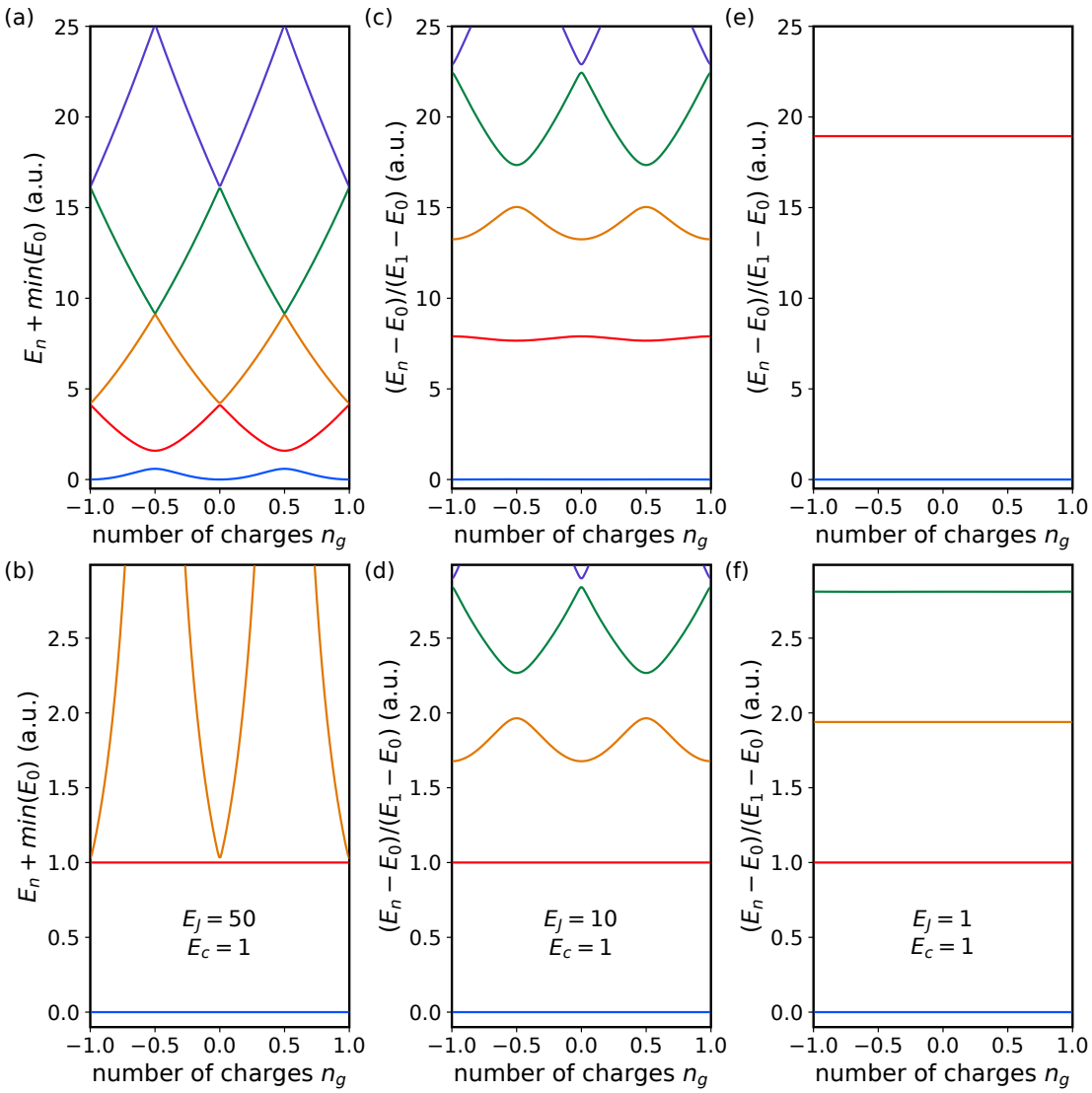

Figure 5.3 – *Simulated energy levels for a CPB as a function of the effective offset charge n_g. In (a), where the charging energy E_c is sufficiently larger than the Josephson coupling E_J, there is a well-defined sweet spot at half integer values such that the bottom two levels form an isolated **charge qubit**. (b),(c) If the Josephson coupling is increased, the level are gradually flattened out in charge space. At some point, E_J becomes the dominating property of the device, resulting in a transformation into a **phase qubit**. (d)-(f) The same energy levels with respect to the energy separation between the ground state and the first excited state. One can see, how the flattening of the energy levels is correlated with a reduction of the **anharmonicity**.*

becomes immediately obvious that the flatness of the dispersion is correlated with a reduction of the level separation, or, to be more precise, with a *convergence* of the different level spacings E_{ji}. Strikingly, Koch et. al [220] could show, that while the dispersion itself decreases *exponentially* with $\sqrt{E_J/E_C}$, the reduction of the anharmonicity just follows an *polynomial* behavior. Thus, it is possible to create a qubit system that is (nearly) insensitive to charge noise but still provides a reasonable large anharmonicity.

5.1.1. DISPERSIVE READOUT

In order to decouple the Transmon from the environment and, more importantly, control the total number and the energy of photons that reach the device, usually a *coplanar waveguide resonator* is used. In this case, the combined circuit mimics the already introduced **Jaynes-Cummings model**, if one considers the resonator as the *cavity* and the qubit as the *atom-like two level system*. If both parts are in *resonance*, i.e. **zero detuning** $\Delta = \omega - \omega_r$, the coupled system forms the already introduced **dressed states** (see Fig. 4.1). In this configuration, it is not possible to manipulate the qubit or read-

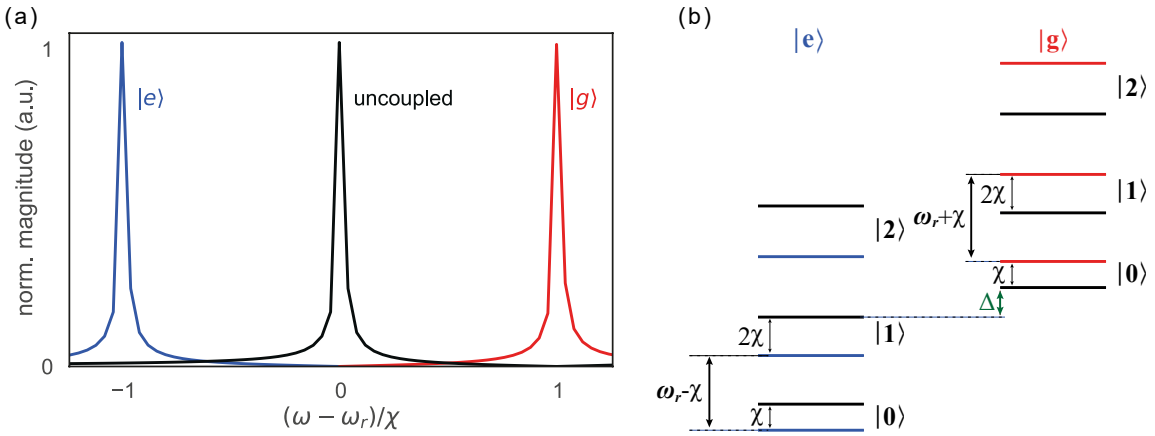

Figure 5.4 – *(a) Transmission profile of a resonator coupled to a Transmon. In the uncoupled case (black), the resonator is located at its designed resonance frequency. However, if the qubit and the resonator are coupled, but* ***detuned*** *by an offset frequency* Δ*, the position of the resonator in the frequency space depends on the state of the qubit. (b) The same mechanism in the excitation picture. For large detunings, the level separation of the formerly dressed states* $\omega_r \pm \chi$ *depends on the ratio between* Δ *and the coupling strength* g*.*

out its current status in a controlled way, as the induced **intrinsic Rabi oscillation** always leaves the TLS in a *pseudo-driven state*. The resulting *anticrossing*, i.e. the **vacuum Rabi splitting**, makes it impossible to distinguish between the resonator and the qubit.

The typical solution to overcome this issue is a so-called **dispersive readout** [224, 225]. Here, the qubit frequency is actively and intentionally misaligned with respect to the resonator. In the case of a nanowire-based Transmon, this can be achieved by means of an applied gate voltage that alters the *supercurrent* through the Josephson junction and, subsequently, the *kinetic inductance*. In terms of the Jaynes-Cummings framework, this is equal to the case

$$\frac{g}{\Delta} \ll 1 \tag{5.6}$$

which is also referred to as *dispersive limit*. The advantage of this approach lies in the fact that the *level separation*, and therefore the *position of the resonator* in the frequency space, directly depends on the **qubit state**. Quantitatively, the resulting Hamiltonian takes the form

$$H_{qr} = \hbar(\omega_r + \chi)aa^\dagger + \frac{\hbar}{2}(\omega + \chi) \tag{5.7}$$

with

$$\hbar\chi = \frac{g^2}{\Delta} \tag{5.8}$$

as the resulting **energy shift**. The corresponding energy spectrum for both the *ground state* $|g\rangle$ as well as the *excited state* $|e\rangle$ is shown in Fig. 5.4(b). If it comes to the real measurement, the resonance frequency is now shifted by $\mp\chi$ for the qubit being either in $|e\rangle$ or $|g\rangle$, respectively. Technically, and under the assumption that the qubit is not exposed to any parasitic drive from the environment and therefore in the ground state, one can now search for the resonator frequency by means of, for example, a *network analyzer*. In the next step, a *second tone* is applied, which is altered in frequency until one hits the transition frequency of the qubit ω. The resulting shift of the resonance frequency is then reflected in the continuous measurement of the first tone, as depicted in Fig. 5.4(a). The required *microwave power* directly depends on the degree of the detuning, as the non-resonant coupling drastically restricts the number of photons that can be transferred to the device. For a given power level, however, one can then extract the *(driven) Rabi frequency* Ω by applying longer and longer ω-pulses. The induced rotation on the *equatorial axis* of the **Bloch sphere** is thereby limited by the *relaxation time* T_1 and the *dephasing time* T_2, resulting in an *expontentially decaying* measurement of the **probability** to occupy the **excited state of the qubit** $P(|1\rangle)$. If $P(|1\rangle)$ hits 0.5, the coherent

system is completely destroyed and the corresponding time scale therefore marks the **lifetime of the qubit**.

It should be pointed out, that in qubits that rely on the *collective excitation* of a macroscopic circuit, e.g. the Transmon, higher levels exist that can also be populated and thereby alter the resonator in a comparable (but parasitic) fashion. Thus, in a real measurement, one has to compare the magnitude of χ, as, for higher levels, the *coupling constant* g increases roughly $\propto (E_J/E_C)^{1/4}$ [220]. However, those higher levels can still act as additionally decay channel and therefore limit the lifetime of the qubit. One way to avoid this is to use system that only host a *single pair of states by*, for example, utilizing a Josephson junction that is deep in the **short channel regime**. This particular setup is known as **Andreev qubit** and the topic of the next section.

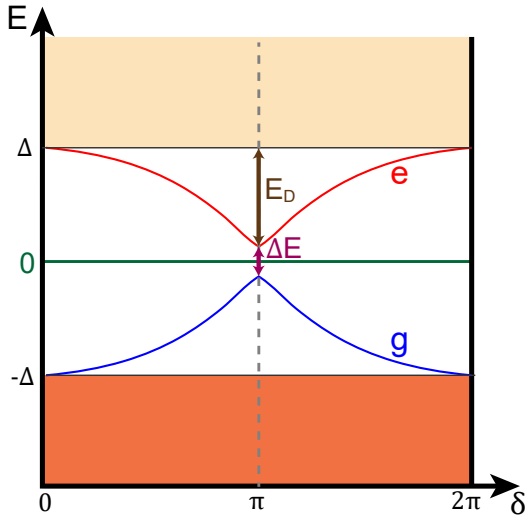

Figure 5.5 – *Single particle energy spectrum of a mesoscopic Josephson junction deep in the short channel regime and with a single state transparency τ close to unity. The even states are tied to the phase difference of the junction and separated by the* ***transition energy*** *ΔE=f(τ). The odd states, on the other hand, are phase-independent and localized in the middle of the gap at zero energy.*

5.2. THE ANDREEV QUBIT

If the dimensions of a mesoscopic nanowire junction become shorter than the corresponding *coherence length* of its *superconducting contacts*, the Josephson coupling, and therefore the supercurrent, is maintained by a single pair of **Andreev bound states**. The dispersion relation of the states is thereby tied to the phase difference δ across the device, while, on the other hand, the minimum in energy is defined by the transparency τ:

$$E_A = \pm\Delta\sqrt{\left(1-\tau\sin\left(\frac{\delta}{2}\right)\right)}. \tag{5.9}$$

A typical, phase-dependent bound state configuration is shown in Fig. 5.5. For $\delta = n\cdot 2\pi$, the states run towards the edge of the continuum states, which results in a complete loss of all stored information. However, for $\delta = \pi + n\cdot 2\pi$, the ABS are located deep within the superconducting gap, with a minimum separation of

$$\Delta E = 2\Delta\sqrt{1-\tau}. \tag{5.10}$$

For high transparencies, the residual gap between the states is much smaller than the energetic distance to the continuum states, i.e. $E_D \gg \Delta E$ (cf. Fig. 5.5) and the ABS can be described as an *isolated two-level system* and therefore act as the building block for a qubit structure, the so-called **Andreev qubit**. It should be pointed out that, even though the active device is also a Josephson junction, the resulting system is fundamentally different from other superconducting qubits like the Cooper pair box or more recent technical realizations like the Transmon or the Fluxonium. All of the latter have in common that they require a collective excitation of an anharmonic, macroscopic circuit with multiple levels and the quantization of an electromagnetic variable, which is typically the flux induced by an applied magnetic field. More importantly, they just exploit the **non-linear inductance** that is associated with the weak link and controlled by the magnitude of the supercurrent as a bulk variable. The Andreev qubit, on the other hand, is fully determined by a pair of spatially localized and isolated **microscopic excitations** of the *BCS condensate*, i.e. the Andreev bound states. Even though they have been already introduced in the description of mesoscopic Josephson junctions, the Andreev qubit requires an in-detail and more rigid view on the exact formation and properties of the relevant excitation channel.

So far, Andreev bound states were described in terms of an upper ($E_A(\delta)$) and a lower branch (-$E_A(\delta)$) of which the dispersion relation is determined by the phase difference. Under the (strong) assumption, that the **spin-orbit interaction** in the system is neglectable, these are also the **even states**, i.e. empty and fully occupied, that carry the actual supercurrent of the Josephson junction. However, there are also two **odd states**, which are, in terms of the so-called **excitation picture** shown in Fig. 5.7 (f) and (g), occupied by a *single quasiparticle* that acts as an *unpaired spin*. Those are fixed in the middle of the superconducting gap and, under the already mentioned restriction, do not interact

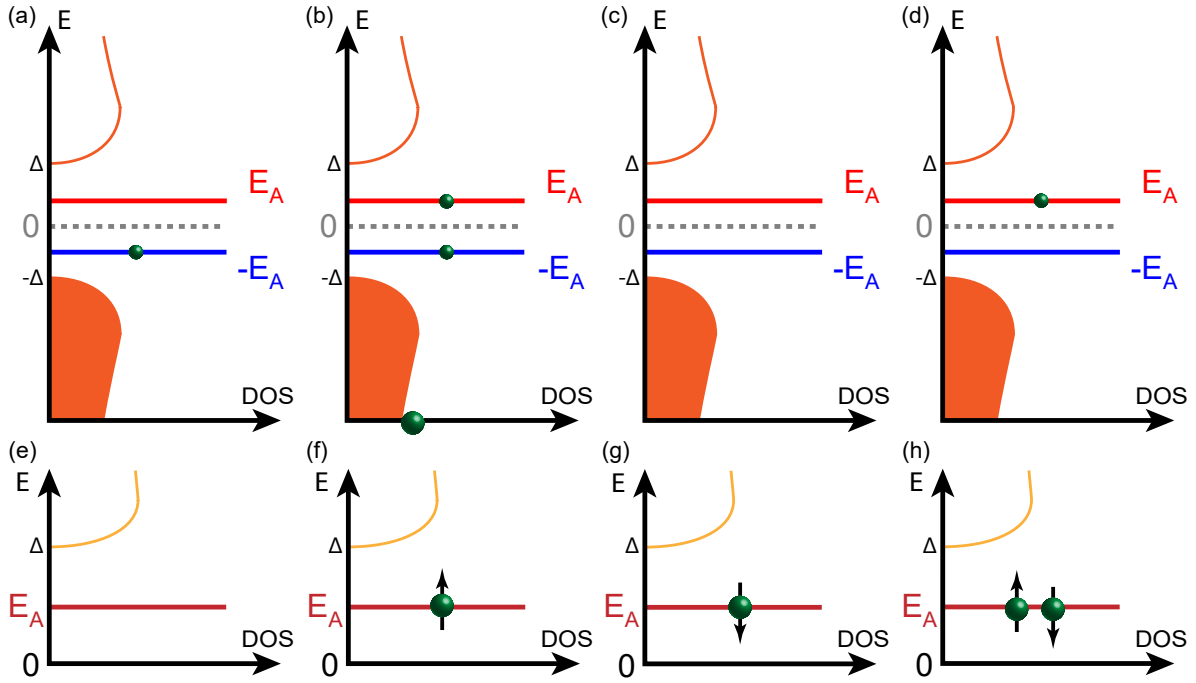

Figure 5.6 – *Even ground state $|g\rangle$, single excited odd states $|o\uparrow\rangle$ and $|o\downarrow\rangle$ as well as the even double excited state $|e\rangle$ in the one-particle picture (top) and in the excitation picture (bottom).*

with the empty or fully occupied state, respectively. To be more specific, due to their different parity, they can only be accessed if a quasiparticle leaves or enters the system. Thus, they also do not contribute to the supercurrent through the system and are usually ignored.

Following again the *excitation picture* in Fig. 5.7 (e) and (h), the Andreev qubit is now defined by means of the two even states that represent no and full occupation, respectively. The corresponding effective Hamiltonian is given by [226, 227]

$$H_A = \Delta e^{-i\sigma_x\sqrt{(1-\tau)}\delta/2}\left[\cos(\frac{\delta}{2})\sigma_z + \sqrt{(1-\tau)}\frac{\delta}{2}\sigma_y\right] \tag{5.11}$$

with the *Pauli spin matrices* [228]

$$\sigma_x = \begin{pmatrix} 0 & 1 \\ 1 & 0 \end{pmatrix}, \tag{5.12}$$

$$\sigma_y = \begin{pmatrix} 0 & -i \\ i & 0 \end{pmatrix}, \tag{5.13}$$

$$\sigma_z = \begin{pmatrix} 1 & 0 \\ 0 & -1 \end{pmatrix}. \tag{5.14}$$

The important finding is, that this Hamiltonian, and therefore the underlying physic, mimics the behavior of a *single spin* that is exposed to an *applied magnetic field* with a **transition energy**

$$hf_A(\delta) = \Delta E(\delta) \tag{5.15}$$

between the ground state $|g\rangle$ and excited state $|e\rangle$.

If it comes to the real experiment, the procedure is relatively straightforward. First, one performs a set of *vector network analyzer* measurements with different microwave powers to determine the resonance frequency of the resonator. In the next step, one selects a frequency that is in close proximity, but not directly in the center of the resonance minimum in order to make the measurement less sensitive to noise. Subsequently, one changes one of the electromagnetic variables that control the state configuration in the system. Typically, this is first done by means of the gate voltage in order to select a energy range that just contains signatures of one (or at maximum a few) states. The

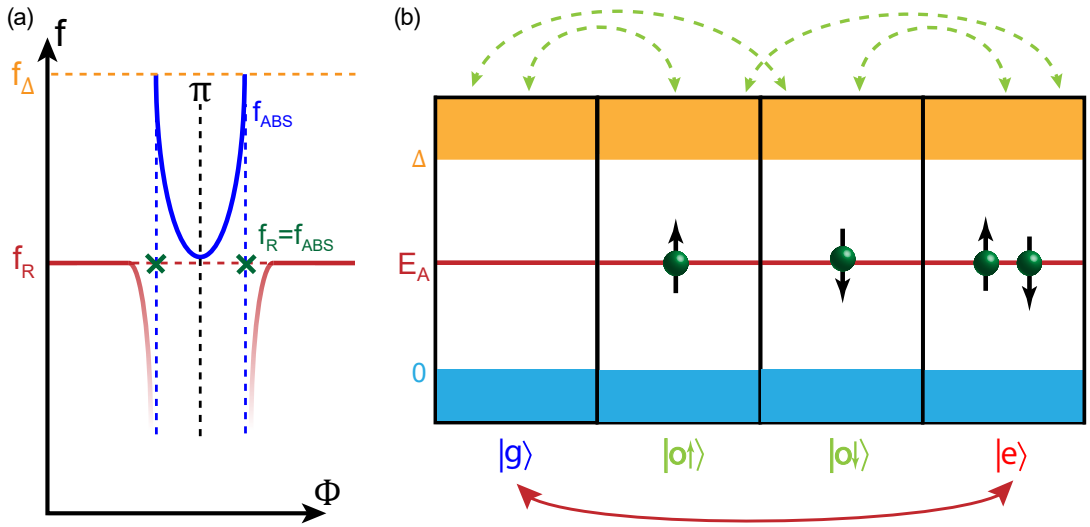

Figure 5.7 – *Model of a single Andreev bound state coupled to a microwave resonator. (a) Exemplary response of a resonator-ABS-system. If the external magnetic field produces a phase difference of π in the junction, the energy of the excitation moves down in energy until it reaches the resonance frequency f_R. The induced coupling allows the coherent exchange of photons between the transmission line and the TLS, resulting in an avoided crossing. (b) Many-body configurations of a spin-degenerate Andreev level in the excitation picture. A microwave transition (red arrow) links the ground state $|g\rangle$ and the double excited state $|e\rangle$, while quasiparticle poisoning (bright green arrows) links the even and odd manifolds, effectively opening up a decay channel for the qubit.*

final step is the alteration of the out-of-plane magnetic field, that controls the flux in the system and therefore the phase difference δ. The resulting (simplified) response is exemplary shown in Fig. 5.7 (a). If the magnetic field is tuned, the Andreev bound state (blue) eventually comes down from the superconducting gap Δ until, close to **flux** $\pi = \Phi_0/2$, the perturbation of the resonator due to the rising **coupling strength** g becomes dominant. At some point, the bound state and the resonator start to form a *coherent system* that is able to exchange photons. In the measurement, this manifests itself as a so-called **avoided crossing**. By performing the same techniques as for the Transmon, i.e. a *dispersive readout* described by the coupling term $\hbar\chi aa^\dagger(|e\rangle\langle e| - |g\rangle\langle g|)$, one can now determine the lifetime of the Andreev bound states by means of driven Rabi oscillations.

For an ideal system, the lifetime of the states would be infinite as their would be no possible decay channel. However, for real systems, this assumption falls way too short. First, the system is always disturbed by a certain amount of *phase noise* induced by flux or gate voltage fluctuations. In the case of high transparencies, i.e. when the two ABS are in close proximity and therefore *theoretically* well-isolated, the phase noise can be large enough to induce spontaneous transitions between $|g\rangle$ and $|e\rangle$. This effect is known as *Landau-Zener-(Stückelberg) transitions* [**LZTs**] [17, 229–231] and can fully destroy the current qubit state. However, due to its dependency on an extremely small energy separation of the ABS, this effect can also manifest itself as a potential signature of a **topological gap**. The second effect, on the other hand, is especially important for systems based on materials like *InAs*, as they can alter the spin degree of freedom of the quasiparticles in the weak link. As already mentioned, the two states of the Andreev qubit are formed by the *even manifold*, consisting out of the *unoccupied ground state* $|g\rangle$ and the *double excited state* $|e\rangle$. The transition between both levels, shown in Fig. 5.7 (b) is **parity conserving** and can therefore be controlled in a coherent way. However, in real devices, there are also parity-breaking transitions that result from an incoherent quasiparticle exchange with the continuum of modes in the junction leads. The latter couples the **even states** with the **odd states**, lifting up the well-isolated state system and opening an intrinsic decay channel. This phenomenon is known as **quasiparticle poisoning** [232–234] and is, for most systems, the main limitation of the qubit lifetime.

II

TOWARDS LOW-LOSS QUANTUM (CONTROL) CIRCUITS

Ever tried.
Ever failed.
No matter.
Try Again.
Fail again.
Fail better.

Samuel Beckett

1

REQUIREMENTS

The general understanding of *how* to realize a solid state qubit, as well as the fundamental physics for its creation and control, is already well-known for many decades. Concepts like Josephson junctions and quantum dots were heavily investigated in terms of different materials, the influence of electromagnetic fields as well as increasingly more complex device layouts. However, while it is relatively simple to create a single, physical qubit as an individual entity, perform actual calculations with it is a much more complicated affair.. In order to fulfill the DiVincenzo criteria, i.e. Scalability, Measurability, Controllability, Initializibility and Robustness, some major challenges have to be addressed during the fabrication:

- The nanowire Josephson junctions, as the heart of all the qubit designs investigated in this thesis, have to be designed properly. The main limitation for the device performance, in this sense, is the superconductor-semiconductor interface. Conventional cleaning methods, which all aim to physically or chemically remove the native oxide on the In-compound nanowires, always lead to a degradation of the interface and reduce its transparency. While the usage of nanowires with in-situ grown superconductor shells bascially eliminates this specific issue, it generates new challenges as it makes it necessary to locally remove the metal in order to create the *weak link*. The etching medium has to be selected in a way that it etches as anisotropically as possible in order to allow the creation of metal-free regions with large aspect ratios (*ratio of etch depth and weak link length*). More importantly, it has to be selective for the specific superconductor, without degrading the superconductor underneath it or the surrounding circuit.

- In order to manipulate the state of the embedded qubit, the surrounding circuit needs to be able to create and control electromagnetic fields. The transmission line and resonators need to be impedance-matched with the macroscopic circuitry and wiring to avoid reflections of the high-frequency signal as well as the formation of standing waves. Besides this general prerequisite of all qubit designs within this thesis, there are also some specific particularities for both the Gatemon as well as the Andreev qubit. In case of the latter, it is necessary to apply both an electric as well as an magnetic field to isolate a single Andreev bound state and fix its position in respect to the phase across the junction. However, while type-II superconductors can maintain there bosonic ground state up to comparably large magnetic fields, this comes with a drawback in the formation of *Fluxons*. These are. normal-conducting vortex cores surrounded by eddy currents, which induce an additional parasitic inductance on top of the *kinetic inductance* of the material. Ultimately, due to the AC-driven motion of the vortices, the resonance frequency starts to change in an unpredictable way, which, in addition to a strong reduction of the Q factor, generally makes the whole circuit unmeasurable. In case of the Gatemon, on the other side, there is no magnetic field involved and the tuning is done with an applied gate voltage. However, due to the fact that the Qubit needs a specific composition of the characteristic energies, i.e. the *charge energy* E_c and the *Josephson energy* E_J, the coupling to the gate electrode and its effectiveness with respect to the control of the charge carrier density of the nanowire is even more critical than for the Andreev design.

II

- The previously mentioned control mechanisms have to be realized in a way that they do not influence the performance of the Qubit by opening up additional loss channels for either the high-frequency components, i.e. transmission line and resonators, or the nanowire Josephson junction. The most critical things here are the intrinsic losses of the superconductor due to surface states, defects and field-induced dissipation as well as losses in the gate dielectric due to unsaturated, active dipoles which act as additional two-level systems.

The following chapters aim to provide an overview of the fabrication of nanowire Josephson junctions and quantum control circuits, starting with an exemplary and detailed description of all the necessary steps for the realization of an Andreev circuit. Subsequently, both ex- and in-situ nanowire Josephson junctions are discussed, with a specific focus on the different cleaning and etching processes. Finally, different approaches for an optimization are presented, which all aim to address the previously mentioned issues like field-stability, dielectric losses and junction performance.

2

FABRICATION OF MICROWAVE QUANTUM CIRCUITS

Even though the exact realization for the Andreev, Gatemon and Emission circuits differ in detail, the general fabrication shows many similarities. The flow chart in Fig. 2.1 summarizes the major processing steps for the two individual versions of Andreev circuits. They mainly differ in the post-processing of the superconductor and the used gate architecture. In order to increase the robustness of the individual fabrication steps, everything was optimized to be as simple as possible. Therefore, only three different kinds of resists are used, which provide good results even for single layer systems. However, all circuits similarly rely on a proper alignment for the different lithography steps in order to fine-tune the coupling factors for the feedline, resonators and qubits as well as to realize a proper flux-engineering. Therefore the first fabrication step on every wafer is the realization of optimized electron beam (**e-beam**) markers, which is described in the first section of this chapter.

II

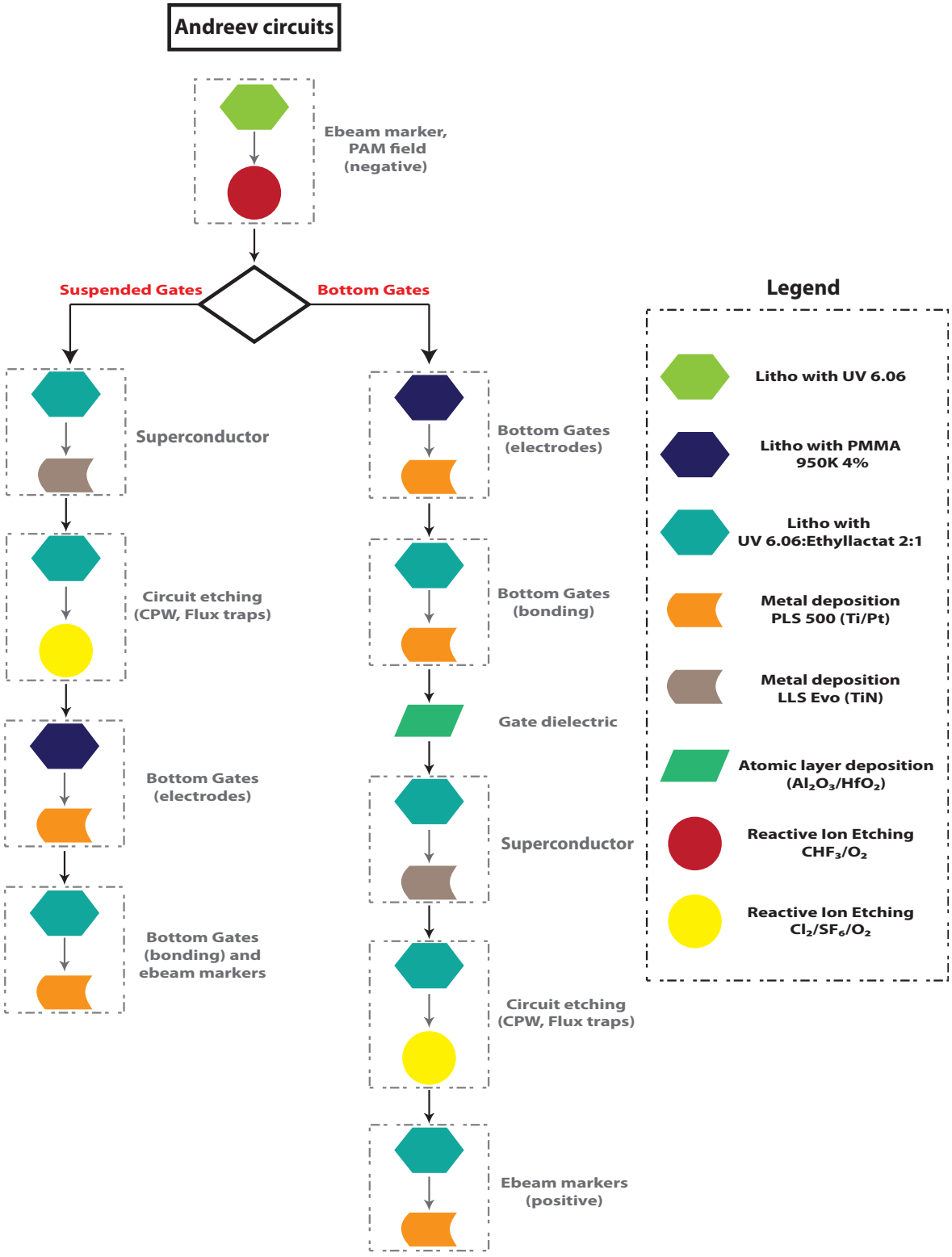

Figure 2.1 – *Exemplary flow chart for the two different versions of the Andreev qubit readout and control circuit to summarize the major fabrication steps.*

2.1. PAM AND EBEAM MARKER

The successful realization of complex high frequency circuits for quantum operations relies on a proper alignment between consecutive fabrication steps and structures of significantly different size and geometry. *Proper*, in this sense, means, that the misalignment between the first step - the definition of the fine gate electrodes - and the last one - the placement of the positive ebeam markers which are used for the lithography in **RIKEN** - has to be below 10nm. Based on a general sample size of (8*4)mm² and (6*6)mm², respectively, this leads to precision requirements for the *tilt* which are smaller than the fraction of one degree. Additionally, most of the patterns have to be written across the whole sample, which generally leads to comparably long exposure times for the individual lithography steps. In order to reduce the influence of *thermal drift*, additional alignment steps are performed between different layers and, in the case of long exposure times, after fixed intervals. Therefore, the conventional e-beam markers are combined with so-called *pre-alignment markers*, henceforth referred to as **PAM**.

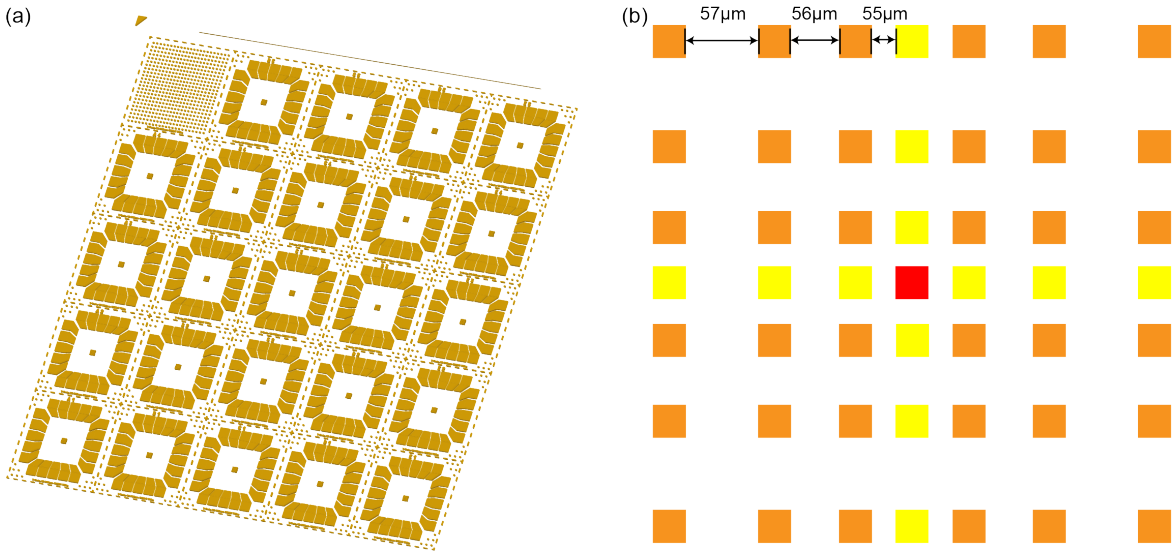

Figure 2.2 – *(a) Model of a typical T-Gate chip consisting of 24 individual samples, including pre-alignment markers, e-beam markers, bonding pads, dicing markers and additional central markers for the nanowire alignment and device fabrication. (b) Schematic overview of the pre-alignment marker array. Starting from the center, the separation between adjacent markers increases continuously. By doing so, an unambiguous coordinate system is formed, which improves the alignment between different design layers.*

While the concept of PAM is widely used in the high-precision fabrication of silicon devices, for this project, it was first introduced in combination with so-called *T-Gate samples*. These chips represent the standard platform for DC measurements in our group and were continuously developed and improved over the last decade. Fig. 2.2 (a) provides an overview of the most recent design iteration, which is prospectively referred to as **T-Gate 12**. Here, a single chip consists out of 25 pieces with a size of (2*2) mm². In order to simplify the sample mounting for the lithography as well as to avoid problems due to *edge effects* during the spin coating, i.e. an increase in resist thickness close to the borders of the chip, an additional, 1mm wide circumferential area is left empty. This leads to a total chip size of (12*12) mm². Due to the fact that these chips were mainly used in the first year of this project and then went slightly out of focus, the actual fabrication recipe for the bond pads, nanowire alignment markers and so on is briefly given in the appendix. However, since every (2*2)mm² piece usually contains a random amount of nanowires with a fortuitous distribution, the ebeam job is usually composed of 24 individual patterns. The actual lithography is then performed as follows: First, the sample is mounted onto the sample holder and roughly aligned by means of an optical microscope. Afterwards, the ebeam machine tries to locate the bottom left marker in the bottom left piece. This has to happen rather fast to avoid accidental exposure of critical structures like the contacts within the actual sample area. In order to obviate the case that the machine begins the process at the

II

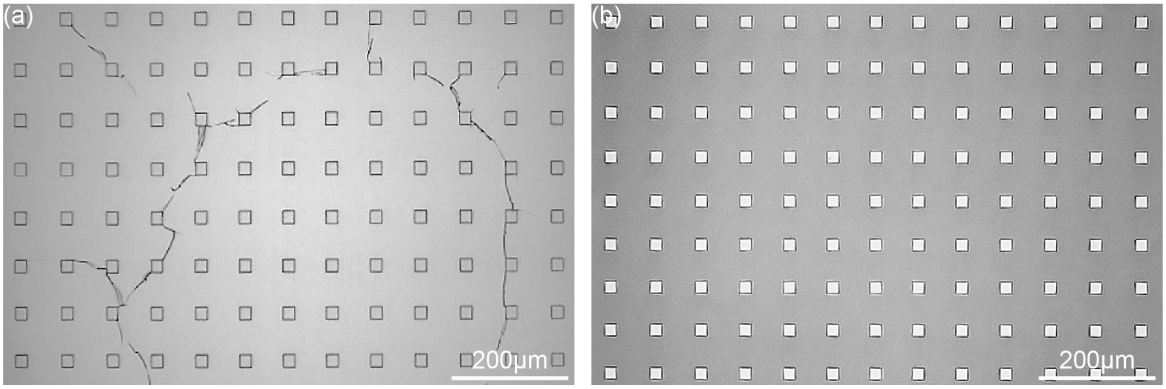

Figure 2.3 – *(a) Optical micrograph of a pre-alignment marker array etched with "CHF_3+O_2" into a silicon <100> wafer. Without an additional pre-heating and post-cooling step, the used resist UV 6.06 tends to crack at the points of maximum strain, i.e. the corner sections of the markers. The resulting "web-like" defects disturb the accurate separation measurement of the ebeam software, which ultimately leads to a complete failure of the automatic alignment process. (b) Optical micrograph of a similar marker array without any defects. Here, the bake of the resist was done in a three-step-approach: 30s at 90°C, 60s at 130°C, followed by another 30s at 90°C.*

wrong coordinates, the separation between adjacent e-beam markers is 100 µm, i.e. five times the width of a single marker. Subsequently, the machine moves on to the PAM array and tries to correct for misaligment in x and y direction as well as any tilt. To this end it uses the artificial, underlying coordinate system of the PAM field: While the separation between the central marker and the four surrounding positions is designed to be exactly 55 µm, this value increases continuously with a fixed stepping of 1 µm, as shown in Fig.2.2 (b). Thus, the distance between the first and second marker is 56 µm, 57µm between second and third and so on. Based on that, the machine can precisely calculate the position of the sample with respect to the actual pattern. However, due to the fact that the whole process of search and alignment requires a comparably long time in which the electron beam has to be active, most of the markers can be used just once. Therefore, the total number of markers has to be quite large, which results in typical array sizes of (1*1) mm², as depicted in the upper left corner of Fig.2.2 (a).

name	**orentiation**	**thickness** (µm)	**nom.** ρ (kΩcm)	**eff.** ρ (kΩcm)	**finish**
Si-Mat	100	525	>30	80	DSP
Siegert	100	525	>100	180	DSP

Table 2.1 – *Supplier specifications for the two different kinds of silicon wafer which were used for the fabrication of superconducting circuits.*

In order to reach its maximum precision, the machine relies on automatic search and detection of the previously defined ebeam marker. However, even though this approach is normally much more *stable* than any manual alignment, it can cause serious issues if the overall quality of the ebeam marker is not sufficient. Due to the fact that the detection method is based on *contrast differences* rather than *structure recognition*, it is especially important that all edges and corners of every single marker are well defined. To fulfill and maintain this condition through the whole fabrication process, including global deposition of dielectrics and metals as well as dry etching, **negative marker** were used. Throughout this project, highly resistive silicon wafer were used in order to reduce microwave-induced losses during the measurements, which are described in Tab. 2.1. Here, *DSP* refers to the fact that all wafers were double side polished.
To etch the marker structures, the wafer is first coated with the resist **UV6** from *DOW*. Since the resist has to be stored refrigerated, it is necessary to add an additional waiting time of approx. 20 minutes before it is used in order to avoid any contamination with condensation water. During the actual spinning process, a rotation speed of 4000 rpm for 60s is used, which usually results in a thickness of 850 nm. A more critical step is the subsequent *baking* of the resist. Fig. 2.3(a) shows the resist profile after development using the simplified baking process of 130°C for 60s as described in [235]: Starting

from the corner sections of the marker, which are the points of maximum strain, a web-like pattern of cracks and defects emerges through the whole array and makes most of the marker structures unusable. Hence, a more complicated approach is used, in which the primary bake is supported by additional pre-heating and post-cooling steps in order to slow down the evaporation of the solvent and reduce the stress in the solid resist. Using a combination of 30s@90°C/60s@130°C/30s@90s, the resulting pattern after development is defect-free, as can be seen in Fig. 2.3(b). For the development, a 5-minutes-long post-exposure bake at 140°C is performed, followed by submerging the sample in the developer **CD-26**[1]. Finally, the sample is rinsed for 10 minutes in flowing DI water.
To achieve the maximum resolution during the electron beam lithography, the markers need to be deep enough in order to maintain a good contrast even after subsequent metal and dielectric depositions. Additionally, all the edges need to be well-defined and homogeneous, which requires a strongly anisotropic etching. Therefore, a dry etching process based on CHF_3 and O_2 was used, which makes use of the fact that CHF_3 does not chemically interact with the SiO_2, which is formed by the reaction of the oxygen plasma and the Si surface. The actual etching is thereby performed by a repetitive sequence consisting out of two steps: First, the O_2 plasma transforms all exhibited Si areas to SiO_2. This is then removed by the **physical** component of the etching process, determined by the applied *RF power*, leaving a shallow hole in the surface. All areas, including the side walls of the hole, are then oxidized again. However, due to the fact that the physical component is strongly anisotropic, i.e. just parallel to the normal vector of the surface, the SiO_2 layer on the side walls stays intact, while the oxide at the bottom of the hole is sputtered away. By repeating this process for 13 minutes, an approx. 400 nm deep hole is etched into the silicon wafer, with a lateral overetching in the range of a few nanometers. These holes can then be used as negative markers to achieve an sub-5 nm-precision during the ebeam lithography and to create all the subsequent structures which are described in the next sections of this chapter.

[1] The reactive component is *Tetramethylammonium hydroxide* (**TMAH**).

II

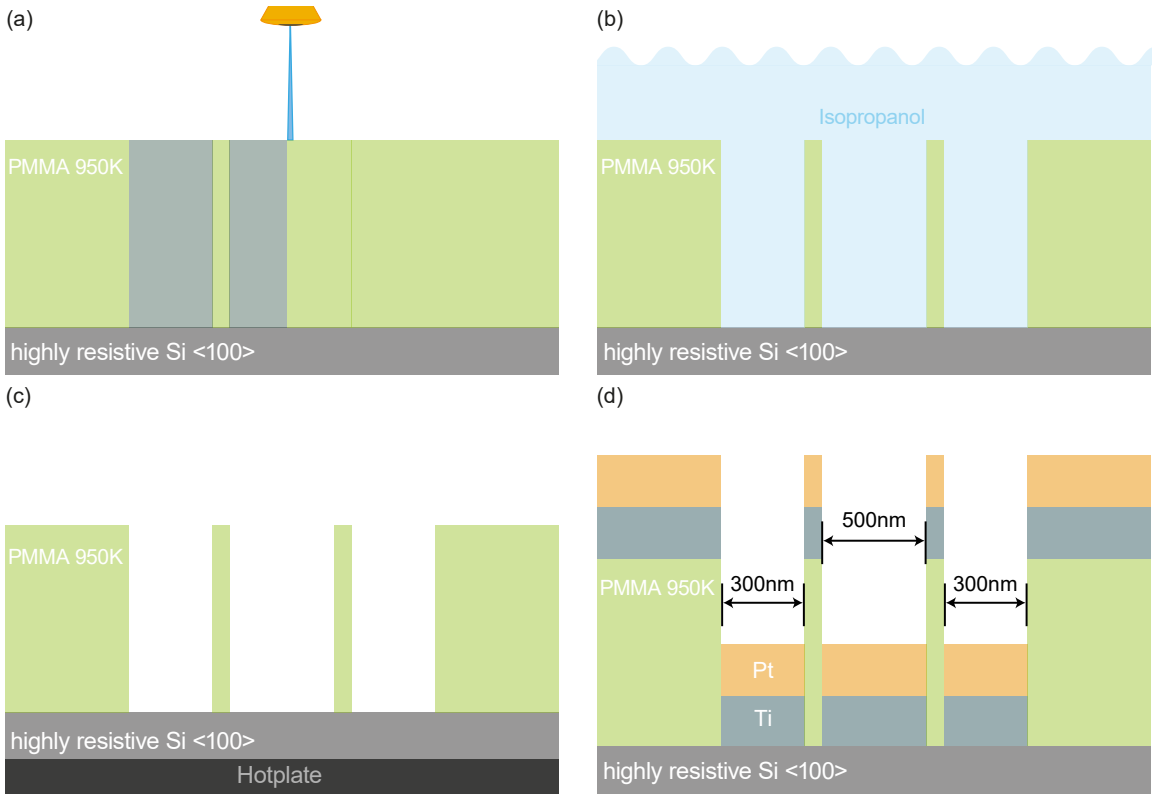

Figure 2.4 – *Schematic overview of the fabrication steps required for the thin and flat bottom gate structures. (a) High-dose ($2500\,\mu C/cm^2$) [236] electron beam lithography is used to transfer the required pattern into a single layer of PMMA 950K. The single layer resist and the large dosage ensure an anisotropic pattern profile with straight edges. (b) Development of the written structure in pure IPA. It is crucial for this process, that the development is not stopped with DI water rather than by just drying the sample with gaseous nitrogen.(c) An additional post-development bake at 100 °C for 10 minutes is performed to remove any IPA that infiltrated the resist during the development. Without this step, the resist swells, leading to blurred edges and reduced contrast. (d) Metal deposition of 5 nm Ti and Pt, respectively. Here, the titanium acts as a sticking layer for the platinum, while the Pt prevents the Ti from full oxidization and ensures low-resistive structures. If the sample is mounted correctly into the evaporation chamber, i.e. such that the evaporated material moves mostly parallel to the long edge of the structures, this will result in completely flat layer of metal electrodes without any side walls.*

2.2. BOTTOM GATES

Semiconductor-superconductor hybrid structures, especially if realized using nanowires, offer some unique possibilites to create advanced quantum devices due to their mesoscopic nature as well as their ability to host exotic topological states like Majorana zero modes. To make use of this increased parameter space, a proper electromagnetic control of the mesoscopic junction is required. However, the devices are normally embedded into complex control and readout circuits, which are quite sensitive to parasitic electromagnetic fields. Thus, the application of the control fields has to be done locally. Another challenge arises from the unique geometry of the nanowires. Due to their aspect ratio and the resulting tubular geometry it is particularly important, that the nanowire lies completely flat on the underlying surface. Especially in the case of wires with epitaxially grown superconductor shells or in-situ junctions, which are described in more detail in one of the following chapters, a comparably large contact separation is sought to suppress the hybridization between the narrow gap superconductor shell and the large gap superconductor for the contact leads. Even a small misalignment from the axis parallel to the surface would thereby induce a noticable tilt of the wire, which ultimately results in broken contact leads or even tore off nanowires.

In order to avoid all described issues, the bottom gate approach, which was already described in [237, 238], was improved by means of an optimized resist recipe and newly available ebeam techniques like *multipass writing*. The full fabrication process is depicted in Fig. 2.4: First, the substrate is briefly cleaned with a short oxygen plasma in the so-called *Gigabatch*. Afterwards, gaseous *Bis(trimethylsilyl)amine* (**HDMS**) is applied to the heated substrate as an adhesion promoter. This is

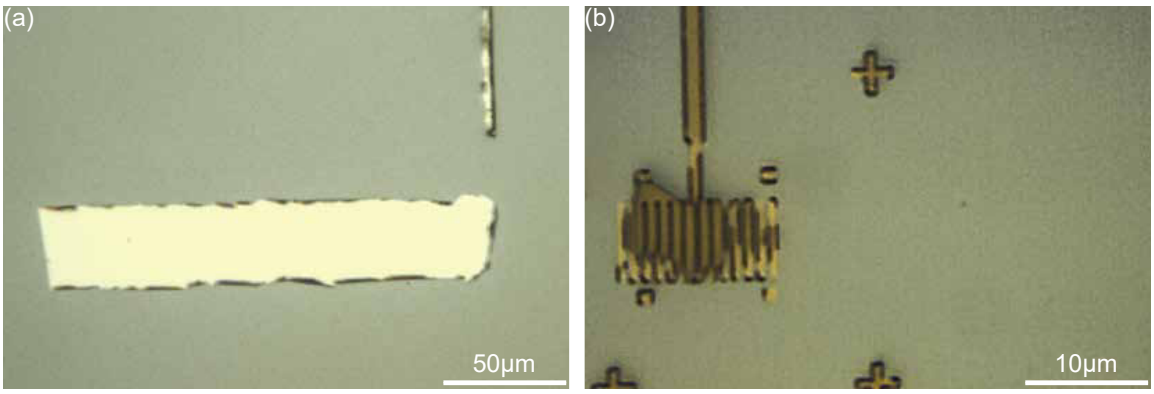

Figure 2.5 – *(a) Optical micrograph of a failed Ti/Au bond pad structure. The large strain within the Au layer leads to a (partial) peel off of the metal from the silicon substrate underneath. (b) Failed lift-off of some bottom gate electrodes caused by the lack of post-development oxygen plasma cleaning.*

followed by a coating process with PMMA 950K at 4000 rpm for 60 s without pre-acceleration. The sample is then baked at 100 °C for 1 min, followed by another baking at 180 °C for 10 minutes. The latter step is necessary to remove all the remaining solvent from the resist, while the first step ensures that there are no bubbles formed due to the rapid warm up of the sample. For the lithography, an ultra-high-dose process is used, with an effective charge density of 2500 μC/cm^2 at 50kV or 5000 μC/cm^2 at 100kV acceleration voltage, respectively. In order to improve the contrast between exposed and unexposed areas and thereby enhance the edge steepness, the so-called *multipass* approach is chosen. By doing so, the intended charge density is not generated in a single shot rather than by *running* over the same area multiple times with a reduced dose. This reduces parasitic intricacies due to the finite beam step size or the proximity effect and leads to much better defined straight edges. This is especially important for structures which run parallel and in close proximity for a significant fraction of their total length.

Instead of the conventional PMMA developer AR-655, the written sections of the resist are removed by means of pure *Isopropanol* (**IPA**), as shown in Fig. 2.4 (b). This process was first presented in [239, 240] and adapted and optimized to our needs in cooperation with Johanna Janßen [236], for example, by using a mixture of IPA:H_2O 7:3 [241] for the development of small structures on top of a dielectric layer to avoid charged defects. However, even if this approach further enhances the quality and steepness of the written structures, it comes with a downside. Due to the chemical similarity of the original resist solvent *Anisol* and *IPA*, the latter one can soak into the resist during the development process. Due to this, the formerly solid PMMA starts to swell around all the edges, leaving the written structures slightly *blurred* and less defined. Thus, an additional post-development bake at 100 °C for at least 5 min is required to remove the IPA from the resist, which is depicted in Fig. 2.4 (c). Additionally, the whole process is quite sensitive to any contamination with water, as already low concentrations boost the development speed by a factor of almost 5.

Finally, the actual metal layer has to be deposited. A series of tests has revealed, that for the utilized evaporation machine (*Balzer PLS 500*), a two-layer stack of Ti/Pt gives the best results. This is especially true if the individual layers have thicknesses of just 5 nm, as is the case for the qubit control circuits, in order to minimize the chance of broken contacts, pinholes in the dielectric or parasitic coupling to the resonator or the Qubit loop. In this case, the metal has a significant built-in tensile strain due to the lattice mismatch between the substrate and the full stack as well as between the individual metal layers. This leads, for example when gold is used instead of platinum, to a whole series of strain-related issues like the peeling of large areas of material or metal flakes which are not removed during the lift-off, as depicted in Fig. 2.5 (a) and (b). Further improvement can be achieved if the post-development bake is followed by another short oxygen plasma step in the Gigabatch. This removes any residual resist and also improves the adhesion between the Ti sticking layer and the native silicon oxide. Finally, the liftoff procedure was changed from a purely Aceton-based process to one which relies on a mixture of **DMSO:Cyclopentanon 1:0.3**. *Dimethyl sulfoxide* , as the main in-

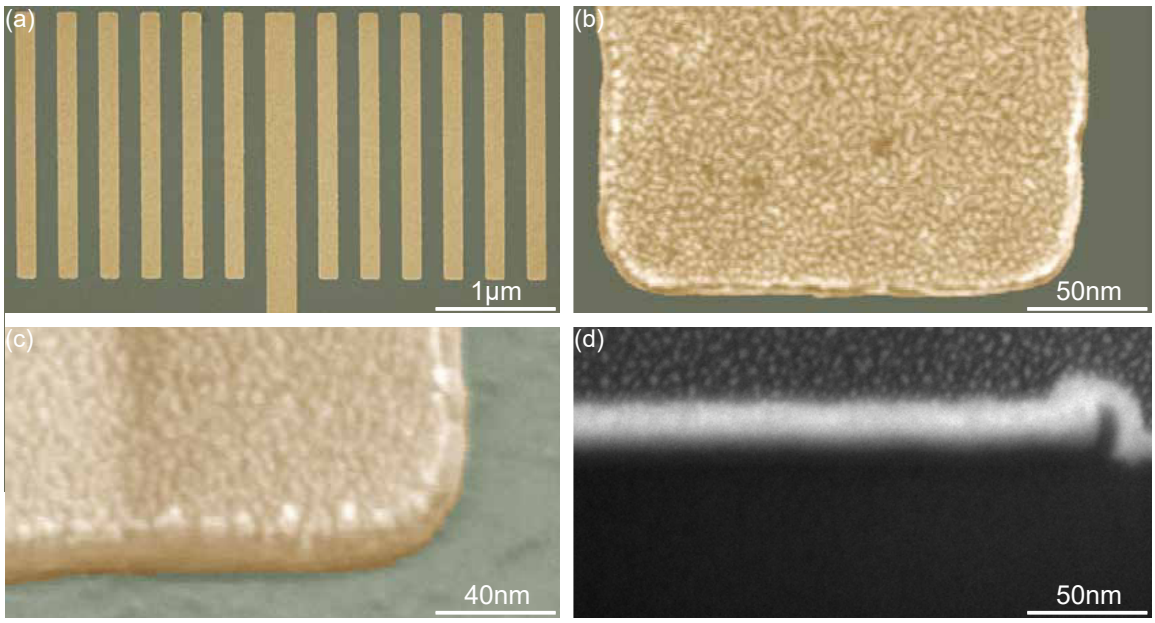

Figure 2.6 – *False-colored SEM micrographs of some finished Ti/Pt bottom gate electrodes with 5 nm/5 nm thickness. (a) Overview of the full gate array. Only the central electrode is electrically connected to the environment. The outer metal stripes act as mechanical support for the nanowire Josephson junction. (b) and (c) Zoom-in of a single gate electrode in top view (b) and under an angle of 60° (c). This shows how the optimized lift-off procedure results in side-wall free structures with well-defined, steep edges. (d) FIB cut through a failed gate structure. Due to an incorrect mounting in the evaporation chamber, which resulted in a misalignment between the developed structures in the resist and the deposition direction of the metal source, metal has accumulated on one side of the structure. The formed side-wall is extremely fragile and can easily induce defects in the deposited dielectric which then ultimately leads to a short to the final device.*

gredient, is polar aprotic with a much stronger dipole moment than Aceton and reduces the chance that metal pieces stick to the surface if the substrate is removed from the liftoff solution. The final structure is shown in Fig. 2.6 (a)-(c). Here, only the central electrode is electrically connected to the measurement setup by means of a large bonding pad whose fabrication is described in the next section. All the other metal stripes act as mechanical supporting pads to planarize and suspend the nanowire and thereby minimize the coupling between the mesoscopic junction and the silicon substrate. The top (b) and 60°-tilted (c) view of the central electrode reveal, that all remaining sidewalls are in the range of 1 nm and below. However, this just holds if the sample is mounted correctly into the evaporation chamber, as can be seen in Fig. 2.6 (d). Here, one misaligned bottom gate was cut by means of a *focused ion beam* (**FIB**) process. This makes it possible to take an image of the cross-section of of the structure, revealing a pronounced sidewall on the right side. However, this issue can be overcome by using a special template for the correct alignment of the sample on the holder, resulting in well-defined, thin gate structures which have to be connected to much larger and thicker bonding pads afterwards.

The latter one is achieved by using the process mentioned in section 2.1 for the deposition of thick metal layers, based on the resist *UV6* and the adhesion promoter *HMDS*. However, in this case things are slightly more complicated due to the required electrical connection to the already deposited, much thinner metal layer of the bottom gate structure. Additionally, the surface roughness of the Pt layer is comparably small, i.e. in the range of 2 nm or less. This has a lot of advantages for the following deposition of the gate dielectric by means of the suppression of pinholes. The final step for the gate fabrication is the deposition of the high-k dielectric in order to improve the performance of the final device.

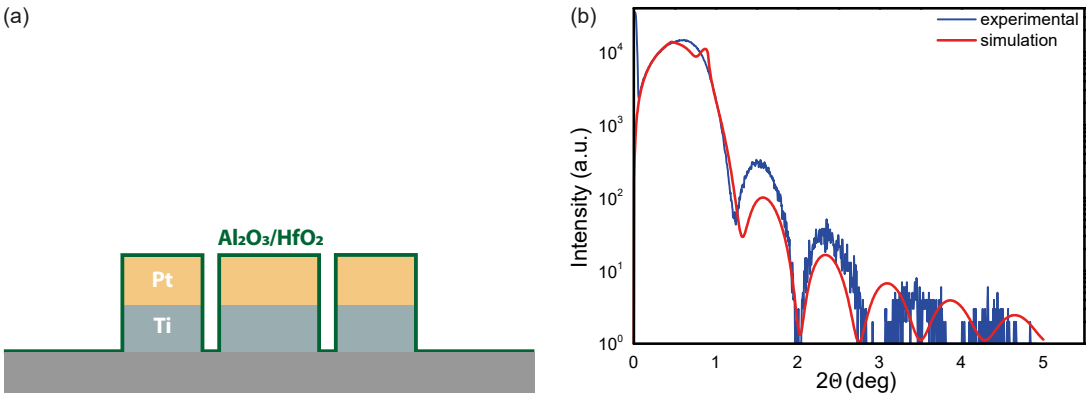

Figure 2.7 – *(a) Schematic overview of the conformal coverage of the previously deposited bottom gate structure with a high-k dielectric. For all quantum circuits, i.e. the Andreev, Gatemon and Shapiro chips, a stack of 3 nm/15 nm Al_2O_3/HfO_2 was chosen, with a typical breakdown voltage of ±9 V. The bottom layer suppresses the formation of crystallites in the HfO_2, which would act as conductive pinholes. (b) X-ray reflection (**XRR**) measurement of an Al_2O_3/HfO_2 stack with nominal thicknesses of 3 nm and 15 nm, respectively. By using a proper fitting routine (red trace), the thickness of both materials can be calculated: t_{AlO}=(3+0.2)nm and t_{HfO}=(15+0.6)nm.*

2.3. GATE DIELECTRICS

One of the main advanvages of semiconductor nanowires is the ability to tune their electronic properties by means of an applied gate voltage. In doing so, it is possible to shift the position of the fermi level E_F, affecting the concentration of free carriers and, in the special case of InAs and InSb nanowires, the slope of the potential well at the surface. Thus, it is possible to control not only macroscopic parameters like the conductance, but also *quantum properties* like the spacing of quantized levels and the strength of the spin-orbit interaction. However, the effectiveness of the gate, i.e the ratio between the externally applied voltage and the resulting energy shift of the fermi level is usually in the range of 1/1000 for global backgates and 1/10 for optimized wrapgate architectures. One way to increase this so-called **lever arm** α is the usage of a high-k dielectric, but materials like $LaLuO_2$ (permittivity $\epsilon > 45$) or GSO ($\epsilon > 30$) require high temperatures to achieve a reasonable small defect density [242, 243]. Additionally, films of these materials are normally fabricated by means of sputtering or evaporation, which limits the smoothness of the layer. Therefore, the decision was made to use a stack of Al_2O_3 ($\epsilon_{th} = 9$) and HfO_2 ($\epsilon_{th} = 21$), even though they are not the materials with the largest available permittivity. Using *atomic layer depositon* (**ALD**), the previously deposited gate structures can be conformally covered with the dielectric, resulting in planar and smooth structures (schematically shown in Fig. 2.7 (a)). The exact thickness of the material is controlled by means of *x-ray reflection* (**XRR**) measurements, as shown in Fig. 2.7 (b).

In order to operate as a proper gate dielectric, the chosen materials have to fulfill a couple of requirements. The most important one, especially due to the large area to be covered, is a small number of defects. The latter can be determined by three different benchmark measurements, which were performed together with Frederik Marx. The first one is the effective permittivity of the material and its deviation from the theoretical maximum. By using *capacitance-voltage* (**CV**) measurements to probe the response of a *metal-insulator-semiconductor* (**MIS**) structure within the accumulation, depletion and inversion region, the so-called *capacitance equivalent thickness* (**CET**) can be determined. F ig. 2.8 (a) shows an example for the thickness-dependent CET values of HfO_2, which correspond to an effective permittivity of ($\epsilon \approx 18.8$). However, more important than the effectiveness of the gate is its robustness with respect to the applied voltage. Fig. 2.8 (b) shows the so-called *breakdown voltage* V_b for the same set of samples and thicknesses. Both ϵ and V_b are mainly limited by pinholes in the material. Especially for HfO_2 on silicon, these parasitic conductive paths are usually formed by *crystallites*, i.e. spatially localized, Hf-rich metal clusters or grains within the amorphous matrix of the dielectric. These are induced by the underlying crystal structure of the semiconductor. The common way to suppress the formation of these defects is the decoupling of the HfO_2 from the substrate by means of another amorphous structure like Al_2O_3 [244–246]. Doing so, the breakdown

II

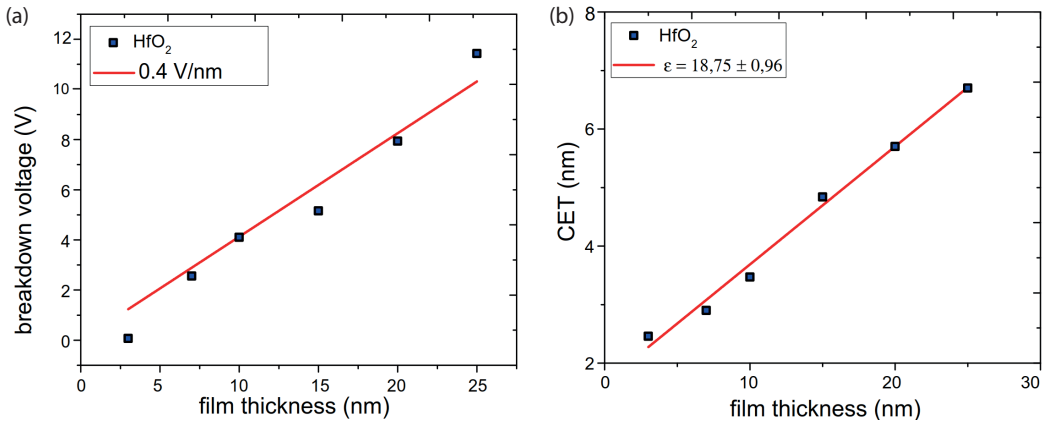

Figure 2.8 – *(a) A set of **CET** measurements of HfO_2 with various film thicknesses. All layers were fabricated in the **Nanocluster** on Si-(100) substrates by means of **ALD**. By performing an analysis of the thickness-dependent CET value, the permittivity of the material can be extracted. The obtained value of $\epsilon \approx 18.8$ is close to the theoretical maximum of $\epsilon_{th} = 21$. (b) Analysis of the breakdown voltage for the same set of HfO_2 samples. The value is mainly limited by the formation of crystallites and pinholes in the material and can be further enhanced by means of a thin Al_2O_3 interlayer, which impedes the crystallization of the HfO_2. All presented measurements were performed together with Frederik Marx. The plots were adopted from his Bachelor thesis and slightly modified [247].*

voltage of the used bottom gate structures can be increased to 8 V for a Al_2O_3/HfO_2 film of thickness 3 nm/15 nm. Finally, there are so-called *interface traps*, which are formed between the silicon and the dielectric and act as parasitic dipoles. They are usually described within the effective capacitance model. Here, they form an additional capacitance with a comparably long time constant. If a positive gate voltage is applied, this *parasitic capacitor* has to charge up first, which causes a time and energy mismatch between the external signal and the effective voltage which is seen by the carriers in the semiconductor nanowire. If the external voltage is then switched to negative values, the system reacts again with a time delay, which ultimately results in a hysteresis between the positive and negative branch. However, this simple description assumes that the entirety of traps can be described as a combined system. For realistic systems, the lifetime of individual traps may be very different, which leads to spontaneous relaxation events and thereby induced **charge or potential reconfigurations**.

In order to minimize all previously mentioned effects and, more importantly, avoid a coupling of parasitic two-level systems to the high-frequency signal[248][249], an additional etching step was added into the process chain. Here, the sample is first covered with UV 6.06 by means of the previously described spinning and baking procedure. The actual pattern is thereby designed in a way that the gate region, i.e. the bonding pad, the large leads and the small gate electrodes, is protected with a resist mask. The size of the latter section is extended such that it includes the whole future qubit region. One possible disadvantage of the chosen etching recipe is the fact that it also attacks silicon. Thus, it is necessary to precisely determine the required etching time for both materials, i.e. Al_2O_3 and HfO_2. Figures 2.9 (a) and (b) summarize the remaining thickness of both materials after increasingly longer treatments with the RIE recipe *PZ-CHF3-20C* and the resulting etching rate. The thickness was determined using an ellipsometer. Based on these results, the actual etching of the Qubit circuits was performed, which is schematically shown in Fig. 2.10(a). As already mentioned, the gate structure is protected by a resist mask in order to avoid the formation of physical defects, i.e. pinholes, or mobile charges in the dielectric. The final result, including the deposited superconductor with etched flux traps, is depicted in Fig. 2.10 (b). Here, three different sections can be identified. The green colorized one marks the area in which the actual device will be fabricated later on. It includes the whole set of gate structures, i.e. the actual electrode as well as the supporting pads, and is confined between the resonator line and the ground plane. However, on the left side of the area, i.e. the one which is opposite to the termination point of the resonator, there is an intermediate region in which the dielectric is removed completely. Finally, on the outer left, the actual superconductor is deposited directly on bare silicon. The remarkable flatness and steepness of the edges and the adjacent areas is achieved by means of a combined liftoff-etching process, which is described in the next

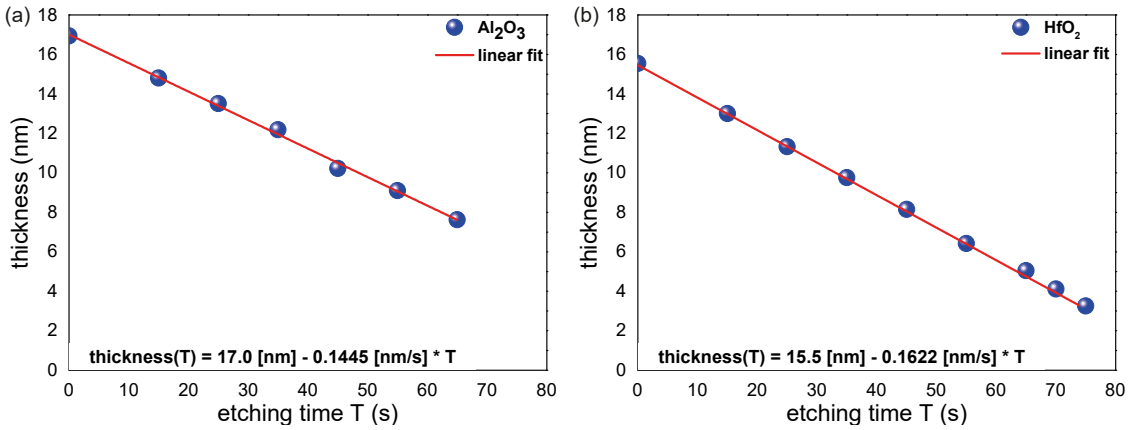

Figure 2.9 – *Time-dependent thickness of (a) an Al_2O_3 and (b) a HfO_2 film after the treatment in a CHF_3-based plasma etching process. The thickness of the dielectric layers was determined by ellipsometry. It can be seen, that the chosen process results in a well-controlled etching depth due to the comparably slow, but constant etching rate during the whole process time.*

section. However, one side effect of this approach is the formation of a trench between the green and purple area, as can be seen in the inset of Fig. 2.10 (b).

It should be mentioned, that an actual quantification of the gain in performance due to the removal of the dielectric is quite hard to achieve. The reason is the comparably small internal quality factor of the superconductor itself, mainly caused by the huge inequality of the crystal structure, which is in fact a random mixture of amorphous, (111), (200) and (100) sections. However, measurements could have clearly shown, that the whole system is less sensitivity to charge-based noise caused by random potential reconfigurations or instabilities. Additionally, the frequency span over which the measured resonator response is distributed around the designed value is much narrower. This can be understood in terms of the complex conductivity and the permittivity:

$$\frac{\delta f_0}{f_0} = \frac{\alpha}{2}\frac{\delta\sigma_2}{\sigma_2} - \frac{F}{2}\frac{\delta\epsilon}{\epsilon} \tag{2.1}$$

Here, $\alpha = L_k / (L_k + L_g)$ corresponds to the *kinetic inductance fraction*, i.e. the deviation of the total inductance of the system from the pure geometric design and its inductance L_g due to the energy stored in the *Cooper pair conglomerate*. F is a filling factor which takes into account that the active region of the resonator is modified by the dielectric [250]. Thus, the coupling between the electric dipoles in the dielectric layer and the electric field, which is spatially distributed along the resonator and also extends towards the ground plane, leads to random, local fluctuations of the permittivity and therefore the waveguide capacitance. This results in different resonance frequencies for every single structure. The change in capacitance is thereby directly related to the thickness of the dielectric due to the increase of the absolute number of dipoles in a larger volume and can be easily reduced by thinning down or removing the dielectric. This effect is especially important in the case of shunted quarter wave resonators, which are used for the Andreev qubit and the spectroscopy measurements. Here, the electrical field has a node at the connection point to the ground plane and an antinode (i.e. maximum) at the end which is capacitively coupled to the feedline. This leads to a strong gradient in the local electrical field strength, which results in different power-induced saturations of the parasitic dipoles and therefore spatial variations in the loss tangent

$$\left(\frac{1}{Q_i}\right)_{total} = \sum\left(\frac{1}{Q_i}\right)_n = \tan(\delta) = \frac{\omega\epsilon'' + \sigma}{\omega\epsilon'} \tag{2.2}$$

Here, ϵ'' corresponds to the lossy, imaginary part of the permittivity, which is attributed to the relaxation of dipoles and bound charge traps, and σ to the contribution of free charges. ϵ', on the other hand, represents the lossless part $\epsilon' = \epsilon_0\epsilon'_r$. Nevertheless, it should be mentioned that this effect only induces a static and constant shift of the resonance frequency. For a dynamic change, i.e.

II

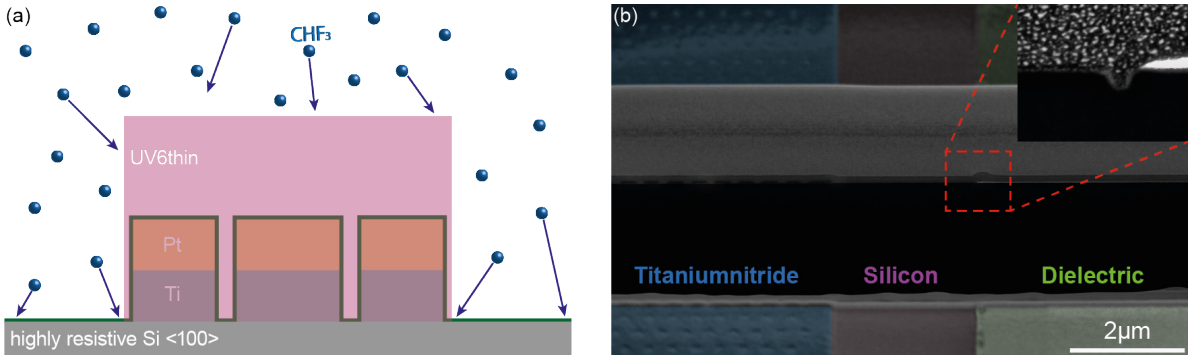

Figure 2.10 – *(a) Schematic overview of the CHF_3-based etching process. In order to minimize losses due to parasitic two-level systems in the dielectric, it is completely removed in all areas which are supposed to be covered with the superconductor later on. The actual gate region is thereby protected with a resist mask consisting out of UV6. (b) Focused ion beam cut through the final circuit. The dielectric within the gate area and the adjacent superconducting ground plane are separated by a section of bare silicon. The inset shows a zoom-in of the border between the gate region and the bare silicon. The Al_2O_3/HfO_2 stack is charged up due to the electron beam exposure and can be clearly recognized. The narrow trench marks the overlap of the region which was first exposed to the CHF_3 plasma to remove the dielectric and , later on, again to an SF_6 plasma to remove the superconductor.*

frequency noise, it is more important how the actual surface of the superconductor is terminated. Previous experiments have revealed, that the noise enhancement is related to the trapping and release of quasiparticles at the interface between the superconductor and the dielectric. This effect is mainly based on a charge transfer due to the change in the density of surface states and thereby induced changes in the local inductance rather than the capacitance [251][252]. This effect also occurs in the case of the native oxide which forms on elementary superconductors like Nb, Al or V and is one of the reasons why they are usually outperformed by N-based compound superconductors like TiN or NbTiN in terms of the loss tangent and the quality factor [253][254]. However, a possible way to get a deeper experimental insight into this effect would be the usage of the Flip-Chip design, as described later. Here, the device chip could be easily covered with different layers of dielectrics with various thicknesses. By doing so, the latter could then be probed with respect to the quality factor. However, due to the fact that all used circuit chip designs rely on the same liftoff-etching procedure, the latter one will be described in detail in the next section.

2.4. FABRICATION OF THE SUPERCONDUCTING CIRCUIT

In order to create a long-living, well-controlled two-level system inside of the mesoscopic Josephson junction, it is necessary to precisely tailor the electrostatic and magnetic environment. Thus, the previously described bottom gate structure is used to directly manipulate the (bound) state spectrum inside the nanowire, which is the *heart* of the hybrid quantum system. Extending the metaphor, the superconducting circuit is the *body*, which couples it to the environment by means of the feedline. It limits and controls the number of photons which reach the actual Qubit and protects it from parasitic sources of external noise. The fabrication of high-quality and low-loss coplanar wave-guides and other on-chip microwave components within the circuit quantum electrodynamics framework is a complex and challenging task which covers a broad spectrum of process techniques and digs deep into the field of material science as well. Thus, the following section covers the fabrication of the ground plane, the feedline, the resonator structures and the flux bias line, which is required to locally apply an out-of-plane field to the qubit loop. Additionally, it provides an overview of the material properties of sputtered Titanium nitride.

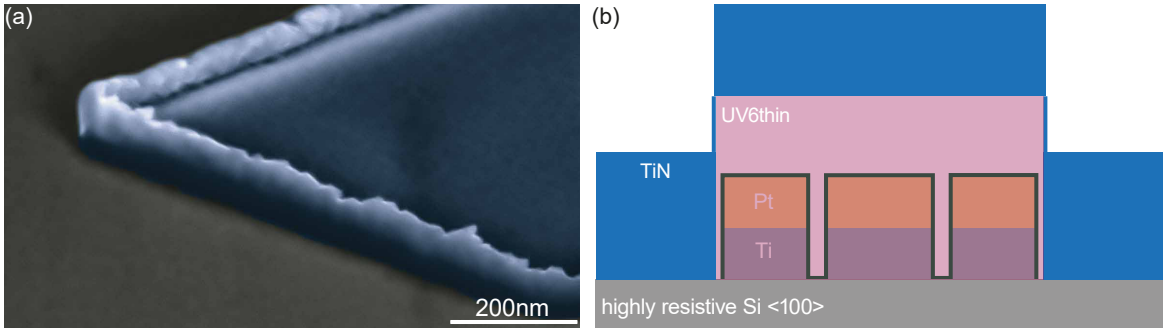

Figure 2.11 – *(a) Typical fence-like structures around the edge of a TiN layer after lift-off due to material deposition on the sides of the resist mask. The height of the sidewalls is mainly determined by the used resist and can easily exceed the actual thickness of the metal film. In the case of materials like Nb, TiN or NbTiN, the sidewalls are robust and free standing. However, during following process steps, there is a significant probability for them to collapse and, in case of narrow structures like the weak link of a Josephson junction, lead to a short. For resonator structures, they can even influence the effective resonance frequency and loss tangent due to local fluctuations in the capacitance and inductance of the coplanar waveguide. (b) Schematic overview of the deposition of the superconductor. The resist mask is formed by UV6thin in order to limit the heigth of the sidewalls.*

Due to the previously described obstacles, there was no out-of-the-box solution for the fabrication of the qubit control circuits and the nanowire-based Transmon and Andreev qubit structures that have been used during this project. However, after numerous experiments with the support of a number of master students, three important **key steps** for the fabrication of microwave-suited superconductor structures could be identified: 1. The pre-treatment of the substrate shortly before the deposition or growth of the superconductor, 2. the actual handling of the process in terms of degasing, substrate temperatur, pressure and deposition rate and 3. details of forming the final structure. Additionally, it is also crucial which superconducting material is used. After some early attempts with Al and Nb, **titanium nitride** was picked as the material of choice. Even though it adds another layer of complexity to the process chain it offers the best state-of-the-art intrinsic quality factors Q_i for resonators and transmission lines in a distributed element design[255][256]. During this project, two different approaches for the formation of titanium nitride have been used:

LLS EVO: Here, the TiN is formed by means of **reactive sputtering**. The relevant (and controllable) parameters are the process gases (Ar, N_2,...), the partial pressures, the voltage of the plasma source, the rotation speed of the sample holder, the background pressure[2] and the chamber temperature.

Nanocluster: In contrast to the LLS EVO, in which the TiN is formed before it reaches the substrate, the fab-

[2] As the chamber is flooded with nitrogen during the actual deposition, this parameter refers to the quality of the vacuum that is achieved prior to the sputtering process

II

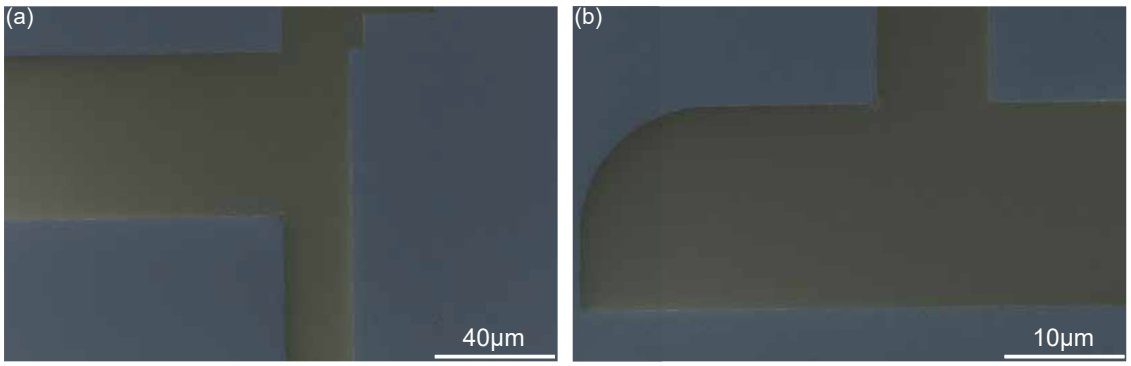

Figure 2.12 – *(a) and (b) False-colored SEM micrographs of TiN structures after the first step of the combined liftoff-etch approach. The bright, whitish lines around the edges correspond to comparably large sidewalls. All metal structures are much larger or just consist of closed areas like in (b). In the next step, the excess TiN is removed by means of dry etching, which effectively removes all sidewalls and also creates the finer structures like the resonator.*

rication within the Nanocluster is achieved by means of a metal MBE and an actual **growth process**. Recent publications have shown, that this method provides a massive boost for the material quality in terms of defect density, quality factor, roughness and resistance-per-square. However, similar to the growth of semiconductor structures, it also comes with the major disadvantage that the substrate is heavily involved in the chemical process, which adds a lot of variability to the process chain. Most importantly, the substrate has to be heated up (and kept at) temperatures of 850 °C or above during the whole growth process. Additionally, due to compound formation on an atomic level, the ratios of the supplied titanium and nitrogen *flows* have to be precisely controlled in order to reach the desired stoichiometric composition. Lastly, the topmost monolayers of the silicon substrate have to be engineered in a way that the lattice-mismatch induced strain is minimized. The state-of-the-art method to achieve this is a preceding, in-situ growth step that creates a thin layer of **silicon nitride** by means of *thermal nitridization*.

With the support of *Tobias Ziegler* and *Benjamin Bennemann* it was possible to create MBE-grown TiN with a comparably small resistance-per-square and a superconductiong phase transition at reasonably low temperatures. However, even though lots of effort has been put into optimizing the MBE-grown TiN, it was not possible to reach a point at which its high-frequency-quality surpassed the one of the sputtered material. Thus, the decision was made to proceed using the Titanium nitride formed by means of reactive sputtering. Therefore, all references to TiN in the following section refer to the films grown by the **LLS EVO**.

A characteristic phenomena of sputtering-based depositions in general is the formation of pronounced **sidewalls** that can easily reach heights of 50 nm or more. This is especially pronounced for superconductors like Nb or TiN due to their special *toughness* (see Fig 2.11 (a)). Previous tests have shown that those sidewalls can massively diminish the overall circuit performance due to the creation of electromagnetic field fluctuations or changes in the local capacitance and impedance . Typically, this is avoided by using a large-scale etching process on a fully covered substrate in combination with an Al_2O_3 *hard mask*. However, at this stage of the fabrication chain and in contrast to structures based on purely-superconducting qubits, the samples are already covered with the bottom gate electrodes and a dielectric (see previous sections). Thus, certain areas of the chip have to be protected with (photo-)resist during the metal deposition, subsequently requiring a *liftoff procedure* as a process (sub-)step. In order to avoid these problems, the following scheme was applied to create the relevant superconducting structures:

1. Coverage of the sample with a single layer of *thinned* UV6, processed in the same way as described in former sections.

2. Ebeam lithography and development of the exposed resist to create the mask for the subsequent metal deposition. The design is thereby chosen such that all superconductor structures

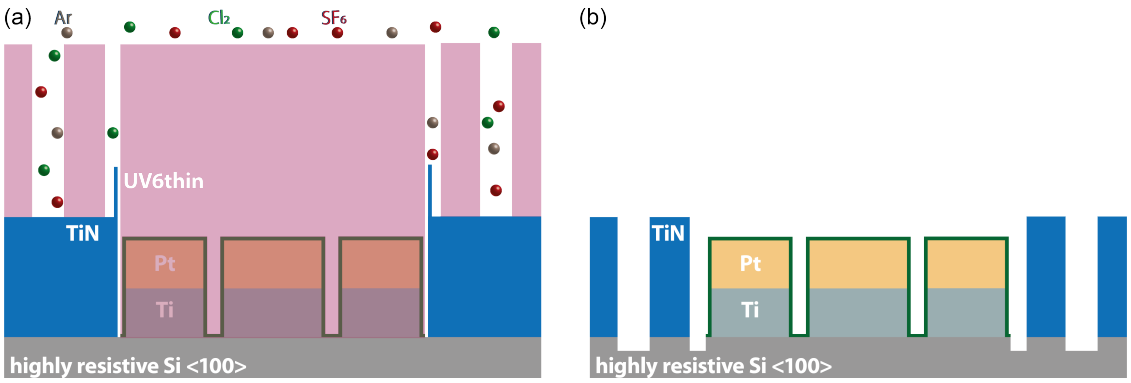

Figure 2.13 – *(a) Schematic overview of the etching process. The resist mask is designed such that it removes all excess areas of the superconductor while protecting the gate electrodes and dielectric at the same time. (b) Overview of the final circuit layout. The ground plane is now terminated with well-defined, sidewall free edges. The additional holes within the superconductor act as flux traps in order to increase the magnetic field robustness of the resonator with respect to the quality factor and the resonance frequency.*

are **larger** than they are designed to be in the final circuit layout (see Fig. 2.11 (b)). For UV6, as a positive resist, this means that the major part of the sample needs to be exposed. Negative resists, like *n-Lof* could potentially reduce the ebeam writing time, but tests have shown that those are much more difficult to handle and therefore more prone to errors in the following process steps.

3. Even though the high-k dielectric has already been removed in the areas that are supposed to be covered with the superconductor, the finite time frame between the different processing steps allow for the formation of native SiO_2 that, exhibits a large number of defects. Thus, by utilizing the existing resist mask, the sample is briefly cleaned with *hydroflouric acid* (**HF**). Here, the chosen etching time is rather critical as it has to be long enough to remove the oxide layer, while leaving the adhesion of the resist with respect to the substrate intact.

4. The formation of TiN is extremely sensitive with respect to the presence of *Hydrogen* and *Oxygen* [257]. Therefore, a so-called **degassing** is performed prior to the metal deposition. In the case of the LLS EVO, however, the temperature control is rather limited via a simple power percentage that is applied to a number of light bulbs inside of the chamber and is thus without direct feedback or any way to measure the actual temperature of the substrate. In order to maintain the properties of the UV6, which starts to lose its chemical stabiliy at temperatures above 180 °C, the degassing procedure is performed in a two-step-approach. First, the transfer and deposition chambers are *baked* at 80 % of the maximum power level for four hours. In the same step, the chamber is then covered with 20 nm of pure Titanium, which should serve as a simple form of **titanium sublimation pump**. After the loading of the substrate into the transfer chamber, the substrate is again baked for another two hours at 30 % power. Afterwards, the heater is turned off and the transfer chamber is pumped down until it reaches a pressure of $1{\cdot}10^{-6}$ mbar. Then, the shutter between the transfer and deposition chamber is opened, with another pumping step until the combined system reaches $1{\cdot}10^{-7}$ mbar. The latter can take up to 12 hours. Finally the actual sputtering process is started, with a deposition rate of 0.0255 nm/s.

5. As mentioned before, both Nb as well as TiN show a remarkably strong *toughness*. This can cause issues during the *lift-off*, as the material tends to rip off in small *flakes* rather than big, closed pieces. In the case of *Aceton*, the already removed metal can even re-attach itself on the circuit structures, which makes it impossible to remove it again. A major improvement could be achieved by switching to a mixture of **Dimethylsulfoxide:Cyclopentanone** 1:0.3. Not only can this solution be heated up to temperatures of about 90 °C, which greatly enhances the *reaction dynamics* between the resist and the solvent, it also leaves an *oil-like film* on the substrate

II

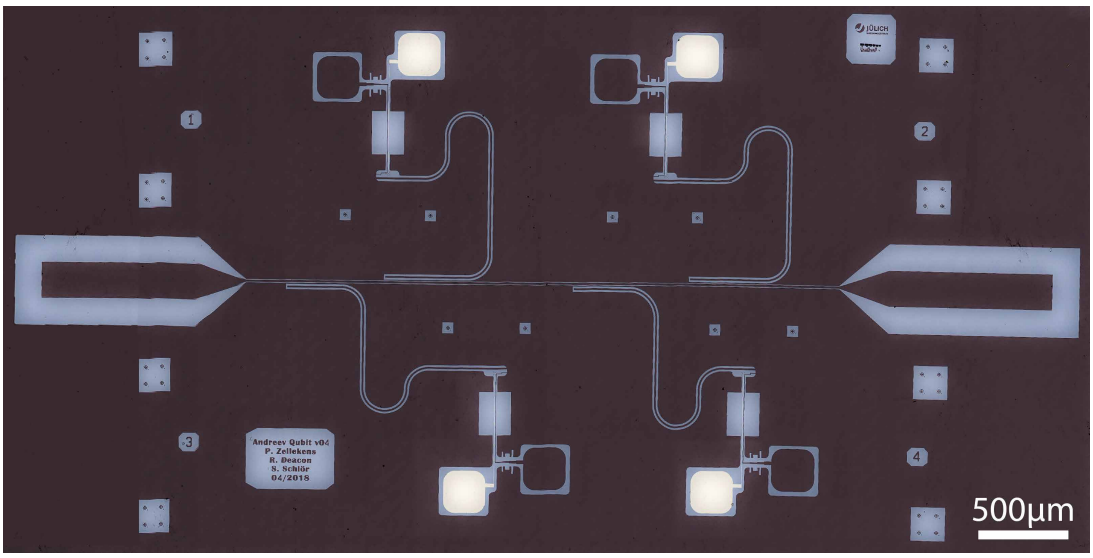

Figure 2.14 – *Optical micrograph of a finished microwave quantum circuit that acts as a platform for Andreev qubits. All microwave-active components are designed in a 50Ω-impedance-matched layout. The central transmission is, via its input and output port, directly connected to the measurement setup and the fridge wiring. The photon transfer to the four resonators is managed with coupling capacitors, realized by means of a thin ground plane stripe between the transmission line and one end of the resonator. All resonators are designed to be located within the measurement range of 5-6 GHz, with an average frequency separation of 200 MHz. All qubits are controlled by means of individual flux bias lines and gate electrodes. Here, the latter is designed in 50Ω-geometry, too, in order to allow the application of microwave pulses up to 25 GHz. The ground plane itself and the resonators are interspersed with two different kinds of flux traps in order to redirect the field lines and suppress dissipative* ***vortex motion****.*

which suppresses the adhesion of lifted material in the already cleaned areas.[3]. To finish the *lift-off* procedure, the substrate is further cleaned by means of *DI water* in an overflow basin. Here, it is important that the wafer is mounted upright in the sample holder, so that the metal pieces are washed away together with the residual solvent.

The circuit layout at the end of the process chain is shown in Fig. 2.12 (a) and (b). It can be clearly seen, how the sidewalls at the edges of the metal induce some reflection artifacts in the SEM. Additionally, finer structures like the resonator are still missing. Thus, in the next step, the unnecessary areas have to be removed by means of **reactive-ion-based dry etching**. This method is preferred as the wet chemical etch of TiN requires a mixture of Ammonium hydroxide, hydrogen peroxide and DI water, which is highly exothermic and can easily damage the resist mask and the gate dielectric.

For the dry etching, a lot of different techniques have been developed over the last couple of years, that are either based on Ar^+-milling, Fluorine- [CHF_3, SF_6,CF_4][259–261] or Chlorine-composites [Cl_2, BCl_3][262, 263]. However, the state-of-the-art method is a combination of all three in order to tackle the individual disadvantages [264, 265]. In the case of pure Ar^+-milling, for example, silicon atoms are deposited on the surface and the edges of the TiN, creating a characteristic, extremely *lossy* fence-like structure[265]. Within this project, a combination of *Chlorine* [$\mathbf{Cl_2}$], *Sulfur hexafluoride* [$\mathbf{SF_6}$] and *Argon* was used in a composition of 12, 2 and 60 *ppm*, respectively (see Fig. 2.13(a)). Here, the actual chemical etching of the TiN is done by the Cl_2, while the Ar, as a purely-physical sputtering component, suppresses the formation of a *bowel-like* undercut. The SF_6, as the final component is supposed to remove both the deposited silicon atoms as well as all chemical byproducts of the chlorine etch [262, 263, 265]. However, the downside of this process lies in the extremely large silicon etching rate, [>10nm/sec], which makes it necessary to precisely time the etching process for a given TiN thickness.[4] If the substrate was etched for too long, the newly exposed silicon facets would re-oxidize and act as sources for parasitic two-level systems or other defects. The best results in terms of

[3] This effect is both related to the much higher *relative polarity* [Acetone 0.35, DMSO 0.44] [258] as well as the influence of the Cyclopentanone

[4] During the actual fabrication, this was usually achieved by a re-calibration of the etching rate by means of a test sample. The latter was then deposited in the same sputtering run as the actual wafer to reduce the influence of random thickness

the circuit performance could be achieved for a *plasma power* [**ICP**] of 400 W, a *microwave power* [**RF**] of 50 W and a gas mixture of Cl_2/SF_6 12 sccm/2 sccm. These conditions also allow the combination of the last two processing steps. By using *thinned UV6*, as shown in Fig. 2.13(a), it is possible to etch both the surplus areas of the superconductor as well as the so-called **flux traps** with the same recipe. Thus, after another cleaning procedure in *DMSO:Cyclopentanone*, the desired circuit structures (see Fig. 2.13(b)) are processed. Fig. 2.14 shows an optical micrograph of a finished microwave circuit, including the (bottom) gates and the *flux bias lines*. A full, tabular overview of all process steps and their corresponding parameters is given in Sec. A of the Appendix.

fluctuations.

3

SUPERCONDUCTING QUANTUM CIRCUITS

3.1. SHAPIRO CIRCUITS

3.1.1. GEN I: ON-CHIP BIAS TEES

The state-of-the-art method to probe the internal state structure of a Josephson junction or, to be more precise, a mesoscopic semiconductor-superconductor hybrid device, is measuring the direct and reversed AC Josephson effect, i.e. the *Shapiro effect* and its counterpart. The latter being an emitted microwave signal proportional to the voltage drop across the junction (*Emission*). Recent theoretical predictions indicate (cf. [266, 267]), that the coexistence of both 2π and 4π-periodic supercurrents lead to strong modifications of the typical spectrum of Shapiro steps. Depending on the relative strength of both contributions, certain steps are suppressed. In the extreme case of a purely 4π-periodic current, only the *even* steps can be observed. Due to the fact that these measurements directly probe the *dynamics* of the junction, which are realized by the coupling to a microwave source, they are usually not affected by most of the relaxation effects that occur for stationary measurements and can potentially render the system back into the 2π-periodic regime. Various experiments of [133, 268–271] could already observe Shapiro spectra in which the first step (n=1) is missing.

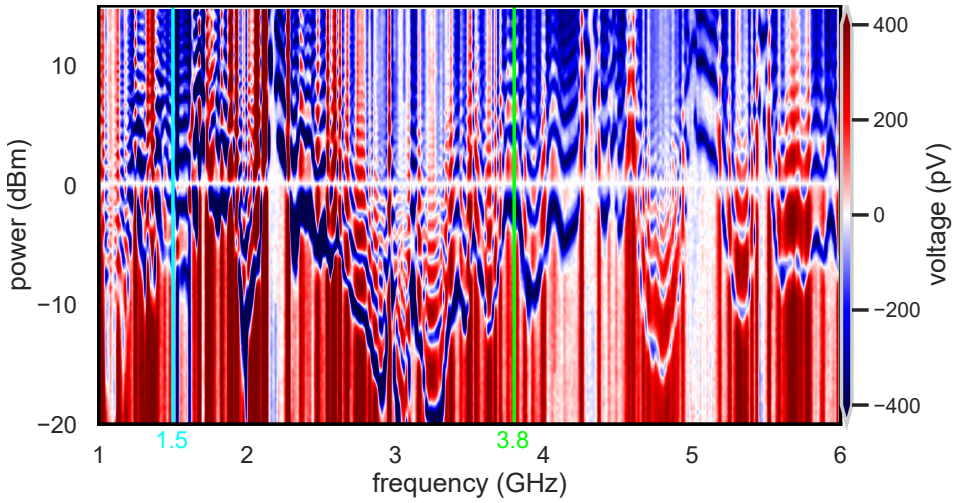

Figure 3.1 – *Frequency-power spectrum of an InAs/Al nanowire Josephson junction which is wirelessly coupled to an antenna. For every frequency, the junction shows a different ratio between the applied microwave power and the voltage drop across the junction. This effect can be attributed to parasitic effects like slotline modes or box modes, which couple to the irradiated microwave signal. In order to perform proper Shapiro measurements, one has to select frequencies for which the junction response shows well separated steps. Two possible measurement configurations are indicated by the yellow and green line. However, for experiments which rely on a detailed inspection of the underlying state structure, like the search for Majorana zero modes, this behavior is a serious issue and has to be addressed by using more advanced measurement configurations.*

However, even though these measurements are not affected by most of the relaxation effects which hamper steady-state measurements, they are still influenced by the properties of the junction. Due to fact that they map out the dynamic response of the junction to an external perturbation

II

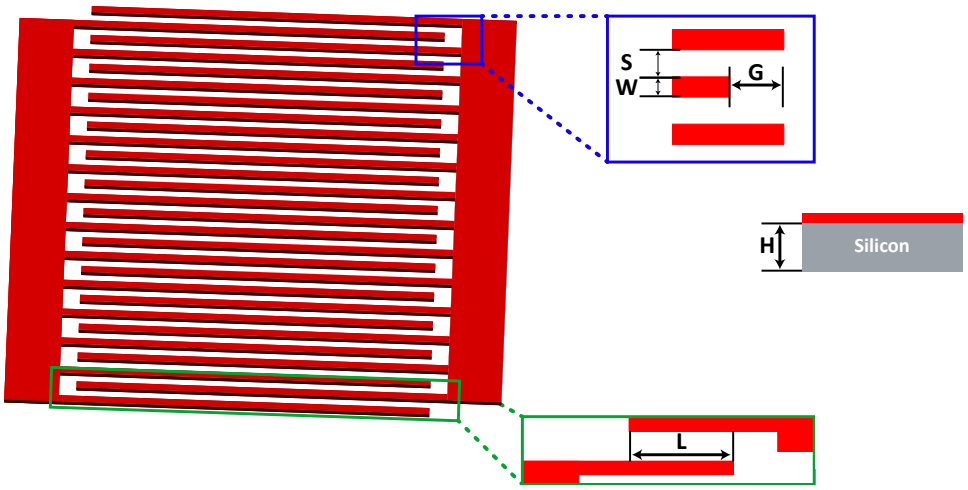

Figure 3.2 – *Schematic model of the interdigital capacitor with all geometric parameters. In contrast to the inductor, the effective capacitance of the structure is a combination of the metal stripes and the substrate underneath. Thus, the calculation includes both the thickness **H** of the silicon wafer as well as an effective permittivity ϵ_{eff}. Due to the special structure of the interdigital capacitor in terms of adjacent, parallel metal planes, the model for the full capacitance consists of three independent capacitors, which are derived by conformal mapping: 1. One which is determined by the width **W** of every individual finger as well as their separation **S**. 2. One which depends on the separation between the tip of each finger and the corresponding pocket on the opposite side, **G**. 3. One which takes into account that the outer fingers have to be modeled as a single three-finger system due to the lack of neighboring structures. This one is mainly determined by the overlap **L**.*

source, they are tightly bound to the *damping characteristics*. Especially in the case of a so-called *underdamped junction*, which can be understood in terms of the *tilted washboard potential* within the *RCSJ model*, the system can be rendered into a configuration in which the phase velocity is not directly related to the tilt of the potential and vice versa. In this case, there is a chance for an additional phase jump of $n \cdot \pi$, which ultimately results in deviations from the classical Shapiro step structure, too. In order to distinguish these damping effects from the emergence of topological states, i.e. Majorana zero modes and the corresponding 4π-periodic current, it is necessary to perform a detailed and continuous mapping of the frequency- and power-space of the junction. However, in the case of an antenna, the irradiated signal can couple to all possible kinds of HF-active parts of the circuit layout as well as the fridge setup. Thus, there is an undefined number of *slotline modes*, *box modes* and so on, which pick up parts of the HF signal and lead to a completely randomized attenuation. This means, that for every single frequency, the junction is exposed to a microwave signal with a different *effective coupling factor*.

Fig. 3.1 shows a frequency-power calibration measurement for an InAs/Al nanowire Josephson junction. Here, every switch between blue and red indicates a sudden change in the measured voltage drop, i.e. a Shapiro step. As can be seen, there is a strong variation in both the number of steps as well as the width of every individual step even for small variations in frequency. In order to obtain a reliable and consistent dataset, positions in the frequency space for which the junction shows a comparable Shapiro response need to be selected. Two examples are marked with the cyan and bright green vertical lines. However, it is obvious, that for this measurement configuration, it is impossible to perform the required mapping of the full power-frequency space. The important parameters are summarized in Table 3.1, resulting in a **coil inductance** L_{coil}=814.72 nH.

One way to tackle this issue is the usage of a so-called **bias-tee**, to split the effective input port of the junction into a two-terminal connection. In order to perform IV sweeps, a DC signal is coupled to one port of the input line via a planar, circular inductor. For the required AC modulation, an interdigital capacitor is used, which blocks all DC transport to protect the AC measurement equpipment and short the second port of the input line with the corresponding bond pad. The latter is thereby impedance-matched to the fridge wiring. In such a configuration, the transmission line, which is realized in a coplanar waveguide geometry, can act both as the source contact of the Josephson junction for the current-driven measurements as well as an electrically connected *antenna*.

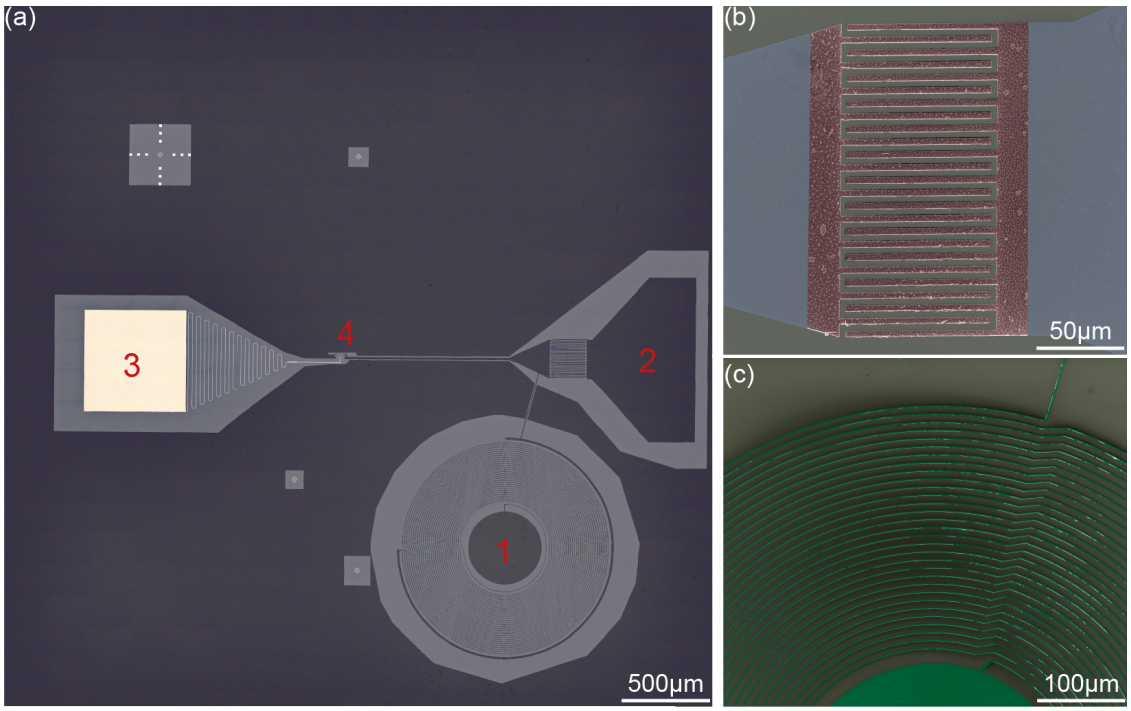

Figure 3.3 – *Optical micrographs of the final Shapiro circuit (a), interdigital capacitor (b) and the planar inductor coil (c). The numbers in (a) correspond to the inductor coil as the DC port [1], the interdigital capacitor that is used to couple in the AC signal [2], the bonding pad of the bottom gate [3] and the actual device area [4]. All superconducting structures were realized by the deposition of 80 nm TiN and a subsequent dry etching step. Doing so, parasitic effects due to sidewall-induced local changes in the capacitance or inductance can be avoided.*

Parameter	Description	Value
K_1	Geometry factor for an octagonal inductor	2.25
μ_0	vacuum permeability	μ_0
n	Number of turns	30
$\overline{d}$	Averaged diameter	758 μm
d_o	Outer diameter	1050 μm
d_i	Inner diameter	466 μm
K_2	Geometry factor for an octagonal inductor	3.55
ρ	Filling factor $\approx \frac{d_o}{d_i}$	0.385

Table 3.1 – *Overview of the relevant parameters used in the modified Wheeler formula (see Eq. 3.1).*

The technical design of the inductor and capacitor is done by means of **conformal mapping** (see Refs.[272, 273], [274] and [275]). For the first one, Ref. [274] has given a mathematical framework which has been further improved by Ref. [275]. The main optimization consists in the consideration of electric stray fields due to the self-capacitance between adjacent *rings* of the **planar inductor coil**. Following Ref. [275] and for the given dimensions and layout of the used inductance, it was assumed that the system can be described in terms of the simple *modified Wheeler formula*:

$$L_{\text{coil}} = K_1 \mu_0 \frac{n^2 \overline{d}}{1 + K_2 \rho} \tag{3.1}$$

For the interdigital capacitor, on the other hand, the calculation is much more complex due to the three different capacities that have to be considered. Following the scheme shown in Fig. 3.2, the first capacitor is defined by the inner, adjacent *fingers* of the device which form a periodic structure with $(N-3)$ elements:

$$C_N = (N-3)\epsilon_0 \epsilon_N \frac{\kappa(k_3)}{\kappa\left(k_3^{\dagger}\right)} L \tag{3.2}$$

II

Parameter	Description	Value
W	Finger width	3 μm
S	Finger separation	4 μm
G	Separation between upper finger edge and counter electrode	8 μm
L	Overlap area between adjacent fingers	163 μm
H	Substrate thickness	500 μm
N	Number of fingers	28
k_1	correction factor #1	0.211
k_2	correction factor #2	0.212
k_3	correction factor #3	0.429
k_4	correction factor #4	0.428
f_0	correction factor #5	-108
f_s	correction factor #6	-20178
e_e	effective permittivity	6.34
C_N	Capacitance between adjacent electrodes	158 nF
C_s	Capacitance between the finger edge and the counter electrode	57 nF
C_3	Capacitance of the outer finger and the central one	19 nF

Table 3.2 – *Overview of the relevant parameter used for the calculation of the total capacitance of the interdigital capacitor.*

Here, κ refers to the *full elliptic integral of the first kind*. The second capacitor is related to the open ends at the end of each finger

$$C_s = \frac{2.2\epsilon_0}{\pi\left(G^{-2}f_s + W^{-2}f_0\right)}N_F \tag{3.3}$$

and the third one models the two outer fingers and the central one

$$C_3 = 4\epsilon_0\epsilon_r\frac{\kappa(k_1)}{\kappa(k_1^\dagger)}L \tag{3.4}$$

The exact formulas for all correction factors, i.e k_1, f_0 etc., are given in [276–278]. For reasons of simplification, Table 3.2 summarizes all values as well as the results for the individual capacitors. The total capacitance is then given by the sum

$$C = C_N + C_s + C_3 \tag{3.5}$$

with $C = 233.8$ nF.

Fig. 3.3 (a) provides an overview of a finalized Shapiro chip with an on-chip bias tee. The circuit was fabricated in a similar fashion as the Andreev circuits in the previous chapter, including the bottom gate electrodes, the dielectric and the general approach for the formation of the superconducting structures. However, due to the fact that the transmission line is also supposed to work as the DC **source contact**, the TiN is significantly thicker than for the purely AC-driven setup. Here, the 80 nm thick metal layer requires almost twice the dry etching time. Thus, instead of *thinned UV6*, conventional *UV6* is used as ebeam resist. Fig. 3.3 (b) and (c) show a zoom-in of the interdigital capacitor (b) and planar inductor (c). The latter is connected to the left hand side electrode of the capacitor by a thin metal line. This effectively decouples the AC and DC sources and allows the application of a combination of both signals to the nanowire Josephson junction.

One of the disadvantages of the current design is the comparably large, parasitic *self-capacitance* of the inductor coil. This could be improved by switching to a layout that consists of multiple, but smaller inductive elements that are interconnected in series. Thus, the total inductance would scale up with $\sum_i L_i$, while the self-capacitance goes with $\sum_i 1/C_i$, resulting in a significantly smaller capacitance and a much higher frequency at which the inductance opens up for the AC signal.

3.1.2. GEN II: MANY-GATE STRUCTURES FOR COMPLEX NANOWIRE DEVICES

Even though this version of the Shapiro circuit is referred to as *Generation II*, it should be considered as an evolution addressing additional requirements rather than a full replacement of the already existing design. To be more precise, at some point during the measurements, it turned out that the chosen gate design, based on a single gate electrode, proved to be too limited in controlling the electronic properties of the nanowire Josephson junctions. Especially the progress in the theory of parafermionic excitations, with *Majorana zero modes* [**MZM**] as its most famous manifestation, constantly raises the bar for the required device characteristics.

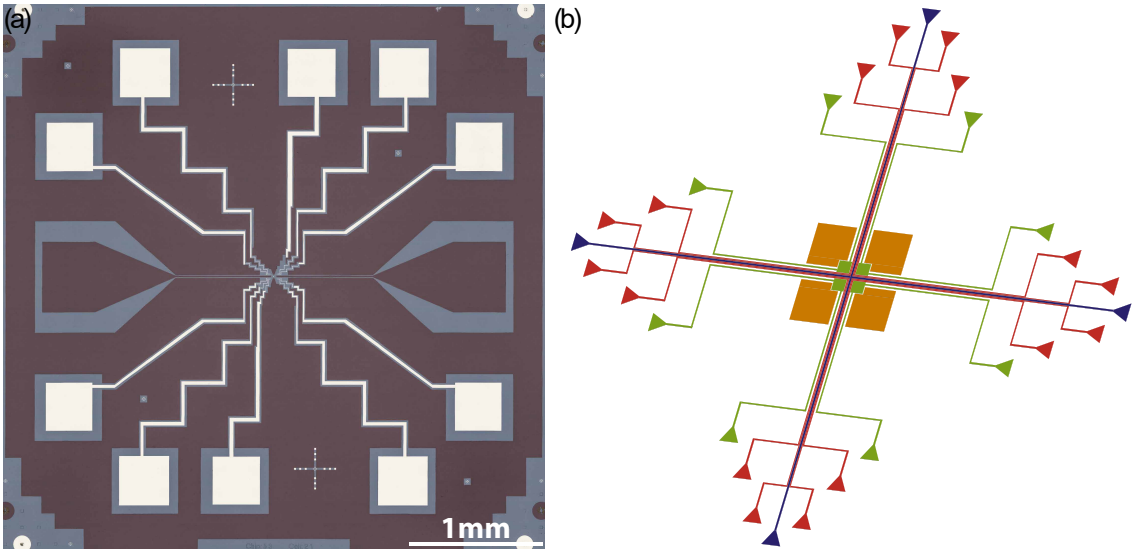

Figure 3.4 – *(a) Optical micrograph of a sample from the 2nd generation of Shapiro chips. In exchange for a more sophisticated control of the microwave signal, the nanowire Josephson junction can now be controlled by up to **nine independent gate electrodes**. This offers a lot of possibilities regarding the formation of tunnel barriers, SQUID structures or crossed nanowires with different coupling factors between the semiconductor and the superconducting leads. The substrate material (highly resistive silicon) and the superconductor for the transmission line and ground plane (titanium nitride) remain unchanged. (b) Exemplary configuration of the gate electrodes. The density of states inside of the nanowire, and therefore the magnitude of the supercurrent, is controlled by the central gate electrode (blue). Due to its importance, this contact has a second, redundant bond pad attached to it. The latter can also be used to apply AC pulses. The two adjacent electrodes on all four sides (red) are supposed to create tunnel barriers or a quantum dot. By using two electrodes, it is also possible to change the dimensions of the confinement potential, i.e. wider for the outer electrode and smaller for the inner one, respectively. The outermost electrodes (green), and the last metal pads that are actually electrically connected, are somewhat special in the sense that the nanowire on top of them is covered with the superconductor. In this sense, they act as mechanical support, too, but their primary role is to control the density of states in the section of the nanowire that is hybridized with the metallic states of the superconducting leads. The large, unconnected pads at the outer border of the structure, however, are arranged such that they planarize the final device with respect to the height difference between the substrate and the gate stripes.*

Fig. 3.4 (a) provides an overview of a Gen.II Shapiro circuit that is intended to be used for more complex devices like SQUIDs or networks of merged/crossed nanowires. While the general fabrication remains the same, the on-chip bias tee has been replaced by *10 gate pads* that are connected to **9 independent gate electrodes**. A schematic sketch of the corresponding layout is shown in Fig. 3.4 (b). Here, the *center gate electrode* [**blue**] is supposed to directly influence the *number of Andreev bound states* within the nanowire Josephson junction. The *two innermost gate leads on each site* [**red**], however, control the coupling between the superconducting electrodes and the nanowire segment in the middle. By using two adjacent but independent gate contacts, it is possible to not only induce a *tunnel barrier*, but also precisely control its potential height and width. In the case of a multi-terminal nanowire network, it is possible to (de-)couple individual "arms" of the structure from and to the primary transport channel, effectively allowing the system to be switched between a two-, three- or four-terminal configuration. The *outer pad-like structures* [**green**] are designed such that they can influence the *density of states* in the semiconductor-superconductor hybrid section of the junction, i.e. the area of the nanowire(s) that is still covered with the Al or Nb shell. The latter approach follows theoretical predictions that the creation of requires not only a single channel within the junction,

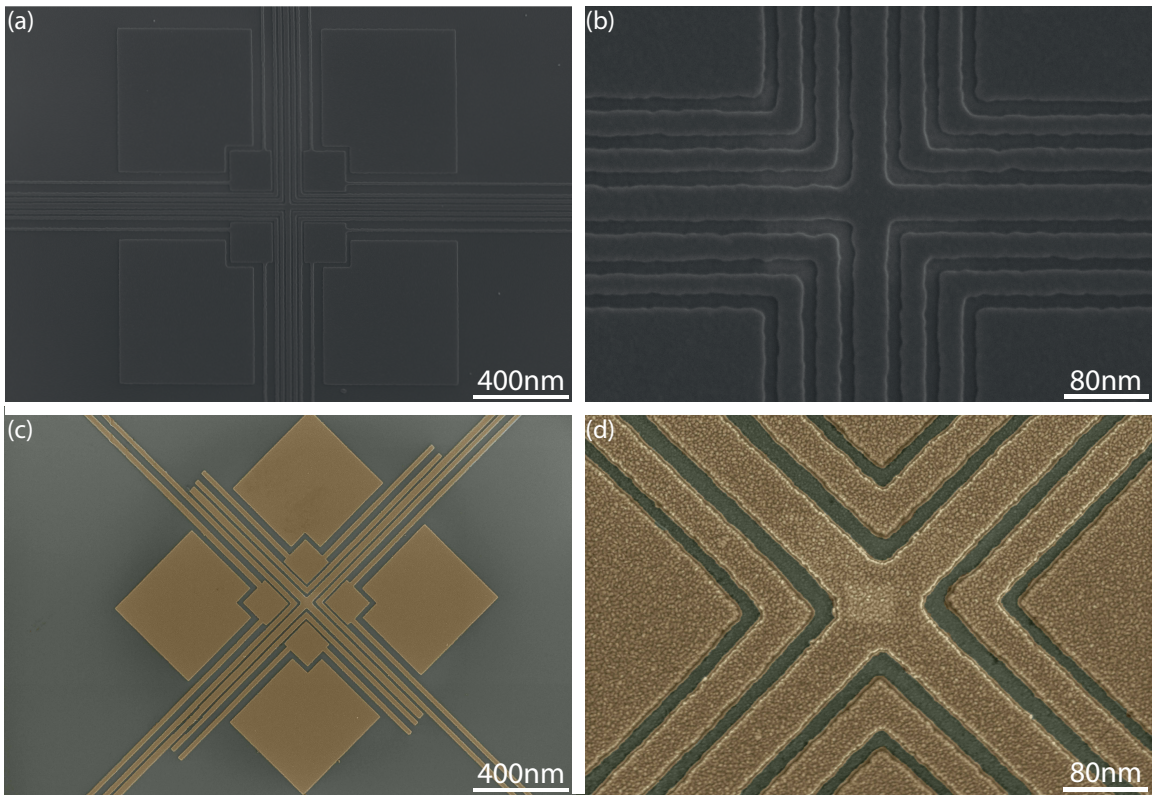

Figure 3.5 – *SEM micrographs of (a)(b) etching- and (c)(d) lift-off-based multi-gate structures. Here, the central electrode is supposed to tune the number of states within the nanowire, while the two outer leads on each side can give rise to electrostatically defined tunnel barriers. Lastly, the large outer pads act as mechanical support structures for the nanowire Josephson junction. Using a globally deposited 10 nm thick layer of Niobium it is possible to achieve well-defined gate electrodes with separations down to 10 nm.*

but also that the effective conductance level of the contact area is tuned to the **first conductance plateau** [279][1]. The **orange pads**, as the outermost structures of the layout, are not connected to the environment and are supposed to mechanically support the nanowire device above them.

In order to work as intended, the neighboring gate leads need to be packed together within a range of 200 nm. Additionally, to enable a spatially localized tuning of the electronic parameters, the lateral dimensions of the individual metal stripes should be as small as possible, i.e. their width should just be limited by the fabrication process. After performing a series of tests, two different approaches to achieve both requirements have been identified:

Etched Nb Here, the gate structures are fabricated in a quite similar fashion as the TiN resonators in the previous chapter, i.e. by utilizing a combined lift off-etch procedure. First, the silicon substrate is globally covered with a 3 nm/5 nm thick Al_2O_3/HfO_2 stack. In the next step, a 10 nm thick layer of Nb is deposited within the device area in the center of the Shapiro chip in Fig. 3.4 (a). By means of *multi-pass ebeam lithography*[2] and *thinned CSAR*, all areas around the desired gate structures are exposed again and, subsequently, treated with a reactive ion plasma [SF6 with a flow of 100, RF power 100, ICP power 0] for approximately 20 s. Fig. 3.5 (a) shows the final structures after cleaning with boiling *DMSO:Cyclopentanon* for 16 hours. It can be seen, that all structures look as intended, without any shorts, or interruptions or signs of residual resist. However, in Fig. 3.5 (b), some small *blob-like* features are visible around the edges of the structure. Those can be attributed to the finite diameter of the electron beam which, even if the smallest beam diameter is used, still maintains his **Gaussian profile**. These imperfections

[1] In terms of the (multi-terminal) Landauer-Büttiker-Formalism for ballistic, fully-quantized systems [280]

[2] Here the same pattern is written multiple times with an **effective dose** (desired dose/number of passes) instead of applying the full dose at once. This reduces the *thermal load* on the ebeam resist as well as the *proximity effect* and results in much steeper and much better defined edges of the patterned structures.

can be avoided or at least significantly reduced if a higher number of passes is chosen during the exposure.

Liftoff Ti/Pt Instead of the large area deposition of sputtered metal and the subsequent removal of large sections of it, it is also possible to directly use a liftoff-based approach. However, due to the small dimensions that are necessary to achieve an ideal function of the gates, most of the issues that have been described already for the fabrication of the bottom gates used within the microwave circuits are still valid and even more pronounced. In order to achieve thin metal lines, it is necessary to use Ti/Pt rather than Ti/Au, as the much higher strain in the former material lead to some *self-peeling* of the deposited structures. Additionally, the grain size of the evaporated Pt is much smaller than the one of Au (see Fig. 3.4 (d)), which results in an extremely smooth metal layer despite the comparably thin films. Furthermore, the sample has to be precisely aligned in the deposition chamber in order to avoid any sidewalls that could collapse and shorten adjacent leads. Lastly, for the lift off, the sample has to be cleaned multiple times in heated **DMSO:Cyclopentatone** in order to avoid the re-adhesion of any metal particles between the leads.

Even though both approaches are working, they should be used for different types of devices. For single nanowire Josephson junctions or networks that are intended to work in the regime of low density of states or tunnel-limited transport, the Nb gates offer a much finer and more spatially localized control of the tunnel barriers and the semiconductor-superconductor coupling due to their smaller width and separation. However, it turned out, that even for thicknesses down to 3 nm, the Nb turns superconductive at the base temperature of a *dry fridge*, resulting in a disturbance of the field lines if a finite magnetic flux is applied. Thus, for SQUIDs or *Little-Parks junctions*, the Ti/Pt gates are used despite their larger dimensions and the more complex fabrication process.

4

OPTIMIZATION

4.1. DEALING WITH FIELDS I: IMPROVED VORTEX CONTROL

4.1.1. STATIC CASE: THE ABRIKOSOV LATTICE

One of the important findings of the **BCS theory** [281], the **Ginzburg-Landau model** [229, 282, 283] and the **London equations** [284] is the fact, that superconducting materials come in two different kind of "flavors" in terms of durability against external perturbations, i.e. temperature, magnetic fields and current flow. In the case of type-I materials like Al, Ti and Pt, the gain in condensation energy, i.e. the difference in the free enthalpy between the normal and superconducting state, is easily overcompensated by the **field displacement work** if an external magnetic field is applied. Typical values for the thermodynamic critical field of the BCS theory are of the order of a few mT or less. On the other hand, most of the compound superconductors like TiN, NbTi or pure Nb, can withstand much higher external fields by *sacrifying* small areas. The mechanism is based on the **London penetration length** λ_L and its relation to the current transport inside of the superconductor: While λ_L is generally understood as the distance over which an external field can penetrate the superconductor despite the Meißner-Ochsenfeld effect, it is also acting as a boundary condition for the current flow within the superconductor due to the displacement of the intrinsically created field $B \propto I$. This means, that the actual thickness of the transport layer, i.e. the region in which the Cooper pairs follow a directed motion, is independent of the dimensions of the superconducting layer as long as width, length and thickness are larger than λ_L.

For fields above the *lower critical field* B_{c1}, the material switches into the **Shubnikov phase** and starts to form normal conducting channels parallel to the magnetic field orientation in order to reduce the field displacement work. The theory of this effect was discovered by Abrikosov [285] and is based on the Ginzburg-Landau theory, especially the specific nature of the interface energy between normal conducting and superconducting sections and its relation to the Ginzburg-Landau parameter $\kappa = \lambda_L/\xi_{GL}$. For a type-I superconductor, $\kappa < 1/\sqrt{2}$, i.e. a local collapse of the superconducting pair condensate would lead to a reduction of the global condensation energy. However, for type-II superconductors, it is exactly the opposite: By introducing small normal conducting areas that act as nodes [1] which are surrounded by cooper pair driven **eddy currents** (also known as *shielding currents*), the material gains energy and can stabilize the pair condensate. The exact definition of *small* is directly related to the quantization of the magnetic flux, i.e. each hole can host only an integer number of flux quanta

$$\Phi_{hole} = n \cdot \Phi_0 = B_{ext} \cdot A_{hole} \tag{4.1}$$

thereby setting limits for the strength of the external field as well as for the pinhole dimensions for which the material can still maintain the superconducting state. If the shielding currents exceed the (local) critical current of the material, the superconducting state collapses on the bulk level. Fig. 4.1 (a) and (b) provide a schematic overview of a single **Abrikosov vortex** embedded in a typical type-II

[1] In terms of *topology charges* as **n^{th}-order phase windings** [286–288] in the spectrum of the macroscopic order parameter Ψ

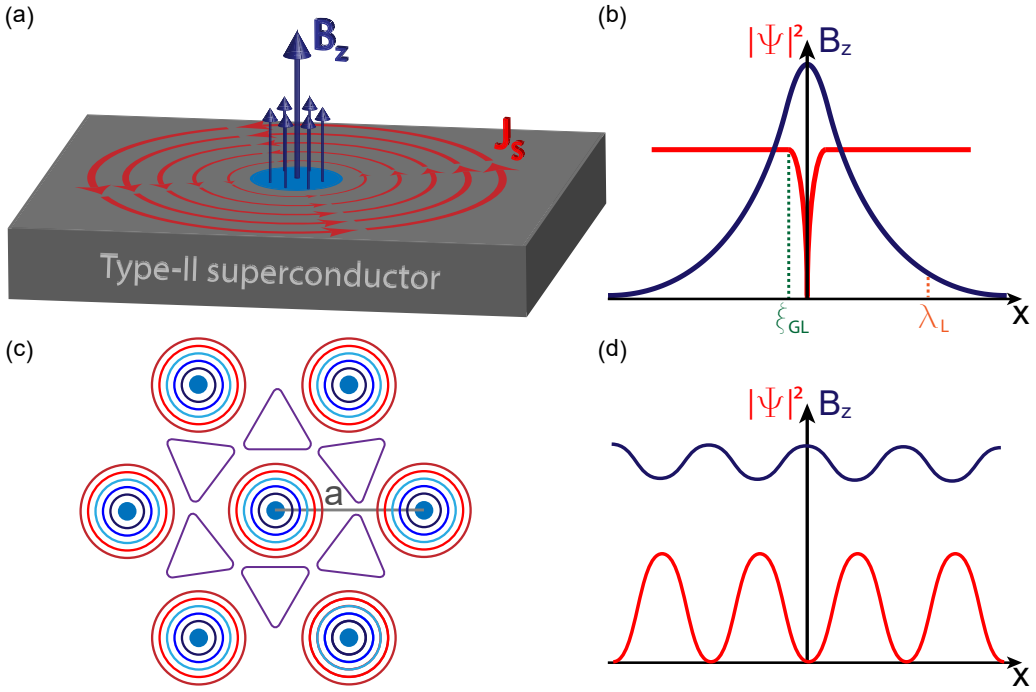

Figure 4.1 – *(a) Schematic depiction of a single **Fluxon** embedded in a type-II superconductor, consisting of a normal conducting vortex core and surrounding eddy currents. (b) Qualitative evolution of the Cooper pair density $|\Psi|^2$ and the magnetic field strength B_z in dependency of the distance from the center of the vortex core. (c) Schematic layout of an **Abrikosov lattice** consisting of multiple Fluxons. The blue spots in the center mark the position of the normal conducting vortex core. The circles with different colors indicate the surrounding eddy currents with different magnitude. (d) Cut along the line a in (c) in terms of the Cooper pair density $|\Psi|^2$ and the magnetic field strength B_z, revealing an almost homogeneous field distribution.*

superconductor, i.e. with the characteristic length scales $\lambda_L \gg \xi_{GL}$. Consequently, while the actual normal conducting area, i.e. the **vortex core** for which the cooper pair density $n_s = |\Psi|^2 \rightarrow 0$, is relatively small ($\xi_{GL} \approx 30\,\text{nm}$) [289], the effective area in which the supercurrent has to circulate in order to compensate the external magnetic field can be hundreds of nm^2 [290]. Due to the huge interaction range and its strong influence on the pair condensate, the combination of a vortex core and surrounding shielding currents is normally referred to as its own kind of quasiparticle, a so-called **Fluxon** [285, 290].

While the description of a single Fluxon is comparably simple, it becomes much more complicated for a real superconducting sample with thousands of vortices. The distance between individual vortex cores is usually only limited by the superconducting coherence length ($d = 2\xi_{GL}$) and therefore independent of λ_L. This means, that the uniaxial field distribution $\mathbf{B}^*(\mathbf{x})$ in the center of two fluxons with parallel aligned fields located at $x_1 = 0$ and $x_2 = 2\xi_{GL}$ is just slightly reduced, typically to values in the range of 40% to 70% of the maximum field amplitude. Consequently, the energy gain due to the formation of vortices is decreased by an additional repulsive interaction energy that scales with the ratio of the vortex separation and the london penetration length. The latter can be easily understood by imagining the two vortices and the trapped flux lines as two bar magnets. This has important consequences, as it creates a sweet spot between the **total number of individual vortices** and the **minimum distance between adjacent Fluxons** which depends on the dimensions and dimensionality of the metal film, the geometry of the actual structure and the number of defects that can act as **pinning centers**[290].

The ideal *steady-state solution* for a conventional type-II-superconductor treated by an external magnetic field, the so-called **Abrikosov lattice** [285, 290], is shown in Fig. 4.1 (c). This *quasiparticle superstructure* consists of an array of **honeycombs** in which every individual one is formed by six single **vortex triangles** around a common center with a separation of $r = 1.075\sqrt{(\Phi_0/B)}$. The vortex cores are depicted in blue, while the outer circles correspond to *stream lines* of the magnetic field, and therefore also the circulating shielding currents, altogether forming the **Fluxons**. Additionally,

one can see how the field is squeezed together between the adjacent vortex cores, effectively creating a repulsive force.

Fig. 4.1 (d) provides an overview of the local magnetic field strength as well as the order parameter Ψ in a superconducting film with multiple vortices [291]. Here, if the external field is increased, the superconductor has to create increasingly strong shielding currents. Additionally, in order to maintain the superconducting phase on the bulk level, the local current density has to stay below the critical current density J_c at all times. Accordingly, instead of increasing the magnitude of the circulating current, the area in which the Cooper pairs flow is enlarged. If one assumes now a given number of distributed vortex cores at some point the corresponding Fluxons will start to overlap. As a consequence, the variation of the magnetic field strength across the whole superconductor is continuously reduced. This goes along with a suppression of the superconducting order parameter, which, ultimately and for fields larger than B_{c2}, results in a global collapse of the Cooper pair condensate.

Nowadays, the physics of single vortices and the dynamics of vortex lattices have again attracted considerable interest due to multiple reasons. Since they represent nodes in the superconducting phase and, more importantly, can also host localized bound states, they are a promising candidate to realize topologically protected systems [292]. Still, if it comes to other quantum systems that are only utilizing the superconductor, the collective motion of vortices can be highly detrimental due to their dissipative nature. This is especially true if it comes to the microwave circuits and qubits used in this thesis, as most of the already described mechanisms fail to work in the presence of AC signals. Thus, in the following section both the high-frequency dynamics of the vortex lattice as well as methods to stabilize and control their collective motion in terms of **artificial flux traps** and the **Bean-Livingston barrier** are discussed.

4.1.2. MAGNETIC FIELD COMPENSATION AND VORTEX STABILIZATION: FLUX TRAPS

If a type-II or an ultrathin type-I superconductor are exposed to a magnetic field $B > B_{c1}$ and if the penetrated area is larger than λ_L^2, the system compensates the magnetic flux by forming an Abrikosov lattice. This effectively creates a much higher critical field B_{c2} at which the Cooper pair condensate in the bulk material starts to collapse. For the DC case, this mechanism allows the measurement of Josephson junctions at comparably large fields despite additional effects like *flux focussing* [293, 294]. However, as soon as an AC signal is applied, the situation gets much more complex.

In a simplified picture [295], a single vortex as a massless particle is spatially localized within the **harmonic pinning potential** $U(x)$ due to the **pinning force**

$$F_p = \alpha p x \tag{4.2}$$

with the *damping constant* α. However, if a current flows through the structure, the collective motion of the *Cooper pair condensate* induces an additional **Lorentz force** on the vortices

$$F_L = J_s \times \Phi_0 \tag{4.3}$$

with J_s as the corresponding density of the supercurrent I_s and the flux quantum Φ_0. The dynamics of the combined system, comprised of the superconductor and the vortex lattice, are then fully determined by the competition between F_p and F_L. Here, the relevant figure of merit is the **flux-flow vortex viscosity** [296–298]

$$\eta = \frac{\Phi_0 B_{c2}}{\rho_n} \tag{4.4}$$

which depends on the *upper critical field* B_{c2} and the *normal state resistivity* ρ_n, effectively providing a connection to the *defect density* within the material. For small driving currents that are constant or only vary slowly in time, the vortices can only oscillate **reversibly** within the *pinning potential* and do not interact with the *Cooper pairs*. Here, the relevant distance over which the vortices can tunnel to adjacent potential wells is the so-called **Campbell length**[299–301]

$$\lambda_{Cb}(\omega = 0) = \sqrt{\frac{B_{ext}^2}{4\pi\alpha}} \tag{4.5}$$

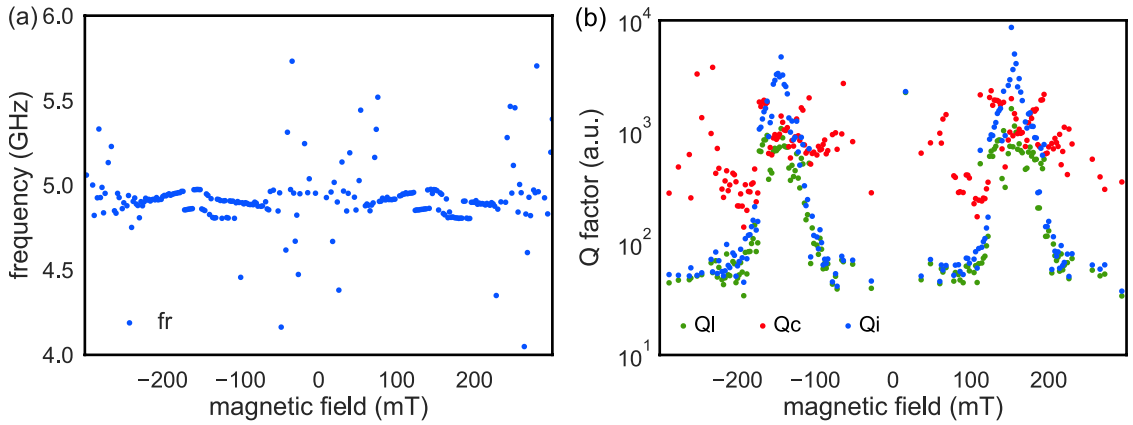

Figure 4.2 – *Flux-dependent (a) resonance frequency and (b) quality factors of a bare 80nm thick λ/4 resonator. Even though there is no qubit-resonator interaction involved, the minimum of the resonance moves periodically if a magnetic field is applied perpendicular to the circuit. This effect is related to the free motion of vortices within the TiN, which ultimately changes the kinetic inductance L_k of the superconductor and subsequently also the resonance frequency.*

However, for the measurements presented in this thesis, the frequency range and magnitude of the used microwave signals is way above the conditions of the *pinning case*. In this scenario, the **friction** caused by the *viscosity* η leads to a significant **dissipation**. The latter is determined by the **total kinetic energy** of the *moving vortices*

$$E_{kin,tot} = \sum_i \int_0 \delta E(x_i) = f_L v dt \propto \sum_i (J_s(\omega, x_i))^2 \tag{4.6}$$

that are spatially distributed over a lattice with x_i grid points.

Fig. 4.2 provides an overview of the out-of-plane magnetic field response of a slightly undercoupled $\lambda/4$ resonator fabricated out of 80 nm thick TiN and probed in transmission configuration. Apparently, the system reacts already heavily to fields in the range of only a few milliTesla. Besides the occasional large jumps, there are also plateau-like regions of constant frequency that are connected via smaller jumps. Here, the latter can probably be attributed to large scale vortex lattice rearrangements or the dissipative annihilation of vortices at the edges of the superconducting structure. Additionally, the average resonator position moves slowly down in frequency, which is a typical signature of an increase of the *reactive contribution* of the vortex-induced losses. It should be pointed out that even the smallest fluctuations of the resonance frequency are already in the range of ~ 100 MHz and therefore comparable to, or even larger, than any possible **qubit-induced shifts** of the resonator.

Due to these issues, a precisely tailored and well-controlled flux management is one of the most important requirements for all experiments based on microwave spectroscopy. The state-of-the-art solution is the stabilization of the vortex lattice by means of a significantly stronger pinning potential. To do so, the randomly distributed pinning centers, which are typically caused by defects in the material, are replaced by artificially created regions that exhibit a *minimum* in the **superconducting order parameter**. In the past and especially for *field-cooling experiments*, this was usually achieved by means of a local thinning of the superconductor to form sections with smaller Δ, i.e. lower and upper critical fields B_{c1} and B_{c2}, respectively. This method of forming **flux traps** has the disadvantage that there is always a finite field for which the whole film is still superconducting though. More recently, the way to go is the creation of so-called **antidots**, i.e. small areas of various geometric shapes in which the superconductor has been completely removed by means of wet or dry etching [302–304]. However, while the actual fabrication of the *holes* is comparably simple, the determination of their required shape and separation as well as the arrangement and distribution across the superconductor is a complex and challenging task that requires a deeper look into theory.

The framework used to describe the vortex dynamics in cQED structures is based on the theory developed for the description of *hard superconductors* [**type-II**] that are exposed to out-of-plane

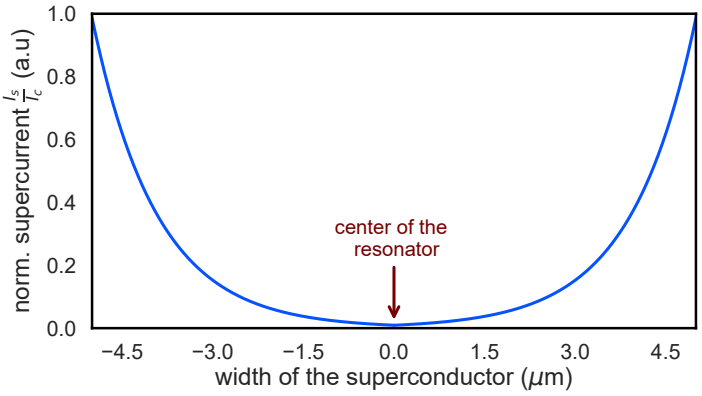

Figure 4.3 – *Simulated and normalized supercurrent distribution for a London penetration length of λ_L=1 μm. The current gradient induces a flux gradient in terms of quantized vortices. The density of the latter is thereby proportional to the magnitude of the current, i.e. the major part of the vortices is located at the edge of the superconductor.*

magnetic fields. The so-called **Bean critical state model**[2] provides a *macroscopic* explanation of the **shielding process** that arises in the **Shubnikov phase** of those materials and induces a pronounced *hysteresis* of the **magnetization** [307, 308]. The first key feature of the model is the fact that a superconductor reacts to the application of an external magnetic field with the induction of a macroscopic **critical current** that shields its interior from the magnetic field lines. As long as the field is below the lower critical field B_{c1}, the superconductor remains in the **Meissner phase** and all external flux is screened by the shielding current within the *London penetration length* λ_L [3] [309]. As soon as the external magnetic field exceeds B_{c1}, the length over which the *critical current* is distributed is not longer limited by λ_L. Instead, it starts to extend towards the interior of the superconductor, which is schematically shown in Fig. 4.3 for $\lambda_L = 1\,\mu$m. This can be considered as the second key feature of *Bean's model*. If the external magnetic fields becomes equal to the upper critical field B_{c2}, the whole superconductor is interspersed with a *current density* that is equal to the *critical value of the system*, which effectively renders the system back into the normal state. However, as long as the system remains in the **Shubnikov phase**, i.e. $B_{c1} < B < B_{c2}$, the gradient in the shielding current induces a macroscopic **flux density gradient**, following Ampere's law. On the microscopic scale, this gradient gets quantized into **Abrikosov vortices**. Here, the distribution of the vortices is a direct function of the flux density, resulting in a gradient of the vortex density with respect to the distance from the edge of the superconducting film.

The last statement of the previous paragraph marks the second key feature of *Bean's model* and is also the reason why it is referred to as *critical state model*. For transport, it has important consequences for the interaction between the AC-driven motion of the Cooper pair condensate and the Abrikosov lattice. First of all, the oscillating supercurrent mainly flows close to the edges of the resonator. Thus, all Abrikosov vortices in this area will experience a larger driving force compared to those that are located closer to the center of the superconducting structure. Additionally, the absolute number of vortices is also much larger near the edges of the resonator. Both effects together make it evident that all approaches towards a better flux management have to put a special focus on this region. Thus, the most simple approach would be to position the antidots as close as possible to the edges of the superconductor. However, in order to utilize the so-called **Bean-Livingston barrier** [310, 311], which prevents the magnetic field from entering the superconductor below and, under some conditions, even above H_{c1} [4],

$$G(b) = \Phi_0 \left[H_e e^{\frac{-x_0}{\lambda}} - 0.5 H_v(2x_0) + H_{c1} - H_e \right] \tag{4.7}$$

the vortex has to be located in a certain distance from the surface x_0. Here, H_v corresponds to the field at the center of the vortex core. H_e, on the other hand, refers to the external field that induces the **Meissner currents** (first term), which push the vortices deeper into the superconductor. The latter effect is counteracted by the attraction between the vortex and its *antivortex*, which is mirrored

[2] Also referred to as *lamina model* [305, 306]
[3] The length scale defined by λ_L is thereby assumed as "the surface".
[4] Therefore also referred to as **superheated Meissner state** [290, 312–314].

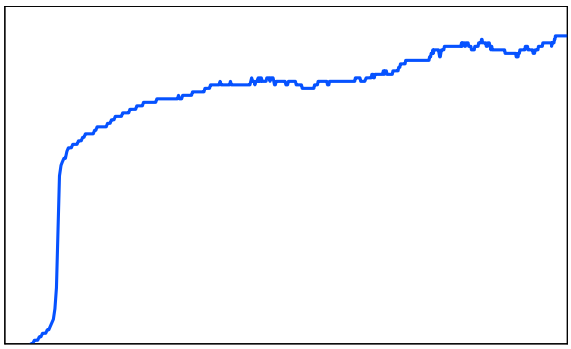

Figure 4.4 – *Temperature-dependent resistance of an exemplary 80 nm thick TiN van-der-Pauw sample, exhibiting a superconducting transition temperature of* $T_c = 4.2\,K$.

II

at the surface [5] [317]. Here, typical values for the *surface-vortex-separation b* are in the range of 0.4 to $0.8\lambda_L$, although the optimal distance depends heavily on the total dimensions of the superconductor with a tendency of smaller b for *thinner films* [318, 319].

In order to get a value for λ_L, multiple 80 nm thick TiN **van-der-Pauw** devices have been analyzed with respect to their **critical temperature** T_c and **sheet resistance** ρ_s. An exemplary measurement for a bias current of 10 μA is shown in Fig. 4.4, revealing $T_c = 4.2\,\mathrm{K}$ and a **superconducting gap**

$$\Delta_{BCS} = 1.764 k_b T_c = 0.638\,\mathrm{meV}, \tag{4.8}$$

which is in good agreement with other works on reactively sputtered TiN [257, 290, 320, 321]. The sheet resistance and **resistance-per-square** are found to be $\rho_s = 4.368\,\Omega\mu\mathrm{m}$ and $\rho_{sq} = 54.6\,\Omega/\mathrm{sq}$. Following the *BCS theory* again, this results in a London penetration length of

$$\lambda_L = \sqrt{\frac{\hbar \rho_s}{\pi \mu_0 \Delta_{BCS}}} = 1.07\mu\mathrm{m} \tag{4.9}$$

which can then be used to determine the alignment of the flux traps.

The final two steps are the choice of the actual *flux trap grid structure* as well as the determination of the required *antidot diameter*. Even though designs based on **Ratchet structures** [322] or customized arrangements obtained from *finite element simulations* [323] are slightly more efficient, due to reasons of simplicity and more freedom with respect to the used *metal thickness*, a classical **Abrikosov layout** has been chosen. However, the determination of the ideal antidot size is less straightforward considering the fact that the optimal pinning effect depends on the applied magnetic field. Here, a combination of both small, i.e. width $\lambda < \mathrm{d} = 75\,\mathrm{nm} < \xi$, and large traps [d=400 nm] was picked, showing some similarities to the design in [304]. The idea behind this approach is, that the large structures act as a *flux reservoir* which not only suppresses the **flux focusing effect** due to the reduction of the effective **ground plane area**, but can also host a large number of *flux quanta*. The significantly reduced amount of flux is then stabilized with the small traps.

Fig. 4.5 (a) provides an overview of a finalized microwave circuit that is intended to be used for two-tone spectroscopy. The red box marks the area that determines the capacitive coupling between the transmission line and the resonator, i.e. Q_c. Here, the comparably wide **decoupling line** ensures that the resonator resides in the *undercoupled regime*. In order to avoid any obstacles with the dipole coupling, no flux traps have been added to this section of the circuit. In contrast, the ground plane is globally interspersed with large flux traps. For the resonator, on the other hand, only small traps have been used to limit the increase of the **kinetic inductance** L_k. Both features become even clearer by looking at one of the termination areas, e.g. Fig. 4.5 (c). The large traps within the ground plane, i.e. in the yellow box and Fig. 4.5 (d), are arranged in a square array with a lattice constant of 150 nm. The small traps, however, follow the typical *honeycomb arrangement* of an ideal **Abrikosov lattice** with a separation of 100 nm between the columns and rows. Additionally, both trap arrays are separated by

[5] The effect arises due to a **conformal mapping** approach [315, 316].

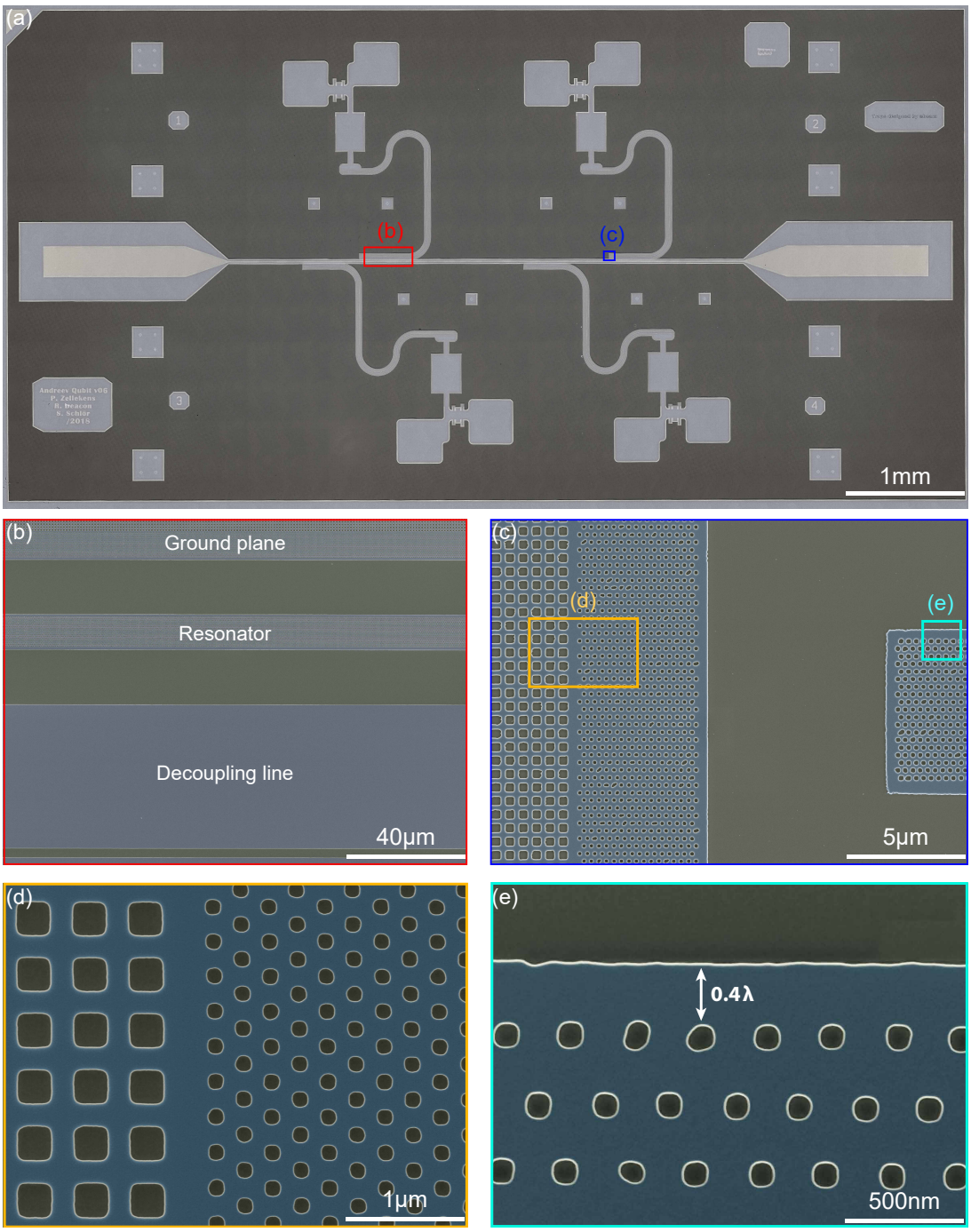

Figure 4.5 – *(a) Optical micrograph of an Andreev microwave circuit with small and large flux traps. (b) Zoom- in on the coupling capacitor section between the resonator and the transmission line and (c) the upper termination point of one of the resonators. (d) Overview of the different flux traps arrangements in the ground plane. The large traps are distributed in a square lattice, while the small traps follow the hexagonal shape of an Abrikosov lattice. (e) Zoom-in on a single resonator, clearly showing the trap-free region around the edge of the structure in order to maintain the Bean-Livingstone barrier. More details are provided in the main text.*

roughly $0.5\lambda_L$ in order to (partially) decouple them by means of a screening current. For the resonator in Fig. 4.5 (e), however, the array of small traps is separated from the edge by a distance of $0.4\lambda_L$ to maintain the *Bean-Livingston barrier*.

In order to probe and benchmark the resonator performance after the implementation of the flux traps, a more in-detail analysis of the circuit response has been performed. Comparing Fig. 4.6 (b) and Fig. 4.2, it becomes immediately obvious that the antidots significantly reduce the frequency shift. Here, at the maximum out-of-plane field of 1 T, which is already more than three times larger

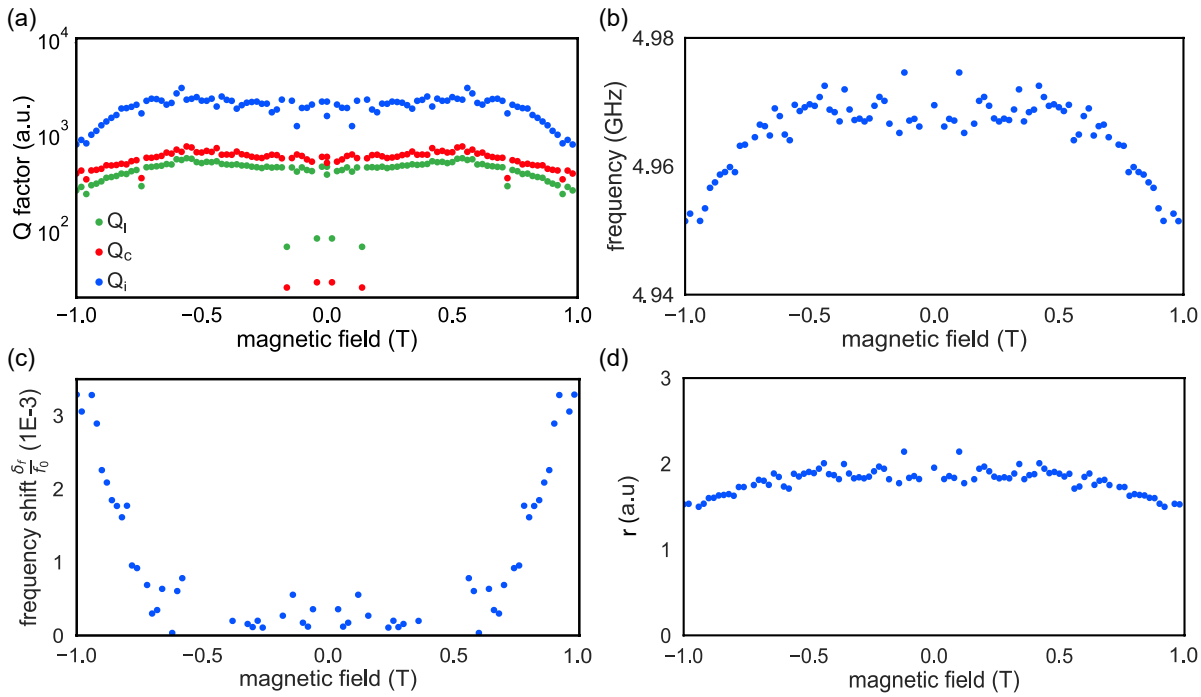

Figure 4.6 – *Overview of the most important parameters of an 80 nm thick TiN λ/4 resonator with small and large flux traps. (a) All three quality factors as well as the resonance frequency (b) exhibit only a small magnetic field dependency. (c) Even at an applied field of 1 T, the total field induced frequency shift is less than 1%. (d) Ratio between the reactive and resistive vortex contributions for increasing magnetic fields. The small decrease at larger fields clearly indicates the onset of dissipative vortex motion.*

than the one used in Fig. 4.2, f_r only shifts for 15 MHz. For the **relative frequency shift**

$$\frac{\delta f}{f_0} = \frac{\left[f_0(B) - f_0(B_0)\right]}{f_0(B_0)} \tag{4.10}$$

shown in Fig. 4.6 (c), this is equal to a change of 3 ‰ with respect to the zero-field resonance frequency $f_0(B_0)$. With the same plot, it is also possible to extract the **threshold field** $B_{th} \approx 0.5$ T at which the antidot-based vortex lattice becomes unstable again [324, 325]. However, just as important is the change of the **quality factors**, as they directly determine the photon lifetimes of the different circuit elements and are also a much more sensitive figure of merit for potential loss channels. Fig. 4.6 (a) depicts the field-dependency of Q_i, Q_c and Q_l. Similar to the resonance frequency, all three parameters only start decreasing at fields slightly above B_{th}. By combining the vortex-induced loss factor

$$\frac{1}{Q_v} = \frac{1}{Q_i(B)} - \frac{1}{Q_i(B_0)} \tag{4.11}$$

with $\frac{\delta f}{f_0}$, it is possible to determine the change of the **surface impedance**[326]

$$Z_s = R_s + i X_s \tag{4.12}$$

with the *surface resistance* R_s and the *surface reactance* X_s, respectively. The corresponding figure of merit is the **r parameter**[327, 328]

$$r = \frac{X_s}{R_s} = \frac{\frac{1}{Q_v(B)}}{\frac{\delta f}{f_0(B)}} = \frac{\mathrm{Im}(\rho_v)}{\mathrm{Re}(\rho_v)} \tag{4.13}$$

Here, ρ_v refers to the complex **vortex resistivity**, with $\mathrm{Im}(\rho_v)$ as the *reactive vortex response* and $\mathrm{Re}(\rho_v)$ as the dissipative losses. The ratio of both is plotted in Fig. 4.6 (d). The resulting values are

always above unity, which is a clear indication that the system is dominated by the *reactive* contribution of the vortices rather than losses caused by **vortex motion**.

The combination of all results provides an immediate and clear prove that the chosen antidot pattern is sufficient to suppress the RF-induced motion of vortices up to an out-of-plane field of at least 500 mT. However, this only holds as long as there is no additional *in-plane field*, which induces a much larger driving force on the vortices. Unfortunately, the latter is a fundamental requirement of all devices based on a single or a few **Andreev bound states**. Thus, the next section focuses on another improvement of the magnetic field resilience by means of geometric adjustments to the metal film itself.

4.2. DEALING WITH FIELDS II:TUNING OF THE CHARACTERISTIC IMPEDANCE

The classification of superconductors into *type-I* and *type-II*, i.e. **soft** and **hard**, based on the ratio $\kappa = \lambda_L/\xi$ is one of the most important achievements of the Ginzburg-Landau theory. However, this strict separation only holds as long as the metal has a sufficiently large **bulk region**. This means that all structure dimensions, e.g. width W, length L and thickness t of a coplanar waveguide resonator, need to be *much larger* than λ_L. Most of the modern superconducting microwave designs can easily fulfill the first two criteria. In the case of the film thickness, however, several experiments have been performed to investigate its effect on typical superconducting and microwave-relevant properties. Strikingly, films made of **type-I** superconductors with thicknesses much less than the bulk coherence length and the London penetration length have been shown to support the nucleation of $h/2e$ Abrikosov vortices in perpendicular magnetic fields just as their *hard* counterparts [329, 330].

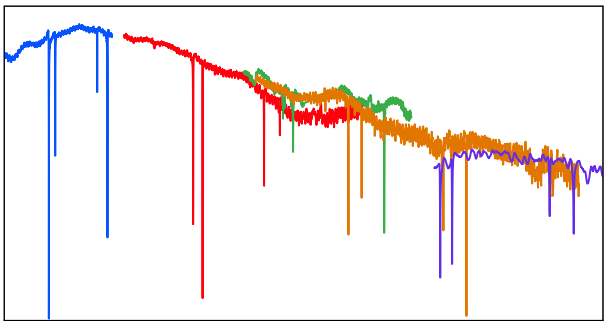

Figure 4.7 – *Single-tone transmission response of five different coplanar waveguide circuits with decreasing TiN thickness. It can be clearly seen how the increase of the kinetic inductance induces a downwards shift of the resonance frequencies. The absolute shift of f_r increases significantly below t=40 nm.*

Even though this seems to be at odds with the usual picture of superconductivity, it can be quite easily understood by stressing the picture of a macroscopic, coherent phenomenon even more. If a superconducting film becomes sufficiently thin, at some point, an external magnetic field penetrates the whole material *homogeneously*. In this scenario, the **superconducting order parameter** shows no local variations, which is equal to a suppression of any screening currents and therefore a vanishing driving force on the *vortices* originating from a previously applied *out-of-plane field*. Several experiments have shown that, in the case of typical type-II superconductors like Nb or TiN, this effect usually takes place for thicknesses below 50 nm [304, 331, 332]. However, at such small dimensions, the influence of confinement on the motion of Cooper pairs is no longer neglectable, leading to a significant increase of the so-called **kinetic inductance** L_k. L_k arises naturally in the Drude model of electrical conduction by considering not only the DC conductivity, but also assuming a long (or infinite for superconductors) relaxation time τ of the charge carriers. In this case, the total inductance of the system does not only depend on geometrical parameters like the **width of the resonator** W or the *resonator-ground separation* S, but also on the change of the Cooper pair condensate **viscosity**. Thus, every adjustment of the film thickness t, which is already the most restrictive dimension, directly influences the *equivalent circuit* of the resonator. The result is a **shift of the resonance frequency** and an **impedance mismatch** which need to be compensated by a corresponding tuning of the other free geometric parameters of the system.

Resonator dimensions				
Parameter	**Resonator 1**	**Resonator 2**	**Resonator 3**	**Resonator 4**
Length L [mm]	2.91	2.84	2.48	2.33
Width W [μm]	10	10	10	10
GND separation S [μm]	15	15	15	15

Table 4.1 – *Overview of the initial resonator dimensions.*

Table 4.1 provides an overview of the initial resonator designs for a TiN film with t=80 nm. In order to determine the *kinetic inductance*, multiple microwave circuits with decreasing thickness have been fabricated and probed by means of *single tone spectroscopy*. The resulting transmission curves

and resonance frequencies are given in Fig.4.7 and Table 4.2, respectively. Here, the influence of L_k on the individual resonators in terms of a shift to lower frequencies is clearly visible. Additionally, comparing the separation between resonators of the same length, shown in Table 4.3, it becomes immediately obvious that the thickness-dependent shift increases significantly below 40 nm.

Resonance frequencies [GHz]				
Thickness	**Resonator 1**	**Resonator 2**	**Resonator 3**	**Resonator 4**
10nm	2.37	2.43	2.78	2.86
20nm	3.58	3.66	4.17	4.30
30nm	4.33	4.41	5.03	5.17
40nm	4.87	4.98	5.67	5.86
80nm	5.64	5.74	6.55	6.75

Table 4.2 – *Summary of the different resonance frequencies.*

Based on those findings, it is now possible to extract L_k by utilizing the general relation between resonance frequency, inductance and capacitance for a coplanar waveguide (CPW) system:

$$f_r = \frac{C_G}{\sqrt{\epsilon^*}} \frac{1}{\lambda_0} = \frac{v_{ph}}{\lambda_0} = \frac{1}{2\pi\sqrt{(L_k + L_G)\, C_G}} \tag{4.14}$$

Here, $\epsilon^* = 11.68$ refers to the **effective permitivitty** of a CPW system on silicon, $v_{ph} = C/\sqrt{\epsilon^*}$ is the

Average thickness-induced frequency shift [GHz]					
Thickness	**Resonator 1**	**Resonator 2**	**Resonator 3**	**Resonator 4**	**Mean**
10nm	1.21	1.23	1.39	1.44	1.32
20nm	0.75	0.76	0.85	0.86	0.80
30nm	0.55	0.57	0.63	0.69	0.61
40nm	0.74	0.76	0.89	0.89	0.83

Table 4.3 – *Overview of the thickness-induced shift of the resonance frequency. The values refer to the absolute difference between the given resonator and the next thicker one.*

phase velocity, C_G is the **capacitance per unit length**, L_G the **geometric inductance per unit length** of the system and λ_0 the wavelength of the fundamental *TEM-Mode* of the resonator. Both C as well as L_G are thereby fully determined by the geometry of the coplanar waveguide resonator and the used substrate. Utilizing **conformal mapping**, one can find for the capacitance

$$C_G = 4\epsilon^* \epsilon_0 \frac{K(k_0)}{K(k_0')}, \tag{4.15}$$

and for the inductance

$$L_G = \frac{\mu_0}{4} \frac{K(k_0')}{K(k_0}, \tag{4.16}$$

with $K(k_0)$ as the **complete elliptic integral of the first kind** with the arguments

$$k_0 = \frac{W}{W + 2S}, \tag{4.17}$$

$$k_0' = \sqrt{1 - k_0^2}. \tag{4.18}$$

$$\tag{4.19}$$

For the resonator dimensions presented in Table 4.1, this gives

$$C_G = 13.67\epsilon_0, \tag{4.20}$$

$$L_G = 0.4639\mu_0, \tag{4.21}$$

$$\tag{4.22}$$

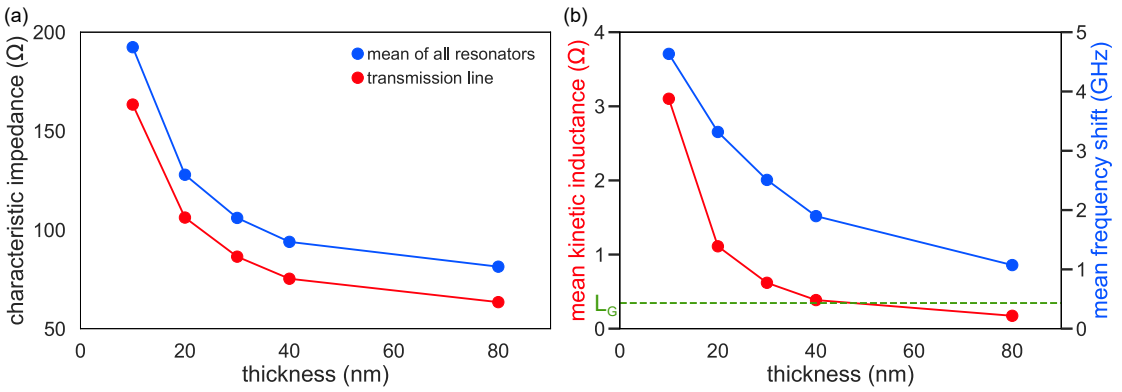

Figure 4.8 – *Overview of the thickness-dependent change of (a) the characteristic impedance Z_0 and (b) the shift of the resonance frequency as well as the kinetic inductance L_k.*

which can then be used to determine the kinetic inductance for the individual resonators

$$L_k = \left(4\pi^2 C_G f_r^2\right)^{-1} - L_G. \tag{4.23}$$

The results for the individual resonators are summarized in Table 4.4. Comparing L_k for the different thicknesses with the result for the purely geometric inductance L_G, it becomes evident that below t=40 nm the whole system is completely dominated by the retarded motion of the Cooper pair condensate and the inductive energy storage capability associated with it. The latter becomes even more prominent when the absolute kinetic inductance is plotted over the film thickness as in Fig. 4.8 (b). Here, the green vertical line marks the constant contribution of the geometric inductance, which becomes almost neglectable due to the almost exponential increase of the kinetic contribution and $L_k(10\,\text{nm}) \approx 7L_G$.

Kinetic inductance per unit length in units of the vacuum permeability [μ_0]					
Thickness	**Resonator 1**	**Resonator 2**	**Resonator 3**	**Resonator 4**	**Mean**
10nm	3.03	3.05	3.05	3.28	3.10
20nm	1.07	1.08	1.09	1.19	1.11
30nm	0.587	0.597	0.606	0.685	0.619
40nm	0364	0.368	0.380	0.430	0.386
80nm	0.155	0.163	0.167	0.209	0.174

Table 4.4 – *Obtained values for the kinetic inductance of the different resonators and thicknesses.*

The significant increase of the inductance has important consequences for the subsequent microwave measurements, as not only the resonance frequency, but also the **characteristic impedance** Z_0 of the line are altered:

$$Z_0 = \sqrt{\frac{R + i\omega L}{i\omega C}} = \sqrt{\frac{R + i\omega\left(L_k + L_G\right)}{i\omega C_G}} \tag{4.24}$$

Here, R refers to the *line resistance*, which can be neglected for superconducting materials that are operated below the critical temperature. As shown in Fig. 4.8 (a) and Table 4.5, Z_0 reaches almost 200 Ω for t=10 nm. In terms of reflection, this is equal to

$$\Gamma = \frac{50\Omega - Z_0}{50\Omega + Z_0} \approx 60\%. \tag{4.25}$$

Consequently, the majority of the signal power would never reach the sample. Additionally, the repeatedly reflected signals can also induce *standing waves* and damage sensitive microwave components like the *cryogenic amplifier*. Therefore, not only the length of the resonators have to be adjusted accordingly. On top of that, also the ratio of **W** and **S** have to be tuned to reduce the geometric inductance. It should be pointed out that the width W of the resonator can usually be changed without

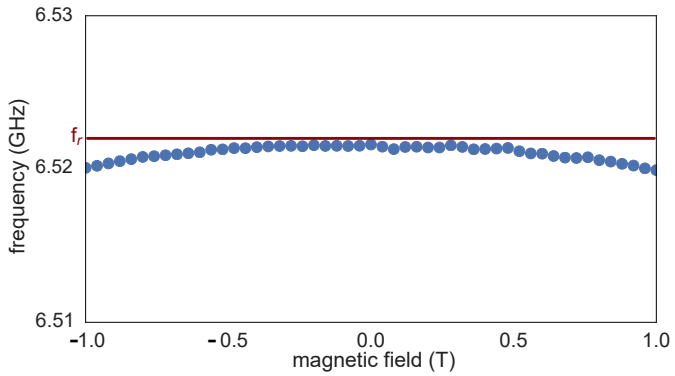

Figure 4.9 – *Flux response of a 30nm thick undercoupled λ/4 resonator with large and small antidots within the resonator and transmission line. The reduced thickness leads to a further stabilization of the vortex lattice, resulting in a much more homogeneous magnetic field dependency of the resonator characteristics.*

the risk of interfering with the *kinetic inductance*, since for the given dimensions the **xy plane** can be considered as *axes of free motion* for the Cooper pair condensate. However, in terms of general device fabrication, small values for S are typically hard to realize due to limitations of the (electron beam) lithography and the resist mask. The width of the resonator W, on the other hand, easier to enhance, but the additional material also increases the chance for losses induced by parasitic two-level systems in the native oxide of the superconductor or by defects in the metal itself. After a series of tests with different resonator dimensions, the set of parameters t=30 nm, W=30 μm and S=8.8 μm has been identified as most suited for our circuit design. The corresponding and adjusted values for the resonator lengths are given in Table 4.6.

Characteristic impedance of the resonators [Ω]					
Thickness	**Resonator 1**	**Resonator 2**	**Resonator 3**	**Resonator 4**	**Mean**
10nm	190.48	190.92	190.95	197.21	192.41
20nm	126.33	126.69	127.21	131.22	127.87
30nm	104.46	104.95	105.39	109.23	106.03
40nm	92.74	92.93	93.60	96.35	93.92
80nm	80.15	80.70	80.94	83.59	81.36

Table 4.5 – *Calculated values for the characteristic impedance Z_0.*

Fig. 4.9 provides an overview of the magnetic field dependent frequency shift of a TiN resonator with the new dimensions. Similar to the measurements shown in Fig. 4.6 (b), the resonance exhibits a gradual shift to lower frequencies. However, in contrast to the circuits with t=80 nm or more, the change happens continuously without any sudden jumps or *plateau-like* features that can be attributed to vortex lattice instabilities. Additionally, the total shift in frequency is now much smaller, with $\Delta f \approx 3MHz$, and also occurs completely reproducible and without any **hysteresis**. This result clearly proves that the carried out adjustments of the film thickness are capable of stabilizing the vortex lattice and, more importantly, significantly suppressing **flux noise**.

Adjusted resonator dimensions				
Parameter	**Resonator 1**	**Resonator 2**	**Resonator 3**	**Resonator 4**
Length L [mm]	2.34	2.22	2.14	2.01

Table 4.6 – *Overview of the changed resonator lenghts for t=30 nm, W=30 μm and S=8.8 μm.*

4.3. HIGH-Q RESONATORS: DESIGN, SURFACE PREPARATION AND FLIP-CHIP BONDING

Over the last couple of years, two different techniques for the fabrication of quantum control circuits have evolved in parallel. The first one aims at the decoupling of the planar superconductor and the substrate by offsetting them in z-direction. This is normally achieved with the so-called **Bosch process**, i.e. an alternating sequence of etching and passivation steps by means of reactive ion etching, which is famous for being well-controlled and the large aspect ratios that can be achieved[333][334]. Based on this approach, it is possible to create coplanar waveguide resonators based on epitaxially grown titanium nitride on silicon with Q factors up to $1{\cdot}10^6$ in the single-photon limit [335]. This is mainly achieved due to the strong suppression of TLS-induced losses at the substrate-air and substrate-superconductor interfaces [336]. However, this process usually uses an Al_2O_3 hard mask, which subsequently has to be removed by a strong etchant. If the etching were to be used as the final fabrication step, it would also damage the nanowire device. However, if the Bosch process would be integrated into the process chain at an earlier stage, the trenches with depths up to 150 μm would render any subsequent lithography impossible due to the accumulation of the liquid photo resist.

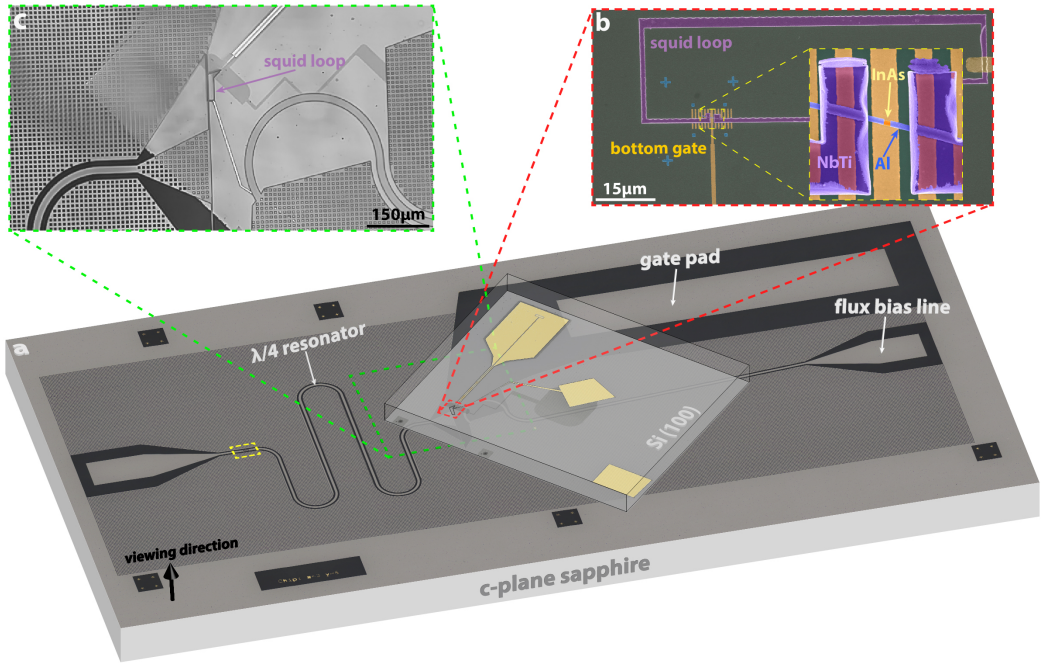

Figure 4.10 – *(a) Optical micrograph of an exemplary microwave circuit with a* 650 μm*-thick sapphire wafer substrate in c-plane orientation. All superconducting structures are made out of 50-nm-thick molecular beam epitaxy grown Nb, which has been patterned by means of dry etching. For the application of the microwave signal, a single* $\lambda/4$ *coplanar waveguide resonator is used, which is capacitively coupled (yellow square) to a short transmission line and an impedance-matched superconducting bonding pad. The electromagnetic tuning of the device is realized with a combination of an on-chip flux bias line and a large bonding pad that acts as the mechanical and electrical connection between the gate electrode on the device chip and the fridge wiring. (b) Scanning electron microscopy image of an in-situ formed InAs/Al nanowire Josephson junction on top of a single bottom gate electrode. The SQUID loop itself and the electrical contacts are made out of 80-nm-thick NbTi. (c) Optical micrograph of a flipped device. The image was taken through the sapphire substrate mounted upon a polymer stamp during alignment. The SQUID loop is aligned such that one side is located above the termination point of the resonator. To ensure a constant and homogeneous reference potential, the device is connected to a large bonding pad that is electrically coupled to the ground plane of the sapphire chip with a conducting epoxy. A modified version of this picture has been already published in [426].*

The second process is more straightforward as it aims at the complete replacement of the defect-contaminated semiconductor substrate by a fully insulating, single crystalline sapphire wafer. Measurements with epitaxially grown aluminium showed easily achievable high power/low power Q factors of $>10{\cdot}10^7$ / $>2{\cdot}10^6$ [337]. However, this approach has two drawbacks: First, due to the fully insulating behavior, every electrostatic control element e.g. gates, leads to the local accumulation of

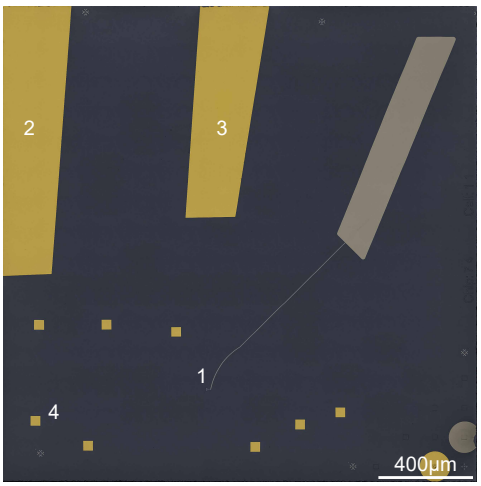

Figure 4.11 – *Optical micrograph of a **device chip** based on highly resistive silicon. (1) corresponds to the gate bonding pad and the lead and electrode associated with it. The the bottom gate has been covered with a 3 nm/15 nm thick dielectric layer of Al_2O_3/HfO_2. (2) and (3) mark the two Ti/Au bonding pads that are subsequently used to glue the **device chip** onto the **circuit chip** by means of Indium or Epoxy. In the same deposition step, small **pillars**, which correspond to the smaller golden squares in (4), are defined. Their intended purpose is to open a small gap in z-direction between both chips in order to protect the nanowire Josephson junction and the associated SQUID loop from electrostatic discharge as well as mechanical damage.*

charges, which results in a significantly increased rate of electrostatic discharge induced device failures. Second, the sapphire substrate prevents the formation of a Si_3N_4 buffer layer, which is one of the main requirements for the growth of single crystalline titanium nitride layers. Both issues can be partially overcome by means of a so-called **Flip-chip** process.

This approach is based on splitting the fabrication process into two independent branches. The actual microwave circuit is shown in Fig. 4.10. In contrast to earlier designs, the substrate was changed to **Sapphire** with an average thickness of 650 μm. Here, the chosen **c-plane** orientation ensures a further minimization of losses due to the smaller **polarity** compared to the other possible crystal orientations. However, the special properties of this material result in a number of obstacles that have to be addressed with an adjusted process chain. First of all is the reduced surface roughness in comparison to silicon and the decreased adhesion of (ebeam) resists and metals associated with it. Thus, the first step prior to any deposition or etching step is a controlled *surface roughening* by means of a pure Ar^+ plasma generated in the so-called *Gigabatch*. By using an additional metal casing, it is possible to shield the substrate from any *ions* which could create *electrically-active defects* like **charge traps**. Instead, only the accelerated, but uncharged *Ar* atoms reach the surface. Due to the reduced efficiency of this modified process, a comparably large power of 600 W has to be applied for a total of 60 s to induce a sufficient substrate roughness for the subsequent fabrication steps. Those are quite straightforward: First, positive Ti/Pt ebeam marks for the *EBL* machines in Jülich and RIKEN are defined by means of *UV6* and e-beam lithography. However, due to the insulating effect of the sapphire substrate, an additional layer of a *charge dissipating agent* has to be applied on top of the actual ebeam resist. Here, the commercially available **ESPACER 300Z**, provided by **Showa Denko**, has been used, as it can be integrated easily into the already existing process chain and, more importantly, removed by means of a brief rinse in DI water prior to the development.

After a careful benchmark of the available superconductors, *MBE-grown Niobium* has been identified and selected as the material of choice due to the combination of high Q factors and a comparably simple patterning process. The deposition of the material is done at ambient temperatures but ultrahigh vacuum conditions, taking into account the oxygen-sensitivity of Nb. For the lithographic definition of the structures, a combination of undiluted **CSAR.9** and the already mentioned E-Spacer is applied on top of the niobium-coated sapphire wafer. Using a **SF6** and *pure-RF*-based dry etching process, all relevant circuit components can be etched in the same step, including large structures like the resonator as well as much finer and complex patterns like the global array of small *flux traps*. The final chip is shown in Fig. 4.10. The system now consists of a single transmission line which is capacitively coupled to a $\lambda/4$-resonator. The exact dimensions of the capacitor are thereby determined at a later stage in order to create an *on-demand* coupling strength for either qubit- or spectroscopy-measurements. Even though this approach significantly limits the number of samples that can be measured simultaneously, it enables a much finer and precisely tailored application of the required electric and magnetic fields. The *flux bias line* is realized via an impedance-matched geometry, ef-

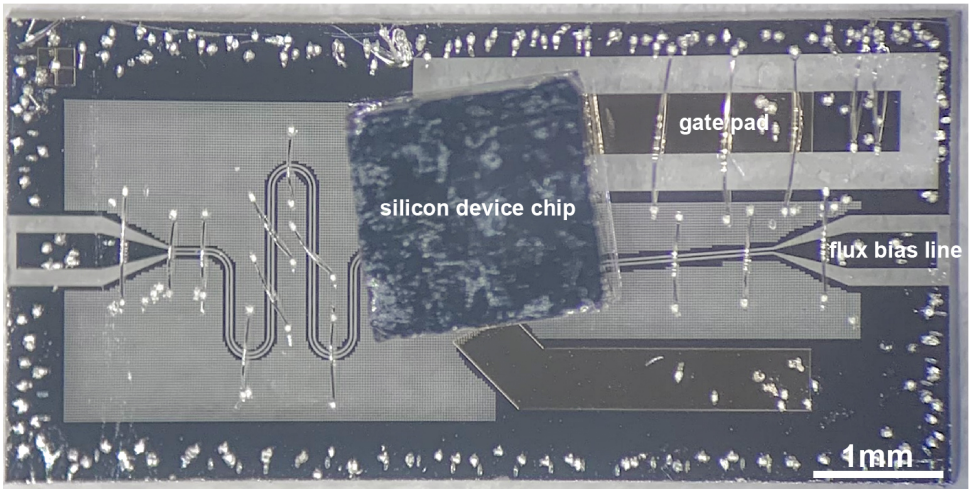

Figure 4.12 – *Optical micrograph of a successfully flipped device chip on top of a Nb-on-sapphire microwave circuit. Indicated are the flux bias line, the $\lambda/4$ resonator for the cavity signal and the gate pad for the application of the pump signal.*

fectively enabling the application of **flux pulses** in the GHz-range. The large, separated pad in the top right part of the chip acts both as a mechanical *anchor* of the bottom gate pad on the *device chip* [see Fig. 4.11] as well as the actual electrical connection between the gate electrode and the *fridge wiring*. The finer substructure corresponds to an array of $(2 \times 2)\,\mu m^2$ flux traps with the purpose to stabilize the vortex lattice that is formed during the magnetic field driven measurements.

The second component of every Flip-chip sample is a **device chip** based on highly resistive silicon, which is shown exemplary in Fig. 4.11. Again, most of the fabrication steps that have been introduced in Chapter 2 remain unchanged or are adjusted only slightly. Worth mentioning here is the coverage with a thin dielectric layer before the deposition of the gate structures and a slightly thicker layer, i.e. 3 nm/25 nm Al_2O_3/HfO_2, after that. Additionally, the latter is not removed by means of a dry etching step despite the induced losses due to parasitic TLS. Instead, it acts as a protective layer between the Nb ground plane on the sapphire substrate and the highly resistive, but not fully insulating silicon chip in order to suppress the formation of short circuits. The gate structures, marked with **(1)**, have been fabricated out of Ti/Pt in order to keep the sample compatible with as many fabrication setups and machines as possible, especially the **Nanocluster**. The layout of the structures follows the same design rule as the bottom gate electrodes used for the conventional Andreev circuits and the first generation of Shapiro chips. The main differences, however, are the two large metal pads, indicated with **(2)** and **(3)**, respectively, consisting of a 600 nm thick stack of Ti/Au as well as the smaller, square-like structures marked with **(4)**. Their purpose is to ensure a proper mechanical and electrical connection between the circuit and device chip by maintaining a small gap in z-direction so that the junction and the SQUID loop associated with it does not touch the surface of the Sapphire substrate. Therefore, both Ti/Au pads are covered with either **Indium** or **epoxy**. The latter has the advantages of low electrical conductivity and large thermal conductance. Subsequently, the device chip is carefully aligned on top of the circuit chip by means of a slightly modified *mask aligner*. A final and successfully flipped sample with a nanowire Josephson junction and its associated SQUID loop is shown in Fig. 4.12.

The typical benchmark routine for a resonator is the analysis of the *single tone response* and its *full width at half maximum* [**FWHM**] in the *transmission-mode*, i.e. in S_{21} direction. By doing so, it is not only possible to extract the **loaded Q factor**, but also to get an idea of the *quality* of the **input** and **output port** as well as losses due to the **substrate-resonator coupling** [338–340]. Non-ideal characteristics of the former two parameters manifest themselves as a pronounced asymmetry between the *pre-* and *post-resonance shape* of the transmission signal. This can also be caused by a misalignment of the fundamental electromagnetic mode (**TEM**) and the (effective) dimensions of the resonator[341–343]. However, in the case of an undercoupled resonator with a large Q factor, e.g. the system shown in Fig. 4.13 (a), this simple approach is not sufficient anymore due to the extremely

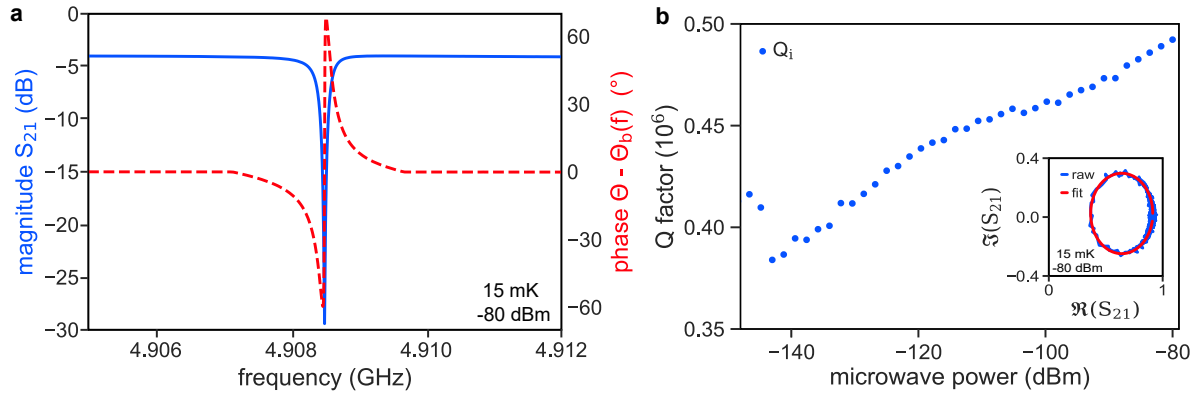

Figure 4.13 – *(a) Response of an **overcoupled** Nb-on-Sapphire resonator with a device chip attached to it in S_{21} transmission configuration. The small FWHM is a strong indication for a high loaded Q factor. More importantly, the line shape is symmetric in the frequency space, which is a prove for a constant input and output coupling, a perfect alignment with the maximum of the fundamental electromagnetic mode [341–343] as well as low substrate-induced losses [338–340].(b) Power-dependent internal quality factors of the very same sapphire-based Flip-Chip sample. Here, the resonator exhibits an internal quality factor of Q_i=0.5× 10^6 in the single photon limit.*

narrow and shallow effect on the transmitted power. In this case, *demodulating* the signal into the **In-phase** [**I**] and **Quadrature** [**Q**] components

$$I = I_0 + A_I \cos(\Theta), \tag{4.26}$$
$$Q = Q_0 + A_Q \cos(\Theta + \delta) \tag{4.27}$$

yields more reliable results. Here, the *magnitude* of **I** describes the **real part** of the output signal, while **Q** is associated with the **imaginary component**. δ corresponds to the phase difference between the two output voltages and I_0 and Q_0 summarize the individual *DC offsets*. A_Q and A_I, account for the unbalanced *gains* of the two channels. For an ideal system, $\delta = \pi/2$, $I_0 = Q_0 = 0$ and $A_Q = A_I = A$. Due to the fact that $\Theta = 0 \ldots 2\pi$, the result is a perfect circle centered around the origin of the *IQ diagram*. However, in the case of a non-ideal system, like an **unbalanced IQ mixer** as depicted in Fig. 4.14, the output traces measured by means of a **phase shifter** form an off-center *ellipsoid-like* shape. If the signal is *mapped* into a new coordinate system with a, b and θ as half the maximum radius, half the minimum radius and the orientation angle, respectively, it is possible to **calibrate** the signal by using the relations between the different IQ parameters:

$$A_I = \sqrt{\left(a^2 \cos^2(\Theta) + b^2 \sin^2(\Theta)\right)}, \tag{4.28}$$
$$A_Q = \sqrt{\left(a^2 \sin^2(\Theta) + b^2 \cos^2(\Theta)\right)}, \tag{4.29}$$
$$\alpha = \arctan\left(\frac{b \sin(\Theta)}{a \cos(\Theta)}\right), \tag{4.30}$$
$$\beta = \pi - \arctan\left(\frac{b \cos(\Theta)}{a \sin(\Theta)}\right), \tag{4.31}$$
$$\delta = \alpha - \beta. \tag{4.32}$$

If the signal of a coupled *transmission line-resonator* system is sufficiently calibrated, it is possible to use the resulting circle to directly extract not only the *loaded Q factor*, but also the *coupling strength of the capacitor* Q_c as well as the *internal quality factor* Q_i. The advantage of this method is the much higher sensitivity with respect to the power transfer between the transmission line and the resonator due to the combined usage of both the **magnitude** as well as the **phase information** of the transmitted signal. Here, a significantly modified version of the *PYTHON*-based framework described in [344] has been used to fit the resonance circle. The changes include several optimizations

II

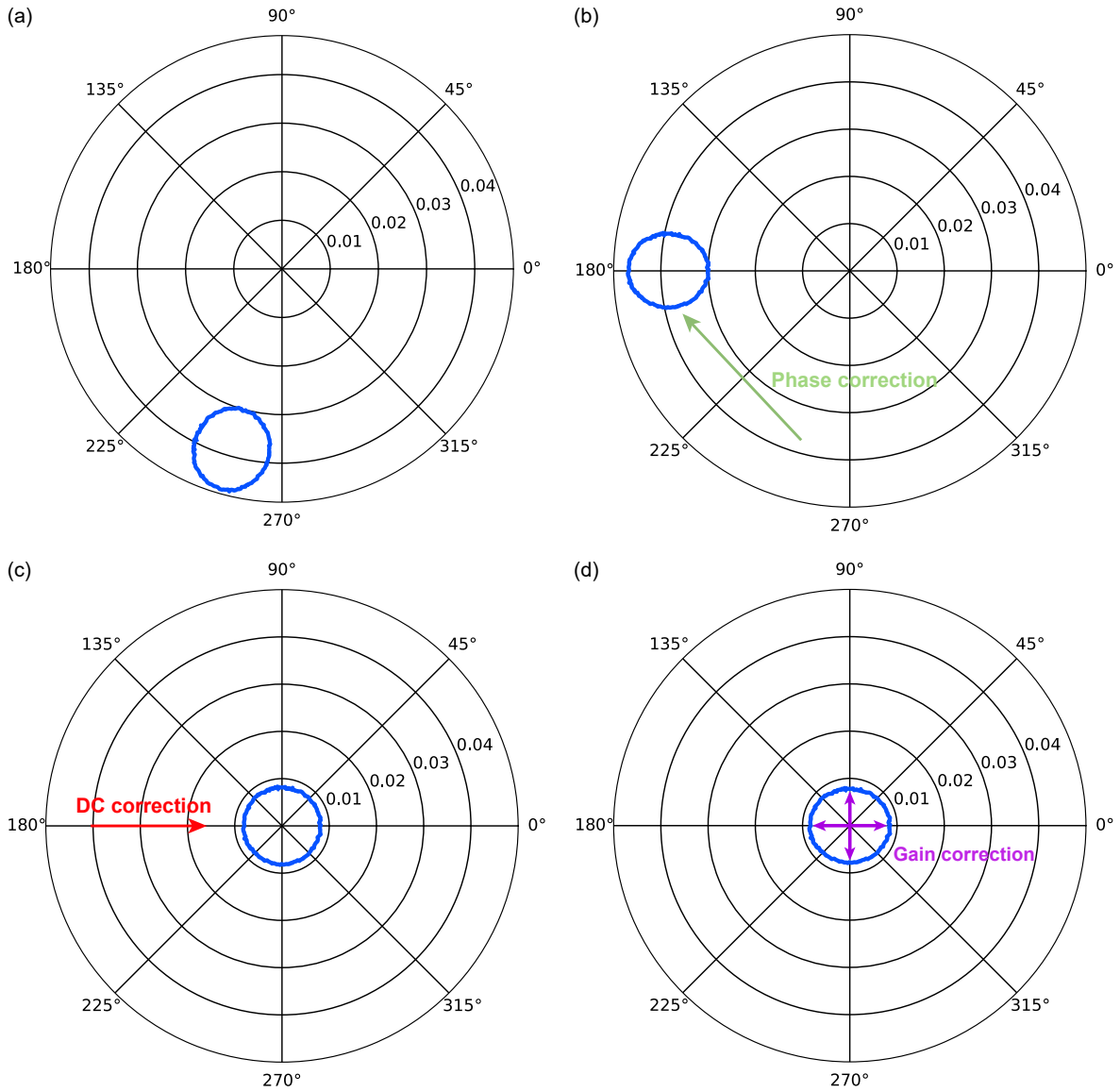

Figure 4.14 – *Exemplary step-by-step overview of the calibration routine for an unbalanced **IQ mixer**. Here, (a) corresponds to the distorted and disturbed response plotted in a so-called **constellation** or **IQ diagram**, while (b) shows the signal after the successful calibration of the **phase** between **I** and **Q**. Subsequently, the **DC offset** is eliminated, which shifts the signal into the center of the chart in (c). Finally, in (d), the **gain** of both components is equalized, which fully restores the circular and symmetric shape signal.*

which, for example, take into account that the resonator is undercoupled and that the additional *RF-capable* Gate and Flux bias lines create some standing waves which manifest themselves as small, additional *ripples* on top of the transmission line signal.

Fig. 4.13 (b) provides an overview of the obtained results for different **input powers** at the sample input port, i.e. by taking into account all attenuations along the fridge wiring. This sets the lowest effective microwave power applied to -160 dBm, which is equal to the single photon limit for the given measurement setup. It can be seen, that for the overcoupled resonator chip ($Q_c \approx 20\times10^3$) the **internal quality factor** Q_i[6] saturates at comparably large values of $\approx 0.5\times10^6$ even within the single photon limit and despite the large coupling strength. Thus, our flip-chip samples situate themselves within the best superconductor-based quantum control circuits that are currently available [9, 335, 337].

[6] Q_i acts as a figure of merit for intrinsic losses caused by defects in the superconductor, parasitic two level systems in the surface oxide or local fluctuations of the capacitance or inductance.

III

EXPERIMENTAL SETUPS AND TECHNIQUES

1

INTRODUCTION

One of the major requirements for the stable and permanent realization of quantum mechanical systems is a strong decoupling from the environment. In condensed matters physics, e.g. solid state systems, this is usually, but not only, achieved by means of low temperatures and the suppression of particle-particle and crystal-particle interactions that is associated with it. The latter is especially important in the case of qubit-like systems based on superconducting microwave circuits that are intended to operate deep within the *single-photon-limit*. Thus, all measurements presented in this Thesis were performed in one of various **cryogenic systems** that have been available. For the *GaAs/InSb* core/shell nanowires, both a ^{4}He bath cryostat as well as a ^{3}He system have been used, which are explained and thoroughly reviewed in great detail in the works of [116] and [235]. In the case of quantum systems based on nanowire Josephson junctions, on the other hand, the electrical and/or spectroscopic device response have been obtained at temperatures T< 20 mK that were achieved by means of *(cryogen-free) dilution refrigerators*.

An image of the most important one, as it served as the platform for the major part of the measurements, is shown in Fig. 1.1. This **BlueFors** system utilizes the principle of **pulse tube refrigeration** to push its minimum bath temperature deep into the sub-Kelvin regime, i.e. down to T≈ 15 mK. One of the major advantages of such a system is the lack of liquid helium in the *secondary section* of the *cooling circuit*. Instead, the required **cooling power** Q_{cl} to drive the system from ambient temperature down to the point at which the *primary part of the cooling circuit* takes over, i.e. when the ^{3}He within the **mixture** starts to circulate between the **still**, **mixing chamber** and **condenser**, is only realized by means of basic thermodynamic principles. By combining a repetitive process of **compression** and **adiabatic expansion**, the system can be cooled down much faster if compared with a classical *wet dilution refrigerator*. However, the downside of the whole approach is the introduction of mechanical vibrations coming from the compressor that is attached to the *pulse tube*, as well as a smaller Q_{cl} due to the lack of the large helium reservoir as a *heat buffer*.

Fig. 1.1 (a) provides a schematic overview of the used cryostat as well as its dimensions. The temperature at the different stages decreases from top to bottom until it reaches its minimum value of T≈ 15 mK in the sample space. During the measurements, the major part of the system is surrounded by an *external μ-metal shield*. The latter, corresponding to the bare metal section in Fig. 1.1 (b), acts an additional decoupling layer with respect to external *electromagnetic perturbations* like the magnetic field of the earth. The upper bit of the fridge contains the major part of the *internal secondary cooling circuit* as well as additional electronic components like **line filter**, **microwave switches**, **cryogenic amplifier**, **circulator**, **DC blocks**, **isolator** and **attenuator**. Examples of the latter two are indicated in Fig. 1.1 (c). One can also see the three metal shields that correspond to the *cryo shield*, *4K plate* and *cold plate*. They do not only act as points of fixed temperature at which the various electronic components can be thermalized into equilibrium, but also as *radiation shields* in order to protect the sample from *thermal photons*. The lower section of Fig. 1.1 (b), however, corresponds to the actual sample area. In the given setup, the cold plate supports three independent **cold finger** and the wiring associated with it, as depicted in Fig. 1.1 (d). Here, the central holder corresponds to the most advanced measurement setup, as it allows not only single- and two-tone spectroscopy, but

III

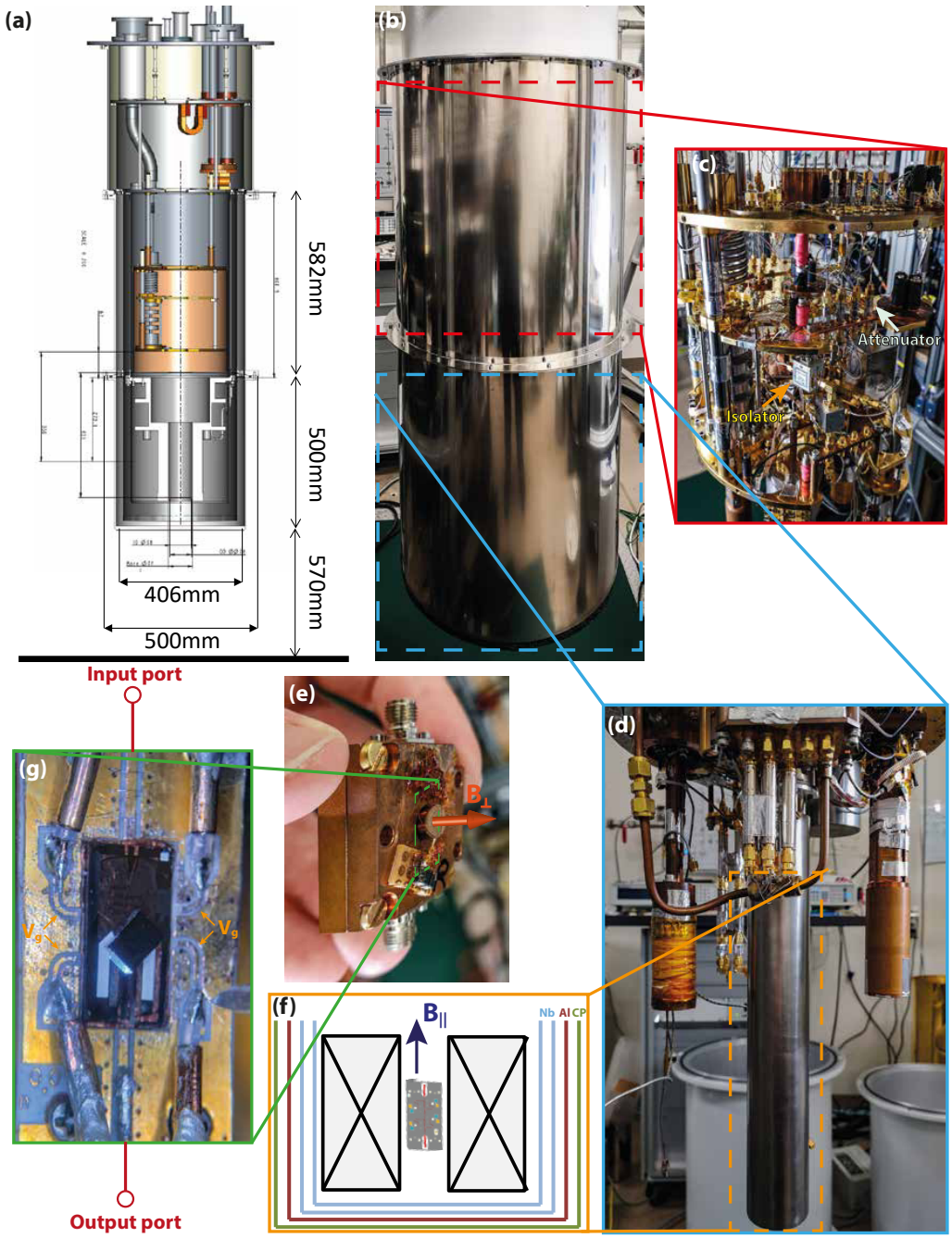

Figure 1.1 – *(a) Schematic depiction of the used cryogen-free dilution refrigerator [**BlueFors**] and its dimensions. (b) Photograph of the same system in the ready-to-measure state. The outer μ-metal shield acts as an additional protection against stray fields from the electrical measurement equipment as well as earths magnetic field. (c) A zoomed-in image of the upper cooling stages and the fridge wiring, consisting out of attenuators, microwave switches, DC blocks, isolators and amplifiers. (d) The actual sample area below the 1 K plate. The system can support three independent microwave chips. However, only the central holder is equipped with both an self-made **NbTi** coil for in-plane fields as well as with additional shielding to sustain fields up to 1.6 T. (e) Zoom-in of a typical sample holder with two microwave ports, three DC ports as well as a small copper coil to induce out-of-plane fields. (f) Schematic depiction of the central holder, consisting out of a large NbTi coil and four layers for magnetic shielding. (g) Optical micrograph of a flip-chip sample mounted on the circuit board of the sample holder. The sapphire chip is connected to the fridge wiring by means of two independent microwave lines, of which one supplies the RF signal to the resonator and the other one acts as a pulse line for the gate.*

also the simultaneous application of an out-of-plane as well as an in-plane magnetic field. The latter is generated by means of a self-made coil consisting out of superconducting NbTi wire with approx. 1000 turns and a **coil constant** of 0.1104 T/A. In the given setup, it is thereby possible to work with fields up to 1.2 T. To protect the field-sensitive microwave components like *circulators* or *microwave*

switches, the whole sample holder is surrounded by a multi-layer magnetic shielding, formed out of self-made niobium and aluminium cylinders. Additionally, both shields are enclosed with a double-layer of commercially available *μ-metal* (**Cryoperm**).

For *InAs*, the required in-plane field to achieve a sufficiently strong Zeeman splitting is typically in the range of 700 mT or above. The magnetic field that controls the flux through the superconducting loop and therefore the phase of the Josephson junction, on the other hand, is significantly smaller. Due to the fact that the measurement range is normally restricted to $\phi = \pm 2\pi$, the out-of-plane field usually does not exceed a few hundred μT. Fig. 1.1 (e) shows a zoom-in of the used sample holder with the small, built-in flux coil. The *cage-like* design ensures a global encapsulation of the sample and suppresses most of the parasitic microwave modes, including resonances from the surrounding cryostat itself or low-energy thermal photons. The connection to the fridge wiring is realized by means of commercially available, 50 Ω-matched **SMA connectors** attached to the upper and lower edge of the *3D cavity*. The three borings on the top facet act as optional feedthroughs for DC or low-frequency AC signals that can be, for example, used to drive the on-chip flux bias line. The actual sample mount is shown in Fig. 1.1 (f). Here, the mechanical connection between the *circuit board* of the sample holder and the actual microwave circuit chip is formed and maintained with *Epoxy*, i.e. a resin consisting out of reactive polymers that combine [**cross-link**] into a sticky layer via *catalytic homopolymerisation*. The main advantage of this solution is based on the most intrigue property of this material, i.e. its outstanding *thermal conductance* that comes hand-in-hand with electrical insulation. Both the *input* as well as the *output port* are realized by means of a hundreds of millimeter wide impedance-matched transmission line made out of Au that, due to its extreme width, does not add a significant *electrical resistance* to the system even at low temperatures. As the earliest design of the microwave chips were build towards sample quantity rather than quality of the individual qubit, every chip required four independent *gate lines* that correspond to the *arc-shaped* metal lines around the two long edges of the chip. Due to the bowing as well as the avoidance of any sharp edges, the lines can also be used to apply **pump signals** up to 25 GHz without the formation of parasitic modes or *standing waves*.

Besides the actual mechanical and electrical realization of the fridge and sample wiring, it is also important which components are used and how they are interconnected. Thus, the following section, provide a more detailed overview about the setup that was used for the two most important measurement routines for qubit-like structures, i.e. **heterodyne manipulation and readout** as well as **pump-probe spectroscopy**.

2

QUBIT MANIPULATION, READOUT AND TWO-TONE SPECTROSCOPY

All fundamental qubit operations, i.e. the **initialization** of a state, the **manipulation** of its evolution in the *time domain*, or its **detection** by means of *dispersive readout* should, idealy, take place on the level of **single photons**. This means that, for the experimental setup, one has to deal with the challenge of coupling a macroscopic *microwave signal* to a meso- or microscopic system and, ultimately, collect and enhance the single or few particle response back up again to a level at which an external *detector* can extract its phase and magnitude information. An exemplary, simplified setup suited for qubit measurements in the **time domain** is shown in Fig. 2.1.

The connection to the electrical environment is realised by means of impedance-matched 50 Ω coaxial cable. To limit the heat and electrical noise transfer into the sample space, a series of -20 dB attenuators and *DC blocks* is embedded into the individual microwave lines. Here, every attenuator dissipates 99% of the incoming signal. Thus, all lines are thermally anchored to the different temperature stages by means of stainless steel wires in order to divert the resulting heat. The latter also improves the signal-to-noise ratio by setting an upper limit to any perturbations coming from the room temperature equipment.

Besides the requirement to push all in- and extrinsic noise sources far below the single photon limit, it is also necessary to detect the emitted particle in a proper way. The latter requires a careful amplification in terms of limiting the corresponding increase of the noise temperature. Following **Friis formula** for the **total noise temperature** T_{tot} (see Ref. [345])

$$T_{tot} = T_1 + \frac{T_2}{G_1} + \frac{T_3}{G_1 + G_2} \tag{2.1}$$

it becomes immediately obvious that the first amplifier with its noise temperature T_1 takes the dominant part in the signal and noise chain, while the contribution of all subsequent amplifiers N_i is reduced by their **gain** G_i. Thus, in most of the measurements a so-called *Josephson parametric amplifier* **JPA** [346, 347] mounted close to the sample space was used due to its small bandwidth and excellent signal-to-noise ratio. At higher temperature stages, additionally *high-electron mobility transistor* **HEMT** amplifier (see Refs. [348–350]) with G≈40 dB ensure a further increase of the signal. In order to protect the amplifiers and decouple the output line from the input line and the microwave sources, two *circulators* are installed between the sample and the subsequent electronic components.

For the **time domain measurements**, including *Rabi cycles* and *Ramsey fringes*, a **heterodyne** approach with **single sideband mixing** has been chosen [351–353]. The setup consists of two digital-analog-converters **DACs** that create the **I** and **Q** component of the microwave signals with frequencies in the range of 30-50 MHz. In order to reach the required resonator frequencies and transition energies of the qubit, the latter is *up-converted* by means of a second microwave source in the GHz range thus that

$$\omega_{DAC_1} + \omega_{source} = \omega_r \tag{2.2}$$

$$\omega_{DAC_2} + \omega_{source} = \omega_q. \tag{2.3}$$

Dispersive readout is the state-of-the-art and least interfering method to probe a qubit [354]. In case of the used measurement approach, the state of the qubit is encoded in the phase and magnitude of the up-mixed and frequency-shifted resonator signal ω_r. Due to (mostly) technical limitations in terms of the sampling rate of the *Digitizer*, the subsequent analysis has to be performed on the **demodulated baseband signal**. The required down-conversion of the HF signal is thereby done with exactly the same microwave source as the up-mixing. Here, in order to suppress phase instabilities or signal drifts, all devices are continuously synchronised by means of a 10 MHz reference clock. Finally, after an additional filtering, amplification and digitalisation, the obtained two quadratures of the signal are *fourier-transformed*. The result are the **complex scattering parameter** that can be directly translated into the state of the qubit.

One of the main advantages of this method is the comparably low disturbance of the qubit system during its free state evolution. The large detuning of ω_r and ω_r act as a filter for parasitic photon transfer and power leakage into the sample. In addition, it is possible to probe multiple resonators and qubits with the same microwave source. More details about the measurements as well as exemplary results are provided in Chapter V .

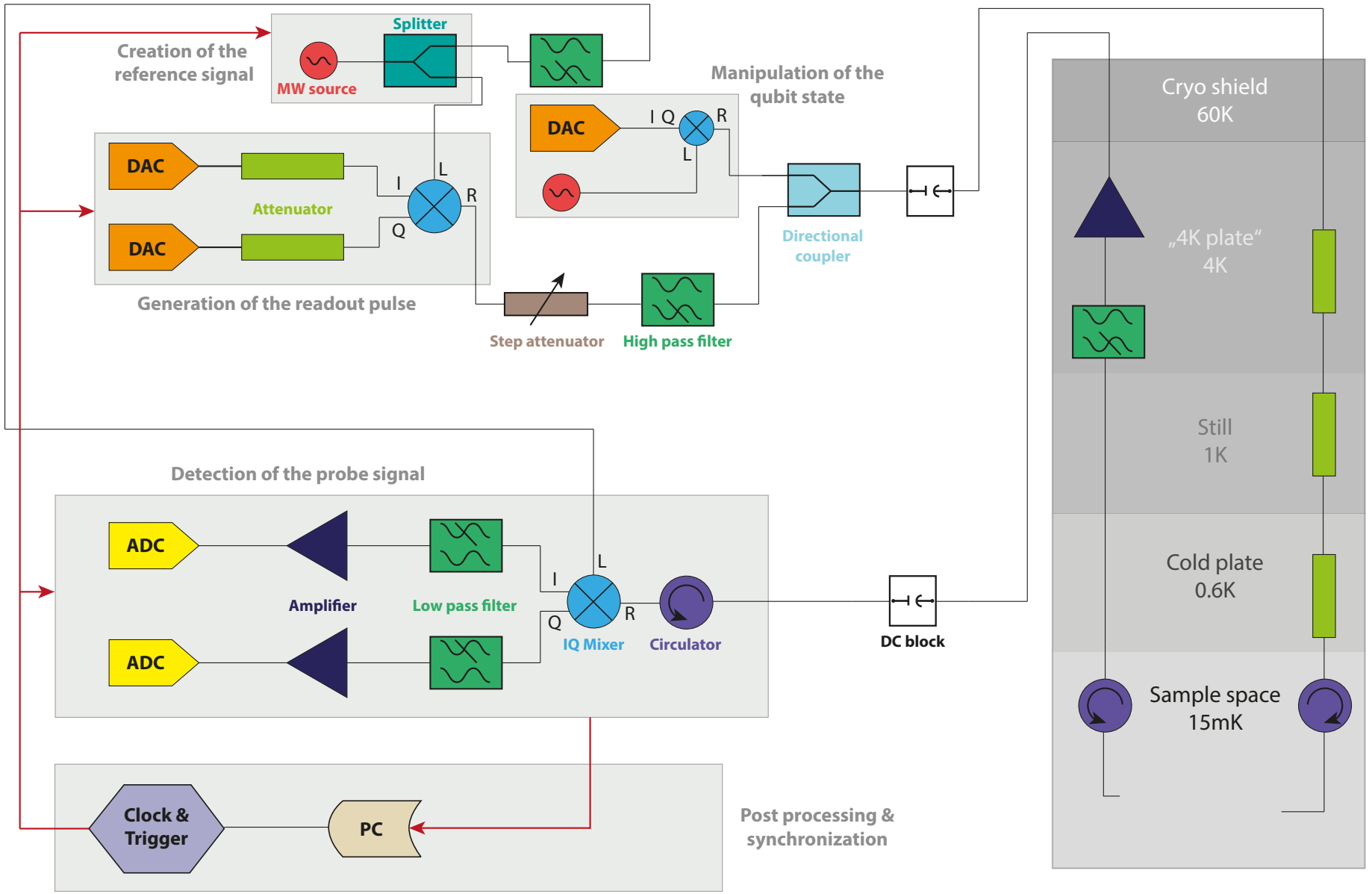

Figure 2.1 – *Exemplary measurement setup for the manipulation and subsequent dispersive readout of a single qubit system embedded in a microwave cavity.*

IV

MESOSCOPIC NANOWIRE JOSEPHSON JUNCTIONS

1

INTRODUCTION

The performance of nanowire-based Josephson junctions depends to a large extent on the properties of the superconductor-semiconductor interface. In most cases, the superconductor is deposited after the growth of the nanowire and its removal from the ultrahigh vacuum chamber. Due to the subsequently formed oxide, which would render the formation of ohmic contacts impossible, a thorough cleaning procedure of the surface has to be performed. In the past, various approaches have been used to reveal the bare semiconductor surface again, ranging from *sulfur passivation* , chemical etching by means of a brief *HF dip* or the purely physical oxide removal with an Ar^+ sputtering process[355]. The structures prepared using these methods are schematically and exemplary shown in Fig. 1.1 (a) and (b), respectively, and have been investigated to a broad extent. They already have proven their capability to act as building blocks for *Josephson quantum electron pumps* [356] or, due to the excellent **gate tunability** of the supercurrent [357, 358], as *Josephson field effect transistors* [359] and *nano-SQUIDs* [81, 82]. However, their ex-situ fabrication leads to the same **non-ideal interface** for all of them. This restricts transport to the regime in which the dissipation-less charge carrier flow is carried by many Andreev bound states with low transparency. Even though the latter would be theoretically sufficient to realize more advanced structures that just rely on the *magnitude of the supercurrent* and its properties, like the **Transmon qubit**, the usual large performance deviations between different devices render any practical realization extremely challenging.

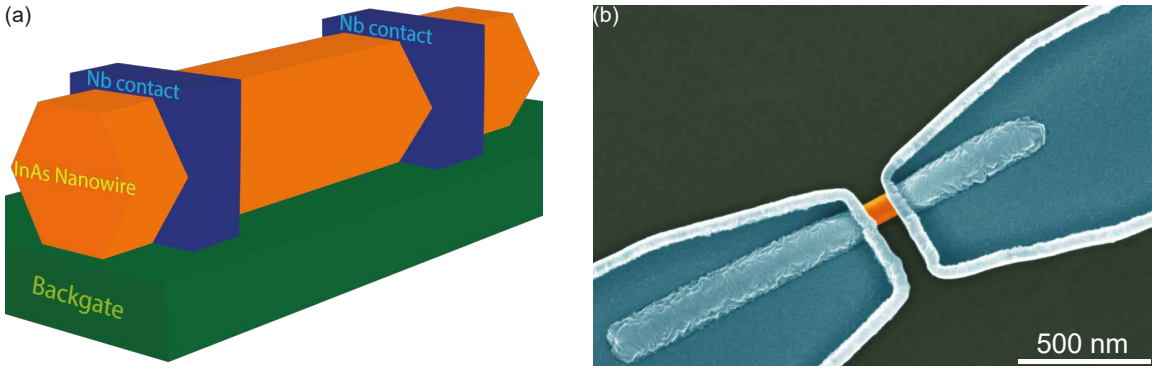

Figure 1.1 – *(a) Schematic overview of an ex-situ prepared nanowire Josephson junction on top of a Si/SiO_2 backgate. Prior to the deposition of the Nb contacts, the nanowire is exposed to an extensive Ar^+ sputtering in order to remove the native oxide. (b) False-colored SEM micrograph of an as-prepared nanowire device. Here, the most remarkable feature is the bright edge around the superconductor structures which are sidewalls caused by the resist-based contact definition and subsequent liftoff-procedure. Additionally, the Nb on top of the nanowire appears much more granular than the one covering the SiO_2 surface. Due to the fact that such a change of the Nb morphology is not observed for in-situ prepared InAs/Nb junctions, the likely assumption is that this is caused by an enhanced roughness of the InAs surface due to the Ar^+ treatment.*

In order to circumvent this problem, major efforts were undertaken to deposit the superconductor in-situ, i.e. without breaking the vacuum after the growth of the nanowires [31, 33, 44, 360]. Another crucial issue is the length of the weak link junction, since it determines the number of Andreev levels involved in the Josephson supercurrent. The conventional method to define a junction in an

IV

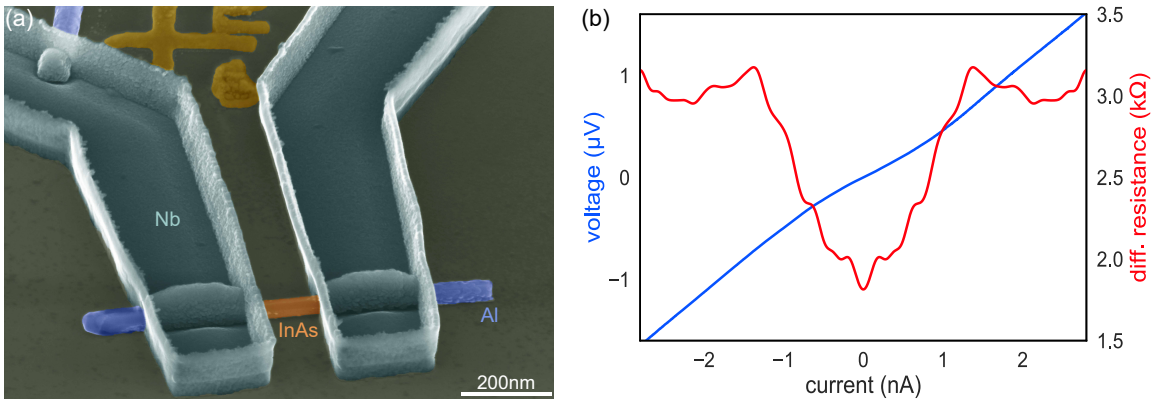

Figure 1.2 – *(a) False-colored SEM micrograph of a first generation InAs nanowire with an in-situ deposited Al shell. The latter clearly shows a non-ideal morphology which rather looks like a chain of droplet-like structures that have been grown together than a smooth and homogeneous metal film. The comparably long InAs weak link is caused by the diffusion-limited nature of the TMAH etch. (b) The corresponding IV characteristic of the presented junction for a backgate voltage of $V_g = 5$ V. The presence of multiple subgap features, caused by multiple Andreev reflections, clearly prove a comparably large (and much better as compared with ex-situ junctions) transparency of the superconductor-semiconductor interface. However, the lack of a clear and pronounced supercurrent branch still renders those devices useless for more advanced structures like Transmons. Due to the fact that later, more optimized devices showed dissipation-less IV sections even for channel lengths $L > 3\xi$, there is strong evidence that the observed issue is caused by the Al itself rather than by the long weak link.*

in-situ deposited superconducting shell wire has been a combination electron beam lithography and wet chemical etching [361]. In the case of Al, those methods rely on **TMAH**-based solutions like the *metal-ion free* [**MIF**] developer *MICROPOSIT MFCD-26*. The latter is classified as *highly toxic* [**GHS06**] and the underlying mechanism for the removal of the Al atoms is **diffusion-limited**. This means that the etching speed is determined by the relatively slow transport of the reactive component on the surface, i.e. in between *adsorption* and the occurrence of the actual *chemical reaction*. Those processes are usually extremely sensitive to local variations of the etchant concentration caused by a highly structurized environment, e.g. metal contacts in close proximity to the area that is supposed to be etched. While the latter can be improved by just performing the etching of the weak link as the first processing step, the chemical reaction itself can interfere with the etching process, too:

$$2\mathrm{Al} + 2\mathrm{OH}^- + 6\mathrm{H_2O} \longrightarrow 2\,[\mathrm{Al(OH)_4}] + 3\mathrm{H_2}. \tag{1.1}$$

The gaseous byproduct H_2 can form *bubbles* in the weak link area and effectively block the liquid etchant from reaching the Al surface. Hence, it is observed that stirring the liquid during the etching process tends to stabilize the etching rate, since a change of the concentration gradient and therefore a flow of molecules is introduced to wash away the bubbles. An even better approach is the repetitive removal of the sample from the etching medium. Here, an etching-removal-etching sequence of 6 s-4 s-6 s has proven to lead to the best results.[1]

Despite the previously described possibilities to optimize the process, the mainly isotropic nature of chemical etches puts constraints on the shortest attainable junction length L, which is clearly visible in Fig. 1.1 (a). Here, $L \approx 160$ nm, which would be already above the **coherence length** ξ of bulk Al even for *perfect transparency* [363]. For thin films, on the other hand, ξ is supposed to be even smaller [364]. This results in an **imperfect proximization** of the weak link, effectively creating a superconducting channel that is extremely sensitive to perturbations like *thermal* or *phase fluctuations*. For the junction shown in Fig. 1.2 (a), for example, there is no clear **zero-voltage state**. Instead, the system behaves like a parallel circuit of a Josephson junction and a parasitic resistive component, also known as **intrinsically shunted** junction behavior. Thus, even though there are clear signatures of *subharmonic gap structures*, those kind of junction is insufficient to act as a platform for more advanced structures like *Qubits*. Together with an optimization of the Al film *smoothness*, other techniques for the creation of weak links have been investigated. For wet chemical etching, the *state-of-*

[1] Further details are provided in the Master theses of Arthur Leis [41] and Naveen Shetty [362].

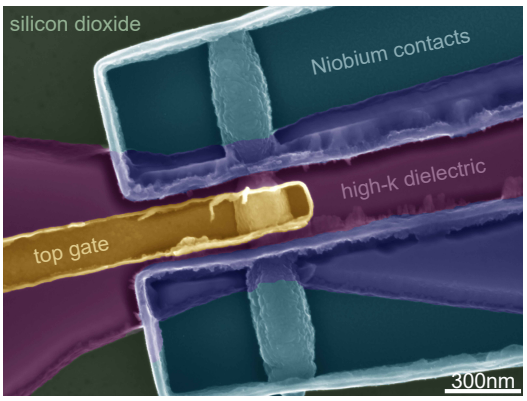

Figure 1.3 – *False-colored SEM micrograph of a second generation InAs nanowire with an in-situ deposited Al shell that has been grown at T=-6°C [33]. The reduced temperature limits the diffusion of metal atoms during the deposition and therefore suppresses the formation of droplets in favor of a more homogeneous Al distribution. The reduced roughness also made it possible to etch a much shorter channel and, more importantly, to cover the whole device with a 100 nm thick $LaLuO_3$ film (purple) in order to realize a local Ti/Au top-gate (yellow) in between the two Nb contacts (blue).*

the-art approach is the usage of **Transene-D**. Here, the etching rate depends only on the temperature and is also much less isotropic. However, even though Transene-D provides selective etching with respect to most of the silicon-based materials, e.g. SiO_2 or Si_3N_4, it affects *transition metals* like *Hf* or *La* which are typical components of **high-k dielectrics**, too. This, and the fact that it also degrades the surface of the nanowire makes the etching time rather critical. For all devices presented in the following chapters, a constant temperature of 50 °C has been used, which results in an etching rate of 0.83 nm/s. The latter is thereby enhanced by *capillary effects* due to the small mask size of only 30 nm. The obtained weak links exhibit extremely steep edges and a comparably small *lateral broadening*, with typical channel lengths of $d = 70 - 90$ nm. The precise temperature-based control of the

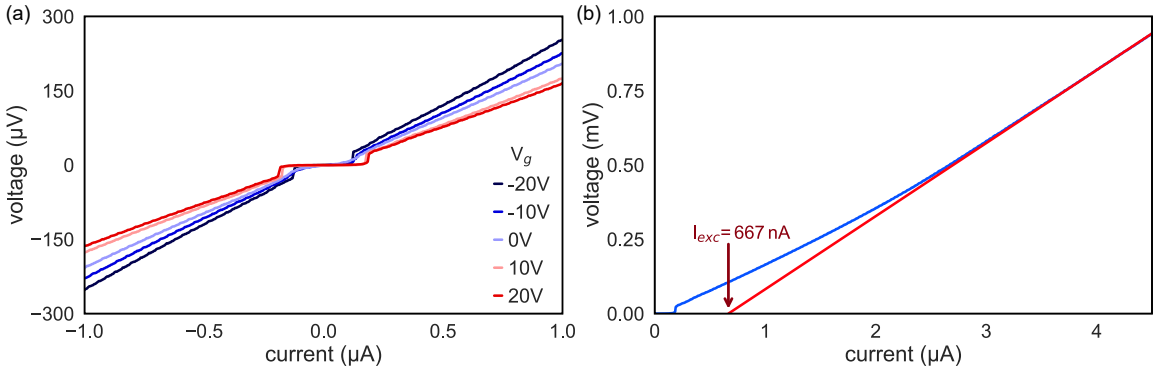

Figure 1.4 – *(a) Current-driven device response of a nanowire Josephson junction similar to the one shown in Fig. 1.3. The device exhibits a clear and pronounced supercurrent for all applied gate voltages. (b) Extraction of the excess current by means of the linear extrapolation of the dissipative, i.e. ohmic, section of the IV curve. The obtained value can be subsequently used to get an estimation of the **OBTK** interface transparency T.*

etching behavior also allows for the intentional formation of longer junctions, which is exemplary shown in Fig. 1.3. Here, the combination of a global back-gate and a local top-gate enables tuning of the lower and upper half of the nanowire almost independently, which could be utilized to perform experiments regarding the *radial quantization* of states. In contrast to the junction shown in Fig. 1.2, the presented device exhibits a pronounced and gate-tunable **zero-voltage state** [see Fig. 1.4(a)], with a critical current of $I_c \approx 200$ nA. However, the relative change of the supercurrent is rather small despite the large gate length. With only 10% difference between the highest and lowest gate voltage, the corresponding change in the *kinetic inductance* would be way below the requirements for the reliable operation of a *Transmon qubit*. Additionally, even though the associated *excess current* in Fig. 1.4(b) is comparably large, with $I_{exc} = 667$ nA, the coupling between the semiconductor and the superconductor is still imperfect. Utilizing the framework of the corrected Octavio–Tinkham–Blonder–Klapwijk theory [164, 365] [**OBTK**], one obtains a barrier strength parameter $Z = 0.83$ and a corresponding contact transparency of only $\mathcal{T} = 0.6$ [365, 366]. Here, the comparably rough and granular morphology of the Al shell has been identified as the main cause for such a small value. Thus, the following two sections are devoted to the further optimization and characterization of all

three aspects that are crucial for the realization and performance of mesoscopic nanowire Josephson junctions: The carrier concentration and crystallographic quality of the semiconductor nanowire itself, the smoothness and stickiness of the superconducting shell and the formation of the actual weak link that determines its length and homogeneity.

2

TOWARDS HIGHLY TRANSPARENT NANOWIRE JOSEPHSON JUNCTIONS

All Josephson junctions rely on the same physical foundation, i.e. the presence of the **Cooper pair condensate** as a *macroscopic* quantum state. Here, the dissipationless supercurrent arises from the coherent tunneling of Cooper pairs between two superconducting electrodes, driven by the *phase difference* δ. In contrast to other quantum systems, e.g. two positions of a *single particle wavefunction*, δ is a **collective** and **distributed** variable that is directly coupled to macroscopic **electric quantities** of the system. In tunnel juntions with large spatial extensions, like the ones used for the experimental confirmation of the **Josephson equations**, the phase can be considered as a *quasi-static* parameter due to the *damping effect* of the large capacitance associated with it. Here, the large *time constant* suppresses sudden changes of the **voltage** $V \propto \frac{\partial \delta}{\partial t}$, which stabilizes the system with respect to *thermal* and *quantum fluctuations*. However, with the on-going miniaturization and the usage of **mesoscopic** systems in the nanometer-range, e.g. nanowires, molecular break junctions or 2D systems made out of graphene, this simplistic picture starts to fail.

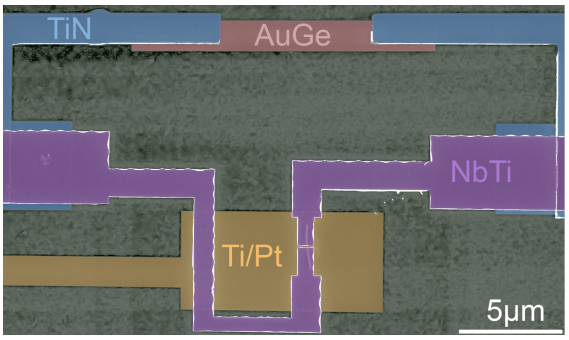

Figure 2.1 – *False-colored SEM micrograph of an exemplary extrinsically shunted nanowire Josephson junction on a so-called **Shapiro chip**. The 10 nm thick AuGe shunt resistor acts as a quasiparticle and noise filter and transforms the sudden and stochastic switching event into the voltage state. The contacts to the nanowire are realized by means of 80 nm NbTi. For the electrostatic tuning, a large bottom gate pad covered with Si_3N_4 is used.*

If one assumes a nanowire Josephson junction, the **phase dynamics** are not longer purely determined by the *SNS stack* itself. Instead, the superconducting leads and the *circuit environment*, modeled as a **admittance** $Y(\omega)$, start to influence the electromagnetic properties of the device. Thus, δ is not a simple parameter anymore but rather a combination of all *phase fluctuation contributions* [136, 140]

$$\sqrt{\langle \delta^2 \rangle} \propto \frac{Z_s(\omega)}{R_K \left(1 + e^{-\hbar\omega / k_b T}\right)} \tag{2.1}$$

Here, R_K corresponds to the *von-Klitzing constant*, T is the *electron temperature* and $Z_s(\omega)$ is the *total impedance*. The latter is thereby determined by the *junction inductance* L_0, the *junction capacitance* C_0 and the admittance of the *external circuit*. In the case of a small junction, L_0 and C_0 are small, too, and $Z_s(\omega)$ is dominated by the external circuit $Y(\omega)$. Such a scenario is usually associated with large phase fluctuations, which ultimately lead to a *stochastic behavior* of the corresponding supercurrent:

$$I(\omega) = \langle I_0 \rangle = I_0 \langle \sin(\delta) \rangle, \tag{2.2}$$

e.g. a widely spread distribution of the switching current or the occurrence of a hysteresis in the zero-voltage state. The latter is especially important in the case of large supercurrents, for which the actual *electron temperature* deviates significantly from the *bath temperature* due to **overheating** effects [367].

The most simple way to limit both *phase noise* as well as *phase diffusion* is the implementation of an **on-chip shunt resistor** in close proximity to the nanowire Josephson junctions [140, 368]. An exemplary realization based on a 1st generation *Shapiro circuit* [see Sec. 3.1] is shown in Fig. 2.1. Here, the Josephson junction is formed by an InAs/Al half-shell nanowire on top of a *global* bottom gate electrode that is electrically connected to the surrounding TiN circuit by means of NbTi contacts. The shunt resistor consists of a 10 nm thick, 1 μm wide and 7 μm long **AuGe stripe** with a resistance of $R_{shunt} = 80 - 140\,\Omega$. The comparably large spreading is mainly caused by thickness fluctuations and *grains* in the metal film and enforces a thorough determination of its precise value for every individual sample. This is especially important as now not only the current is split between the junction and the resistor, but the former also defines the absolute *voltage scale* of the **IV characteristics**. The following section is therefore devoted to the introduction of the general *calibration technique* for such a parallel circuit and to provide an overview of the effectiveness of a novel **doping** technique for InAs wires based on *Tellurium*.

2.1. INFLUENCE OF DOPING ON THE JUNCTION PERFORMANCE

All presented samples within this Thesis can be divided into two different categories: On one hand, there are the nanowire Josephson junctions that are supposed to act as the inductive element in *Transmon circuits* or as a detector wire in *SQUID structures*. Here, a gate tunable but **sinusoidal** current-phase-relation is desired without any *stochastic effects* or pronounced *fluctuations* of the supercurrent that could form an unpredictable potential landscape. The most straightforward way to achieve this condition is an increase of the junction length in order to flatten the dispersion relation of the Andreev bound states and an increase of the nanowire carrier concentration. Both methods push the device into the *many channel limit*. On the other hand, there are qubit-like structures in which the phenomena of interest take place on the level of individual states. The typical operation point of those *mesoscopic* devices usually resides close to the tunnel- or Coulomb blockade regime. Thus, short junctions with a low number of conducting channels in the semiconductor are desirable so that it is possible to push the device into *pinch-off*.

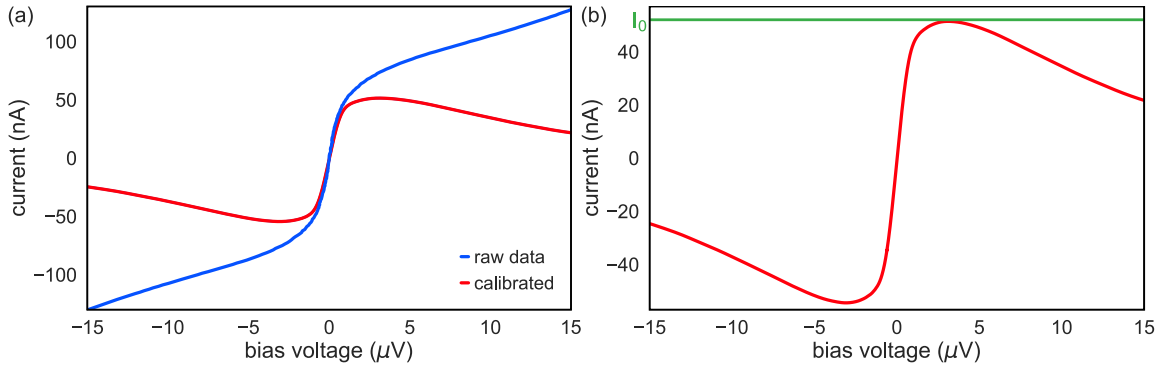

Figure 2.2 – *Exemplary IV characteristics of an extrinsically shunted nanowire Josephson junction. (a) Comparison between the raw and calibrated current trace. (b) Zoom-in of the corrected device response. The green line indicates the maximum supercurrent, i.e. the critical current of the nanowire Josephson junction. Image taken from [369].*

Although both requirements are somewhat contradictory, there is a common solution in terms of a controlled **doping** of the semiconductor nanowire. For InAs, the usual dopants of choice are *silicon atoms*. However, several experiments could already show that the incorporation of silicon leads to a degradation of the crystal structure caused by the large size of the donor atoms [370–373]. Additionally, is has been shown that Si atoms in GaAs nanowires exhibit **amphoteric behavior**. Thus, they can act as acceptors on anion lattice sites or donors on cation lattice sites, depending on the actual growth conditions and the orientation of the nanowire facets. In order to circumvent those issues and increase the overall quality of the nanowires for this project, **Tellurium** has been used as the dopant material, due to its smaller atom size and much lower *ionization energy*. The latter ensures a pure donor-behavior and (theoretically) a much higher doping level if compared with silicon [374, 375]. Even though it has already been proven that Te-doped InAs wires indeed show smaller perturbations of the crystal lattice even at high doping levels [376], low temperature electrical measurements are still missing. Here, the most important question is the correlation between the room temperature carrier concentration and the magnitude of the **real junction current**.

The following measurements have been performed in a ^{3}He/^{4}He dilution refrigerator with a base temperature of 15 mK, equipped with two independent superconducting magnet coils [in the future referred to as **Vector fridge**]. The IV traces have been measured using a current bias supplied from a battery-powered current source ["**Delft-Box**"] and a battery-powered differential voltage amplifier. All measurement lines within the refrigerator are heavily filtered, using low-temperature copper powder filters, custom low pass filters in addition to room temperature π-filters in order to limit *external noise sources*. For the junctions, three different nanowire growth runs have been used: Samples of type **A** with no intentional doping [referred to as **undoped**, n$\approx 1\times10^{17}\,$cm^{-3}], type **B** with n$\approx 1\times10^{18}\,$cm^{-3} [**intermediate doping**] and type **C** with n$\approx 1\times10^{19}\,$cm^{-3} [**high doping**] [1]. The super-

[1] Further details about the nanowire growth are given in Chapter 1 and in the theses of Nicolas Güsken [32] and Pujitha

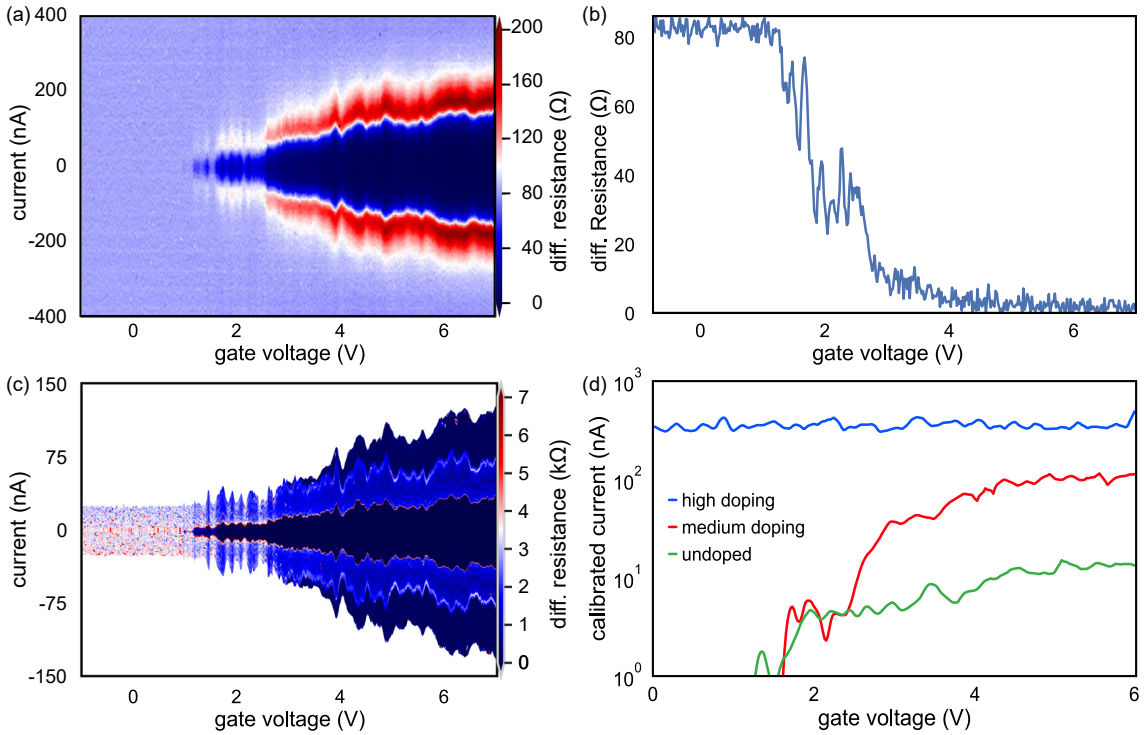

Figure 2.3 – *Exemplary calibration procedure and comparison of multiple nanowires with different Te doping levels. (a) Uncalibrated Gate- and current-dependent differential conductance map. For gate voltages below $V_g = 1\,V$, the nanowire is pinched-off and the current only flows through the normal conducting shunt resistor. For voltages above this value and up to $V_g = 2.5\,V$, the system exhibits pronounced Coulomb diamonds as a signature of tunnel-limited transport through the nanowire. If the gate voltage is increased even more, the nanowire starts to host a dissipationless supercurrent. (b) Extracted zero-current differential resistance trace, clearly showing the transition from shunt-dominated to junction-dominated transport. For the determination of the shunt resistance, the median value of the gate voltage range $V_g = 0\,V$ to $V_g = 1.7\,V$, i.e. $\tilde{R} = R_s = 82.7\,\Omega$, is calculated. (c) The same differential conductance map as in (a) after the calibration with the shunt resistance obtained in (b). (d) Extracted calibrated current traces for three InAs nanowires with different Te-doping concentrations. Data taken from [369].*

conducting contacts have been fabricated by means of Ar^+ sputtering and the subsequent deposition of 90 nm NbTi.

"In order to limit the influence of the electromagnetic environment on the junction performance, all devices have been measured in parallel to an *on-chip shunt resistor* as shown in Fig. 2.1. Fig. 2.2 (a) provides an overview of an exemplary IVC for a sample of type *B*. Here, the blue curve corresponds to the as-measured junction response. Due to the normal conducting shunt resistor, the switch between zero voltage state and dissipative transport no longer happens abruptly. Instead, there is a smooth and continuous transition between both branches, effectively providing experimental access to the full voltage range. After the subtraction of the shunt resistance, the remaining trace exhibits the typical decrease of the current above a critical value, which is a clear signature for the suppression of the *Cooper pair* driven transport. By extracting the turning point of the *supercurrent peak*, as shown in Fig. 2.2 (b), it is possible to obtain the **critical current** I_0.

An example for a quantitative and full calibration procedure is given in Fig. 2.3: First, the gate dependency of the supercurrent is investigated in order to measure the shunt resistor independently. Thus, the nanowire has to be pushed into *pinch-off*. Now, by applying a linear fit within the range of the supercurrent branch to every individual IVC, it is possible to obtain the combined resistance of the parallel circuit. For gate voltages $V_g = 1\,V$ and below [see Fig. 2.3 (a)], the latter becomes equal to the normal conducting shunt resistance. In order to limit the influence of noise and measurement uncertainties, the whole saturation region in Fig. 2.3 (b) is used to calculate a median value of $R_s = 82.7\,\Omega$. The contribution of the normal conducting shunt resistor, which acts as an additive and

Perla [39]

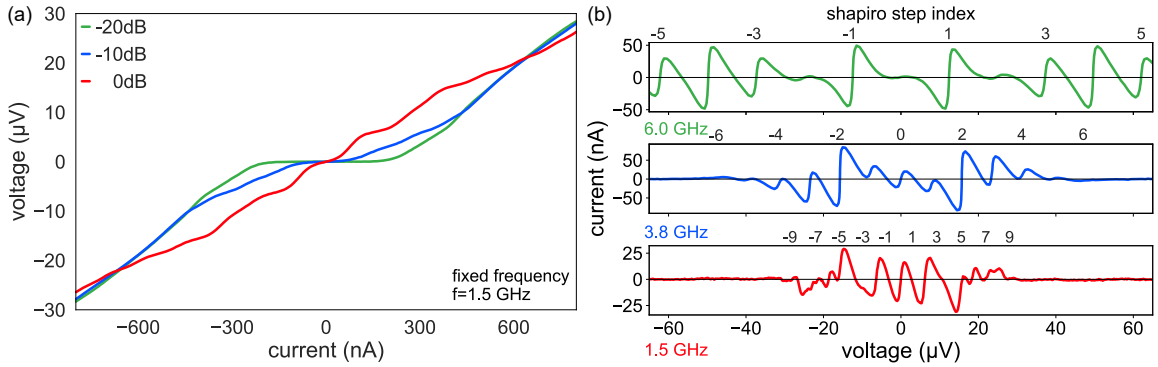

Figure 2.4 – *Shapiro response of an exemplary InAs nanowire Josephson junction with intermediate doping concentration. (a) IV traces at a constant microwave frequency of f=1.5 GHz and an input power of 0 dB, -10 dB and -20 dB. For low power levels, the junction almost mimics the response of an unperturbed system. However, if the AC contribution is increased, the system starts to exhibit pronounced and periodic constant-voltage-plateaus, i.e.* ***Shapiro steps****. (b) Shapiro spikes of the same junction after subtraction of a linear fit and for a constant microwave power of 0 dB. For small frequencies, the device response consists of a comparably dense and less distinct series of peaks. If the frequency is increased, the spikes become increasingly separated in voltage, clearly showing the frequency-voltage relation of the AC Josephson effect. Data taken from [369].*

linear perturbation, can then be removed by a *point-wise* extraction of the junction resistance and calibration of the measured voltage

$$R_j = \frac{V_{\text{meas}} R_s}{I_{\text{signal}} R_s - V_{\text{meas}}}, \tag{2.3}$$

$$I_j = \frac{V_{\text{meas}}}{R_j}, \tag{2.4}$$

with I_{signal} as the externally applied current. "[2]

Fig. 2.3 (c) shows the device response as measured in (a), but in dependency of the calibrated current and taking only the resistive contribution of the junction into account. The seemingly weird resistance distribution can thereby interpreted as follows: The inner dark blue area corresponds to the section of the supercurrent peak in Fig. 2.2 (b) that does not overlap with the dissipative branch, the light blue area marks the superposition of both and the upper dark blue area is the section close to the turning point of the IVC. The outer borders of the data map therefore directly translate into the maximum current the junction can sustain, i.e. the critical current I_0. However, it should be pointed out that, for an ideal determination of R_s and subsequent calibration, $I_0 \rightarrow 0$. Thus, for the given measurement Fig. 2.2 (c), we interpret the remaining current for $V_g < 1\,V$ as the corresponding level of uncertainty in terms of an overestimation of I_0. The latter could be potentially improved by performing slower measurements to ensure a perfect re-thermalization of the shunt resistor as well as a significant increase R_s so that small fluctuations or deviations have less effect on the calibration procedure. Nevertheless, by applying the same calibration procedure with the individual shunt resistances it is still possible to use the corresponding values of I_0 to compare the three different types of nanowires on a more quantitative level, as depicted in Fig. 2.3 (d). Comparing the device characteristics at the largest gate voltage V_g=6 V with respect to the undoped wires, the magnitude of the supercurrent is more than 6 times larger for the devices with an intermediate doping level. In contrast, there is only a factor of 3 between *type B* and *type C*. Here, the reduced doping efficacy could be an indication for a significant increase in crystal lattice defects that limits the concentration of free charge carriers. Additionally, in terms of the bare transistor performance, both *type A* and *type B* show a clear pinch-off with a *threshold voltage* of $V_{th} \approx 1.7V$. For the highest doping, its impossible to fully deplete the transport channel. However, the change in current of ≈ 15% over the full gate range clearly proves that this effect is not caused by a full *metalization* of the semiconductor rather than by the limits of the bottom gate electrode. We would like to point out that the number

[2] Paragraph taken from [369].

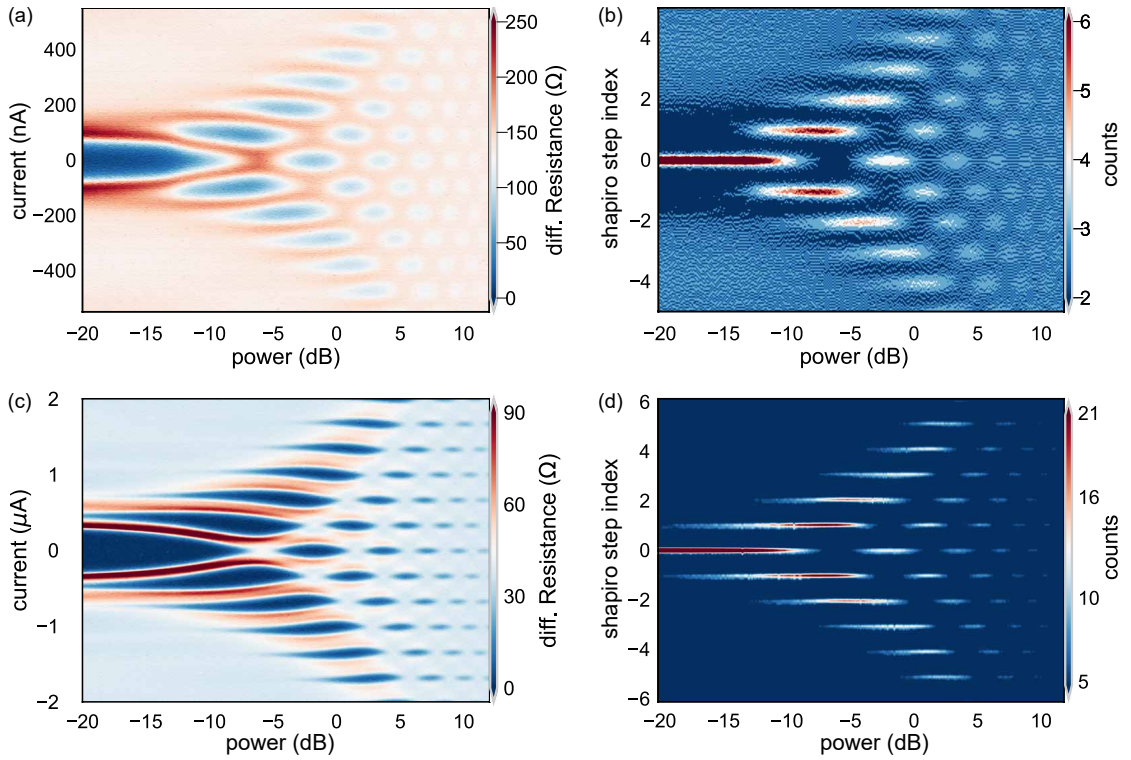

Figure 2.5 – *Power- and frequency-dependent Shapiro spectra and corresponding histograms of two nanowire Josephson junctions with no Te doping [(a),(b)] and a high doping concentration [(c),(d)]. More details are provided in the main text. Data taken from [369].*

of measured samples is too small to justify proper statistics. However, the significant difference in current between the various doping levels is, to our knowledge, way too large to be explainable only within the frame of random device fluctuations. One disadvantage of the bare IVCs is the fact that they do not distinguish between a pure superconductor and a Josephson junction as long as there are no clear signatures of SNS-related effects like multiple Andreev reflections. However, the latter become hard to observe if the transparency between the semiconductor and the corresponding superconducting contacts is low and/or if the number of transport channels in the *weak link* is near or in the *many channel limit*. A more reliable method is the investigation of the AC Josephson effect in terms of *Shapiro measurements*. Here, an irradiated microwave signal induces a dissipative voltage spike whenever the junction is in resonance with the external drive. Those temporary switches into the *running state* are a direct fingerprint of the underlying current-phase-relation and therefore contain information about, for example, the internal state structure. In the case of shunted Josephson junctions, the full voltage range $V_{dc} \propto f_{ac}$ is accessible, allowing the detection of all Shapiro steps even at comparably low frequencies. This is shown exemplary in Fig. 2.4 (a) for a wire of *type B* and different microwave power levels. The latter thereby correspond to the externally applied values, without taking into account the various attenuators and input losses in the cryostate. While the trace at −20 dB mimics the one of the pure-DC response, the corresponding curve for 0 dB clearly shows pronounced and periodic voltage plateaus. By subtracting an extrapolated linear fit of the voltage drop above the superconducting gap, it is possible to extract the individual Shapiro steps, as shown in Fig. 2.4 (b). Here, the upper x-axis corresponds to the index of the Shapiro step in units of the *characteristic Josephson voltage* for the given microwave frequency. Obviously, it is possible to detect all features even down to 1.5 GHz.

The conventional way to measure the AC Josephson effect is based on the irradiation of the high frequency signal by means of an external antenna. However, this method usually induces different kinds of parasitic microwave loss channels like slotline modes, box modes, standing waves etc. which alter the effective microwave power that reaches the sample for every single frequency. In our case, we use a so-called *on-chip bias tee* coupled to an impedance-matched transmission line to realize a

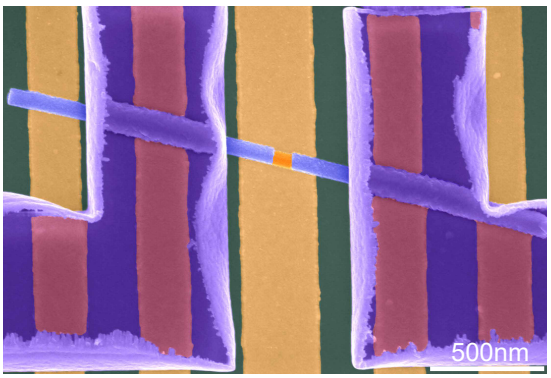

Figure 2.6 – *False-colored SEM micrograph of an InAs/Al half shell nanowire Josephson junction above an Al_2O_3/HfO_2 covered 5 nm/5 nm thick Ti/Pt bottom gate. The Al shell has been partly removed by means of Transene-D, effectively forming a normal conducting weak link with an average length of 80-100 nm. The leads that connect the Al shell with the surrounding TiN circuit are made out of 80 nm thick NbTi. Image taken from [369].*

common *source contact* for both the DC and AC signal. Therefore it is possible to map out the full *power-frequency space* of every nanowire Josephson junction, which is shown exemplary in Fig. 2.5 (a) and (c) for an undoped and highly doped nanowire, respectively, with their corresponding *histograms* in (b) and (d). Here, the most important observation is the fact that both systems can still form a real Josephson junction without any intrinsic dissipative bypass or the formation of a *pseudo-metallic* short due to a too-low or too-large carrier concentration. However, as expected for junctions with **ex-situ** contacts, there are no signs of *missing* or *fractional* Shapiro steps in (b) and (d), which would be an indication for the formation of a 4π-periodic current-phase-relation due to topological-protected states [133, 269]. Therefore, even though the just presented results clearly prove that it is possible to create nanowire Josephson junctions with *specially tailored* supercurrents, their overall performance at that stage is still not good enough to act as building blocks for Transmon or Andreev qubits or as a platform for Majorana fermions. Thus, the following section is devoted to the (quantitative) investigation of the **interface** between the semiconductor nanowire and its superconducting contacts.

IV

2.2. MEASURING HIGH TRANSPARENCIES

The conventional way to determine the transparency of a SNS Josephson junction is based on the extraction of the *excess current* and the *normal state resistance*. By comparing the product of both with the superconducting gap and applying the *OBTK model* [164, 365], it is then possible to calculate the corresponding barrier strength and transparency. However, it becomes immediately obvious that this method has some intrinsic problems. The most important one lies with the description of the weak link as a kind of *valve* and a *flow rate* of charge carriers associated with it. Even though this simple picture holds as long as the junction resides in the *many channel limit*, in which the spectrum of densily packed Andreev bound states basically forms some kind of continuum, it starts to fail as soon as the junction properties are determined by only a few or a single transmitting channel. In such systems, which are the fundamental building blocks of more advanced structures like the Andreev qubit, the lifetime of the corresponding two-level system depends largely on the exact shape of the dispersion relation or, to be more precise, the smallest achievable phase-dependent energy. Thus, it becomes important to not only know some kind of ratio between input and output rather than the exact transmission of every individual bound state. The latter is also known as **mesoscopic pincode** [136, 140, 377, 378].

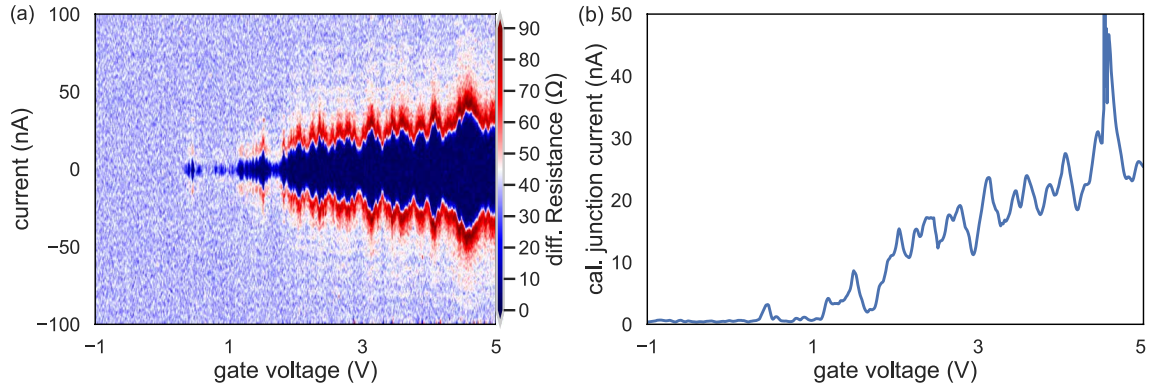

Figure 2.7 – *(a) Exemplary gate- and current-dependent differential resistance map of an extrinsically shunted InAs/Al half shell nanowire Josephson junction. The general behavior is similar to the measurements shown in Fig. 2.3(a), which is a strong proof that the epitaxially grown superconductor shell does not interfere with the properties of the semiconductor itself. (b) Extracted gate-dependent critical current of the junction. Even though the nanowire is undoped, too, the maximum supercurrent it can support is three times larger as for the undoped wires with ex-situ contacts.*

Simply speaking, the mesoscopic pincode τ_i is a figure of merit for the efficiency of the transfer of the superconducting properties into the normal conductor. In tunnel junctions, $\tau_i = 0$ and the Cooper pairs are just transferred *through* the barrier without interfering with its electrical properties. In SNS devices, however, the supercurrent is based on Andreev bound states within a certain energy range, the **proximity gap** Δ_p. Thus, for $\tau_i = 1$ one obtains $\Delta_p = \Delta$ and a **full proximization** of the normal conductor. Consequently, the state-of-the-art method to characterize the semiconductor-superconductor interface in a more precise way is based on the energy-resolved investigation of its internal state structure. The so-called **tunnel spectroscopy** [379–381] allows a direct detection of the *superconducting gap edge*, the *proximity gap* and any transmitting levels in between[3]. As the indicated by the name, this approach only works if the transport through the system is *tunnel-limited*, which requires either an initially low number of channels so that the junction can be gate-tuned into pinch-off or the combination of one superconducting and one normal conducting contact. However, the latter approach, which effectively forms a *SNN* system, renders all measurement that rely on the DC or AC Josephson effect impossible.

An alternative method, which offers more flexibility, is based on the already introduced on-chip shunt resistor and the corresponding calibration of the supercurrent. Fig. 2.7 (a) shows the gate response of an **undoped in-situ grown InAs/Al half shell nanowire** as depicted in Fig. 2.6. Interestingly the qualitative behavior looks remarkably comparable to the one shown in Fig. 2.3 (a). Again,

[3] A more detailed description of this approach and exemplary measurements are provided in Chap. 3

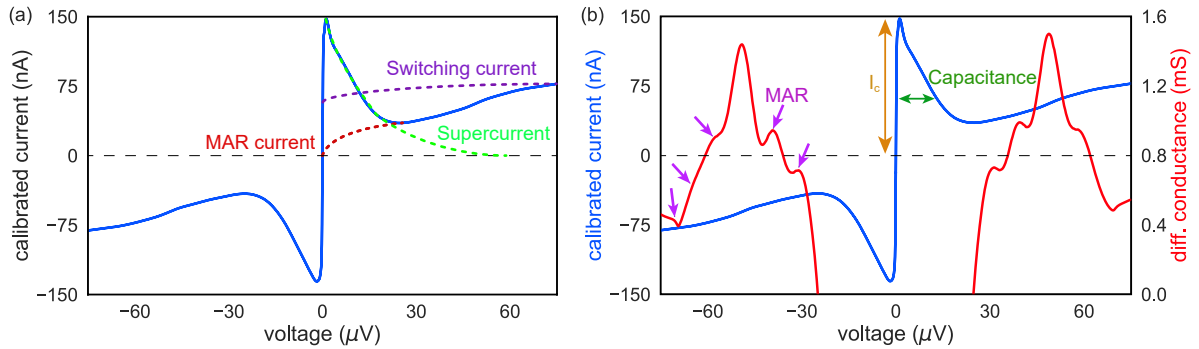

Figure 2.8 – *Calibrated VI characteristic of the same nanowire Josephson junction shown in Fig. 2.7. (a) The on-chip shunt resistor modifies the Josephson junction response such that the stochastic and fluctuation-driven switching event (purple) is suppressed. Instead, with increased voltage drop, the crossover from a decaying Cooper pair based supercurrent (green) into a dissipative transport driven by multiple Andreev reflections (red) can be observed. (b) The supercurrent peak contains a lot of information regarding the electrostatic properties and dynamics of the nanowire Josephson junction. Here, the height of the peak is related to the maximum supercurrent and the amount of thermal fluctuations. The width of the peak, on the other hand, scales with the junction capacitance. Finally, the subharmonic gap structures (purple) stem from multiple Andreev reflecitons with order Δ_p/n and are therefore a direct footprint of the* ***induced proximity gap****.*

the nanowire Josephson junction exhibits strong fluctuations of the supercurrent, with a threshold voltage slightly below the one for the undoped and intermediate doped wires with ex-situ contacts (cf. Fig. 2.3 (d)). However, the latter lies within the typical deviation range of the gate lever arm. In contrast, the magnitude of the calibrated junction current, shown in Fig. 2.3 (b), is significantly larger than the one measured for the undoped wires without an Al in-situ shell despite the same junction length of $\approx 100\,\mathrm{nm}$. The similar gate behavior proves that the general device characteristics, e.g. the total number of electronic channels or the energetic positions of the Fermi level, the valence and conductance band, are fully determined by the semiconductor nanowire itself and exhibit, at maximum, only a weak influence from the coupled superconductor. More importantly, they also indicate that the half-shell geometry does not cause a significant screening of the local electric field induced by the applied gate voltage.

In the case of a junction that is expected to be highly transparent, the obtained calibrated current trace is supposed to contain much more information. First of all, the transition between the actual *supercurrent* and the dissipative transport based on *multiple Andreev reflections* is revealed, as depicted in Fig. 2.8 (a) and indicated with the purple arrows in (b). Additionally, the shape of the peak is influenced by the electromagnetic environment and can therefore provide clues about all perturbations away from the ideal junction performance. Here the *peak height* represents the ratio between the real junction current and a virtual *intrinsic bias current* that originates from *thermal fluctuations* in the shunt resistor. In terms of energy, it compares the thermal fluctuations with the *Josephson energy* of the individual Andreev bound states i [136, 140, 142, 143]:

$$I_c = \frac{k_b T}{E_J(\tau_i)}. \tag{2.5}$$

The *peak width*, on the other hand, is a direct footprint of the **junction capacitance** and any other electric stray fields between metallic structures in close proximity to the device, therefore referred to as C_s. Here, larger values are correlated with a slower suppression of the supercurrent and a (purely) ohmic environment. In the case of nanowires, C_s is comparably small and only in the range of a few pF, effectively adding a frequency-dependency to the transmission behavior of the parallel circuit. In this scenario, the dissipation of the purely ohmic case R has to be replaced by a complex impedance $Z(\omega)$ that might differ for every applied DC voltage.

The most important features become only clearly visible by calculating and plotting the differential conductance as in Fig. 2.8 (b), revealing a series of peaks. These can be attributed to multiple Andreev reflections occuring at *fractions* of the **induced proximity gap**. Due to the shunt resistor, even higher order processes with $n > 5$ can be observed, which are usually superimposed by the

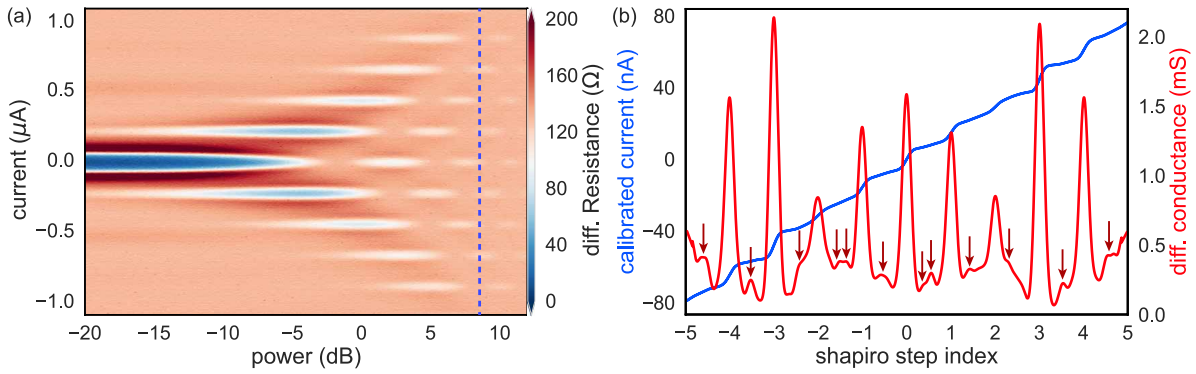

Figure 2.9 – *(a) Power- and current-dependent Shapiro spectrum of an InAs/Al nanowire Josephson junction for a constant frequency of f=14.1 GHz and a gate voltage of V_g=7 V. (b) An exemplary cut through the spectrum at a microwave power of 5 dBm. Besides the dominant integer Shapiro steps and the corresponding peaks in the differential conductance, the device response exhibits reproducible and symmetric* ***subharmonic features*** *at 1/2× n and 1/3× n.*

switch into the voltage state. Earlier works [136, 140] have shown that it is possible to extract the *mesoscopic pin code* τ_i of every individual bound state by applying the theoretical frameworks of Ivanchenko-Zil'berman [141] and Ambegaokar-Halperin-Kurkijärvi [142**?** , 143]. Here, the conductance peaks are fitted by means of the *modified Bessel function of the first kind*. However, in the case of our nanowires, this method leads to unrealistic or even unphysical results. After an in-depth evaluation and re-modeling of the system, the conclusion has been made that this issue can be most likely attributed to the fact that, in contrast to *break junctions* with their well-defined and isolated state structures, the Andreev bound states in our mesoscopic nanowire Josephson junctions usually cannot be considered to be independent [382]. This is consistent with results presented at a later stage of this thesis that show the existence of *single quasiparticle transitions* through *spin-polarized* Andreev levels, which is only possible via a certain degree of *crosstalk* between states due to **scattering**. In this scenario, the MAR can not be simply and directly related to the ABS. In the same context of a much more sophisticated microscopic modeling and simulation of our nanowire Josephson junctions by means of the **Qutip** [383, 384] and **Kwant** [385] frameworks, it has been revealed, too, that the original models of [141] and [142**?** , 143] need to be significantly modified to describe our nanowire systems [386]. Unfortunately, within the time frame of this thesis, it was not possible to establish a new model. Thus, the observed MAR features can only be analyzed on a qualitative level. Here, a *smoking gun* simulation in *Qutip* [383, 384] indicates that such features only appear with the observed clarity if the **average transparency** is > 0.9, proving the high quality of the in-situ formed InAs/Al interface [386].

2.2.1. SUBHARMONIC SHAPIRO STEPS

One of the most intriguing properties of Josephson junctions is the tight relation between the macroscopic phase difference across the weak link and the magnitude of the dissipationless supercurrent that flows through the device. In mesoscopic systems, this effect becomes even more important, as it directly determines the dispersion relation of the Andreev bound states. Additionally and in contrast to tunnel junctions or systems that host a quasi-continuum of channels, the transparency τ of the system plays a significant role in the actual *form* of the transport. In energy space, it determines the separation from the middle of the superconducting gap, i.e. the minimum energy at phase π, which is the most important parameter for the realization of an Andreev qubit. However, besides that *internal phenomenon*, which can usually just be probed by means of **spectroscopy**, τ also affects the external DC and AC response of the device. This offers further possibilities to obtain a more reliable value for the interface transparency.

Fig. 2.9 (a) shows the power-dependent Shapiro spectrum for f=14.1 GHz of an in-situ grown InAs/Al core/half-shell nanowire Josephson junction, as presented in the former section. Here, the large frequency leads to pronounced plateaus of constant voltage despite the on-chip shunt resis-

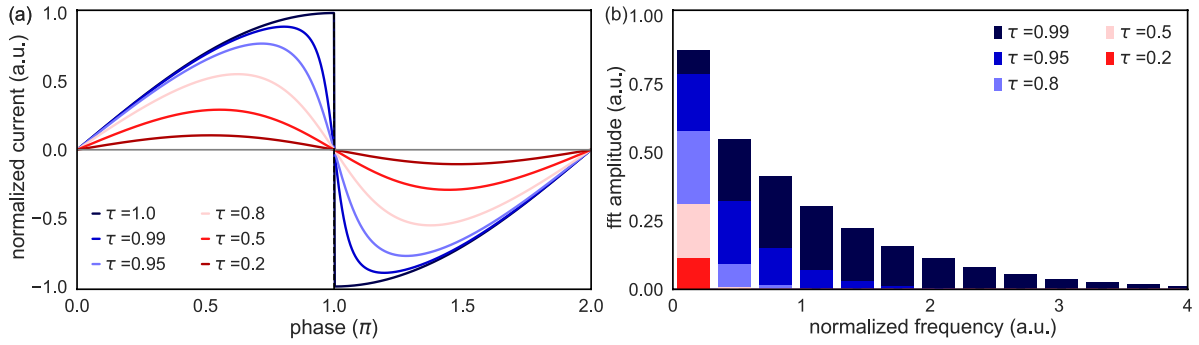

Figure 2.10 – *(a) Simulated and normalized current-phase relationships of a set of mesoscopic nanowire Josephson junctions with different values of the mesoscopic pin code τ. Based on Eq. 2.6, the CPR evolves from a sign function into the sinusoidal behavior of a classical tunnel-junction. Here, the special case of $\tau = 1$ also represents the theoretical maximum of the transmitted supercurrent. (b) Normalized frequency spectrum of the curves shown in (a) obtained by a fast-Fourier transformation. For large transparencies, i.e. more distinct deviations from the sinusoidal case, the spectrum consists of a set of higher order components which are a possible source for the subharmonic features in Fig. 2.9(b).*

tor. Furthermore, looking at a single trace at a constant microwave power, like in Fig. 2.9 (b) for 5 dBm, the corresponding differential conductance reveals some additional features at **fractions** of the *characteristic Josephson voltage* $V_J(f)$. Such a phenomenon has been recently predicted in terms of the search for Majorana fermions for which the coexistence of 2π and 4π-periodic supercurrents with different magnitudes can lead to a complex AC response if the device resides at the border of the *topological* and *trivial* regime [269]. However, experimentally this effect is supposed to manifests itself in **missing steps** rather than additional ones [133, 270]. Even though the fact that the features in Fig. 2.9 (b) can only be observed at certain microwave powers could be somehow explained with competing capacitive effects or relaxation processes, it renders this explanation just more unlikely. Nevertheless, as the Shapiro effect originates from the *Josephson equations*, it has to be related to the *shape* of the **current-phase relation**.

Another explanation can be derived by taking the amount of current that is carried by an Andreev bound state into consideration. Assuming a *single channel system*, the latter is given by

$$I(\delta,\tau) = \frac{\Delta}{4\Phi_0}\frac{\tau\sin\delta}{\sqrt{\left(1-\tau\sin^2\delta/2\right)}} \tag{2.6}$$

and is extremely sensitive to the transparency. For $\tau \to 0$, the CPR converges towards the conventional **sinusoidal shape** of a tunnel-junction. However, if the coupling between the superconducting contacts and the normal conducting weak link is improved, the relation between phase and current becomes more and more *anharmonic* (cf. the simulated curves in Fig. 2.10 (a)). In the most extreme case $\tau = 1$, i.e. for a perfect coupling, the CPR takes the form of a **sign function** with $I(\pi,1) = \pm I_{\max}$. Thus, by calculating the **Fourier spectra** of the transparency-dependent CPRs in Fig. 2.10 (a), not only a single 2π component is obtained, but rather a fundamental mode and *higher harmonics* associated with it. Strikingly, the maximum order of the harmonics is extremely sensitive to τ, e.g. the **fourth** and **third** order contributions already vanish at $\tau = 0.95$ and $\tau < 0.8$, respectively. Based on that model, it is now possible to use the **subharmonic Shapiro steps** in Fig. 2.9 to obtain further information about the junction transparency. In contrast to the already presented approach based on *multiple Andreev reflections*, the latter method becomes even more sensitive if $\tau \to 1$. Since even $n/3$-contributions can be observed in Fig. 2.10 (a), a rough simulation[4] reveals a corresponding transparency of $\tau > 0.93$. It should be pointed out that even though the $n/2$ and $n/3$ higher harmonics are still visible in the *Fourier spectrum* for even lower values of τ, it turns out that they need to exceed a certain *magnitude* with respect to the fundamental mode in order to be detectable in the experiment. Nevertheless, this method offers another possibility to derive the transparency of mesoscopic Josephson junctions

[4] Most importantly, the model does not take the existence of more than one Andreev bound state into account.

without the need of more advanced and complex measurements like *two-tone spectroscopy*. Additionally, it proves again that the in-situ deposition of the required superconducting shell results in highly transparent hybrid devices, effectively fulfilling one of the main requirements for the future realization of topological systems. Thus, the following chapter is devoted to an optimization of the remaining parameter of a mesoscopic Josephson junction, i.e. the formation and length of the **weak link**.

3

TRANSPORT IN SHADOW-MASK DEFINED NANOWIRE JOSEPHSON JUNCTIONS

3.1. STRUCTURAL CHARACTERISATION

"The structural properties of the InAs-Al core-half-shell nanowires were examined using scanning transmission electron microscopy (STEM). To this end, the nanowires were transferred to holey carbon Cu grids by simply sweeping the arrays with the grid. The InAs nanowires grown by the current catalyst-free method showed polytypic crystal structure containing thin, defective wurtzite (WZ) and zincblende (ZB) segments.

Figure 3.1 (a) shows a low magnification image of a core/half-shell nanowire. The Al layer is uniform along the nanowires and has a smooth surface with no significant faceting [31]. Cross-sections prepared by focused ion beam revealed that the Al thickness is not uniform around the half-shell, as shown in Fig. 3.1 (b). The balling up is related to the relative high deposition temperature (−6° C). A similar but less pronounced tendency is observed at −30° C (Ref. [31]) and only decreasing the temperature even more (−120° C in Ref. [360]), a conformal deposition can be obtained. The maximum thicknesses of the Al layers in these nanowires lie between 30–50 nm. The Al half-shell is formed by large grains (> 25 nm) with different orientations. These differently oriented grains can be seen in the two viewing directions with grain boundaries marked by red arrows in Figs. 3.1 (a) and (b). Some of the observed grain orientations include $([110]_{\mathrm{Al}} \,||\, [0001]_{\mathrm{InAs}})_{||} \times ([1\text{-}12]_{\mathrm{Al}} \,||\, [11\text{-}20]_{\mathrm{InAs}})_{\perp}$ and $([110]_{\mathrm{Al}} \,||\, [0001]_{\mathrm{InAs}})_{||} \times ([1\text{-}10]_{\mathrm{Al}} \,||\, [11\text{-}20]_{\mathrm{InAs}})_{\perp}$ (using WZ notation for InAs). These orientations are different from those shown in some of the previous works [31, 44, 387], but consistent with some of those seen in our prior results [33]. It should also be noted that the size of the Al grains is much larger than the width of a single crystal type region in the polytypic nanowire (which is generally less than 10 mono-layers), and these grains span multiple phase changes and defects. This means that change in phase of the nanowire does not directly induce change in metal grain orientation. The interface between the Al and InAs was analysed using the cross sections, as this viewing angle avoids simultaneous contribution to the projection from Al growth on multiple facets. Fig. 3.1 (c) shows a falsely colorized higher magnification image of the InAs-Al interface from a nanowire cross section (different to Fig. 3.1 (b)). It can be seen that the interface is sharp and smooth with no amorphous material in between crystalline InAs and Al, as a result of fully in-situ deposition of the electrodes and absence of processing steps such as Ar^+ sputtering. Edge dislocations which have been previously attributed to AlAs formation [31, 33], were observed in the side view of these nanowires. These dislocations were located ~ 2.5 nm from the interface within InAs. Evidence supporting an AlAs layer as thick as 2.5 nm was not seen in energy dispersive x-ray (EDX) data or lattice spacings of high resolution images, although a smaller lattice spacing ($d_{\{11-20\}}$) was observed between the edge-most lattice planes in some nanowire facets, accounting to a possible AlAs or AlInAs formation of thickness less than 0.5 nm. This shows that almost all of the As on the entire nanowire surface has been desorbed prior to Al deposition and it is consistent with transport measurements (shown later) which show no evidence for the presence of a significant intermediate AlAs layer. Figure 3.1 (d) shows an annular dark field (ADF) image and the corresponding EDX map of an InAs-Al junction. A clear sharp gap in

IV

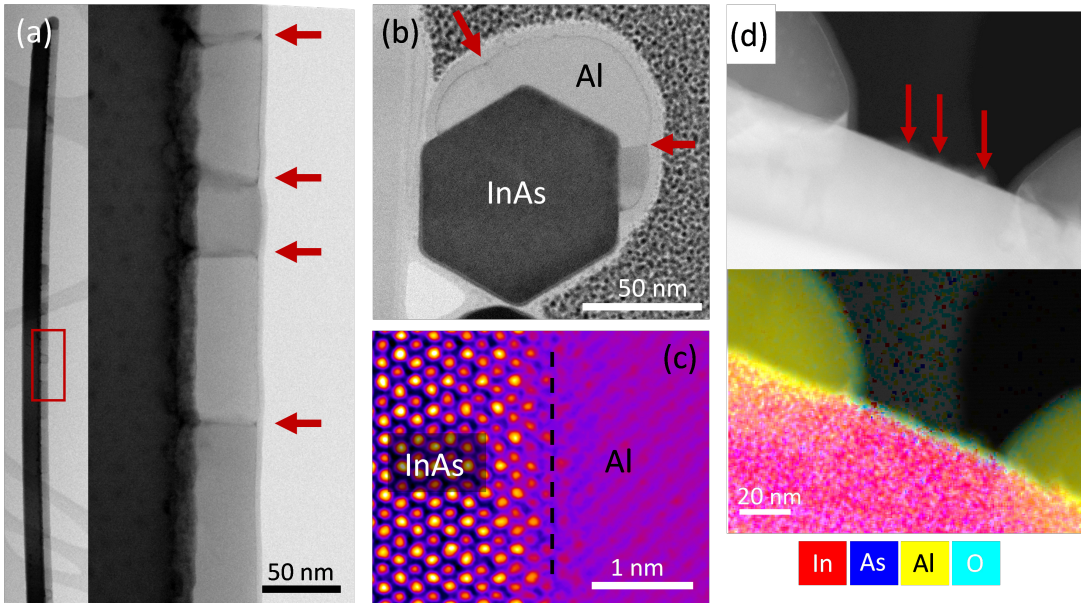

Figure 3.1 – *(a) A low magnification bright field (BF) scanning transmission electron microscope (STEM) image from the region indicated in the core-halfshell nanowire shown in the inset. Zone axis for imaging is WZ* $\langle 11\bar{2}0 \rangle$ *(ZB* $\langle 110 \rangle$ *equivalent) of InAs and the red arrows mark the grain boundaries. (b) A BF STEM image of a nanowire cross-section along WZ InAs* $\langle 0001 \rangle$ *(or ZB* $\langle 111 \rangle$*) direction showing the Al half-shell and red arrows indicating the grain boundaries. (c) A false color high magnification cross sectional image of the InAs-Al interface. The broken line marks the interface from a different nanowire to (b). (d) An annular dark field (ADF) STEM image and the corresponding EDX map of an InAs-Al junction showing the elemental distribution. The red arrows in the ADF image indicate the isolated oxidised Al droplets within the gap. The zone axis for (d) is WZ InAs* $\langle 1\bar{1}00 \rangle$ *(ZB* $\langle 112 \rangle$*). Image taken from [388].*

the Al layer is formed in the shadowed region with a junction width of 75 nm. Few small, oxidised and isolated droplets of Al were formed during its deposition and can be seen within the junction (indicated by red arrows in the ADF image). However, these seem to get removed by etching during the subsequent device processing steps as no evidence of parallel metallic bypass is observed in the transport measurements.

3.2. BASIC JUNCTION CHARACTERISTICS

All presented transport measurements were performed in a He3/He4 dilution refrigerator at a base temperature of 15 mK equipped with a superconducting magnet coil. $I-V$ traces were measured using a current bias supplied from a battery-powered current source and measured using a battery-powered differential voltage amplifier. The measurement lines within the refrigerator are heavily filtered with thermocoax, low-temperature copper powder filters and custom low pass filters in addition to room temperature 'pi'-filters.

The efficiency of the gate response is one of the key properties of a nanowire junction. Therefore, we measured the conductance of the junction in a voltage-biased configuration. In Fig. 3.2 (a) a gate sweep for one of the in-situ devices is shown. For these measurements a constant voltage drop of 400 μeV is maintained across the junction, i.e. above the induced proximity gap. Depending on the applied gate voltage V_g, four different regimes can be distinguished. For gate voltages below -6.7 V, the nanowire is completely pinched off. Above this value, the current is mediated by single electron transport through an intrinsic quantum dot. For gate voltages larger than -5 V, the nanowire opens up, but the conductance is still limited by a low-transparency tunnel coupling to the electron reservoirs in the contacts. This results in a conductance increase of just $2e^2/h$ over a gate voltage range of 2 V and just a weakly pronounced superconducting branch. For the last section, i.e. voltages above -3 V, the current voltage (IV) characteristics show a classical Josephson junction response (cf. Fig. 3.2 (a) (inset)) with a clear supercurrent. In addition, signatures of subharmonic gap structures are found in the differential resistance [164, 365].

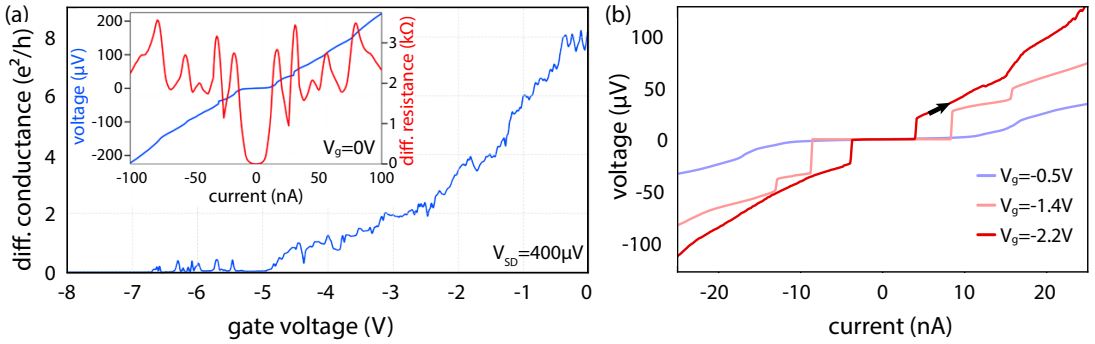

Figure 3.2 – *Conductance G vs. gate voltage measured in a voltage-driven setup with a constant voltage drop of 400 μeV. Four different transport regimes can be distinguished (negative to positive gate voltage): Pinch-off, Coulomb blockade, tunnel-dominated transport, and classical Josephson junction behaviour. The inset shows the current voltage (IV) characteristics at zero gate voltage, with a supercurrent of approx. 21 nA and signatures of subharmonic gap structures in the differential resistance. (b) IV curves at gate voltages of −0.5, −1.4, and −2.2 V, respectively. The black arrow indicates the sweep direction. The small asymmetry can be attributed to thermal effects, e.g. overheating, or an underdamped junction behavior. Images taken from [388].*

Figure 3.2 (b) shows a set of IV curves at three different gate voltages within the Josephson-junction-regime. It can be seen, that the switching current of the device is tunable between 3 nA and 10 nA. The additional constant-voltage-sections are related to self-induced Shapiro steps, caused by the transmission-line circuit on the sample. At $V_g = -0.5$ V we obtained a critical current of $I_c = 11$ nA and a normal state resistance of $R_N = 6.33\,\text{k}\Omega$, which results in an I_cR_N product of 70 μV. We would like to stress that the presented I_cR_N value just holds for the given gate voltage. For the other two IV curves we obtained $I_cR_N(V_g\text{=-1.4V})=72\mu$V and $I_cR_N(V_g\text{-2.2V})=75\mu$V with $R_N = 8.7\,\text{k}\Omega$ and $11.8\,\text{k}\Omega$, respectively. Although the normal state resistances are quite different for the three gate voltages the I_cR_N product varies only slightly. A similar behaviour was observed before in nanowire-based Josephson junctions [358, 389]. Here, it was found that the critical current changes essentially in the same way as the normal state conductance. Owing to the mesoscopic nature of the nanowire bridging the superconducting electrodes R_N is affected by interference effects such as universal conductance fluctuations. By extrapolating the current voltage characteristics at the normal state in the range $V > 400\,\mu$V a finite excess current I_{exc} of 72.6 nA is extracted. The excess current can be used to get an estimation of the dominating type of transport within the channel by comparing the

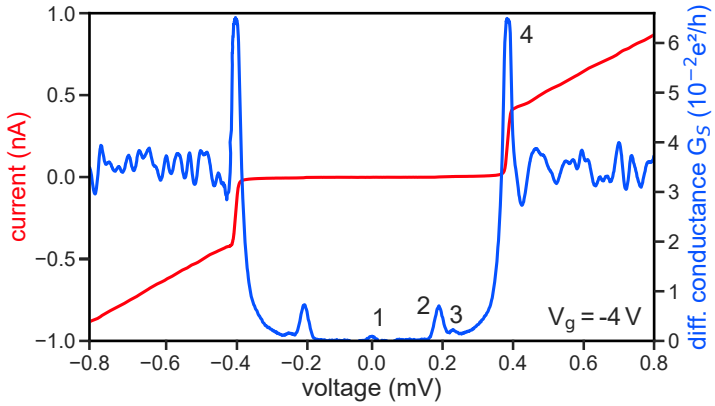

Figure 3.3 – *Voltage-driven tunnel spectroscopy measurement of an InAs/Al nanowire junction at $V_g = -4$ V: Current as a function of voltage (red) and corresponding differential conductance in units of e^2/h (blue). The four peaks correspond to (1) the superconducting state, (2) (3) sub-gap structures and (4) the induced proximity gap. Image taken from [388].*

$I_{\text{exc}}R_N$ product with the superconducting gap Δ. Following the framework of the corrected Octavio–Tinkham–Blonder–Klapwijk theory [164, 365], we obtain a ratio of $eI_{\text{exc}}R_N/\Delta = 1.31$ at zero gate voltage. This value can be converted to the barrier strength parameter $Z = 0.38$ and a corresponding contact transparency $\mathcal{T} = 0.88$ [365, 366]. This transparency is comparable to values obtained for hydrogen cleaned superconductor/nanowire junctions, i.e. Al/InSb [45] or NbTiN/InSb [390].

3.2.1. HARD GAP SPECTROSCOPY AND YU–SHIBA–RUSINOV STATES

The second benchmark of a superconductor-semiconductor hybrid structure is the hardness of the induced proximity gap, i.e. the coupling strength between the nanowire and the metal shell, in the single-channel or tunneling limit. Previous experiments on similar systems used tunnel spectroscopy between one superconducting and one normal conducting contact to detect the strong change in the density of states of the device close to the gap edge [391]. Even though our structure is slightly different in terms of the contact setup, we can obtain comparable conditions by applying a negative gate voltage which sets the device into the tunnel-limited regime [355]. Figure 3.3 shows a typical spectroscopy-like measurement of a self-defined InAs/Al nanowire Josephson junction.

As indicated in the figure, four pronounced peaks are identified. Feature (1) is thereby related to the superconducting state, while (2) and (3) correspond to sub-gap structures. Finally, the dominating peak (4) marks the edge of the induced proximity gap $2\Delta = 380\,\mu$eV. Similar to the tunneling experiments of Chang *et al.* [391] the density of states in the nanowire segments underneath the superconducting electrodes is probed by our measurements. Due to the proximity effect an induced gap is created in the InAs nanowire. However, in our structure two proximitized nanowire segments are separated by tunnel barriers forming the quantum dot, therefore 2Δ is measured. The value of Δ is close to the bulk Al gap ($\Delta_{Al} = 200\,\mu$eV) indicating a good coupling between Al and InAs. An important figure of merit is the ratio of the conductance for in- and out-of-gap transport, i.e. G/G_N. Between (4) and (2), the conductance drops to $G/G_N \approx 0.02$, with a further reduction between (2) and (1) to $G/G_N < 0.001$. Such a strong decrease of the conductance is an indication that our devices host a so-called hard gap [355, 391].

As already shown in Fig. 3.2, the actual junction behavior is strongly correlated with the applied gate voltage. Thus, we performed a gate batch measurement between -8 and 0 V in steps of 29 mV, which covers both the tunnel-limited regime as well as the range in which the transport is dominated by multiple Andreev reflections. Figure 3.4 (a) shows the stability diagram of the junction for gate voltages between -8 and -4 V. Here, the transport is dominated by single electron tunneling, which results in pronounced Coulomb diamonds. By mapping out the size of the diamonds in terms of their individual gate and bias voltage, we obtain a lever arm $\alpha = 0.095$ and charging energy $E_c = 11.6$ meV for the large diamond in Fig. 3.4 (a) and $\alpha = 0.021$ and $E_c = 8.5$ meV for the small one. The large values of E_c indicate that the corresponding quantum dot has to be rather small and is most likely caused

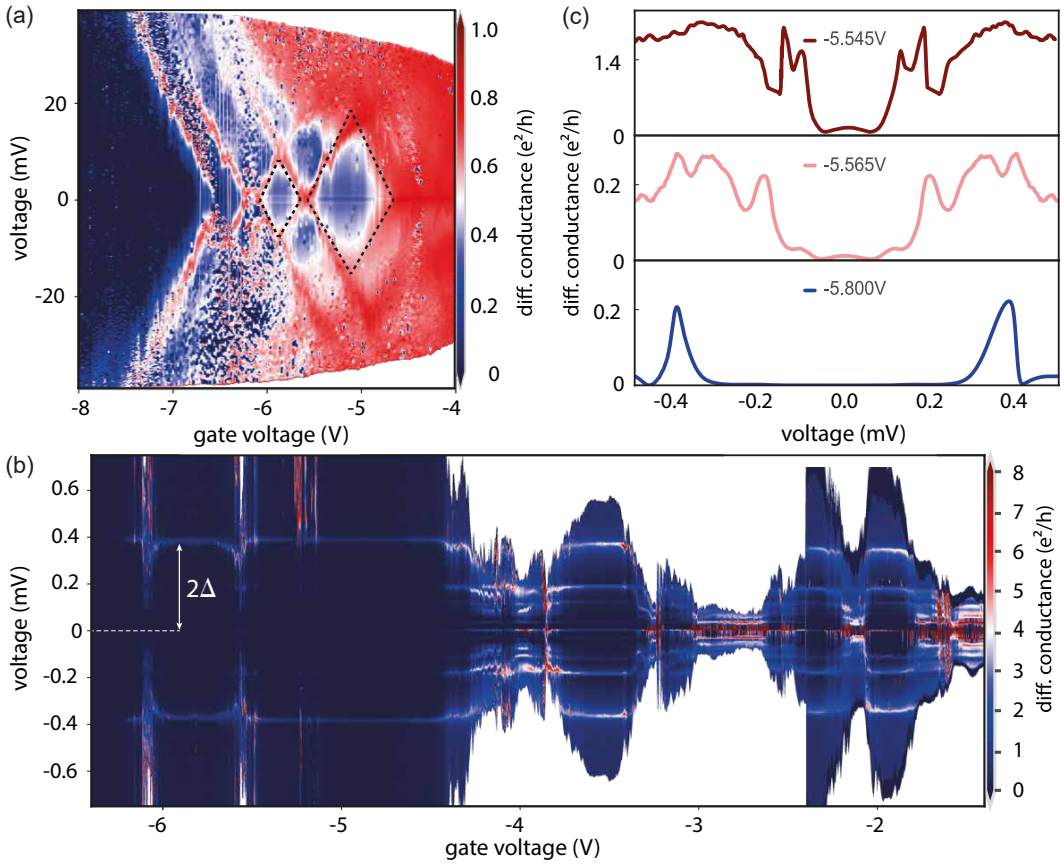

Figure 3.4 – *(a) Full gate response for gate voltages between* −8 *and* −4 *V, showing a set of Coulomb diamonds (indicated by the black dashed lines) which are related to a single quantum dot, with a charging energy of* $E_c = 11.6\,meV \approx 60\,\Delta$ *and* $E_c = 8.5\,meV \approx 44\,\Delta$*, respectively. (b) Differential conductance vs. bias voltage measurements with a high resolution gate voltage stepping for* V_g = -6.4 … -1.4 *V. The measurement covers the in- and inter-diamond section as well as the open-junction-regime. Within the Coulomb diamonds found in the range of* $V_g < 5.5$ *V, the only visible feature is related to the edge of the proximity gap. However, for voltage values close to the section in which the quantum dot is open, Yu–Shiba–Rusinov states are observable. (c) Differential conductance vs. bias voltage traces at different gate voltages, depicting the evolution of the sub-gap structure in and out of the Coulomb diamonds. For* −5.8 *V (dark blue), there are only two peaks which are related to the edge of the proximity gap. At* −5.655 *V (light red), multiple sub-gap states become visible. For* −5.545 *V (dark red), the spectrum completely changes, ending up in a trace with a 7 times larger conductance and a pronounced peak at zero energy. We attribute this behavior to a mixture of both multiple Andreev reflections and Yu–Shiba–Rusinov states. Image taken from [388].*

by twinning defects or lattice-type changes in the nanowire junction area. Based on these values, especially due to $\Delta < E_c$, we assume that the transport, in the sections in which the quantum dot is open, is mediated by Yu–Shiba–Rusinov (YSR) states rather than by conventional Andreev bound states [171–173].

In order to probe the actual state structure, we performed differential conductance vs. bias voltage measurements at a high resolution gate voltage stepping in the range of −6.4 to −1.4 V, which is shown in Fig. 3.4 (b) [1]. We can distinguish between three different regimes. For less negative gate voltages, i.e. values above −4.3 V, (multiple) sub-gap states arise. However, for more negative gate voltages and, especially inside of the Coulomb diamonds, the sub-gap transport is completely suppressed. Nevertheless, the edges of the induced proximity gap are still present, represented by two straight light-blue lines at a constant voltage of ±375 μV. On the other hand, for certain gate voltage ranges, in which the quantum dot is open, several sub-gap features become observable. In Fig. 3.4 (c) three exemplary curves in the range around −5.7 V are shown. For a gate voltage of −5.8 V, the junction characteristics exhibit a clear hard-gap without any sub-gap features. If the voltage increases up to −5.565 V, a single state moves into the gap and additional peaks appear, which are probably related

[1] Compared to the measurements shown in Fig. 3.4 (a) the pattern is shifted slightly because of gate drift.

IV

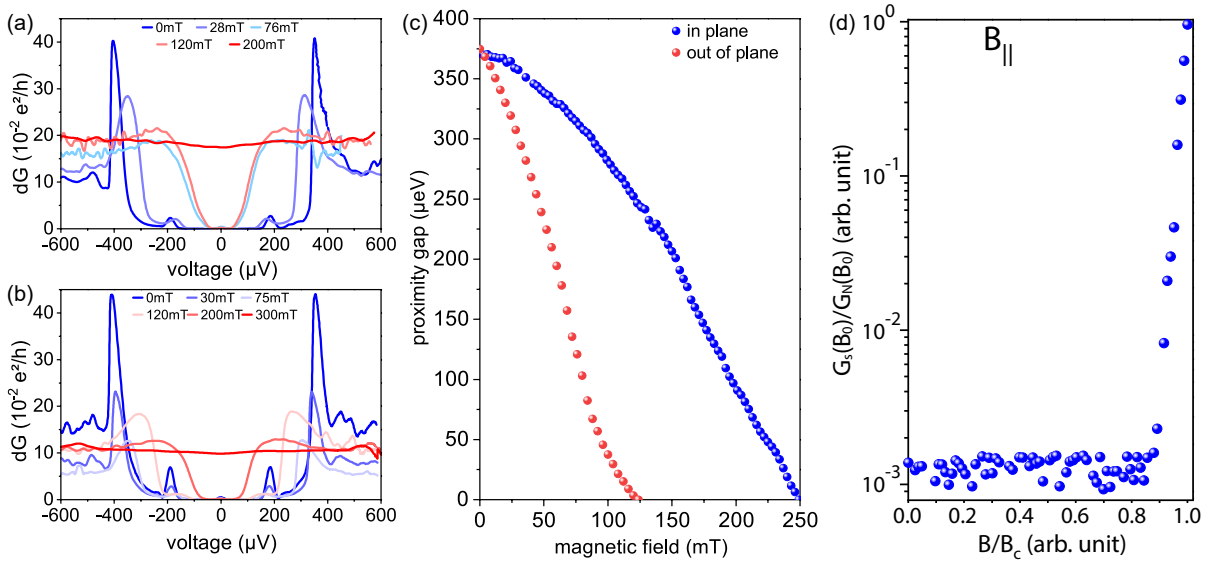

Figure 3.5 – *Differential conductance traces as a function of bias voltage for various magnetic fields in both (a) perpendicular and (b) parallel orientation to the nanowire axis. For increasing field values, the peaks corresponding to the edge of the proximity gap are damped and move closer to zero energy. (c) Width of the proximity gap 2Δ for an increasing magnetic field between 0 and 250 mT. The energies were extracted using the first derivative of the differential conductance. For an perpendicular orientation, we find a critical field of B_c =130 mT, while for the parallel field we obtain B_c =250 mT. (d) Ratio of the averaged parallel-field-dependent zero bias conductance relative to the conductance above the critical field. As long as the field is less than 90% of the critical field, the zero bias conductance is mainly determined by the noise floor of the system, without any parasitic sub-gap states, which is another proof for the hard-gap behavior of the junction. Image taken from [388].*

to coherent reflection events of the same state. For a gate voltage of $-5.545\,V$, the state reaches zero energy, which, together with the onset of single electron tunneling, results in a 4 times increase of the in- and out-of-gap conductance as well as the emergence of a pronounced zero bias peak, probably caused by the interplay of multiple Andreev reflections and a single Yu–Shiba–Rusinov state. Based on the strong gate asymmetry, as well as due to the relatively large charging energy of $E_c \approx 60\Delta$, this behavior could be an indication for a quantum phase transition from a singlet into a doublet state, which effectively changes the nature of the junction from "0" to "π" [387, 392, 393]. However, due to the fact that the junction does not carry a real, non-dissipative current in this specific gate voltage range and is not embedded in a phase-sensitive device like a superconducting quantum interference device, there is no direct way to probe the resulting reversal of the supercurrent. Nevertheless, these states could still offer some advantages for devices based on mesoscopic Josephson junctions by adding an additional energy-tunability of the states besides the superconductor-semiconductor interface transparency.

3.2.2. IN-PLANE AND OUT-OF-PLANE MAGNETIC FIELD TRANSPORT MEASUREMENTS

The common requirement for all devices based on Andreev bound states is the manipulation of the phase across the junction in order to move along the dispersion relation and set the system to a fixed operational point. This is normally achieved by means of a superconducting loop connecting the junction and applying a small external out-of-plane magnetic field which generates a flux-induced phase shift. In the case of semiconductor nanowires, and more specifically for materials like InAs or InSb, the strong spin-orbit coupling as well as the large g-factor can be used as an additional way to manipulate the state structure both in energy and momentum space. Here, an additional in-plane field is required to induce a Zeeman splitting, with field values which can easily overcome the bulk critical field of Al by one or two orders of magnitude. Combined,this makes the magnetic field sustainability the second key benchmark of a nanowire Josephson junction.

In order to probe the magnetic field stability of the in-situ junctions we performed voltage-driven measurements at a gate voltage of −4.3 V, which is close but outside of the regime dominated by the

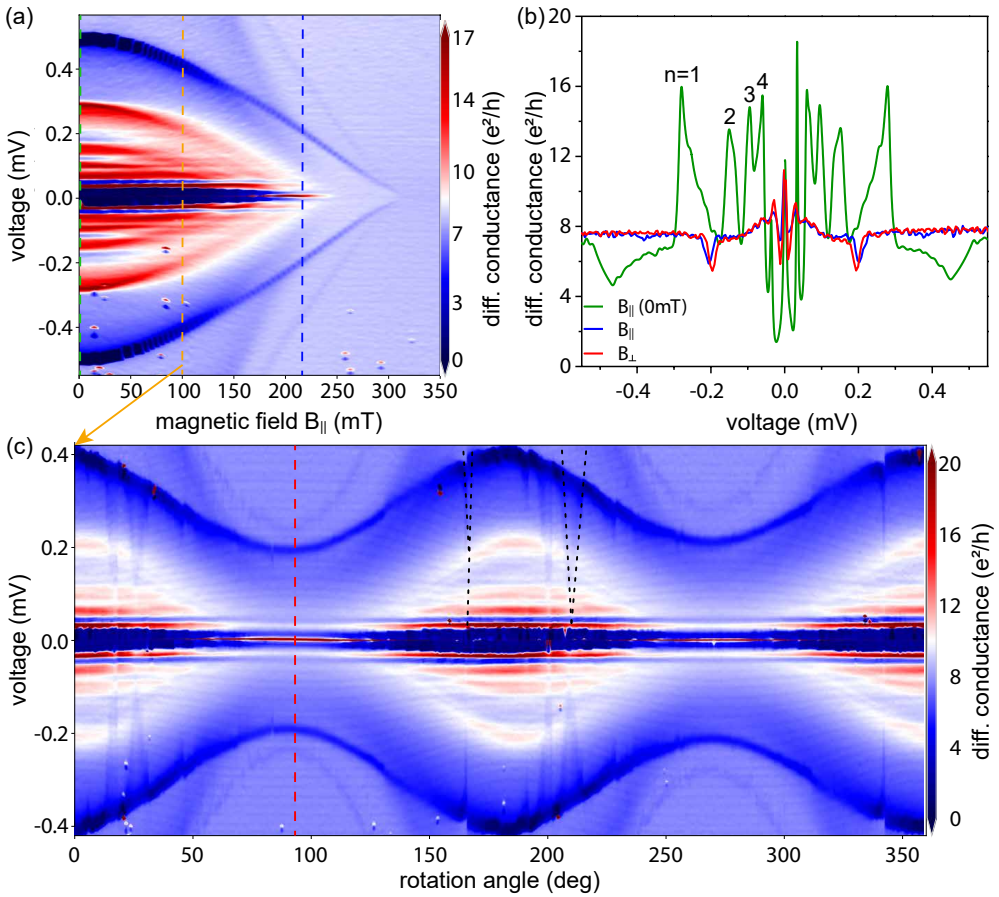

Figure 3.6 – *(a) Differential conductance as a function of bias voltage and magnetic field at zero gate voltage. The field is oriented in-plane and parallel to the nanowire axis. The data along the orange dashed line correspond to the data at* 0° *in (c). (b) Traces of the differential conductance vs. bias voltage. The green curve shows the differential conductance at zero field. The red curve corresponds to the data along the red line in (c) for* $B_\perp = 100\,mT$*, while the blue trace corresponds to the differential conductance along the blue dashed line in (a) at* $B_{||} = 215\,mT$*, respectively. The curves were chosen so that the gap energy matches. (c) Differential conductance as a function of bias voltage and of the magnetic field orientation. The magnitude of the magnetic field was kept fixed to 100 mT and the gate voltage was set to zero. Zero angle corresponds a magnetic field orientation along the nanowire axis. At* 90° *the field is perpendicular to the substrate. The dashed black lines highlight some irregular features observed in the differential conductance. Image taken from [388].*

quantum dot. Figure 3.5 (a) and (b) show the conductance vs. bias voltage for an out-of-plane field as well as for a magnetic field applied parallel to the nanowire axis, respectively.

As can be seen, both measurements show the typical damping and smearing out of the gap edge peaks, which is related to the continuous closing of the induced proximity gap if the magnetic field is increased. The field-induced changes in the normal-state conductance are most likely related to quantum fluctuations in the nanowire, i.e. the previously mentioned universal conductance fluctuations. However, these should just affect the background conductance rather than the transport below the superconducting gap. Using the first derivative of the differential conductance, it is possible to extract the actual gap width for each trace. Even though this method underestimates the gap width for small magnetic fields, it enables us to find reliable values when the actual gap edge peaks are already completely suppressed. Fig. 3.5 (c) summarizes the field-dependent gap width in terms of energy for both the parallel (blue) as well as the perpendicular (red) field. For the latter, we obtain a critical field of $B_c = 130\,\mathrm{mT}$, while the first is almost two times larger, with $B_c = 250\,\mathrm{mT}$. These comparably small values of B_c with respect to other works can be attributed to the much thicker Al shell of 25 nm in our case [31, 394]. Additionally, both traces shown in Fig 3.5 (c) deviate from the conventional BCS-behaviour, resulting in a much weaker field-dependency of Δ. However, we would like to stress that the closing of the gap is not necessarily coupled to a softening of the gap, as can be seen in Figure 3.5 (d). Here, we analyzed the change of the ratio between the averaged field-dependent zero

bias conductance $G_S(B_0)$ and the conductance above B_c, $G_N(B_0)$, as a function of fractions of the critical field. As long as the applied in-plane field is smaller than $0.9B_c$, $G_S(B_0)$ is mainly limited by the noise floor of the system. However, above this value, the conductance increases continuously, until it reaches $G_N(B_0)$. We interpret this as another proof of the hardness of the induced proximity gap in our system, which is not disturbed by parasitic sub-gap states even for comparably large magnetic fields.

Finally we present differential conductance measurements where the gate bias is set to zero, i.e. the nanowire bridge is conductive and no tunnel barrier is present. In Fig. 3.6 (a) the differential resistance vs. bias voltage is measured as a function of a parallel magnetic field. The conductance modulations for bias voltages in the range of $\pm 300\,\mu$V can be attributed to subharmonic gap structures due to multiple Andreev reflections [164, 365, 366]. The differential conductance trace at zero magnetic field is shown in Fig. 3.6 (b). We assign the feature found at about $280\,\mu$V to $2\Delta/e$. The value for Δ extracted here is smaller than the bulk gap of Al. We attribute the lower value to the fact that the induced proximity gap in InAs is relevant instead of the bulk gap of Al. In contrast to the previously discussed measurements in the tunneling regime, here the induced gap is probably weakened towards the center of the junction, since no tunnel barrier is blocking the diffusion of carriers. In addition to the structure at $2\Delta/e$, higher order subharmonic gap structures are also identified at $2\Delta/ne$ with $n = 2$, 3, and 4. We attribute the sharp feature at around $500\,\mu$V to some parasitic junction in series presumably at the boundary between the NbTi contact fingers and the Al shell. Upon increasing the magnetic field the positions of the subharmonic gap structures move towards zero bias reflecting the decrease of the superconducting gap with increasing field. At the critical field of 250 mT the subharmonic gap structures vanish. The critical field found here is in accordance to the value determined from the measurements in the tunneling regime.

In order to find out how the magnetic field orientation affects the junction characteristics, the differential conductance as a function of bias voltage was recorded for a full rotation of magnetic field within the plane defined by the nanowire axis and the normal to the substrate (cf. Fig. 3.6(c)). Here, the magnitude of the magnetic field was fixed at 100 mT. The trace of the differential conductance at 0°, parallel to the nanowire, is indicated by the orange line in Fig. 3.6 (a). When rotating the magnetic field out-of-plane and perpendicular to the wire the sequence of subharmonic gap features shifts towards zero bias. This can be attributed to the fact, that the gap of the Al film is more strongly suppressed for a perpendicular magnetic field than for a fields aligned along the thin superconducting layer. The positions of these features scale with the superconducting gap.

To find out whether the magnetic field orientation changes the pattern of the differential conductance tracks, we compared the characteristics at a perpendicular field (90°) with the curve at a parallel field (0°) at correspondingly higher field strength (cf. dashed blue line in Fig. 3.6 (a)) to provide the same superconducting gap energy. As can be seen in Fig. 3.6 (c), both curves are matching very well and no significant difference is observed.

Although the general conductance pattern varies smoothly with the magnetic field direction, some distinct features are found, as indicated by the dashed black lines in Fig. 3.6 (c). These features are reproducible since they appear again after a field rotation by 180°. So far, we have not yet been able to assign the exact cause of these structures. However, we speculate that they are related to magnetic field dependent states moving in and out of the superconducting gap, e. g. controlled by an angle-dependent g-factor [395] or are induced by the orientation-dependent vortex dynamics within the NbTi or Al layer.

3.2.3. DISCLAIMER

The major part of this section, including figures and captions, have been already published by the author in [388]. All additional segments or those who have been altered are indicated with footnotes. For images, the phrase"Image taken from..." was added to clarify their origin. The nanowire growth was performed by Pujitha Perla, Timm Mörstedt and Mihail Lepsa. The fabrication of the devices was evenly split between Russell Deacon and Patrick Zellekens. The transport measurements at low temperature were carried out by Patrick Zellekens and Russell Deacon. The TEM analysis was performed by Aruni Fonseka and Steven Hindmarsh. The manuscript [388] has been written by Patrick Zellekens, with scientific supervision and advisory from Thomas Schäpers, Koji Ishibashi, Ana Sanchez and Mihail Lepsa.

V

QUBITS AND MICROWAVE SPECTROSCOPY

1

HYBRID QUBITS I: THE GATEMON QUBIT

As already pointed out within the theoretical background in Sec. 5.1, the **Transmon** qubit is based on the collective excitation of a macroscopic quantum circuit. To be more specific, a two-level system (**TLS**) is realized between the ground state and first excited state of an **anharmonic oscillator** consisting of a *capacitor* and a *tunable kinetic inductance*. Traditionally, the latter is formed by means of a **SQUID**, for which the required tunability is determined by the externally applied magnetic flux. However, instead of two static Josephson junctions in parallel, a single but *active* device is used in this thesis. Using a semiconductor nanowire as the *weak link* and coupling a local gate electrode to it, the magnitude of the supercurrent and therefore the kinetic inductance can be tuned purely electrostatic. The result is a potentially highly versatile system in which the coupling between adjacent qubit structures could be realized by means of *floating gates*. However, besides the actual Gatemon, the circuit also requires well-defined *input* and *output* ports for the high frequency signal. There are two different approaches to achieve this. The first of them is based on a dedicated **3D cavity**, which not only encapsulates the qubit chip and the required Gateline but also determines the mode distribution and spectrum due to its shape. The other one aims for a 2D on-chip combination of the qubit with manipulation and readout structures by means of *circuit quantum electrodynamics*. Both approaches are investigated and compared within the two following sections.

V

1.1. GATEMONS COUPLED TO 3D CAVITIES

Chronologically, planar layouts in which the qubit is directly embedded within the circuit have been replaced by **three-dimensional cavity resonators** as they offer several advantages. This can be easily understood when considering that the transition from an excited state into the ground state goes alongside with the emission of a photon. Thus, the whole process is a function of the mode volume of the **final photon state**. Thus, 3D transmons aim towards the combination of a high coupling strength with significantly longer coherence times [396–398]. In conventional circuit layouts or other qubit system the latter is usually hard to achieve, as strong coupling to the cavity fields normally implies a strong coupling to the environment.

Simply speaking, a 3D cavity can be understood as a finite volume of space fully enclosed by metal. In our case, the metal shielding is realized by means of superconducting Al in order to minimize **cavity losses** that would otherwise arise from the *surface resistivity*. The input of microwave signals into the cavities and the output signal coupling are done using **SMA pin connectors** which penetrate the shielding, reach into the *cavity volume* and can be treated as a **two port network** (cf. Fig. 1.1). The *insertion depth* thereby directly determines the coupling strength between the cavity and the environment. The lowest electromagnetic field mode that can exist within the system is the $\mathbf{TEM}_{010}$ mode. It should be pointed out that, in contrast to planar and circuit-based structures, the 3D design provides less flexibility with respect to the *working point* in frequency space. As the coupling between the Gatemon and the cavity occurs via the **capacitance**, the qubit chip needs to be located in an **anti-node** of the distributed electric field. Thus, the length of the 3D resonator has to be set to $\lambda/2$ to allow exactly one *standing wave anti-node* in the propagation direction.

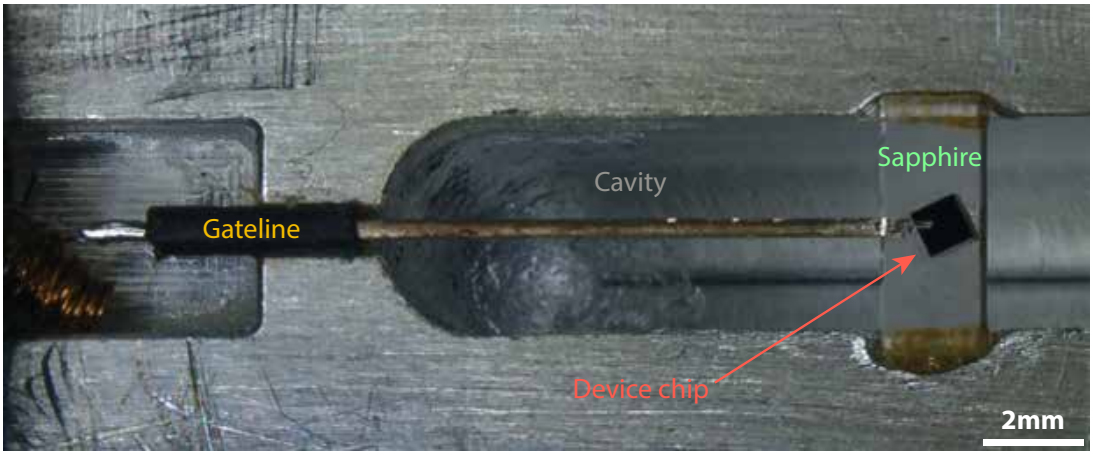

Figure 1.1 – *Optical micrograph of an opened 3D aluminium cavity with a single device chip glued to the sapphire holder ("bridge"). The incoming metal line acts as the connection between the DC fridge wiring and the on-chip gate electrode.*

A general advantage of 3D cavity systems is the well-defined eigenmode spectrum of the electromagnetic field [396, 397]. This field exhibits a highly diluted and distributed field strength and large vacuum participation with a minimum of lossy components inside the mode volume. Consequently, it is comparably easy to operate such systems even at low photon numbers. However, besides the inner walls of the cavity, internal losses can also arise from parasitic two-level systems in dielectrics present within the mode volume, such as the qubit chip substrate. Thus, special care was taken to minimize the chip dimensions and the carrier structure. For the latter, a thin **sapphire bridge** has been selected. As shown in Fig. 1.1, the dimensions of this support structure are only slightly larger than the actual qubit chip in order to further minimize the potential loss channels. However, one intrinsic loss channel is given by the macroscopic gate line, which limits the external Q factor due to its influence on the number of photons that leave the cavity through the dedicated input or output lines. The design of the 3D Gatemon (cf. Fig. 1.2 (a)) is inspired by the layout of conventional Transmon qubits [220, 400]. Here, two large, adjacent and 100 nm thick niobium pads form the capacitive element. However, instead of a *SQUID* structure, both pads are coupled by means of a single, gate-tunable nanowire Josephson junction. The coupling between the fundamental cavity mode, i.e.

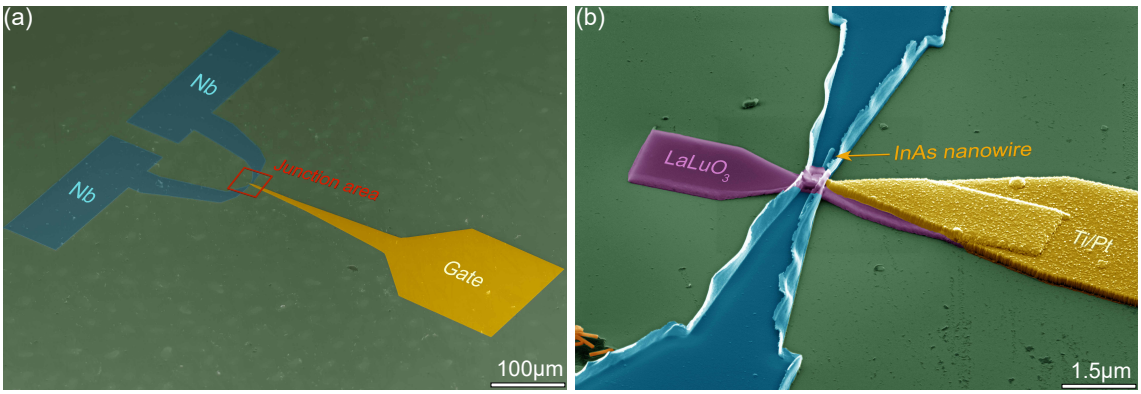

Figure 1.2 – *False-colored SEM micrograph of a nanowire-based 3D Gatemon structure on a Si/SiO_2 substrate. (a) The large niobium pads act both as an antenna as well as the capacitive element of the Gatemon. The rectangular shape ensures a stronger localization of the macroscopic dipole moment and thus an improved coupling to the electric field in the cavity. The DC connection between the gate electrode and the fridge wiring is realized via 100 nm thick Ti/Pt bond pads. (b) Zoom-in of the InAs nanowire Josephson junction. The contacts are formed by means of an ex-situ approach with an Ar^+ pre-cleaning step and the subsequent deposition of 90 nm Nb. In order to enhance the gate tunability, a 60 nm thick layer of $LaLuO_3$ is used as the dielectric (k=26 [399]) and to decouple the Nb contacts and the nanowire from the top-gate electrode above them.*

TEM_{010}, and the Gatemon structure is determined by the **dipole moment** $\vec{d}$ of the qubit structure. To be more precise, $\vec{d}$ is formed by the spatial displacement of $n \times 2e$ **Cooper pair charges** between the two superconducting pads [401, 402]. The dipole moment couples to the *y-contribution* of the **root-mean-square vacuum electric field** of the first cavity mode [403, 404], effectively behaving like an **antenna**. Thus, the dimensions of the pads have a large influence on the properties of the whole system, as they determine the **charging energy** E_c of the *anharmonic LC oscillator*.[1] In addition to their direct influence on the formation of the two-level system, the pads also determine the **cavity-qubit coupling strength** g

$$g = \mu \sqrt{\frac{\omega}{2\hbar\epsilon_0 V_m}}, \tag{1.1}$$

with V_m as the mode volume of the first resonant cavity mode:

$$V_m = \frac{\int_V \epsilon_{r_c} E^2(r_c) d^3 r}{\epsilon_{r_q} E^2(r_q)}. \tag{1.2}$$

Here, the term in the numerator refers to the three-dimensional field distribution $E^2(r_c)$ in the whole *cavity volume* V with permittivity ϵ_{r_c}, while the term in the denominator corresponds to the field strength at the location of the qubit [2].

The coupling strength g needs to be large enough in order to induce a sufficient shift of the cavity tone and allow a **dispersive readout** of the qubit state. On the other hand, if g becomes too large, the system is not longer limited by the **coherence** of the TLS rather than by *parasitic decay channels* due to **spontaneous emission**. This phenomenon is known as the **Purcell effect** and describes the enhancement of the **spontaneous radiative transition rate** for atoms embedded within a resonant cavity. The latter is a direct consequence of **Fermi's golden rule**, which relates the transition rate to the total density of accessible final states. However, in the far detuned limit, the decay rate is instead suppressed by the Lorentzian-like frequency response of the cavity, resulting in the so-called **Purcell rate**

$$\Gamma_P = \Gamma_F K \frac{\lambda^3}{8\pi V_m} = \frac{g^2}{\Delta^2} \kappa_L, \tag{1.3}$$

[1] This is different to conventional Transmons based on *tunnel junctions* in a *SQUID circuit*, as in this case E_c is also a function of the junction dimensions due to the non-neglectable junction capacitance caused by the large spatial extension of the structures.

[2] As the Gatemon chip is small compared to the fundamental mode wavelength, its dimensions may be neglected for this analysis.

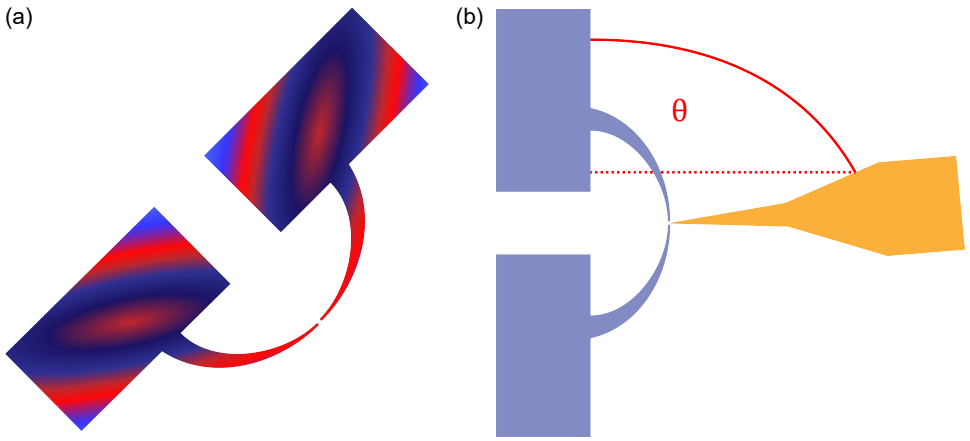

Figure 1.3 – *Schematic depiction of the two main issues that manifested themselves during the microwave measurement. (a) The large dimensions of the niobium pads induce spatial variations of the electric potential due to fluctuations of the superconducting order parameter. However, in contrast to the ground plane in microwave circuits, it is not possible to drive the potential back into equilibrium by means of additional bond wires. The consequence is a strong relation between the external Gatemon properties, e.g. the dipole, and the position of the niobium leads between the pads and the actual nanowire Josephson junction. (b) As a dipole-based quantum system, the Gatemon is controlled with a spatially focused electric field that is coupled in by means of a $\lambda/2$ resonator. Unfortunately, the latter makes the whole system sensitive to other capacitive components. The most prominent ones are the gateline and the corresponding bonding pad, which can cause a performance drop of almost 90% if there is an angle mismatch between the gate lead and the niobium pads with respect to a perfect perpendicular alignment [405].*

with Q as the quality factor of the system, K as an geometric factor, Δ the detuning between the cavity and the qubit and κ_L as the total loss rate. Here, it has turned out that an **asymmetric** design of the superconducting pads (cf. Fig. 1.2 (a)) as well as a smaller separation results in an improved coupling with a still comparably low Purcell rate [401, 402].

In order to simplify the device fabrication procedure for the Josephson junctions, the required nanowires have been placed with the so-called **tissue method**. Here, a large amount of nanowires is picked up at once from the growth substrate by means of a *cleanroom tissue* and then mechanically transferred on the device chip. By utilizing SEM images, the most promising nanowire is selected for the subsequent device formation, which consists of the already described procedure for *ex-situ junctions* (cf. Sec. IV) as well as the deposition of a thick layer *high-k dielectric* and a *top-gate electrode*, as shown in Fig. 1.2 (b) [3].

Unfortunately, most of the 3D Gatemon qubit samples were not suitable for measurements at low temperatures due to significant *leakage currents* through the gate dielectric. However, earlier works have shown that it is possible to use rare-earth-based dielectrics like $\mathbf{LaLuO_3}$ or $\mathbf{HfO_2}$ in combination with semiconductor nanowires without a significant degradation of their insulating properties. Thus, the deposition temperature of the dielectric has been identified as the most likely source for the observed behavior. Unfortunately, this became a permanent issue, as the maximum temperature for the *liftoff resist mask* is located far below ideal growth temperatures. Additionally, the niobium tends to degrade heavily in oxygen-rich atmospheres at high temperatures.

Two other issues arose from the sample design itself. First of all, it turned out that the geometric dimensions of the metal pads already exceed the point at which they can be considered as a **homogeneous** superconductor. Thus, when the high frequency signal is irradiated, the plates react with pronounced potential fluctuations, which go alongside spatial variations of the **superconducting order parameter** (cf. Fig. 1.3 (a)). In the experiment, this leads to an alteration of the supercurrent that is flowing through the Josephson junction. To be more precise, the system response and the strength of the cavity-qubit coupling depends on the position of the superconducting leads with respect to the edge of the large metal pads. An even more serious problem is related to the macroscopic gate connection between the fridge wiring and the actual Josephson junction. As already mentioned, the

[3] Further details about the fabrication and optimizations are provided in the Master Thesis of Arthur Leis [41]

Gatemon relies on a capacitive coupling between the dipole moment of the qubit and the electric field. However, in contrast to a 2D system, the latter is distributed across the whole macroscopic cavity instead of being *spatially localized* within a transmission line and/or a resonator. Thus, everything that *can* couple to it *will* do so. Here, as shown in Fig. 1.3(b), both the gate line that comes from the outside as well as the gate electrode on the chip can induce an additional, *parasitic capacitance* if they are not carefully aligned, i.e. orthogonal to the qubit (capacitor). A systematic analysis has shown that a misalignment of only 5° leads to a power loss of already 85%. Due to the fact that the gate line has to be manually attached to the device chip, a situation in which a significant portion of the irradiated microwave signal never reaches the qubit structure is very likely. Of course, the same holds for the photon that is emitted from the qubit itself, making the whole system hardly control- and measurable.

In view of the problems outlined above, the conclusion was made that the potentially larger lifetime of a 3D Gatemon is usually overcompensated by the obstacles and difficulties that come hand in hand with the requirement to reach an ideal condition of the isolation, coupling and gate tunability. Together with the limited scalability, this motivated switching to 2D circuit-based systems, which are the focus of the following section. For further details regarding the measurement *peculiarities*, please check the PhD thesis of Steffen Schlör [406]. For the actual fabrication and optimizations of the 3D Gatemons, more informations are provided in the Master thesis of Arthur Leis [41].

V

1.2. 2D GATEMONS BASED ON CIRCUIT QED

As discussed in Chapter II, the microwave circuit needs to fulfill several criteria to allow the reliable initialization, manipulation and detection of the **qubit state**. One of the most important ones is a well-defined coupling between the transmission line, the resonator and the actual qubit structure. For the **TiN-based** design shown in Fig. 1.4, the latter is determined by the separation between the termination point of the $\lambda/2$ resonator and the **circular capacitor** (purple) d_q, as depicted in Fig. 1.4 (b). However, this is just one part of the **coupling quality factor** Q_c, as the main contribution comes from the width of the **decoupling line** between the transmission line and the resonator d_{tr} (cf. Fig. 1.4 (c)). Here, $1/Q_c$ is proportional to the width of this superconducting segment (green) which shorts the *ground plane* sections around the resonator.

As the setup is intended to be used for **dispersive readout**, d_{tr} is set to 3 μm in order to push the whole system into the **overcoupled regime**. In contrast to conventional **pad-based geometries**, the radial-symmetric and concentric shape of the hollow, **circular capacitor** leads to a reduced and more spatially confined electric dipole moment. The latter results in a suppression of **radiation losses** and the **Purcell effect** [407, 408]. Additionally, the embedding of the **inductive element**, i.e. the *Josephson junction*, into the capacitor structure leads to a significant reduction of the *qubit footprint*. Based on the outer $r_{o1} = 100\,\mu$m, $r_{o2} = 175\,\mu$m and inner $r_{i1} = 50\,\mu$m, $r_{i2} = 130\,\mu$m radii, respectively, the capacitor shown in Fig. 1.4 (a) is supposed to exhibit a capacitance of C$\approx$ 60 fF [406] [4]. In order to reach the **Transmon regime**, $E_J/E_c > 50$ (see Sec. 5.1), the desired **supercurrent** for the **qubit operations** is $I_s = 100$ nA, which results in a *designed resonance frequency* of $f_r = 11$ GHz.

An exemplary Josephson junction with a channel length of $l = 90$ nm is shown in Fig. 1.4 (e). The used nanowire originates from the already introduced growth run **C** (cf. Sec. 2.1) with a doping level of n$\approx 1 \times 10^{19}\,$cm^{-3}. The gate electrode has been realized in a **sidegate** geometry (Fig. 1.4 (f)). Due to the chosen deposition method for the nanowires (**optical micromanipulator** [5], the separation between the gate and the junction is rather large and typically in the range of 1 μm. Thus, the corresponding *lever arm* is usually $\alpha \approx 1/1000$ (cf. Sec. 3.3), which raises the required gate voltages to induce a sufficient shift of the supercurrent to several volts. Even though this makes it necessary to alter the DC wiring within the measurement system, this issue is overcompensated by removing the dielectric in close proximity or around the semiconductor weak link.

As already discussed in Sec. 4.2, the exact prediction of the final resonance frequency of a resonator structure is rather difficult due to parasitic effects like *stray capacitances*, impurities within the superconductor or the contribution of the *kinetic inductance*. Thus, in the beginning of every microwave-based measurement, the position of the resonator in frequency-space has to be determined. A typical **single tone measurement**, driven by a *vector network analyzer* [**VNA**], is shown in Fig. 1.5 (a). Here, the **transmitted signal** $|S_{21}|^2$ exhibits three pronounced *dips*. Every single one of those *Lorentz-like* features can be attributed to a successful photon transfer to a resonator structure. However, comparing the measured signal with the design shown in Fig. 1.4, it becomes immediately obvious that one feature is missing. An optical investigation after the measurement revealed that this could be attributed to a broken *bond wire* which shorted the resonator number (2). Additionally, it also induced the *wide band* drop in magnitude around 9 GHz by adding a parasitic bypass to the ground plane. Unfortunately, the latter is a common issue in microwave circuits due to the extensive requirement of bond connections between different sections of the ground plane and was one of the reasons for the development of the **Flip-Chip** architecture presented in Sec. 4.3 [6]. Despite this problem, the remaining resonators reveal an internal quality factor of Q_i=12000 and a loaded quality factor of Q_l=5000. It should be pointed out again, that in contrast to the structures shown in Sec. 4.3, the currently used resonators are intentionally *overcoupled*, i.e. the effective coupling strength is determined by the layout rather than the quality of the superconductor.

In order to conserve and protect the quantum state of the Gatemon, the whole system is probed

[4] The underlying simulations and calculations have been performed by Steffen Schlör and are based on a 2D model of the microwave circuit within the software framework **Sonnet** [409–411].

[5] Further details are given in [412] and the master thesis of Patrick Liebisch [413]

[6] Further details about this issue are provided in the Thesis of Steffen Schlör [406]

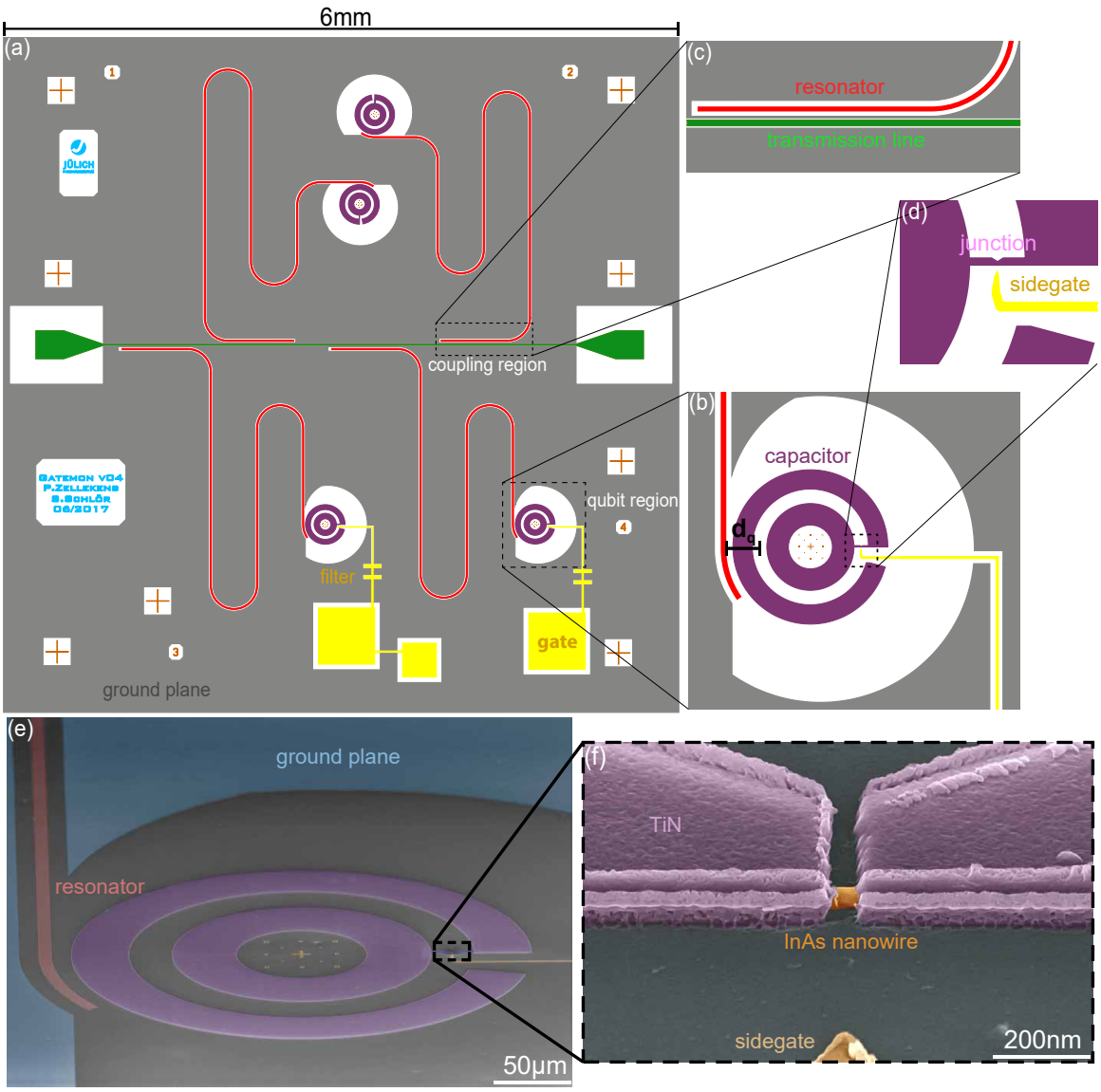

Figure 1.4 – *(a) Schematic illustration of a 2D Gatemon circuit in coplanar waveguide geometry. The connection to the external microwave source is realized via a common transmission line (green) which is terminated by two 50Ω impedance-matched bonding pads. A large scale ground plane ensures a shielding of the four qubit structures (purple). Here, every Gatemon can be addressed by means of a λ/2 resonator (red) . In order to ensure an independent manipulation and control of the qubits, all resonators are frequency-mismatched with Δf_r=300 MHz. The embedded microwave filter (orange) are intended to put an upper limit to the photon loss rate through the gateline. (b) The Gatemons are designed in a hollow circular geometry to improve the localization and strength of the qubit dipole moment. (c) The efficiency of the photon transfer between the transmission line and the resonator, i.e. the coupling strength, is controlled with a superconducting decoupling line between the resonator and the transmission line. (d) The side-gate structures (yellow) allow an electrostatic tuning of the supercurrent of the nanowire Josephson junctions. (e) False-colored SEM micrograph of a finalized and ready-to-measure Gatemon structure. The hollow circular capacitor (purple) ensures an increased spatial localization of the qubit dipole moment compared to pad-like structures. The surrounding ground plane (blue) shields the λ/2 resonator (red) and the qubit from external parasitic microwave signals, e.g. box modes, and focuses the electro(-magnetic) field into the resonator line. (f) Zoom-in of the nanowire Josephson junction that is embedded within the capacitor structure and acts as the nonlinear inductance. The weak link is realized by means of an Te-doped InAs nanowire with ex-situ fabricated TiN contacts. For the electrostatic tuning of the supercurrent, the device is coupled to a Ti/Pt side-gate in close proximity to the junction. The use of an air bridge instead of a high-k dielectric decreases the chance for parasitic two-level systems ("trap states") that could potentially interfere with the antinode of the electric field at the qubit position.*

by means of a **dispersive readout**. Thus, instead of directly measuring the occupation of the qubit, only its back-action on the resonator is read out. Here, a successful coupling to the qubit induces a shift of the resonator frequency, which is exemplary shown in Fig. 1.5 (b) and (c). The large hysteresis between the forth- and backsweep can probably be attributed to a combination of the comparably

V

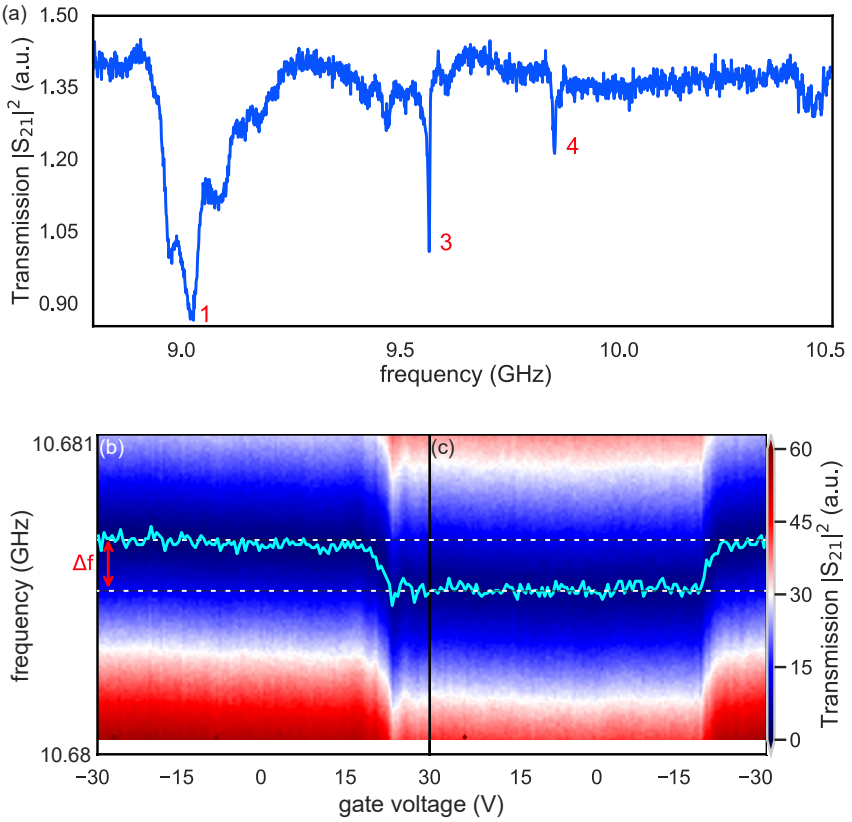

Figure 1.5 – *(a) VNA-driven single-tone measurement of a CPW transmission line in the range of 8.8 to 10.5 GHz coupled to four individual $\lambda/2$ resonators. Indicated with 1, 3 and 4 are the corresponding resonances which appear as Lorentz-like "dips" in the transmitted microwave power. The broad band feature around 9 GHz and the missing resonator (2) can be attributed to a broken bond wire that created a short between the resonator line and the surrounding ground plane. (b) and (c) Gate dependent single-tone transmission measurements performed on a Gatemon qubit coupled to a resonator with $f_r \approx 10.68$ GHz. The response of the resonator is probed for two different gate voltages. In both measurements, a small but pronounced frequency shift $\Delta f \approx 200$ kHZ is observed as an indication for a successful coupling and photon transfer between the Gatemon qubit and its drive resonator. Here, the bright green line indicates the gate-dependent position of the center of the resonance. However, the exact gate voltage for the on- and offset of the coupling exhibits a large hysteresis. The underlying microwave measurements have been carried out by S. Schlör [406].*

small lever arm as well as the large **surface state density** on the uncapped and untreated nanowire section. However, despite the non-ideal electrostatics, one can observe a clear downward shift of the resonator frequency, with $\Delta f \approx 200$ kHz. The latter is a clear proof for a successful coupling between the macroscopic microwave components and the microscopic quantum system formed by the nanowire Josephson junction and the superconducting capacitor attached to it. However, it should be pointed out, that there is no obvious avoided crossing, which would be the signature of a photon transfer into a single two-level system.

The most important and fundamental property of a qubit-like system is its resilience to intrinsic and extrinsic decay processes. Experimentally, the latter can be investigated by means of a so-called **Rabi measurement**. This method, which is carried out in the **time domain** and a **heterodyne two-tone setup** (see Sec. 2), consists of a series of excitation- and enforced relaxation-processes. The idea is to send a **set** [π] signal to the system and, right after that, perform a **cavity readout** [$\pi/2$ pulse] operation and probe the state of the qubit. By repeating this measurement N times for different delays Δt between set and read, the **time-dependent probability** to find the qubit in the **excited state** can be determined. Fig. 1.6 (a) shows the resulting Rabi response for the cavity-qubit system introduced in Fig. 1.5. Here, the y-axis represents the *state inversion* of the qubit, which corresponds to the logical states $|0\rangle$ and $|1\rangle$ of the two-level system. Every single data point is formed by averaging the outcomes of 1000 individual $\pi \rightarrow \Delta t \rightarrow \pi/2$ pulse operations. In order to ensure a full relaxation of the system, all measurements were separated by an additional waiting time of 200 μs. The time-

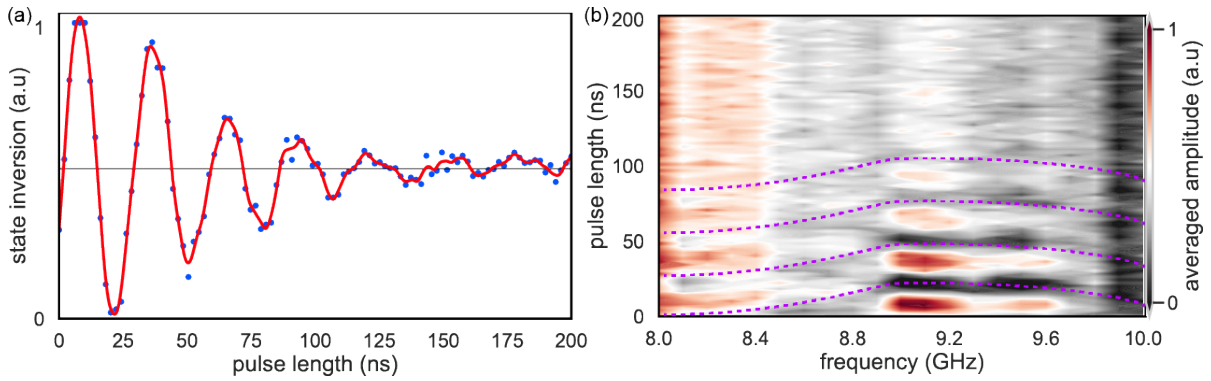

Figure 1.6 – *Exemplary microwave-driven time-domain characterization of a single Gatemon qubit. a) At the qubit frequency of f_q=9.0 GHz, the system exhibits pronounced oscillations of the state occupation, i.e. Rabi cycles. Here, a Rabi frequency of Ω=210 MHz and a qubit lifetime of T_1=100 ns can be extracted considering a quality factor of the resonator of Q=13000. b) The same measurement for different detunings Δ between the resonator and the Gatemon. The weak frequency dependency of the Rabi response, i.e oscillation period and magnitude, indicates a non-sufficient **anharmonicity** of the Gatemon and/or the simultaneous excitation of multiple levels.*

dependency of the state inversion, i.e. the **Rabi oscillation**, is thereby a clear signature of a qubit-like two-level system. For the given measurement shown in Fig. 1.6 (a) a **Rabi frequency** Ω = 210 MHz, a **lifetime** T_1 = 100 ns and a **Rabi quality factor** Q_R=4 could be extracted. Here, the fast decay of the oscillation is a strong indication for additional, higher order relaxation mechanisms. The latter are usually caused by excitations into higher levels with faster spontaneous emission rates. Besides the single-spot Rabi signal, it is also important how the system reacts to small deviations from the actual state transition frequency. Fig. 1.6 (b) shows the system response for increasingly larger frequency mismatches (**detunings**). Here, an ideal TLS should show a characteristic and strong decrease of the Rabi amplitude for small frequency perturbations (**Chevron plot** [414–416]). In our case, the system exhibits a rather constant Rabi frequency with only a small modulation. This, together with the fast decay visible in Fig. 1.6 (a), is a strong hint for an insufficient **anharmonicity**. In this case, the small difference in transition energies allows the excitation into higher states, which can be understood as a superposition of multiple Rabi systems. For the given device, the most likely cause is a too large critical current, which results in a too large Josephson energy E_J. Thus, even though the presented device acts as a controllable TLS, it should be considered as a non-ideal (i.e. "bad") qubit.

2

HYBRID QUBITS II: THE ANDREEV QUBIT

2.1. GENERATION I: INDUCTIVE RESONATOR-QUBIT COUPLING

The **Andreev qubit**, as described in Section 5.2, is realized by means of a single Andreev bound state (**ABS**) that forms the required two-level system. Being a strongly spatially-localized and well-isolated excitation, it should be much less affected by external noise sources. However, at the same time and in contrast to the Gatemon qubit, it also put much stricter demands on the experimental realization of the system itself as well as for the manipulation and readout mechanisms.

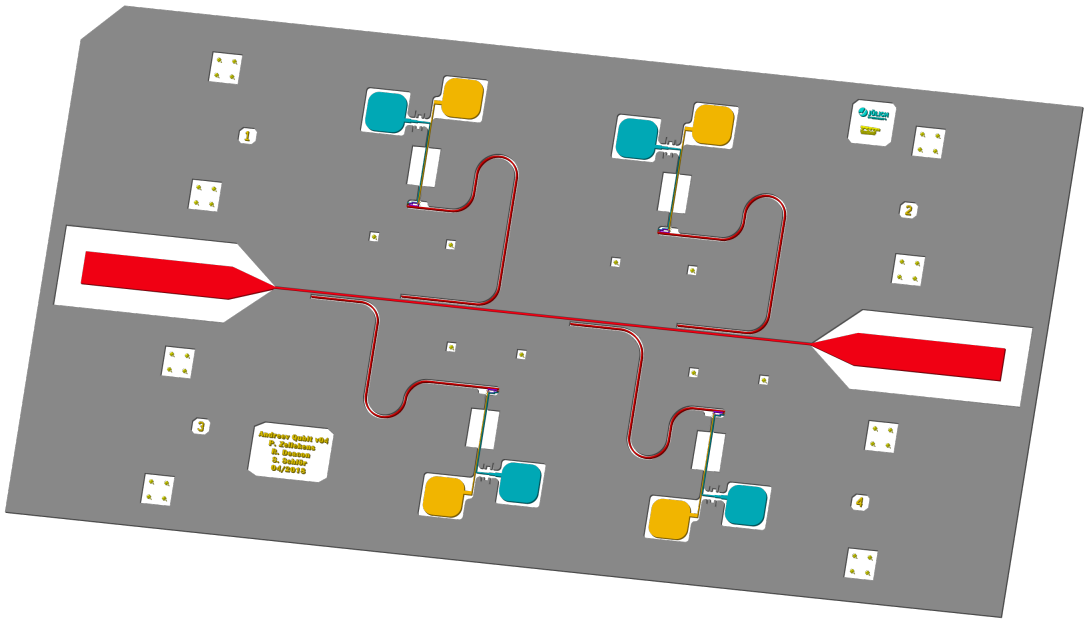

Figure 2.1 – *Schematic depiction of a 1st generation **Andreev circuit**. All superconducting structures, i.e. the ground plane (grey), the transmission line and $\lambda/4$ resonators (red) as well as the flux bias line (blue) consist of reactively sputtered TiN (see Sec. 2.4). The gates are designed according to the already introduced **bottom gate** geometry, with a large and thick Ti/Pt bonding pad as the connection point to the fridge wiring. Manipulation of the individual qubits is done via a combination of gate-based electrostatic and field-based flux tuning. For the given design, the application of the second tone has to be done by means of the coplanar waveguide structure, as the DC flux bias line just supports frequencies up to* 10 *kHz. This issue has been resolved in later revisions.*

Fig. 2.1 provides an exemplary overview of the used microwave-circuit. The main difference, compared to the previously described Gatemon circuits, is a much larger number of connections to the fridge wiring and the electronic environment. Additionally, even though still realized in a transmission line based CPW geometry (red), the readout is now performed by means of $\lambda/4$ resonators. Following the resonator theory in Section 4.2, this is equal to a maximum in the **magnetic field**. Thus, it is necessary to induce an **inductive coupling** to transfer the microwave signal into the device. In order to manipulate the states, on the other hand, both an electric as well as a magnetic field are required. The latter is thereby generated by means of a so-called **flux bias line** (blue), which consists

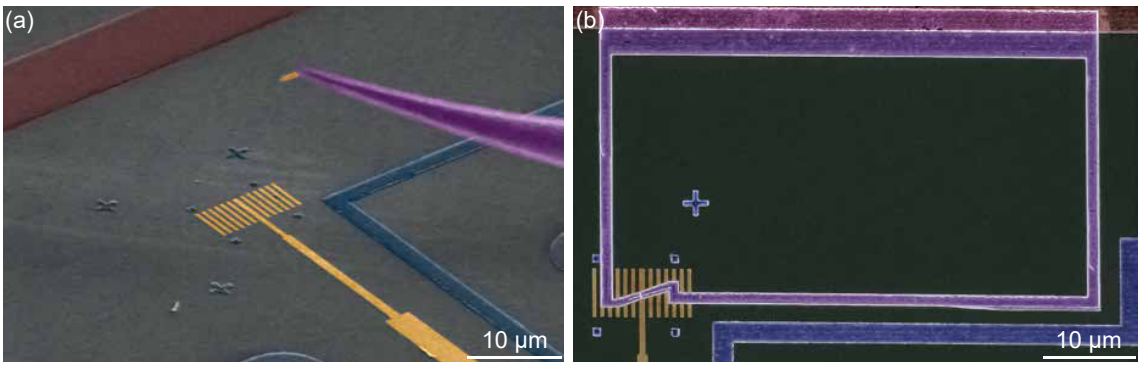

Figure 2.2 – *(a) False-colored SEM micrograph of a single InAs nanowire that has been picked up from the growth substrate by means of a **tungsten tip** attached to a **micromanipulator**. Doing so, it is possible to place nanowires with sub-micrometer precision on the bottom gate electrodes underneath. (b) A final Andreev qubit structure consisting of a InAs nanowire Josephson junction above the bottom gate electrodes and a **SQUID loop** (purple). The loop is electrically connected to the $\lambda/4$ resonator (red) in order to ensure a strong **inductive** coupling. The dedicated flux bias line (blue) allows the manipulation of the superconducting phase using a tunable out-of-plane magnetic field.*

of a 2 μm wide and 50 nm thick *NbTi* layer. To minimise the coupling to the resonator, the line is terminated with the same reference potential, i.e. an nearby section of the global ground plane. For the electrostatic control, the already described bottom gate layout (yellow) is utilized.

The large number of pre-patterned structures requires precise control of the nanowire positioning. Thus, a SEM-based micromanipulator setup was used to transfer individual nanowires from the growth substrate to the bottom gate electrodes on the microwave circuit, as shown in 2.2 (a). In contrast to the method presented in [412], the used setup can also be used to perform **focused ion beam** operations, which makes it possible to sharpen the transfer tip occasionally.

Figure 2.2 (b) provides an overview of a finalized device after the successful placement of a nanowire (orange) which is connected to a superconducting *ring* (violet), thus effectively forming a **RF-SQUID-like** structure [417, 418]. The latter is thereby electrically connected, i.e. inductively coupled, to the termination point of the $\lambda/4$ resonator (red). In order to tune the **dispersion relation** of the system, i.e. $dE/d\delta$, the DC flux bias line (dark blue) is used to drive a current between a dedicated bonding pad and the ground plane. The induced out-of-plane field subsequently generates a magnetic flux within the SQUID loop, which ultimately changes the phase difference across the junction δ. Lastly, the bottom gate electrode (yellow) is used to tune the number of states within the nanowire. Here, the desired working point is usually close to pinch-off, but above the tunnel-limited Coulomb blockade regime.

The basic requirement for a fully functioning Andreev system is a successful coupling of the individual states to the resonator. Following the current-phase relation of a mesoscopic Josephson junction, this means that the transparency, i.e. the figure of merit for the *strength* of the projected superconductivity, needs to be large enough to push the minimum energy of the ABS close to the center of the gap. However, just as important is the number of channels in the semiconducting nanowire itself. Fig. 2.3 shows the flux-dependent single-tone response for a Josephson junction consisting of an InAs nanowire of type **C** (cf. Sec. 2.1) with ex-situ NbTi contacts at two different gate voltages. For 0 and multiples of 2π, there is no accessible state for the photons on the resonator and the system response is equal to the *effective resonance frequency*. The latter thereby refers to the fact that even though there is no direct energy transfer between both components, i.e. the resonator and the SQUID loop, for certain flux values, they still act as a coupled system. This manifests itself, for example, as a correction to the inductance with respect to the bare resonator and induces a shift of the resonance frequency.

For odd phase values, on the other hand, i.e. multiples of $\pm\pi$, it is not longer possible to probe the resonator by means of the transmission line. Here, the system response is suppressed exponentially and, at the same time, pushed down in frequency space. However, instead of an **avoided crossing**, which is the key signature of a successful coupling between a single Andreev bound state and the

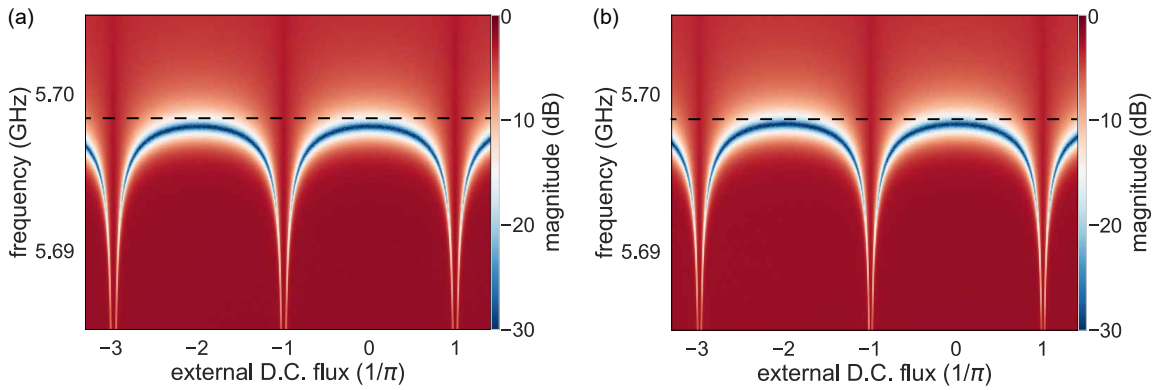

Figure 2.3 – *Flux-dependent single-tone response of an Andreev qubit based on a highly doped InAs nanowire with ex-situ contacts. A change of the applied gate voltage from (a) V_g=-5 V to (b) V_g=5 V, respectively, induced a small (≈ 3 MHz) but reproducible shift of the resonator frequency.*

resonator, the latter exhibits just a switching between an *on* and an *off*-state. This behavior is well known for **flux qubits**, in which the two quantum states are realized by a magnetic field dependent switch of the flowing direction of the persistent current [419–421]. For the given system, the observed response can be attributed to an extremely large supercurrent. The first assumption would be a short between the left and right superconducting electrode due to, for example, lift off problems. However, a sufficiently large change of the applied gate voltage, i.e. from −5V in Fig. 2.3 (a) to +5V in (b), leads to a small but reproducible and temporally stable shift of the resonance frequency for even flux values. This is a proof that the nanowire acts (at least) weakly as a current valve. Nevertheless, the system behaves more like a **macroscopic** Josephson junction in the sense that its properties are dominated by the pair wavefunction in the SQUID loop rather than the mesoscopic state structure within the nanowire channel. Consequently, it is not possible to probe transitions between individual Andreev levels.

Besides the obvious solution to use less conductive nanowires, a couple of circuit- and device-related issues could be identified during the check-up of the first generation chips. Thus, the following section focuses on a presentation of the performed optimization steps and a characterization of the 2^{nd} revision of Andreev circuits.

2.2. GENERATION II: IMPEDANCE-OPTIMIZED RESONATORS AND HIGH-FREQUENCY GATES

Based on the findings in the previous section, a number of changes have been applied to the circuit- and device-design. First of all, it turned out that the direct coupling of the SQUID loop to the resonator structure induces some instabilities in the combined system response. The most likely explanation is the partial removal of the flux traps in the resonator due to the coverage with the superconducting material of the SQUID loop. In addition, there were strong indications that the large width w of the leads allowed the formation of unpinned vortices within the SQUID loop itself. Thus, all superconducting structures of the SQUID have been reduced in width so that their dimensions are below the London penetration length of the NbTi, i.e. $w < 1\mu$m. Additionally, instead of a direct electrical connection, a normal conducting bypass consisting of a 10 nm thin layer of AuGe has been implemented between the SQUID loop and the ground plane. By doing so, as shown in Fig. 2.4 (a), it is possible to set an upper limit for the resonator-TLS coupling strength by maintaining an equal and homogeneous distribution of the electrical potential.

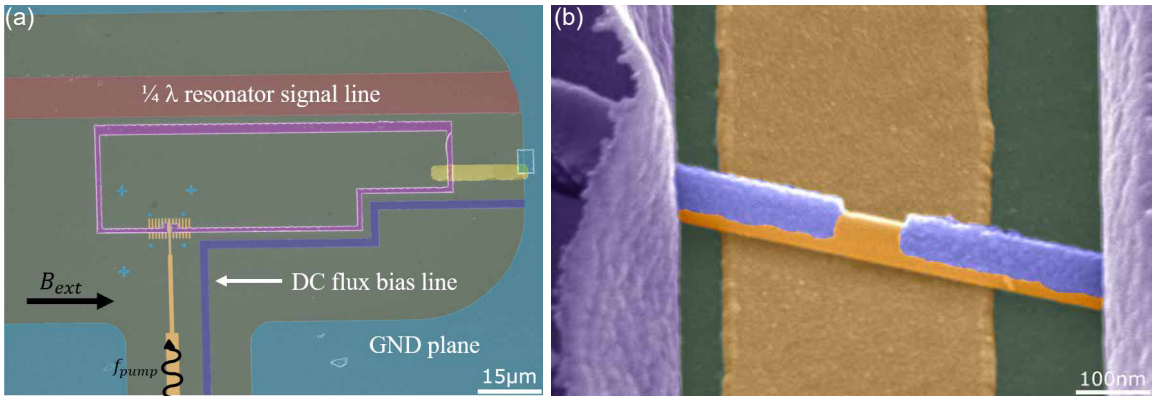

Figure 2.4 – *(a) False-colored SEM micrograph of an improved Andreev SQUID device. Here, the coupling between the resonator and the superconducting loop is realized by means of a normal conducting AuGe bypass. Additionally, all dimensions of the SQUID have been reduced in size to be smaller than the London penetration length of NbTi in order to suppress the formation of vortices. Lastly, the gate has been redesigned to be 50Ω-impedance-matched. The latter allows the simultaneous application of a DC and a HF-pump signal. (b) Zoomed-in sideview of an InAs/Al half shell nanowire Josephson junction. Here, the junction has been formed by means of wet chemical etching with* ***Transene-D****.*

In addition, a couple of changes have been applied on the level of the individual device and its electrostatic tuning. First of all, InAs nanowires with in-situ deposited Al shells are now used as the *active element*, as shown in Fig. 2.4 (b). Here, the actual junction is formed by means of wet chemical etching with Transene-D. The second change is related to the gate architecture. From the measurements of the previous section, we found that the initial plan to use the flux bias line as the **pumping channel** for spectroscopy experiments caused some serious issues in terms of device control. For frequencies above 10 kHz, the kinetic inductance induced an offset between the externally applied AC current and the actual motion of the Cooper pair condensate within the narrow superconducting metal stripe. Consequently, it became impossible to predict the amount of flux that was generated within the SQUID loop for a given current. In order to circumvent this problem, the decision was made to use the gate line instead. However, this required a thorough redesign of the structures to make them impedance-matched with the HF fridge wiring.

Following the same approach as in the fabrication chapter, it becomes immediately obvious that there are some major differences between a proper impedance-matched design of a superconducting and a normal conducting structure. In terms of the pure inductance, the design becomes much more simple as normal conductors do not exhibit a considerable kinetic inductance for frequencies below < 100 GHz due to the small **relaxation times** [422–424]. However, they have a small ohmic contribution that has to be considered. More importantly, due to the fact that the impedance relies on the actual resistance rather than the electric resistivity, there is again a geometric contribution. After testing different metal systems, including Ti/Au, Ti/Pt, Cr/Au and Cr/Pt, a 40 nm/200 nm thick

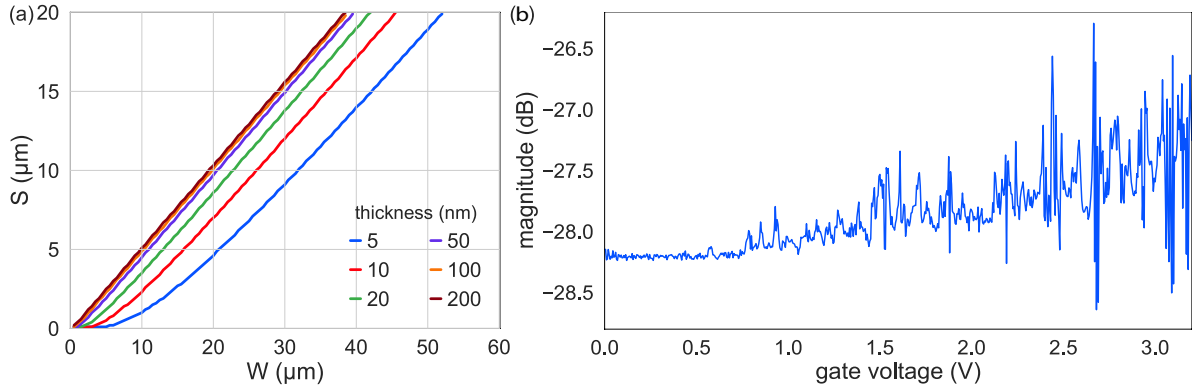

Figure 2.5 – *(a) Simulated geometry-dependent resonator impedance for different Pt thicknesses t. The lines indicate the perfect 50Ω-match for various combinations of resonator width (**W**) and ground plane separation (**S**). Above t=100 nm, the impedance becomes almost independent from the resistive contribution of the normal conducting metal layer. (b) Gate-dependent and VNA-based single tone measurement on the device shown in Fig. 2.4. Below a gate voltage of V_g=0.5 V, the device is pinched-off and no Andreev bound states are accessible by the resonator. Between V_g=0.5 V and 1.5 V, the nanowire exhibits pronounced Coulomb resonances that can be attributed to intrinsic quantum dots in the semiconductor channel. Above, the number of ABS increases continuously until the junction is pushed into the macroscopic limit.*

stack of Ti/Pt with a **resonator width** W=20 μm and a **ground plane separation** S=10 μm has been selected. A comparison for different Pt thicknesses is provided in Fig. 2.5 (a), which clearly shows that above 100 nm the contribution of the ohmic resistance becomes almost neglectable so that only the geometric inductance Z_k has to be considered.

The newly designed gate structures can be used for pulse frequencies up to 40 GHz. It should be pointed out that, in principle, Ti/Au would be more suitable due to its theoretically smaller specific resistance. However, for the available deposition methods, it turned out that Pt has a much higher quality [1]. Additionally, in the case of gold it is much harder to make a contact to an already existing metal structure, i.e. the bottom gate electrodes for the SQUID. Because of the larger internal strain of the available Au layers, the material tends to peel off. This effect becomes even stronger if the thickness of the gold layer is increased. As the new gates are intended to be used for both DC and AC signals, there are much higher demands on the external circuitry. However, in contrast to the Shapiro chips, there was not enough space to implement on-chip bias tees of sufficient performance onto the chips itself. Thus, the fridge wiring was altered in a way that the gate could be controlled by two separate lines that are decoupled by means of *circulators*, *RF filters* and *DC blocks* and joint together with a commercially available cryogenic bias tee.

Fig. 2.5 (b) shows a VNA-driven single-tone measurement of an device similar to the one shown in Fig. 2.4 (a) at $\Phi_{ext}=\pi$. In contrast to the wires used in the previous section, the system now exhibits a strong variation of the measured signal if the gate voltage is changed. For low gate voltages, the device is pinched off and the effective magnitude remains constant. Above a threshold of V_g=0.6 V, the nanowire opens up for transport through quantum dot states, which manifests itself as discrete Coulomb resonances in the measured magnitude. For even higher gate voltages, i.e. V_g=1.4 V, the resonator response exhibits pronounced spikes and dips that can be attributed to coupling events with Andreev bound states. However, due to the large lever arm of the used gate structure ($\alpha \approx 0.1$, see Chapter 3), the effective gate voltage range over which a single state goes down in energy and couples to the resonator is rather small. Thus, Fig. 2.6 provides a high-resolution magnitude map of the same device for gate voltages between V_g=3.9 V and 4.0 V and a frequency window of ±15 MHz around the resonance frequency. Here, the most prominent features are several interruptions of the bare resonator signal (black). Instead of a single and continuous line, the system exhibits multiple upwards-pointing parabola-like features that are separated from the straight resonator response by small sections of much higher magnitude. This effect can be attributed to the interaction between the resonator mode and the TLS-like Andreev bound states. In terms of the underlying quantum

[1] Van-der-Pauw-measurements at cryogenic temperatures revealed ρ_{Au}=220 Ωnm and ρ_{Pt}=130 Ωnm

V

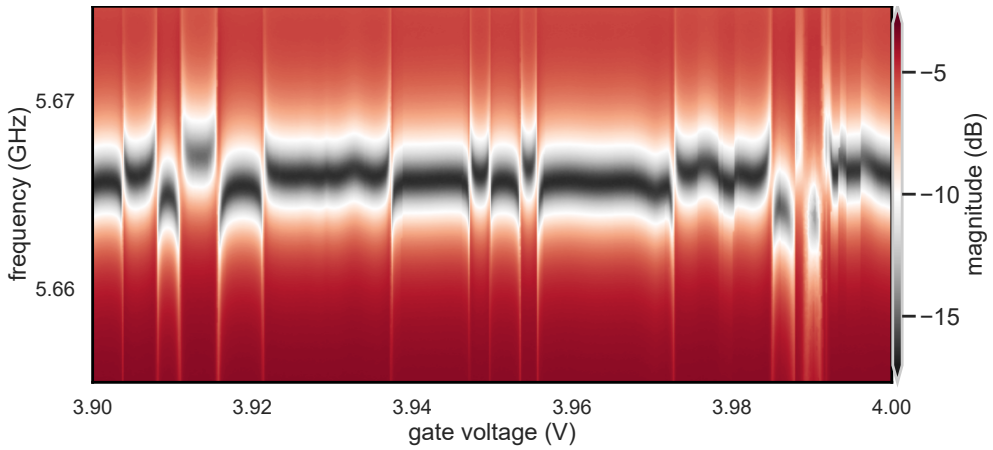

Figure 2.6 – *Exemplary transmission measurement of a λ/4 resonator that is inductively coupled to an InAs/Al shadow mask defined nanowire Josephson junction and phase-biased at π. The black area around 5.665 GHz corresponds to the coupling of the resonator to the transmission line. At certain gate voltages, the resonator is interrupted by avoided crossing events that can be attributed to an Andreev bound state coming down in energy until it can coherently exchange photons with the resonator.*

mechanics (cf. the Jaymes-Cummings model in Sec. 4.1), the direct intermixing of both systems is forbidden, which results in the observable **avoided crossing** features.

It should be pointed out that the observed parabolic behavior can not be directly translated into the dispersion relation of the system dE/dδ. This becomes immediately obvious since the gate can not tune the phase within the SQUID loop. Instead, the observed features should be interpreted as a combination of changes in the number of transmitting states within the nanowire segment as well as a modulation of the **effective coupling strength** between the superconducting system and the normal conductor. This relation is thereby only loosely connected to the interface-related **transmission** τ in the sense that it sets a global minimum for the bound state energies. For a specific energy range,i.e. above the quantum dot limit but also before the total number of states pushes the whole system into the macroscopic junction range, it is possible to tune the **effective transmission probability** τ_n of the individual states[2]. The latter can thus be interpreted as an electrostatic analog of the *mesoscopic pincode* introduced for the mechanically tune- and switchable high transmission channels in atomic break junctions [136, 140, 377]. Following this picture for a **1D system**, the gate leads to the emergence of an Andreev bound state from the quasiparticle continuum, which then approaches the minimum energy set by τ and, lastly, returns to the continuum.

In the measurement shown in Fig. 2.6, the system is kept at the sweet spot $\Phi=\pi$, i.e. the point of minimum energy, in order to reduce the influence of phase- and flux-noise. However, in general it is more convenient to tune the bound state dispersion at a constant gate voltage via the externally applied magnetic flux. This is exemplary shown in Fig. 2.7 (a) for six different voltages. For V_g=0 V, the nanowire is pinched off (cf. Fig 2.5) and the system does not exhibit a drop in magnitude. At the next higher value, an ABS couples to the resonator and induces a flux-dependent modulation of the resonator response. However, the comparably weak interaction indicates that the state energy is still quite above the resonator. If the gate voltage is increased further, the interaction between the resonator and the SQUID loop becomes more prominent in terms of the induced frequency shift. At the highest gate voltage, i.e. at V_g=3.07 V, the system exhibits a pronounced avoided crossing. The latter can be used to extract the characteristic timescales and coupling factors. Using **QuTip** [383, 384], it is possible to fit the measurement in Fig. 2.6, which is re-plotted in dependency of the effective frequency shift in Fig. 2.7 (b), with the standard **Jaymes-Cummings transmission model** (see Section 4.1). Doing so, a **cavity-qubit coupling strength** g=78.3 MHz and a **cavity decay rate** γ=980 MHz, with a **state lifetime** of only a few nanoseconds is found. The latter is also the reason why no *zero mode Rabi splitting* could be observed. The presented measurements were taken by means of a preliminary

[2] In literature, this is also known as *visibility of the states* [136, 140, 377, 378].

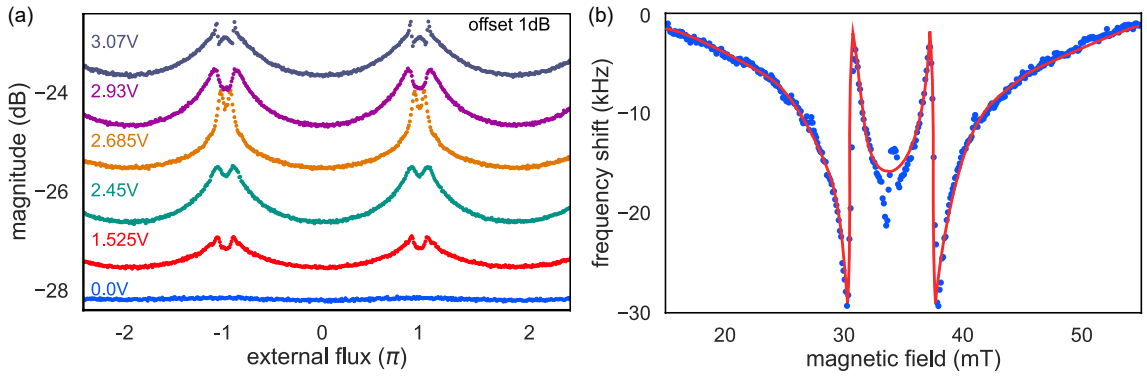

Figure 2.7 – *(a) Gate- and flux-dependent evolution of Andreev bound states probed by means of single tone measurements. For V_g=0 V the nanowire is pinched off and no states are present within the gap. If the gate voltage is increased, Andreev bound states emerge from the continuum and eventually couple to the resonator. This manifests as the signature of an avoided crossing around π. (b) Exemplary flux-dependent single tone response of a device similar to the one shown in Fig. 2.7. The avoided crossing is subsequently fitted by a modified Jaynes-Cummings model in order to extract the cavity-qubit coupling strength g and the cavity decay rate γ.*

version of the shown microwave circuits. Here, the internal quality factor was typically in the range of $Q_i \approx 15000$, which is an indication of a significant number of defects in and on the superconductor itself. However, in order to probe if the performance of the system is circuit- or device-limited, another measurement technique has to be utilized. The **two-tone spectroscopy** (**TTS**) is quite similar to the already presented concept of **dispersive readout** (cf. Sec. 1), with a key difference in the way in which the second tone is applied to the device. Here, instead of the resonator, the impedance-matched gate line is used as a second and independent microwave channel. Additionally, the device should be **undercoupled** to minimize the decay of the **probe signal** on the resonator, i.e. $Q_c \geqslant Q_i$. The measurement scheme is as follows:

1. Frequency-dependent measurement of the cavity response to find the resonance frequency f_r of the resonator
2. Application of the first tone (**probe**) $f=f_r$
3. Mapping of the gate- and flux-dependent single-tone response to localize a range of parameters in which the resonator couples to an Andreev bound state
4. Selection of a proper gate voltage V_g **or** flux Φ that is then kept constant throughout the measurement
5. Application and variation of the second tone (**pump**) f_p. For $f_r=f_{ABS}$, the system will become excited through the absorption of a photon. This induces a significant alteration of the inductance of the SQUID loop.
6. Measurement of the induced phase shift ΔΘ and modulated magnitude ΔM of the *probe signal*.
7. Variation of the remaining electromagnetic variable, i.e. V_g or Φ

The advantage of this approach is a very high sensitivity and the possibility to directly map out the energy space of the combined system far below and above the actual resonance frequency. Assuming an undercoupled system, the only limitation is set by the bandwidth of the experimental setup and the fridge wiring. Fig. 2.8 shows the flux- and frequency-dependent spectrum of the same device shown in Fig. 2.7 for energies $E \leqslant \Delta_{Al}/4$. Here, the parabolic signature of four Andreev bound states can be observed. The topmost feature can most likely be attributed to a *two-photon process* driven by an extra resonator photon, making it a replica of the lowermost parabola. Besides that, all of them exhibit a strong deviation from the behavior of a single channel system as discussed in Sec. 3.1. Most importantly, the difference between E_π and E_0 is only ≈ 4 GHz and therefore much smaller than

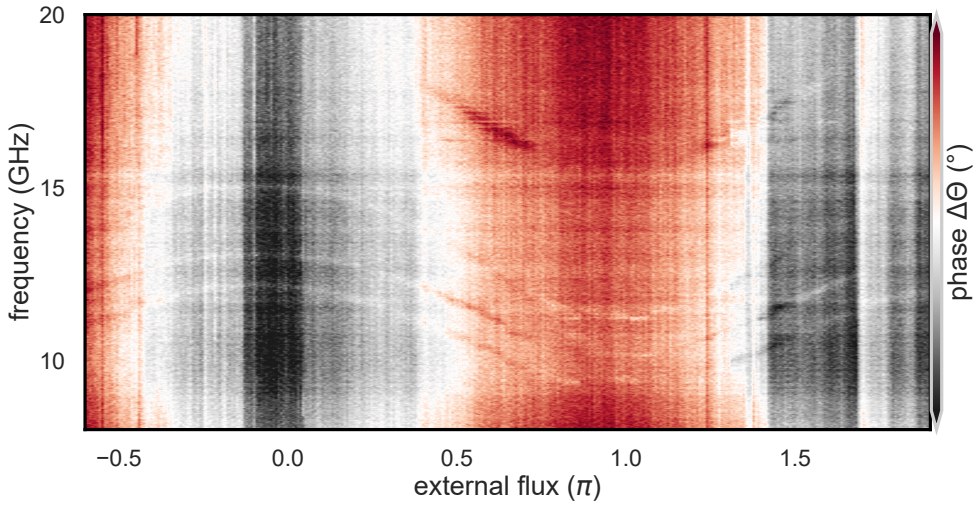

Figure 2.8 – *Exemplary flux-dependent two-tone spectroscopy measurement of the same junction as in Fig. 2.7 at a constant gate voltage of V_g=2.17 V, showing that four levels are present in the observed pump frequency range.*

the effective gap width $\Delta_{Al}/2h \approx 80$ GHz. This is a typical signature of a **long junction**, in which the large number of Andreev bound states and the *repulsion* between them induces a flattening of the dispersion. Just as in the case of the Gatemon (cf. Sec. 1), this is accompanied with an increased chance for inter- and multi-level transitions that ultimately limit the lifetime of the qubit-system. This could explain the comparably poor performance of this device (cf. Fig. **??**). Here, the underlying nature of the nanowire Josephson junction has been identified as the most likely explanation for this behavior, as the used etching method sets a limit to the shortest possible junction length. In addition, it has to be considered that the nanowire is a quasi-3D object rather than a planar system. Thus, there are multiple valid *paths* to bridge the semiconductor weak link, of which the one that connects the two superconducting electrodes through the top facet of the nanowire is only the shortest. The following Section is devoted towards possibly solutions for the described issues as well as further two-tone spectroscopy measurements. Most importantly, **self-defined nanowire Josephson junctions** are used. Here, the junction is formed by means of a shadow mask process, which allows the formation of short channels with steep and well-defined contact areas (cf. Sec. 3 for more information about the DC and magnetotransport properties of this type of nanowires).

3

SPIN-POLARIZED ANDREEV BOUND STATES

One of the most intriguing properties of the *edge states* in topological insulators (**TIs**) is the so-called **spin-momentum locking**. This direct coupling between the motion of the individual electron and its magnetic moment is the reason why they are also often referred to as **helical**. However, the underlying principle is not restricted to TIs. For semiconductor nanowires, the presence of spin-orbit interaction, i.e. the Rashba and the Zeeman effect, can also alter the observed excitation spectrum in single- or few-channel Josephson junctions such that its properties are dominated by the magnetic moment of the fermionic quasiparticles.

Fig. 3.1 (a) and (b) show the state spectrum of an InAs/Al nanowire with an in-situ shadow mask defined Josephson junction embedded in a 2D silicon-based CPW circuit (cf. Fig. 2.4(a)). Here, two different types of features can be observed: The parabolic curves (red and blue) in 3.1 (b) are associated with conventional Andreev bound states and only allow *pair transitions* in which two quasiparticles are excited at once. However, around 14 GHz and at B=380,mT, one can see how the state spectrum resembles a **spider web**-like shape with multiple bands of which some even move down in energy for $\delta \neq \pi$. The observed effect corresponds to single quasiparticle transitions and can be understood in terms of **atom-like transitions** of a quasiparticle from one Andreev level to another. It should be pointed out that both types of transition are parity conserving. Pair processes, first observed in atomic contacts by the *Quantronics* group in *Saclay*, give rise to the **Andreev qubit** [136, 140, 377]. Single quasiparticle transitions, on the other hand, provide an alternative to quantum dots by coupling a *single fermionic spin* with a microwave resonator and thereby develop an **Andreev spin qubit** without the need of complex and error-prone *multi-gate structures* [378, 425].

Fig. 3.2 provides a schematic overview of the underlying quantum mechanical mechanisms. Assuming a single channel nanowire system, as in Fig. 3.2 (a), that is decoupled from the superconducting electrodes, a reasonably strong *Rashba effect* enforces a **spin polarization** of the current. This *effectively* creates an effect that is quite similar to the spin-momentum locking in TIs, but without its additional protective component. In terms of the dispersion relation, as shown in Fig. 3.2 (b) one ends up with two different energy parabolas, one for each spin direction, that are displaced in momentum. In a long junction, such as the one shown in Fig. 3.2 (e), more channels are accessible. Here, the spin-orbit interaction couples subbands with different spin orientations. Consequently, those states are hybridized, which goes alongside with a pronounced rearrangement of the dispersion relation in the nanowire (cf. Fig. 3.2 (f)). If the semiconductor is coupled to superconducting electrodes, the spin polarization transfers into the spectrum of the *Andreev bound states*, which leads to a lifting of the spin-degeneracy for $\delta \neq \pi$ [378, 425]. It should be pointed out that the described effect does not require the presence of an **external magnetic field**.[1] However, a spectrum, as shown in Fig. 3.1 (h), is only observable if there are at least **two Andreev bound states** present, as the single state dispersion with spin-orbit interaction mimics the one without any spin degree of freedom (cf. Fig. 3.2 (d)). Nevertheless, the *single channel limit* is still of special experimental interest as it can

[1] In the experiment, one only needs a finite *out-of-plane* field to control the phase through the junction and drive the system close to *flux* π in order to limit the frequency range that has to be probed.

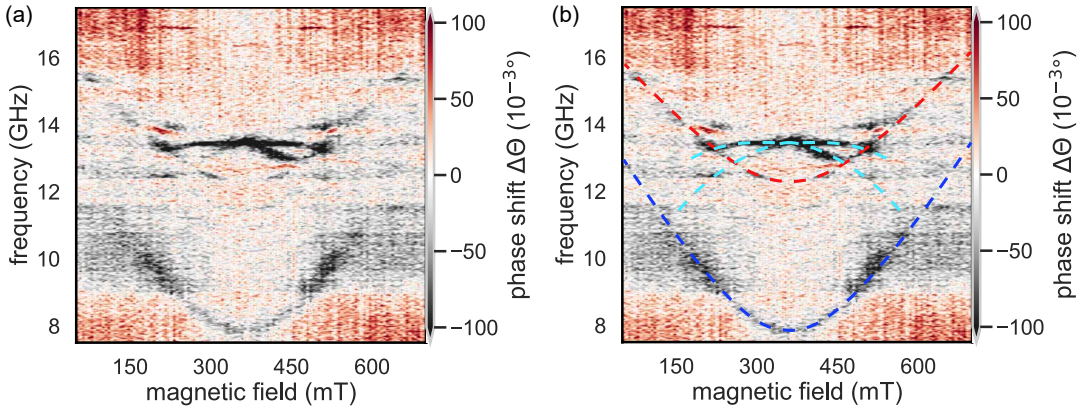

Figure 3.1 – *(a) Two-tone spectroscopy of a nanowire Josephson junction with only two Andreev bound states. The lower parabola corresponds to conventional two-particle transitions. At higher frequencies, the states exhibit a non-trivial behavior, resulting in a spider-like shape. The latter is a potential signature of spin polarization and an intermixing of the states by means of single quasiparticle transitions caused by the comparably strong Rashba effect. (b) The same image as (a) but with superimposed indications of the observable states. Besides the already mentioned spin-splitting, one can also see that the lower parabola is replicated with a much smaller slope at 13GHz (red curve). This feature can probably be attributed to a two-photon process, which indicates a not-too-short lifetime of both the cavity as well as the actual qubit-like system.*

open the path towards the formation of a *helical gap* if the system is exposed to a reasonably strong *in-plane field*. The induced *Zeeman effect* creates an additional energetic shift between the already momentum-displaced and spin-polarized state branches, ultimately giving rise to a full decoupling between the different spin orientations. The created energy gap exhibits, in the case of a correctly positioned *Fermi level*, exactly the configuration required for the formation of **Majorana zero modes**.

In order to further investigate the spin-related phenomena, more samples have been fabricated based on the already introduced Flip-Chip design. As one can see in Fig. 3.3, the much higher quality of the microwave circuit improves the visibility of the Andreev bound states significantly. The shown measurement was thereby performed on an InAs/Al nanowire Josephson junction with an etched weak link that was intentionally designed to form a *long junction*. This make the presence of multiple bound states more likely and makes it possible to investigate the different kinds of interactions. Here, Fig. 3.3 focuses on the relation between the Andreev bound states and the externally applied gate voltage for a constant phase difference $\delta=\pi$. It should be pointed out that, in general, the gate-driven change of the bound state energy for a constant phase difference across the junction can originate from two different effects, depending on the exact transport regime of the semiconductor nanowire. Close to pinch-off, i.e. where the nanowire is dominated usually by Coulomb blockade, the transport through the weak link is determined by hybridized quantum dot levels, the already introduced **Yu-Shiba-Rusinov states** [171–173]. Stemming from the quantum dot, their energy is a direct function of the applied gate voltage. On the other hand, if the nanowire is fully open, the 1D levels in the system are influenced by the change of the fermi velocity. The main difference between both cases is the determination of the minimum bound state energy as well as their evolution with respect to the re-entry into the continuum states.

The efficiency of how much the absorption of a pump-photon is transferred into a change of the resonator response, i.e. the degree of sensitivity for the Andreev bound state spectrum, is directly determined by the separation of the resonator frequency and the bound state in energy space. On the other hand, a strong coupling limits the lifetime of the bound states due to the increased interaction with the system environment. Thus, all presented measurements were performed as a combination of the pump-driven two-tone spectrum and the single tone response of the resonator, which is shown in Fig. 3.3(b). Here, a strong modulation of the resonator phase occurs for gate voltages between $V_g = 0.19$ and 0.20 V, which corresponds to the region in Fig. 3.3(a) in which a multitude of transitions cross the resonator frequency. Proceeding to the lower gate voltage section in Fig. 3.3(a) one finds a rather complex spectrum with an abundance of transitions between $V_g = 0.19$ and 0.20 V. In addition, on its right side, one observes a single spectral trace which can be attributed to a pair transition close

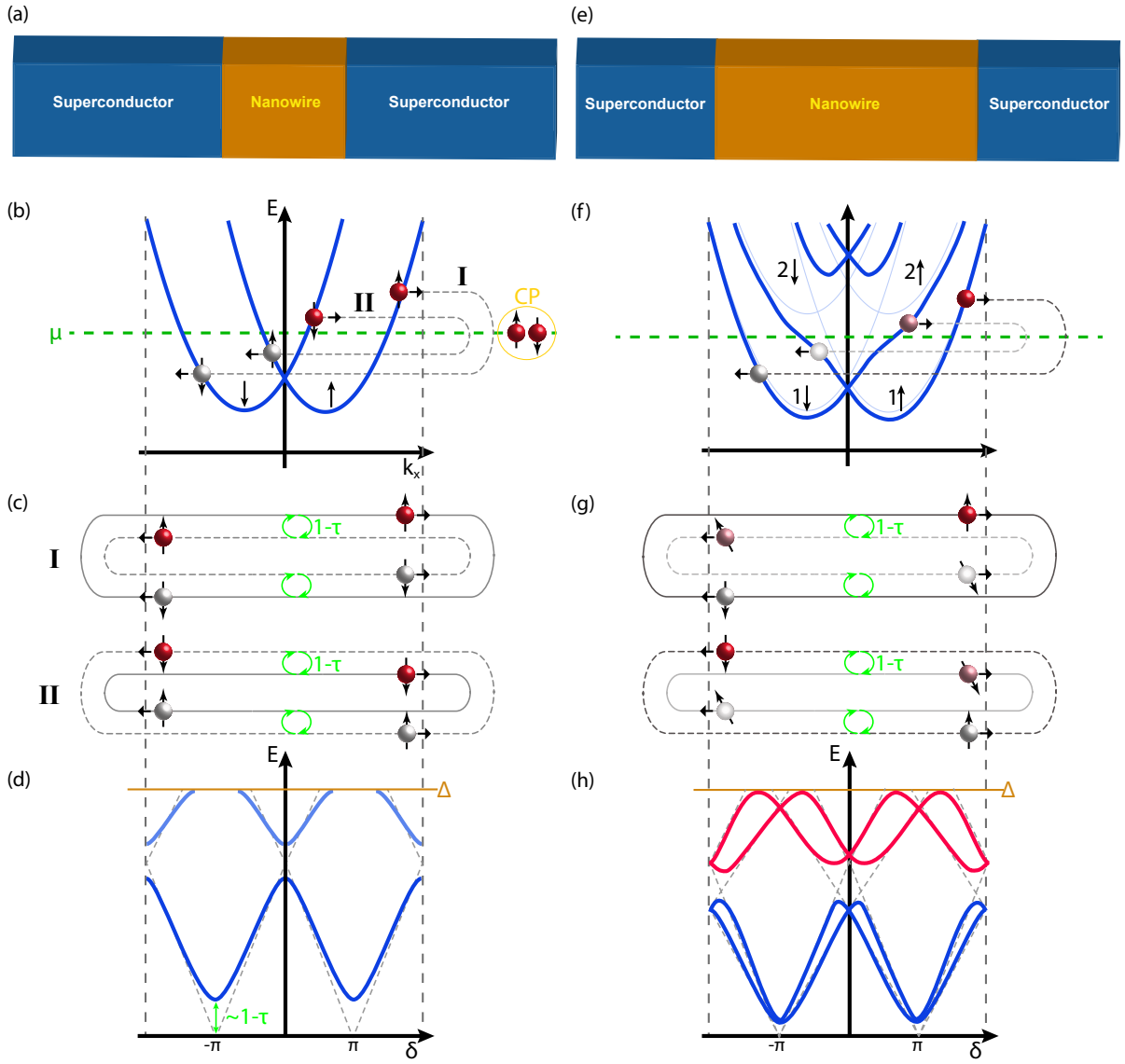

Figure 3.2 – *(a, e) Schematic depiction of the S-Nanowire-S junctions with (a) a short and (e) a long nanowire weak link, a non-ideal interface τ<1 and a finite number of scattering centers in the channel. (b, f) Dispersion relations of the bare nanowires. In the one-dimensional single channel limit, the finite spin-orbit interaction lifts the spin degeneracy, inducing the formation of two separate branches with different spin polarization (indicated by black arrows) that are shifted in momentum space. If at least two channels are present, the Rashba effect leads to an inter-subband coupling of the states (light blue solid lines) and thus enforces a pronounced reconfiguration. One possible coupling configuration of charge carriers with different spin orientation is indicated with the dashed grey lines. The thick blue lines correspond to the hybridized subbands. (c, d) Formation of Andreev bound states due to retro-reflection of electron and holes of different velocities and spin orientations (solid and dashed lines in (c), dashed line in (d)). For non-ideal interfaces, represented by a finite back-scattering probability 1-τ, the coupling of the states modulates the dispersion relation, opening gaps at the former crossing points and also increases the minimum energy. It should be pointed out that the resulting states (solid lines) are indistinguishable from the ones obtained without any spin-orbit interaction. (g, h) Formation of Andreev bound states in a two-channel-system with strong Rashba interaction and a complex spin texture. The hybridization of the spin polarized states in the nanowire with the states in the superconducting contacts leads to a lifting of the spin degeneracy and provides access to single quasiparticle transitions. The images are based on the work of Tosi et al. [378].*

to V_g=0.22 V, induced by an Andreev level that approaches the resonator frequency. In the single tone response, this corresponds to a section in which the phase shift has a smooth maximum.

If the gate voltage is increased above V_g=0.38 V, the spectrum becomes much richer and contains many features in the investigated spectral range. In the corresponding single tone data (cf. Fig. 3.3(b)), the strongest coupling is achieved when the transitions shown in Fig. 3.3(a) are matching with the resonator frequency, i.e. at gate voltages around 0.39, 0.405, and 0.415 V. At even larger gate voltages, i. e. V_g >0.42 V, only a single transition is observed in the frequency window and then

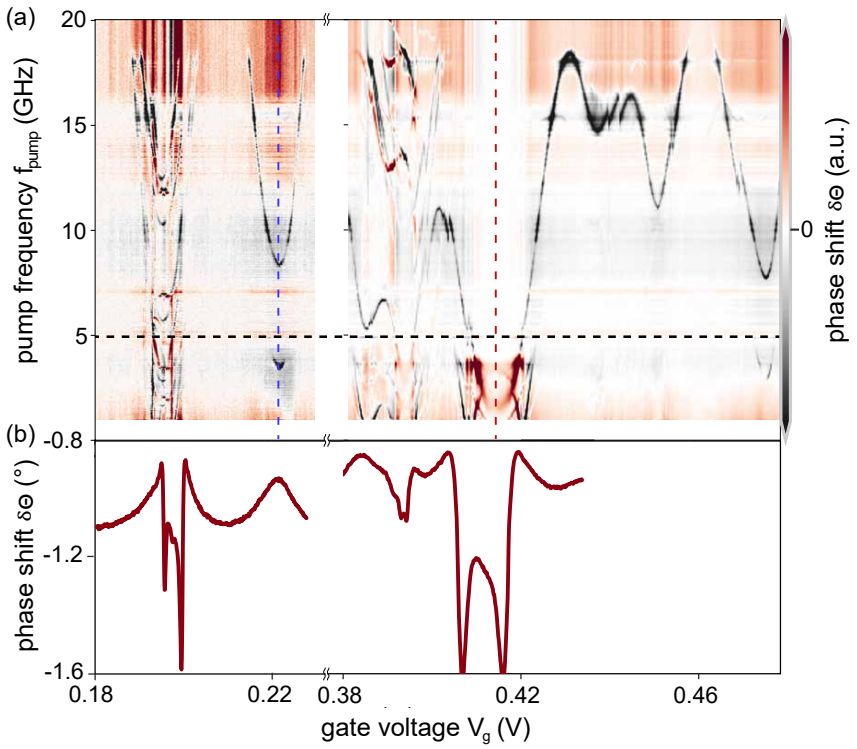

Figure 3.3 – *(a) Gate-dependent two-tone spectrum at a constant phase difference $\delta = \pi$ across the junction. The gate voltage was varied from 0.18 to 0.23 V and from 0.37 to 0.48 V. The colormap refers to the induced phase shift of the transmitted resonator signal. The bare resonator frequency f_r is indicated by a dashed black line. We assign the abrupt shifts of the transitions, e.g. around 0.43 V to changes in the background charge. (b) Corresponding resonator phase-shift obtained by single-tone spectroscopy in the gate voltage range corresponding to the measurement shown in (a). The slight shifts compared to the measurement in (a) is due to some gate drift. Image taken from [426].*

further modulated by increasing the gate voltage. This state can be attributed to a quasi-particle pair transition $2E_A = f_{pump}$ from the ground state [378, 425]. From measurements performed as a function of the phase across the junction, which are discussed at a later stage, it was possible to deduce that there must be additional higher lying states with transition frequencies above the pump signal of 20 GHz. The random jumps in the dispersion of the state are most likely caused by potential fluctuation in the nanowire channel. Here, one possible explanation is based on the combination of a randomly formed intrinsic quantum dot with low charging energy coupled to the superconducting reservoirs and a diffusive weak link with transparent normal superconducting interfaces[427]. Similar features have been already observed in other nanowire-based junctions in terms of random modifications of the critical current induced by electron interference effects in the semiconductor, e.g. universal conductance fluctuations [358, 389]. Between 0.41 and 0.42 V the level shifts below the resonance frequency. This goes alongside with a pronounced flipping of the dispersion, resulting in a crossover of the conventional energy parabola with a reversed one. A similar, but less prominent feature is observable around $V_g > 0.195\,V$ and also in the phase-dependent measurements in Fig. 3.4.

In the next step, the phase-dependency of the Andreev bound state spectrum was investigated. For the measurements shown in Fig. 3.4 (a) and (c) a constant gate voltage of 0.251 and 0.4347 V, respectively, was chosen. Here, the spectrum shown in Fig. 3.4 (c) is of special interest as it corresponds to the gate voltage at which the bound state in Fig. 3.3 (a) crosses the resonator frequency.[2] The most prominent feature in Fig. 3.4 (c) is the pair transition with $2E_A = h f_{pump}$ with the according fit given by the dashed darkblue line. The latter was obtained by employing a model assuming a long junction $L > \xi_c$ with strong Rashba spin-orbit coupling [221, 378]. Following this fit, one can extrapolate that the maximum of the Andreev level in energy space is well below $2\Delta \approx 0.380\,\mu$eV (see Sec.3 for a detailed analysis of the superconducting gap in InAs/Al nanowire Josephson junctions). Consequently,

[2] Owing to a gate drift the gate voltage was slightly readjusted for the phase-dependent measurements.

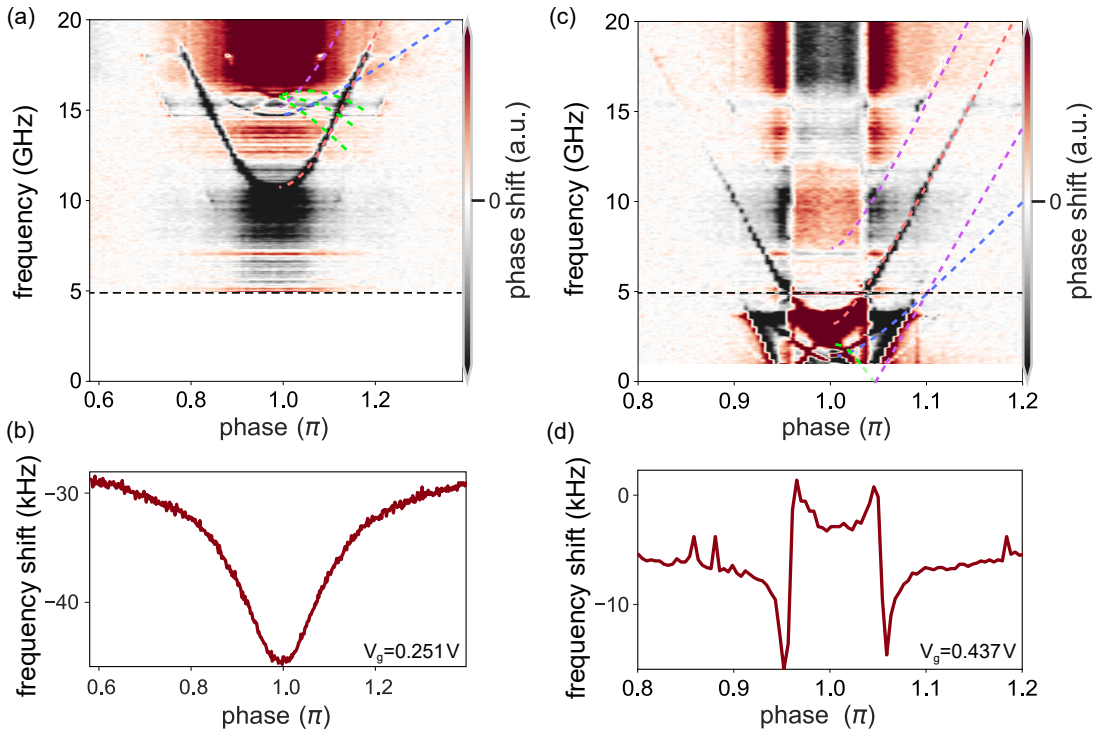

Figure 3.4 – *(a) Flux-dependent two-tone spectrum of the same junction as in Fig. 3.3 at a gate voltage of V_g=0.251 V. Here, the x-axis represents the phase difference δ across the junction. The dashed red line indicates the fitted pair transition, while the dashed purple line above correspond to its replica of second order transitions involving an emission of a resonator photon. The dashed green lines indicates a single quasiparticle transitions between Rashba spin-splitted Andreev levels (see Fig. 3.2). (c) Two-tone spectrum at a gate voltage of V_g=0.4374 V. The dashed red line indicates the fitted pair transition, while the dashed purple lines correspond to its replicas of second order transitions involving absorption or emission of a resonator photon. The dashed blue line indicates a pair transition by a pair of pump photons. Lastly, the dashed green line corresponds to a higher-order transition induced by the combination of a single cavity photon with another one that is created by the relaxation of an Andreev level. (b) ,(d) Corresponding phase-dependent single-tone response for both gate voltages at f=f_r. A modified version of this picture has been already published in [426].*

this means that Andreev levels must be present at energies far above the measurement range which then modify the conventional energy-transparency-phase relation E(δ,τ). The pair transition crossing the resonator frequency is also responsible for the strong modulations of the frequency shift in the according single-tone data set (cf. Fig. 3.4 (d)). Apart from the $2E_A = hf_{pump}$ feature in Fig. 3.4 (c), their are some additional, but weaker transitions in the spectrum. First of all, there are second order transitions that can be attributed to the absorption or emission of a resonator photon, i.e. at $2E_A \pm f_{res} = hf_{pump}$, respectively (fits: dashed purple lines). Such features only occur in case of a strong resonator-device coupling and high microwave power levels. Additionally, one finds a transition involving two pump photons, i.e. $2E_A = 2hf_{pump}$ (dashed blue line). Again, close to the phase sweet spot $\delta = \pi$, there is a transition with an inverted dispersion (dashed green line). This feature can most likely be attributed to a higher-order transition in which a single resonator photon is created upon pump irradiation with the assistance of the Andreev energy, i.e. a process that is quite similar to *spontaneous emission* in a laser. Extending this picture, the occurrence of this feature points to a significant thermal occupation ("*poisoning*") of the Andreev state. It should be pointed out that all transitions enter the pump frequency window only in the vicinity of the phase sweet spot δ=π. This is a strong indication that the junction is indeed not a single channel system, but still so short that the dispersion of the Andreev levels E(δ,τ) is not modified significantly.

For the phase-dependent measurement at $V_g = 0.251$ V (cf. Fig. 3.4 (a)) the most prominent feature is again the pair transition at $\delta = \pi$, with a minimum energy of around 10 GHz. Upon approaching the resonator frequency an increase of the frequency shift is observed in the single-tone spectroscopy measurement shown in Fig. 3.4 (b). However, a closer inspection of the two-tone spectrum

reveals a set of lines around 15 GHz which are caused by single quasi-particle transitions [221, 378, 425] (dashed green lines). These four-fold transitions originate from SOI-induced modifications of the bound state dispersion relation. More precisely, the coupling between adjacent (in terms of energy) spin-split states in the nanowire leads to different Fermi velocities for different spin orientations. This, as a consequence, results in an effective spin polarization of the Andreev bound states.

The observed phenomena is an important step towards the creation of topologically-protected states as it, in principle, allows the formation of a **helical gap**. However, the latter would require an additional out-of-plane field in order to shift the levels that are already displaced in momentum space in energy, too. For the investigated InAs/Al nanowire system, the magnetic field that would be necessary to induce a sufficiently large energy gap would be in the range of 1 T. Unfortunately, within the timeframe of this thesis, it was not possible to apply such large fields without a strong degradation of the resonator properties due to vortex-induced dissipation. One possible solution for that issue would be the use of semiconductors with a larger intrinsic spin-orbit interaction. Thus, the last chapter of this focuses on the investigation of another nanowire system that consists of a GaAs core and an InSb shell (cf. Chapter VII).

VI

EXCITATION-BASED PHENOMENA

1

THE LITTLE-PARKS EFFECT

1.1. INTRODUCTION

The requirement for **braiding** remains one of the major challenges in the field of Majorana fermions. Thus, several groups are trying to find ways to induce a **phase winding** without the need of *spatially exchanging* the particle-antiparticle pair. Based on the **Oreg-Lutchyn model**, such systems usually require a strong spin-orbit interaction to induce Majorana zero modes and/or the transition into an 1-dimensional topological superconductor [428, 429]. However, another solution goes back to the early days of superconductivity and has first been utilized to prove the concept of **fluxoid quantization** in superconducting structures with an *Aharonov-Bohm-type topology*. The so-called **Little-Parks effect** can be understood in terms of *trapped vortices* in a *radial-symmetric* superconductor with *non-compact* geometry that cause a **phase winding** in the superconducting order parameter $\Delta(\vec{r}) = \Delta(r)e^{(-in_\theta)}$ [1, 430]. Experimentally, it manifests itself as a *flux-periodic* suppression and re-

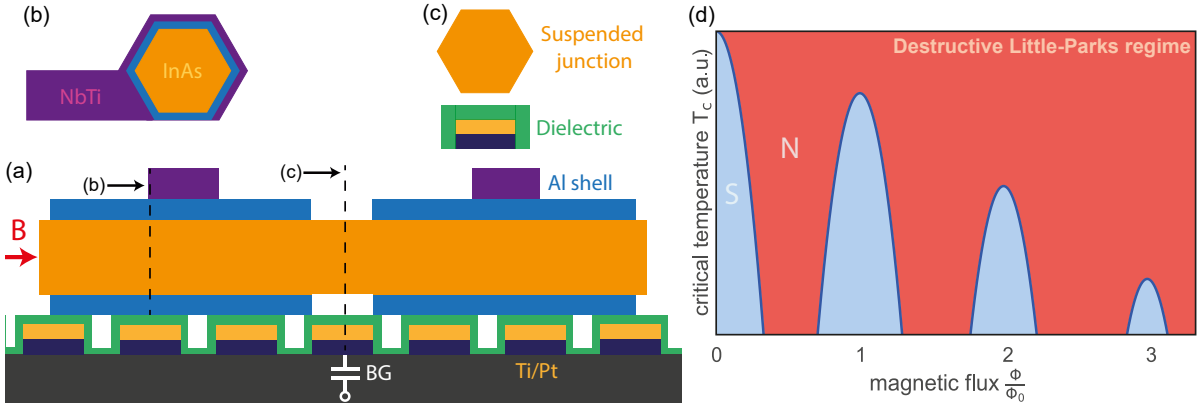

Figure 1.1 – *Schematic depiction of an InAs fullshell nanowire device used for Little-Parks measurements. (a) The system consists of two InAs/Al cylinders that are coupled by means of a pure-InAs weak link, effectively forming a strong twist in the superconducting phase. (b) The outer Nb leads are designed in a way that they only cover a short segment of the Al shell such that they do not change its superconducting properties due to hybridization of the different Cooper pair condensates. (c) The bottom gate electrode allows a precise control of the density of states in the semiconductor and therefore a tunable coupling of the two cylinders. (d) Qualitative representation of the destructive Little-Parks effect and the lobe structure associated with it. The latter is induced by the flux-periodic suppression of the critical temperature and a transition of the system from the superconducting [S] into the normal state [N].*

currence of the *supercurrent* that is **not** caused by exceeding the *critical field*. Instead, it arises due to a simultaneous counteraction between the applied magnetic flux, which increases the kinetic energy of the Cooper pair condensate, and the creation of superconducting vortices that periodically enter the superconducting tube. This effectively compensates the flux effect and reduces the kinetic energy. However, the kinetic motion of the condensate directly translates into its *heat*. Thus, the system exhibits a periodic oscillatory reduction of the **critical temperature** which results in **lobe-like** structures in the conductance that correspond to the quantized number of turns of the superconducting

VI

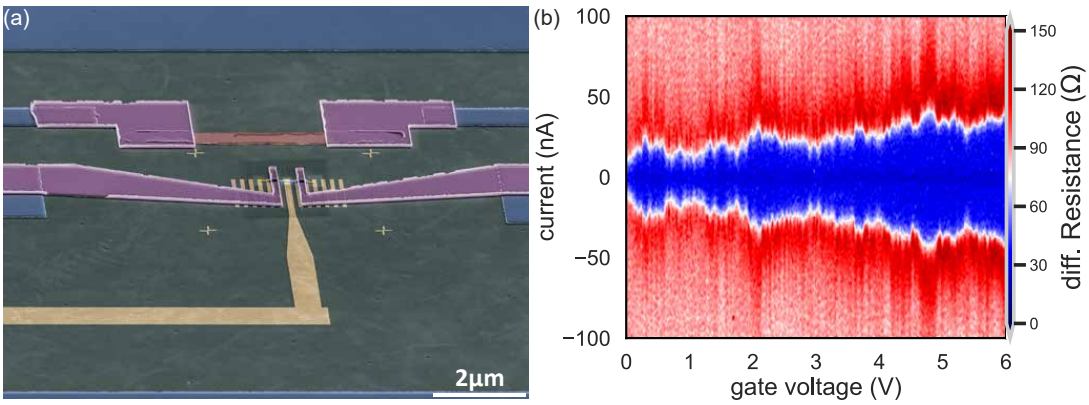

Figure 1.2 – *(a) False-colored SEM micrograph of an InAs/Al full shell nanowire Josephson junction that is extrinsically shunted by a normal conducting AuGe resistor. (b) Gate- and current-dependent conductance map of the same device. The device exhibits a clear and gate-tunable supercurrent that is superimposed by quantum fluctuations in the InAs segment. For negative gate voltages, a full pinch-off of the nanowire could be achieved without any signatures of Coulomb blockade or tunnel-limited transport (not presented).*

phase. Those are separated by *destructive* Little-Parks regimes in which the free energy is minimized [1]. The *Little-Parks effect* has to be considered as a collective quantum phenomenon that is strongly connected to the *superconducting phase* via the creation of **nodes** and **twists** in the distribution of the superconducting order parameter.

Fig. 1.1 provides a schematic overview of an InAs/Al fullshell nanowire Josephson junction that has been designed to support the formation and subsequent hybridization of two Majorana pairs. It mainly consists of two InAs/Al hybrid segments in which the semiconductor is fully enveloped by the superconductor. The coupling between both sections is realized by a *mesoscopic weak link* in the center. A local bottom gate electrode enables the tuning of the density of states in the uncovered section of the semiconductor. This translates into the number of accessible Andreev bound states. In order to generate the required fluxoid quantisation, both ends of the nanowire have to be exposed by a (partial) etch of the surrounding Al shell. The advantage of such a system lies in a major increase of the topological phase space. This means, it lifts the strict requirement for strong spin-orbit interaction in terms of a modified version of the **Oreg-Lutchyn model** [430]. The downside of this approach, on the other hand, is a weakened protection of the Majorana zero modes with respect to subband mixing perturbations.

The electrical measurements are usually carried out in a *transmission line* environment. The circuit is powered by both DC as well as an AC source which are coupled via an on-chip **bias tee**. Thus, it is possible to locally apply microwave excitations, which circumvents most of the issues caused by external macroscopic antennas. The result is an undisturbed access to the full *frequency-power parameter space* that is needed for a systematic map-out of the *AC Josephson effect*, i.e. the detection of **Shapiro steps**. The latter does not interfere with the possibility of typical DC measurements like the probe of the gate and magnetic field dependent device response.

Fig. 1.2 (a) shows a typical device with an **on-chip shunt resistor** (purple). The purpose of the shunt is the suppression of the pronounced *switching event* into the *voltage state*. These thin metal stripes, usually made of **AuGe** with a resistance around $\approx 0.1\,\mathrm{k\Omega}$, effectively dampen the *phase instability* and transform the sudden *jump* in voltage into a continuous *slope*[1]. An exemplary gate dependent measurement of such a sample is shown in Fig. 1.2 (b). Here, the most remarkable feature is the tunable supercurrent $I_s(V_g{=}0V){=}10\,\mathrm{nA}$ and $I_s(V_g{=}6V){=}40\,\mathrm{nA}$. The residual normal state resistance can be attributed to the on-chip shunt resistor. The fluctuations of the supercurrent, on the other hand, are related to universal conductance fluctuations within the nanowire. For negative gate voltages, a clear pinch-off is achievable ($V_{th} = -1.9\,\mathrm{V}$).

[1] For further details about this method please check Sec. 3.1.1 and Sec. 2.2.

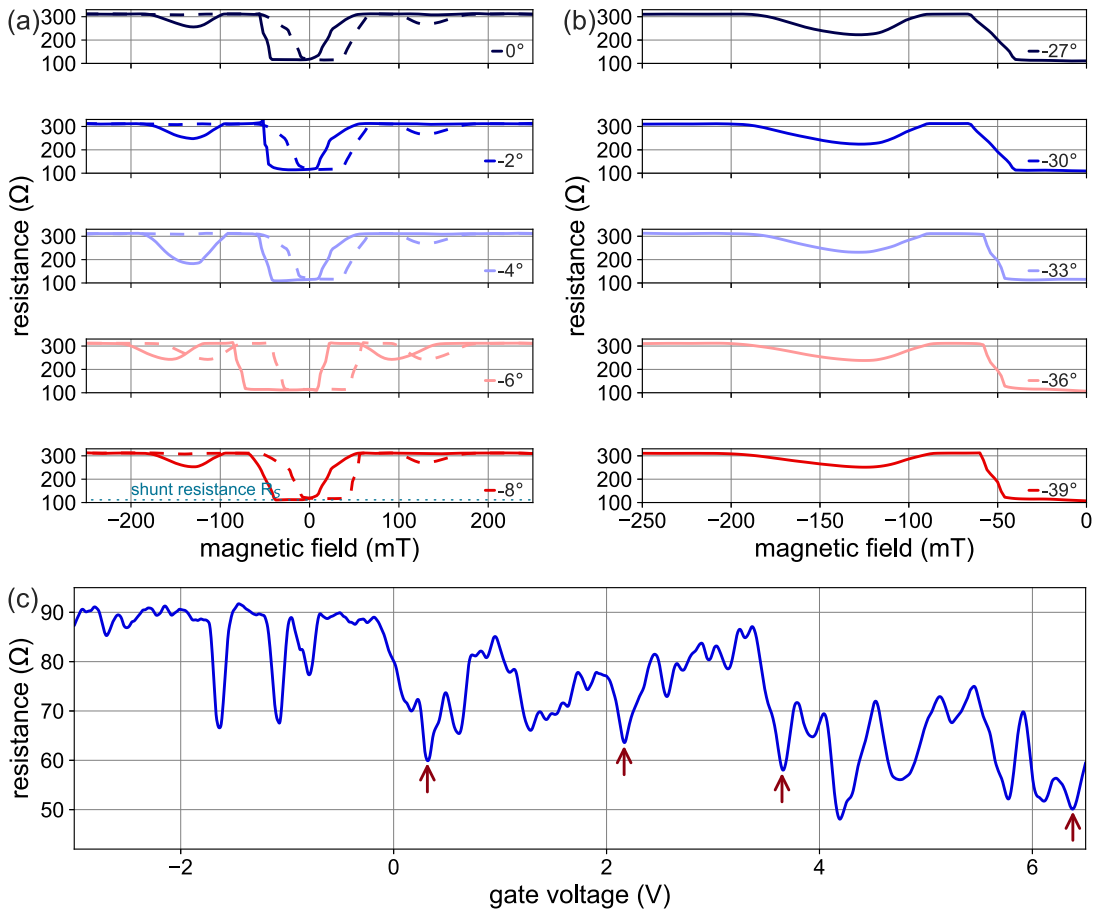

Figure 1.3 – *Exemplary calibration procedure to optimize the setup for the detection of the Little-Parks effect. (a) Tuning of the out-of-plane misalignment α that is usually introduced during the sample mounting. Here, the ideal device response with a field-symmetric lobe structure is achieved for -6°. (b) Adjustment of the angle between the in-plane field and the nanowire axis to compensate the xy displacement of the device β. At -30°, the first outer lobe reaches its minimum resistance value of $R(125\,mT) \approx 210\Omega$. (c) Gate sweep within the first outer lobe to find the point of minimum resistance. The measurement has to be highly resolved with respect to the number of individual gate steps in order to address the quantum corrections of the conductance. For the given device, a gate voltage of $V_g = 6.3\,V$ has been selected.*

1.2. MAGNETOCONDUCTANCE MEASUREMENTS

All presented devices and measurement techniques require a thorough and precise calibration of the applied electromagnetic fields. For our measurements, we use a *Four-Steps-Approach*, which is shown exemplary in Fig. 1.3. First, the magnitude of the gate voltage and the in-plane magnetic field are set to values at which the device response exhibits a clear **node pattern**. Then the misalignment of the device with respect to the out-of-plane direction has to be compensated. This is caused by imperfections of the sample mounting procedure and could alter the effective B-field that penetrates the two Little-Parks cylinders. Using a vector magnet it is possible to apply a magnetic field in **z-direction** with different tilt angles α as shown in Fig. 1.3 (a). For $\alpha = -6°$, the left hand side lobe in the up-sweep branch (solid line) has the same depth as the right hand side lobe in the down-sweep branch (dashed line) and vice versa. In the next step, a similar procedure has to be performed for the in-plane field. Again, this is done to suppress all magnetic field components except the orientation parallel to the nanowire axis. Thus, a second vector magnet is used to alter the field angle in the **xy plane** β. As shown in Fig. 1.3 (b), even small deviations from the ideal alignment induce a significant suppression of the Little-Parks feature in terms of a reoccurence of the supercurrent and a corresponding drop in resistance. For example. $R(125\,mT, \beta = -30°) \approx 210\Omega$ and $R(125\,mT, \beta = -39°) \approx 270\Omega$. Finally, the applied gate voltage has to be tuned in order to find the (global) resistance minimum. Here, the diffusive nature of the normal conducting InAs segment can give rise to superimposed universal conductance fluctuations (see Fig. 1.3 (c)).

VI

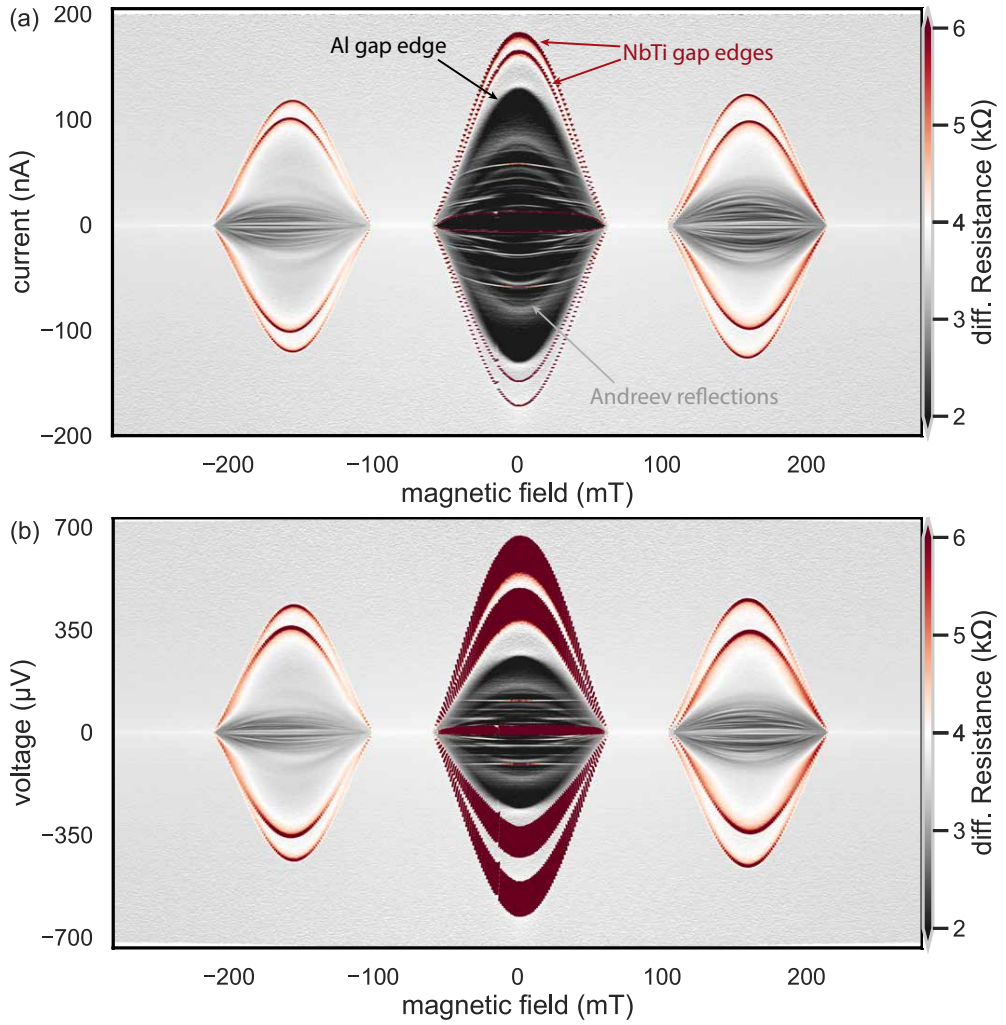

Figure 1.4 – *Magnetic field dependent differential resistance map of an InAs/Al fullshell nanowire Josephson junction plotted as a function of the (a) supercurrent and (b) voltage drop. The field was aligned such that it just penetrates the nanowire in-plane and parallel to its axis. The most prominent features are the **lobe-like** sections which are surrounded by areas without any supercurrent. The latter are a clear signature of the **Little-Parks effect** and a collapse of the Cooper pair condensate in the superconductor due to phase winding. Interestingly, the center lobe shows two different effects. The iris-like lines, which reshape the curvature of the superconducting gap edge (dark red), can be attributed to conventional Andreev bound states. In addition to that, these features are superimposed by straight lines [see (b)] that **do not** interfere with the Andreev spectrum and, more importantly, do not follow the gap-suppression of the superconductor itself, which makes it quite unlikely that they are caused by (multiple) Andreev reflections even though they are periodic in energy.*

The current-dependent magnetoresistance map in Fig. 1.4 (a) shows the device response of a InAs/Al full shell nanowire Josephson junction with a layout that is comparable to the one shown in Fig. 1.1 but without the bypassing shunt resistor. The most remarkable features are the *iris-shaped* regions at 0 mT and ±150 mT which perfectly follow the field periodicity that is required to create (multiples of) a fluxoid for the given device dimensions. These **lobes**, that are surrounded by regions without any supercurrent, are a direct manifestation of the **Little-Parks effect**. Here, the outer dark red lines can be attributed to the phase change that occurs as soon as the current exceeds the critical current of the junction. This signature of the superconducting gap edge is periodically replicated within the black area in terms of multiple Andreev reflections. However, specifically in the center lobe there is a second set of parabola-shaped traces with increased resistance but different curvature. When plotted in dependence of the measured voltage drop, as depicted in Fig. 1.4 (b), those features turn into *straight lines*. Fig. 1.5(a) shows the voltage-dependent magnetoconductance at B=0 T. A *Fast-Fourier transformation* without prior background subtraction (cf. Fig. 1.5(b)) and reveals a clear periodicity in energy space with $\Delta V = 30\,\mu V$. Following the conventional theory of SNS

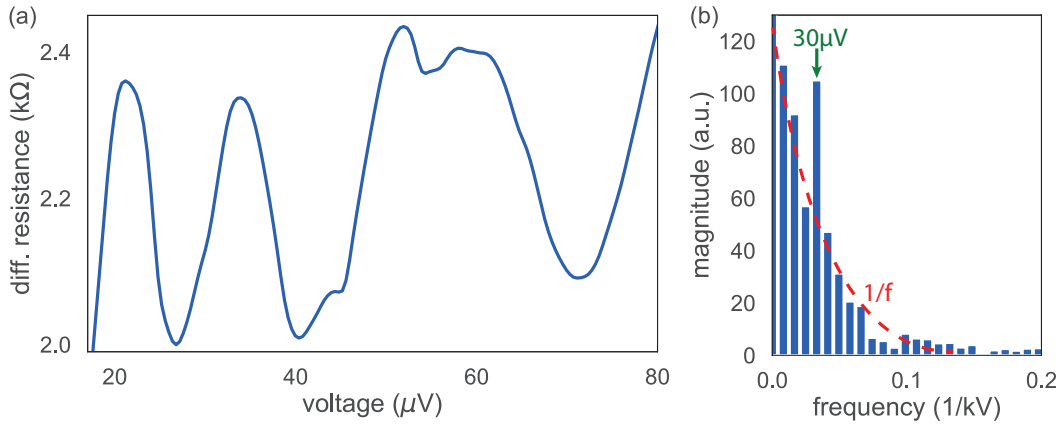

Figure 1.5 – *(a) Zero-field differential resistance trace taken from Fig. 1.4 (b) without background subtraction. (b) Fourier spectrum of the oscillation pattern shown in (a). The red dashed line indicates the* $1/f$ *component that is mostly caused by the background. Additionally, the spectrum reveals a voltage period of* $30\,\mu V$ *which is constant within the the field range of the center lobe in Fig. 1.4 (b).*

junctions, the first obvious interpretation would associate those features with **multiple Andreev reflections**. However, an argument against this assumption is the fact that they do not follow the *global curvature* of the *superconducting gap*. Additionally, even though they are clearly restricted to the magnetic field regions in which the superconductor and the semiconductor form a hybrid system, they only show up in the center lobe. This is a strong indication that they are not part of the conventional *Andreev transport space* that emerges from the *induced superconductivity*. However, one of the downsides of using two superconducting contacts instead of a tunnel-spectroscopy layout is the lack of information about the actual number of states, their specific energies and the *shape* of the current-phase relation. In order to probe the latter, Shapiro measurements for various frequencies have been performed.

VI

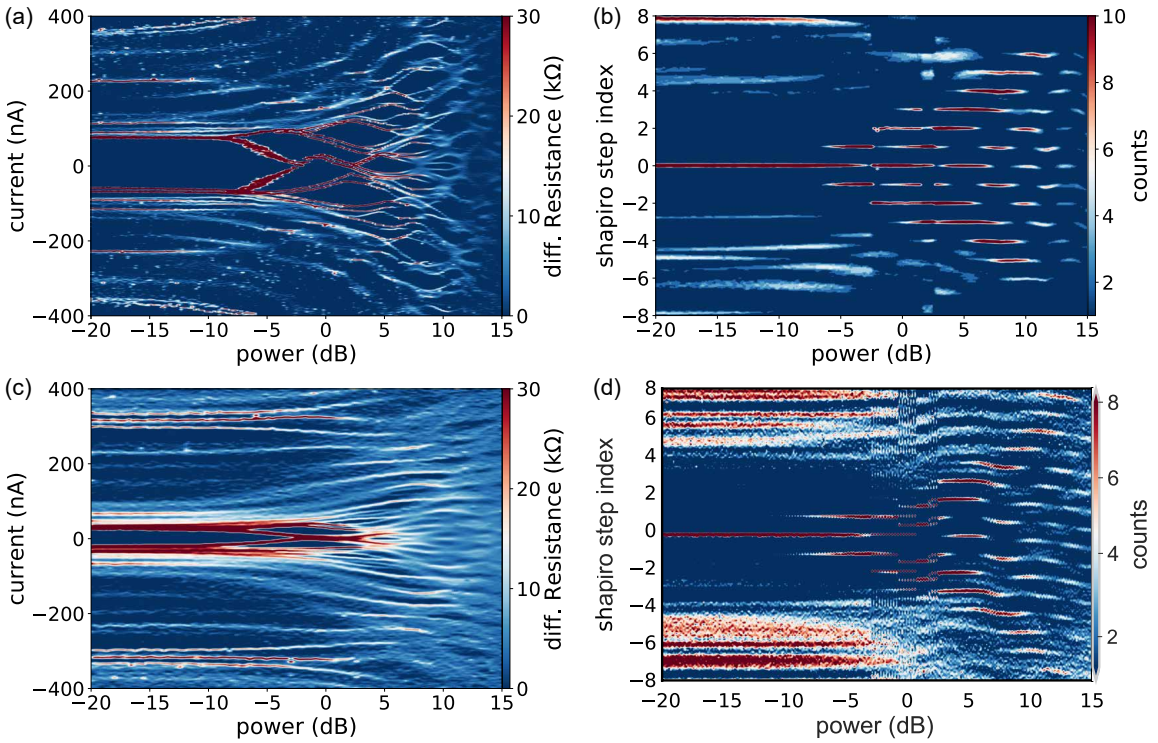

Figure 1.6 – *Shapiro response of a nanowire Josephson junction (a) without and (c) with an applied in-plane magnetic field of B=120 mT for a constant microwave frequency of f=2.4 GHz and external microwave powers between -20 dB and 15 dB. Without a penetrating flux, the junction exhibits a complex pattern of Shapiro steps and a chevron-like behavior at low power levels. Accordingly, the corresponding histogram (b) includes wide sections of either missing odd or even steps. The latter could be an indication for a slightly overdamped junction or additional Landau-Zener transitions. Interestingly, if a magnetic field is applied, the corresponding pattern in (c) becomes much more stable and "tidy". However, here, the histogram does not only exhibit some missing steps, but also includes sections with additional subharmonic steps at* ***half integer*** *values.*

1.3. SHAPIRO AND EMISSION MEASUREMENTS

Fig. 1.6 (a) and (c) show the device response for a constant microwave frequency of f=2.4 GHz but different power levels without and with an applied in-plane magnetic field, respectively. Here, the measurement without an enclosed flux exhibits a supercurrent of about 100 nA, which is almost twice as big as the value in Fig. 1.6 (c). Additionally, the Shapiro pattern shows a pronounced *Chevron-like* structure at low microwave powers. The latter can either be attributed to a slightly *overdamped* junction or, which is more likely, a current-phase relation that deviates significantly from the conventional sinusoidal shape. This is supported by the fact that the histogram in Fig. 1.6 (b) contains multiple power ranges in which either the first (and sometimes the second) odd step or all even steps are suppressed. For a finite field of 120 mT, which is supposed to drive the system into the first outer lobe, the corresponding Shapiro spectrum in Fig. 1.6 (c) appears noticeably more *cleaned up*. This effect is probably caused by the much smaller supercurrent. However, especially in the range of -5 to +5 dB, the voltage-resolved histogram Fig. 1.6 (d) shows some **subharmonic features** which are most pronounced at **half integer** values. This is a strong indication that this effect can not be fully attributed to the reduced supercurrent and the corresponding *stabilization* of the junction dynamics rather than a more fundamental change of the quantum state of the system. However, as already pointed out at various occasions, all Shapiro measurements share the same built-in uncertainty due to their dependency on the resistive, capacitive and inductive properties of the Josephson junction.

In order to be less sensitive to possible parasitic side effects of the junction dynamics that could arise from the unconventional device geometry, we also performed *emission measurements* on a set of InAs/Al full shell nanowires that were all shunted by on-chip resistors. In order to detect the emitted photons, the drain contact of the junction was connected to a wide-band cryogenic amplifier that has been decoupled from the DC circuitry by means of DC blocks. To improve the signal-to-noise ratio, additional low- and high-pass filters were implemented into the fridge wiring. However, this

also restricted the lossless accessible frequency range to 3-8 GHz. Fig. 1.7 (c) shows the frequency-dependent response of a typical device in terms of the normalized magnitude of the amplifier signal. It should be pointed out that, due to the selected gain needed to properly detect the photons, the amplifier switches into overload as soon as the voltage drop across the nanowire Josephson junction reaches a certain threshold. Thus, all data above $\approx \pm 30\mu$V (outer red/dark red areas) does not contain any valuable information.

The black dashed lines in Fig. 1.7 (a) indicate the theoretically expected frequency-dependent increase of the photon energy, which is in (almost) perfect agreement with the experimentally obtained signal. Subsequently, after proving the successful emission and detection of photons, the nanowire Josephson junction dynamics have been probed with respect to the applied magnetic and electrical field. The measurement depicted in Fig. 1.7 (b) ($B_{||}$=0T) shows that the junction is able to emit a photon for only a limited number of gate voltages. This could be caused by strong quantum fluctuations of the supercurrent or Coulomb blockade within the nanowire channel. Fig. 1.7 (c) shows the device response for an in-plane magnetic field applied parallel to the nanowire axis (corrected rotation angle β=-65°) and a constant gate voltage of V_g=4.8 V. Here, one of the most prominent features is the replication of the lobe structure shown in Fig. 1.4 in terms of a magnetic field range of 50 mT without any emission response. Even more intriguing is the fact that the emission signal reaches its maximum magnitude for a finite magnetic field of 45 mT rather than for the zero-field case and the corresponding unperturbed supercurrent. This, in combination with the *instabilities* of the Shapiro signal shown in Fig. 1.6 (a), could be an indication of a more complex behavior beyond the conventional junction dynamics. However, despite the much larger sensitivity of this measurement method, the device shows the same susceptibility towards a rotation misalignment as the measurement shown in Fig. 1.3 (b), with a valid rotation range of only $\Delta\beta$=-25°(cf. Fig. 1.7 (d)).

Despite the acquisition of multiple **emission** and **Shapiro spectra** at various gate and magnetic field configurations, it was not possible to directly probe *multiples of the Josephson frequency* besides the conventional 2π-mode or observe any robust signatures of missing Shapiro steps that, following the theory of Majorana zero modes, could be attributed to topological excitations. However, as a major downside of both approaches, it turned out that most of the features within the *lobe* structures are masked by the ohmic contribution of the on-chip shunt resistor. Thus, even though the conventional signatures of the Little-Parks effect are still visible, all information about the (Andreev) state structure is lost. In that sense, it is impossible to tell if the measured devices show the same energy-independent states that have been observed in Fig. 1.4 (b) at all.

VI

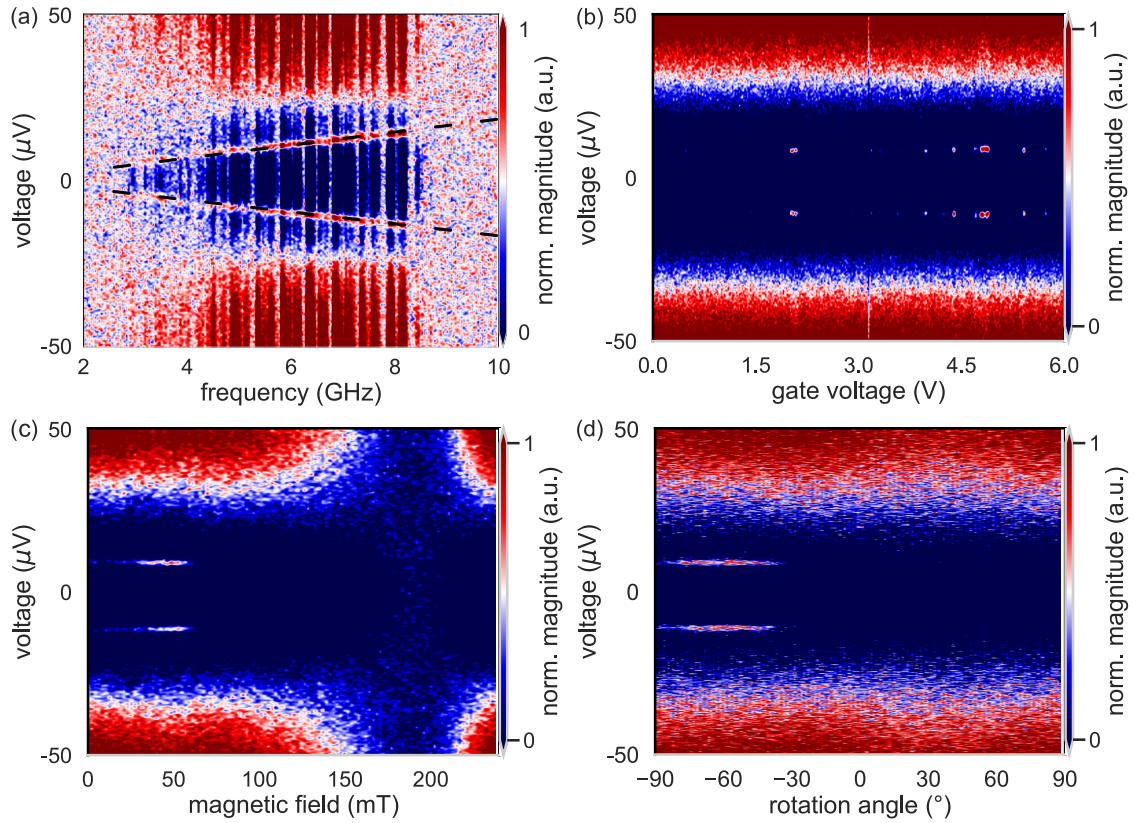

Figure 1.7 – *(a) Frequency-, (b) gate- and (c),(d) magnetic field-dependent emission measurements on a InAs/Al fullshell nanowire Josephson junction. Here, the normalized amplitude of the narrow bandwidth amplifier signal is color-coded. The device exhibits a clear and pronounced photon emission rate for certain gate voltages (b). Additionally, it mimics the lobe structure of Fig. 1.4 in terms of a complete signal suppression for finite magnetic fields (period of* $\approx 120\,mT$*).*

1.4. SQUID MEASUREMENTS

After the investigation of several different samples which exhibited the Little-Parks effect in terms of the *lobe*-structure, a fundamental change of the device layout was made. Instead of probing single and individual nanowires, the setup was changed to the **SQUID** design shown in Fig. 1.8 (a). Here, the InAs/Al fullshell nanowire Josephson junction (see Fig. 1.8 (b)) is connected to another nanowire Josephson junction in parallel which acts as a **detector**. The idea is inspired by the idea of the theoretically proposed **Majorana-Transmons** [431–434]. This is based on the assumption that the creation of a *Majorana fermion* in terms of the transition from the *trivial* to the *topological* regime is associated with a pronounced **parity change** of the system which translates into a **phase jump** of π [435–438]. Thus, during the measurement, the SQUID is first driven into an out-of-plane magnetic field configuration in order to detect the corresponding *interference pattern*. In the next step, the out-of-plane field magnitude is kept constant such that it resides on top of one of the interference maxima, as shown in Fig. 1.8 (c). Here, every individual data point corresponds to the average of 1000 **switching current** measurements (ramp frequency 1 kHz), which reduces the sensitivity to stochastic processes and noise even further [2]. Finally, an in-plane magnetic field with varying magnitude and alignment is applied in order to tune the *phase winding* of the Little-Parks effect. If this field manages to push the system into the *topological regime*, the creation and hybridization of the Majorana pairs should significantly alter the **current-phase relationship**, effectively changing the response of the whole *SQUID* device. Unfortunately, so far the measurements could not be performed as planned, since for most of the devices that have been fabricated the *gate electrodes* of the **detector-wires** provided insufficient control over the supercurrent of the corresponding devices. Nevertheless, the angle-dependency with regards to the out-of-plane field for the device in Fig. 1.8 (a) (shown in

[2] The measurements have been carried out using a *Keysight MSOX3104T* Mixed-Domain-Oscilloscope.

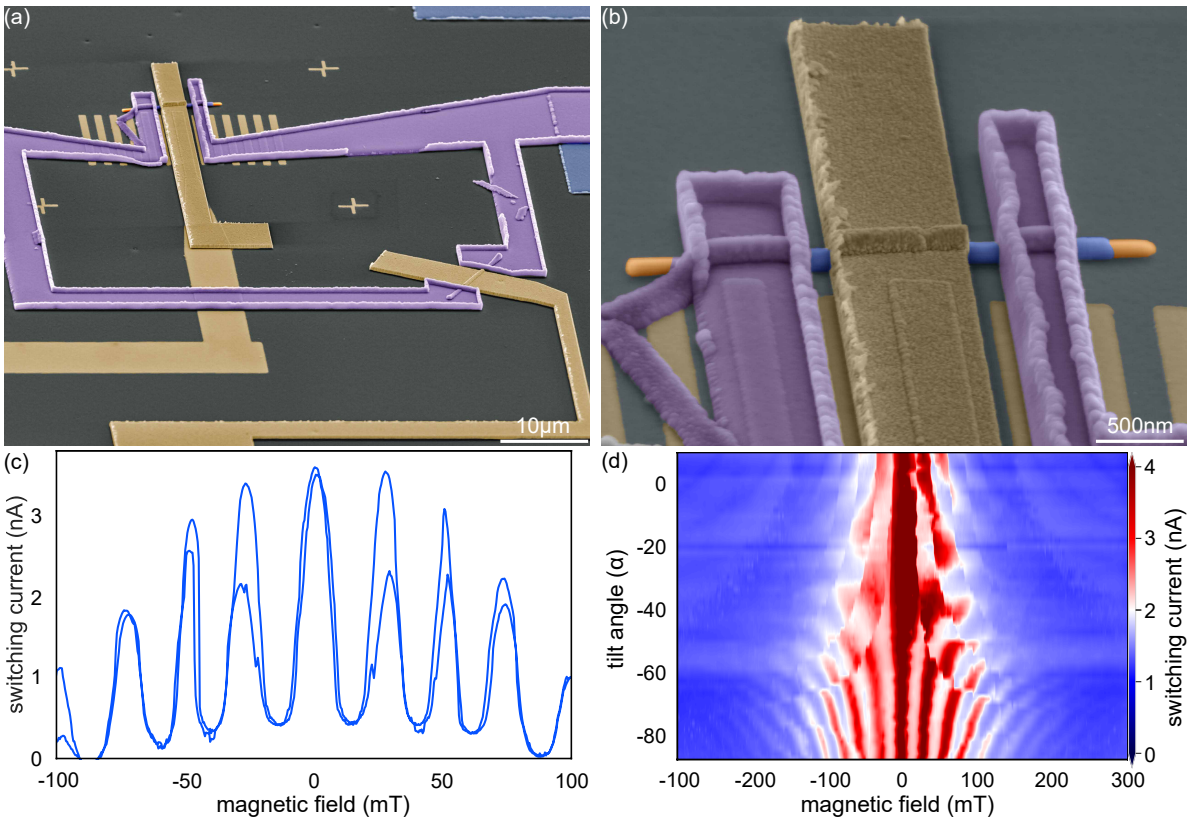

Figure 1.8 – *(a) False-colored SEM micrograph of an exemplary SQUID device consisting of an InAs/Al fullshell and an InAs/Nb halfshell nanowire Josephson junction. Both devices are connected via an NbTi loop and can be gated independently . (b) Zoom-in of the fullshell nanowire, clearly showing the pseudo-wrap gate geometry, the open ends to allow the in-plane field penetration and Al-free weak link in the center of the nanowire. (c) A back-and-forth measured SQUID trace without an applied in-plane field, showing a small, but clearly visible interference spectrum. (d) The same trace but with an additional in-plane field in order to push the system into the first Little-Parks lobe and at various tilt angles with respect to the out-of-plane field. The formerly periodic SQUID response gets interrupted by additional* ***phase jumps*** *of* π *which could, potentially, be associated with an intrinsic parity change of the system.*

Fig. 1.8 (d)) exhibits strong indications for effects that can not be explained in terms of the conventional SQUID behavior. Besides the expected response, i.e. the *cosine*-dependency for the position of the minima and maxima if the tilt angle is changed with respect to the $-90°$ position, the latter are superimposed by additional features *cutting through them*. These features are associated with a **reproducible** and **symmetric** *phase jump* of $\Delta\varphi \approx \pi$.

In order to clearly pinpoint the physical origin of the observed effect, the device layout needs to be altered such that the *detector*-wire can be fully pinched-off to enable an independent investigation of the InAs/Al nanowire Josephson junction as the actual *Little-Parks* platform. First attempts with ex-situ contacted and undoped InAs wires showed promising results but could not be included due to the limited time of this thesis. However, based on the presented findings, the Little-Parks effect remains a powerful and very interesting approach to detect and manipulate Majorana zero modes. This is all the more relevant as the conventional method, i.e. the search for **zero bias anomalies** by means of tunnel spectroscopy, has come under increasing pressure due to new results that could identify fundamental issues which make it highly doubtful that they are a proper tool to search for topological excitations [268, 439–442].

VII

(Quantum) Transport in antimony-based core/shell nanowires

1

INTRODUCTION

Nanostructures based on InSb, in particular nanowires, have attracted considerable interest because of the small electron effective mass and the related very high electron mobility of InSb. This makes this material very interesting for high-speed nanoelectronic applications [443–447]. Furthermore, the very small band gap of about 180 meV at 300 K, results in ambipolar behaviour when changing the gate voltage in a field-effect transistor allowing for switching between p- and n-type transport [71, 443]. Because of the very large g-factor and the presence of spin-orbit coupling, spin-related coherent quantum transport can be studied in detail and applications with respect to spintronic devices and topological quantum computation are suggested [45, 448–450]. "Regarding the latter, evidence of the presence of Majorana zero modes was reported in structures based on InSb nanowires partly covered by a superconducting electrode [390, 451]. However, recent theoretical predictions suggest, that the phase space in which Majorana zero modes may form can be significantly enhanced in terms of the required strong spin-orbit interaction, if a narrow-gap semiconductor like InAs or InSb is combined with a wide-gap semiconductor as a core material [2]. This is due to the shift of the electronic states towards the outer surface of the core/shell system, where the slope of the bands and the corresponding electrical field is much larger."[1]

For the future realization of devices based on nanowire/superconductor devices, the underlying core/shell nanowire system has to fulfill a couple of benchmark criteria, including a sufficiently long phase-coherence length l_φ. In prior magneto-conductance measurements on GaAs/InAs core-shell nanowires, clear Aharonov–Bohm-type oscillation patterns could be resolved when a magnetic field was threading the cross section of the nanowire [79–81]. For the present GaAs/InSb core-shell nanowires, the situation is more complex because of the stronger effect of the Zeeman energy due to the much larger g-factor of InSb compared to InAs. By performing transport measurements in a parallel magnetic field, we analyzed the resistance modulations with respect to Aharonov–Bohm-type oscillations and a possible influence of Zeeman-splitting on the energy dispersion of the flux-periodic energy spectrum. In order to gain information on l_φ, we also performed transport measurements in a magnetic field oriented normal to the wire axis. By analyzing the resulting universal conductance fluctuations (UCFs) spectrum in terms of the correlation field, we obtain values for l_φ in wires with different geometries. One of the key differences to our previous nanowire system based on GaAs/InAs is the occurrence of weak antilocalization (WAL), indicating the presence of spin-orbit coupling. Using a combination of gate-averaging and a fitting model, we extract values for the spin-orbit scattering length l_{SO}.

In the following two chapters, nanowires with a highly conductive narrow-gap InSb shell and a high-resistive wide-gap GaAs core are studied by (magneto)-conductance measurements at ambient and low temperatures. The tubular shell topology of the conductive channel offers a good control of the action of the magnetic field and the gate voltage on the circulating electron current. From previous studies on the defect structure and transport properties at room temperature, the InSb shell is revealed to be fully relaxed due to the high lattice mismatch between GaAs and InSb [71]. This is

[1] Added as additional information.

VII

confirmed by comparing gate-dependent IV characteristics for various core and shell geometries at different temperatures with simulations based on standard bulk values of all relevant properties, e.g. carrier concentration, mobility and band offsets.

2

ROOM TEMPERATURE TRANSPORT

2.1. DEVICE FABRICATION AND MEASUREMENT TECHNIQUES

"The GaAs/InSb core/shell nanowires were grown in two steps using molecular beam epitaxy. Details on the growth parameters can be found in Ref. [38]. First, GaAs nanowires were grown from Ga droplets formed in pinholes of a thin layer of native silicon oxide on a Si (111) substrate. In the subsequent step the InSb shell was grown on the sidewall facets of the GaAs core nanowire. Here, a nucleation of InSb V-shaped islands on the side facets of GaAs nanowires was followed by a coalescence of the islands leading to the formation of an InSb shell. The (average) shell thickness increases linearly with the growth time and the growth rate is about $20-25\,\mathrm{nm/h}$. We investigated samples of four different growth runs which are summarized in Table 2.1. Due to the shorter growth time, the shell of the first growth run (sample A) has a rather pronounced roughness leading to the non-uniform average shell thickness. In contrast, the surface of the nanowires of the last growth run (sample D) is smoother and the shell thickness is nearly uniform along the nanowire. The GaAs core nanowires have a hexagonal morphology and mainly consist out of a zinc blende crystal structure, which is adopted by the InSb shell."[1]

The GaAs/InSb core-shell nanowires were contacted individually by first transferring them to a highly n-doped silicon substrate with a 200-nm-thick SiO_2 layer. Next, the contact fingers with a width of 250 nm were defined by means of electron beam lithography and a three layer resist stack consisting of PMMA/Copolymer/
PMMA. Prior to the metal deposition, the contact areas on the nanowire were cleaned by Ar^+ sputtering. Subsequently, a Nb/Au (3 nm/60 nm) layer was sputter-deposited and lift-off was performed to obtain ohmic contacts. The contacts had a separation of about 500 nm. A scanning electron microscopy image of a typical sample is shown in Fig. 2.1. The magneto-transport measurements were performed both at ambient temperatures and in a ^{4}He variable temperature insert with a minimum base temperature of 1.4 K. In the latter setup, magnetic fields up to 13 T were available. In some measurements the highly n-doped substrate served as a back-gate electrode to modulate the carrier concentration. All transport measurements were performed in a two-terminal configuration. For the low temperature and magnetotransport measurements, a lock-in technique with an ac voltage bias of 40 μV was used. Here, the current was measured by means of a current-voltage converter. The contact resistance was of the order of 20 to 100 Ω, and therefore considered negligible.

[1] Changed and adjusted to make sample naming consistent and provide more information about the selection of the growth runs.

VII

2.2. AMBIPOLAR TRANSPORT AND SIZE-DEPENDENCY

To obtain first insights into the transport behavior, we performed electrical measurements at room temperature. Table 2.1 lists the dimensional characteristics of GaAs/InSb core-shell nanowires obtained from four growth runs used for room temperature electrical transport measurements. From sample A to D the InSb shell thickness t_s successively increases from 9 to 33 nm. These samples are representative examples of their specific growth run. Fig. 2.1 (b) and (c) show the current-voltage-characteristics (IV curves) of the GaAs/InSb nanowires with the thinnest (sample A) and thickest shell (sample D) at different back gate voltages V_{bg}, respectively. Clearly, both wires behave differently. While the measurements of the sample with the thin InSb shell reveals a p-type field-effect transistors behavior (cf. Fig. 2.1 (b)), i.e. a decrease of the slope for increasing (positive) gate voltages, the situation is opposite for the wire with the thick shell (cf. Fig. 2.1 (c)). In the latter case an n-type behavior is observed, i.e. with increasing gate voltage the source-drain current increases, accordingly.

Sample	Core radius r_c [nm]	Shell thickness t_s [nm]	r_c / ($r_c + t_s$) [%]
A	40	9	82
B	32	13	71
C	41	21	66
D	25	33	43

Table 2.1 – *Overview of the different nanowire dimensions.*

In order to take a closer look at the relation between the shell thickness, and the type of conductance in the transport channel, the transfer characteristics were measured. The corresponding results are shown in Fig. 2.1(d). For the nanowire with the thinnest InSb shell (sample A) the field-effect characteristic is essentially p-type, i.e. the conductance decreases with increasing positive gate voltage, with just a slight n-type contribution at higher gate voltages. For the nanowire with the next larger shell thickness of 13 nm (sample B) a prominent n-type region is found for positive gate voltage, while p-type transport is observed at negative gate voltages. With increasing shell thickness the p-type branch of the gate-dependent conductance is more and more suppressed until the nanowires become purely n-type for the sample with the largest shell thickness of 33 nm (sample D) . The smaller conductance of sample D comprising the largest shell thickness compared to sample C with the next smaller shell thickness can probably be attributed to larger contact resistances. The measurements are performed in a two terminal configuration, thus the contact resistance is included in the total conductance and may vary from sample to sample. For the theoretical determination of the type of transport for different geometries, the band profile as well as the carrier occupation were calculated by a Schrödinger-Poisson solver using the band offsets [452, 453]. Here, the envelope functions of electrons and holes in the conduction and valence bands were determined within the effective mass approximation [454]. For reasons of simplicity, we assumed that the nanowires are infinitely long and have a circular cross-section (Fig. 2.2 (c), inset). The used core diameters and shell thicknesses of the cylindrical nanowires are equal to those measured experimentally (see Table 2.1). Additionally, the electron effective masses were set to 0.063 (GaAs) and 0.017 (InSb) and the hole effective masses were assumed to be 0.31 (GaAs) and 0.245 (InSb) times the free electron mass [455]. As can be seen in Fig. 2.2 (a) and (b), the band structure calculations reveal that charge carriers populate only the InSb shell of the nanowire while the GaAs core does not contribute to the conductance [81]. This finding holds for both a completely undoped GaAs core as well as for low doping concentrations of 5×10^{15} cm^{-3}. Due to the small bandgap of 150 meV an electron and hole concentration of about 5×10^{17} cm^{-3} is present in both the conduction and valence band of the InSb shell at room temperature. This is considerably higher than typical background doping concentrations of MBE grown films and thus it is reasonable to assume a position of the Fermi level close to the middle of the band gap. However, due to the strong asymmetry of the bandstructure for electrons and holes, the number of hole states close to the valence band edge is very large, whereas the number of states close to the conduction band is small. Thus the number of available states in the conduction band limits the amount of thermally activated carriers. Moreover, this asymmetry will slightly shift the Fermi level towards the conduction

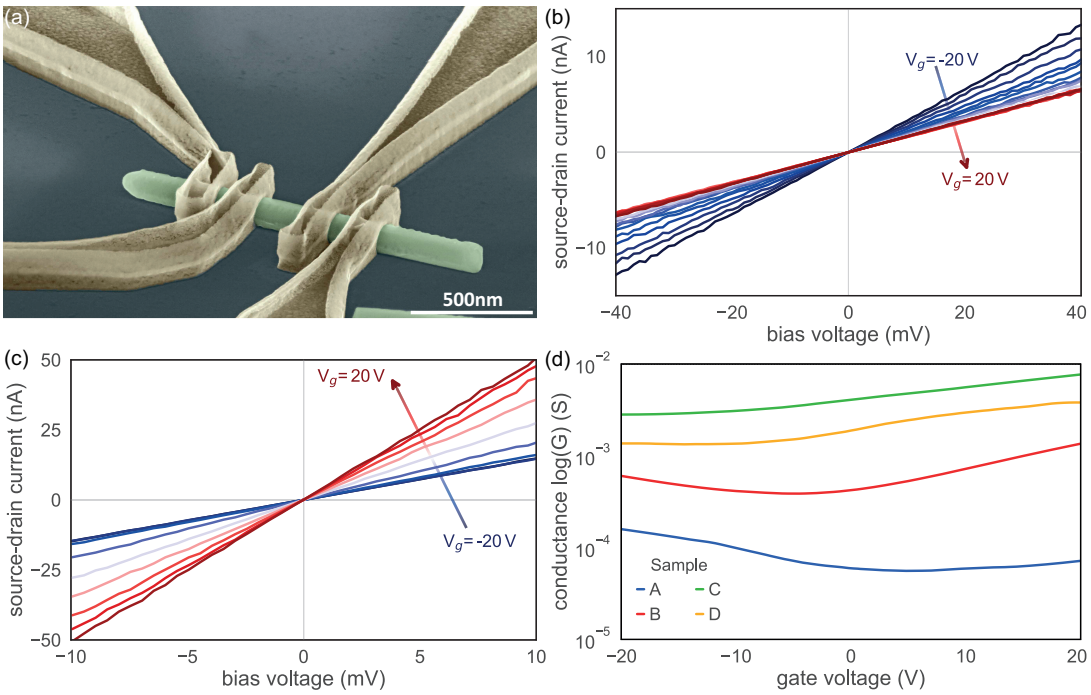

Figure 2.1 – *(a) Scanning electron micrograph of a typical GaAs/InSb nanowire device. The leads are made out of a 3 nm/60 nm thick Nb/Au layer. The SiO_2 covered silicon substrate acts as a backgate. (b) Gate dependent current-voltage characteristics for a GaAs/InSb core-shell nanowire with a shell thickness of 9 nm, which shows p-type transistor behavior. The gate voltage changes in steps of 2 V between the different curves. (c) Corresponding measurements on sample D with shell thickness of 33 nm, which acts as an n-type transistor. The gate voltage steps are 4 V. (d) Transfer characteristics of samples A to D at room temperature using bias voltages of V_{sd}=100 mV, 25 mV, 10 mV and 10 mV, respectively. The samples **A** to **C** exhibit a continuous increase in conductance for thicker InSb shells. Sample **D**, on the other hand, is less conductive than **C**. The latter could be an indication for a threshold in the geometry-induced resistance drop caused by a switch to another scattering mechanism that dominates the charge carrier transport. Image content taken from [71].*

band edge. In the case of thin InSb shells this asymmetry is further enhanced due to small effective mass of electrons leading to a large confinement shift of quantized states in the conduction band whereas the corresponding shift of the subbands in the valence band is small due to the large effective mass of holes. As a result the number of thermally activated carriers is reduced. In this situation of a basically intrinsic, narrow band gap semiconductor it is quite natural that p- and n-type conductivity can be induced by a back gate voltage. In order to simulate the effect of an applied back gate voltage, we varied the boundary condition for the Poisson equation at the nanowire surface, via changing the position of the Fermi level (E_F) with respect to the conduction band edge at the nanowire surface (E_c). This shift in the position of E_F is denoted as ΔE_{FC}. It needs to be kept in mind that a small shift of E_F towards the valence band (E_v) at the nanowire surface leads only to a small upward bending of the bands; however, due to the large number of states at the valence band edge this will strongly increase the number of holes. This situation, induced by a negative gate voltage, is depicted in Fig. 2.2 (a). To induce the same number of carriers in the conduction band, a much stronger shift of E_F towards the conduction band is required with the corresponding downward bending of the bands at the surface. This is attributed to the smaller number of electron states close to E_c compared to the large number of hole states in the vicinity of E_v. This situation, induced by a positive gate voltage, is shown in Fig. 2.2 (b). A reduction of the shell thickness and the corresponding strong confinement shift for the subbands in the conduction band further increases the asymmetry. In turn, this leads to an even larger shift of E_F required to induce the same amount of electrons into the conduction band in narrow shells compared to thick shells. It has to be noticed, that due to the strong asymmetry of the bandstructure, there is neither a linear nor a symmetric dependence of the position of E_F on the applied back gate voltage. However, it becomes clear that a larger positive backgate voltage is needed in nanowires with thin shells than in those with thick shells in order to achieve the same

VII

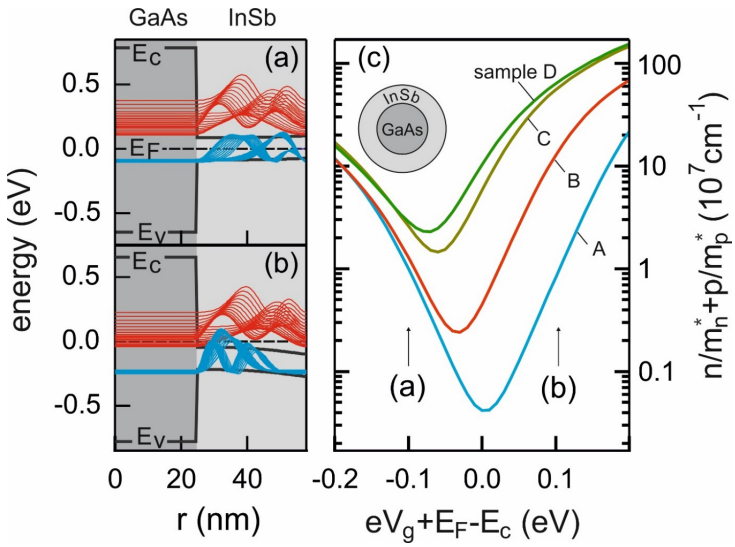

Figure 2.2 – *Calculated conduction and valence band profiles of a GaAs/InSb core/shell nanowire, for (a) negative and (b) positive gate bias voltages. The corresponding probability densities of the confined electron and hole states for the first and second radially confined states at various angular momentum quantum numbers are plotted in red and blue, respectively. (c) Calculated values of* $\left(n/m_n^* + p/m_p^*\right)$ *assumed to be proportional to the conductance as a function of gate bias voltage with respect to E-*E_c *corresponding to samples A to D. The two gate bias conditions assumed in (a) and (b) are also indicated in (c). Image content taken from [71].*

n-type conductivity, which is qualitatively in agreement with the experimental observations.

To calculate the conductance in the presence of both electrons and holes we use the relaxation time approximation which is given by [456]

$$\sigma = \frac{e^2}{m_e}\left(\frac{n\tau_n}{m_n^*} + \frac{p\tau_p}{m_p^*}\right). \tag{2.1}$$

Here, n and p indicate the one dimensional electron and hole densities, m_n^* and m_p^* are the electron and hole effective masses, and τ_n and τ_p indicate the average relaxation times for electrons and holes, respectively [456]. The latter ones are determined by the different scattering mechanisms in the core-shell nanowires. However, in first approximation we neglect the complicated origin of the scattering and assume that the conductance is only determined by the corresponding charge carrier densities and effective masses, thus

$$\sigma \propto \left(\frac{n}{m_n^*} + \frac{p}{m_p^*}\right) \tag{2.2}$$

"Fig. 2.2 (c) shows the result of Eq. 2.2 calculated for all four measured GaAs/InSb core-shell nanowires".[2]. It can be seen, that our theoretical model fits quite well, at least qualitatively, to the experimentally obtained gate dependent conductance curves in Fig. 2.1(d). Both reveal an increase in conductance for sufficiently large positive and negative gate values. These two branches are thereby separated by a gap-like minimum, which shifts to more negative gate voltages for thicker InSb shells. It should be mentioned that this shift is just slightly visible in Fig. 2.1(d) due the missing ambipolarity for samples C and D, but additional field-effect transistor measurements over a larger backgate range showed that ambipolarity is observable for all kinds of wires if a sufficiently large negative gate voltages is applied.

However, especially for the wires with the thinnest shell, the strong confinement could possibly lead to a change of the in-plane effective mass compared to the bulk values due to the partial leakage of both the electrons and the holes into the core layer. Therefore, we recalculated the effective mass of the system by taking into account that for materials with parabolic energy bands the inverse of the

[2] Adjusted to make sample description consistent

effective mass value is the sum of the product of the inverse of the two masses and the corresponding occupation probabilities of the core and the shell [457]. The calculation of the effective mass values shows that the leakage of the wave-functions into the barrier layer leads to the slightly higher value of the in-plane effective masses. The difference between the bulk values and the recalculated ones is about 1% for the nanowire with the shell thickness of 9 nm and less than 0.5% for the thicker shells. A comparison of the IV curves based on the bulk values with the ones which have been modeled using the recalculated effective mass shows that both datasets are completely identical over the whole range of the surface potential, i.e. the influence of the core on the effective mass is negligible. In order to investigate if there is any other correlation between the core dimensions and the electronic properties, we recalculated the IV curves of the wires C and D for constant shell thicknesses but varying core diameter. It was found, that a large radius of the core slightly affects the charge carrier population in the nanowire, even if the change of the total carrier density is below 1%. However, due to the radial symmetry of the nanowires, the charge carriers are confined in radial as well as in azimuthal direction. An increase of the core diameter leads to a broadening of the azimuthal quantum well. Thus, the energy states with the different angular momentum quantum number are getting lower and more densely distributed over the energy scale. This gives rise to a higher charge carrier population in the shell of the C nanowire and could possibly explain the experimental finding that the measured conductance is larger compared to the D nanowire with a thicker InSb shell.

The presented results demonstrate, that despite the large lattice mismatch core/shell nanowires with a highly conductive InSb shell can be realized thanks to the efficient strain relaxation at the interface. This opens up the possibility to use these structures as an alternative to bulk InSb nanowires for spin-based devices or more exotic phenomena such as Majorana bound states. Thus, the following chapter focuses on the electrical investigation of GaAs/InSb core/shell nanowires at cryogenic temperatures.

3

ELECTRON INTERFERENCE AND SOI IN GAAS/INSB CORE-SHELL NANOWIRES

3.1. AMBIPOLAR BEHAVIOR

"For the low temperature measurements, samples of two different growth runs (cf. Table 2.1) were investigated. Sample A was fabricated using a nanowire of growth run **D** with a core radius $r_c = 25\,\text{nm}$ and a shell thickness of $t_s = 50\,\text{nm}$, while the samples B1 and B2 consist of nanowires of growth run **C** with $r_c = 35\,\text{nm}$ and $t_s = 22-30\,\text{nm}$. For nanowires with thinner shells, i.e. growth run **A** and **B**, respectively, it was not possible to fabricate any measurable devices. The latter was most likely caused by a full depletion of the InSb shell at cryogenic temperatures which made it impossible to drive the device out of pinch-off for reasonable backgate voltages (V_{bg}<70 V)."[1] General information on the type of transport in our GaAs/InSb core-shell nanowires is gained by measuring the conductance as a function of back-gate voltage V_g. Figure 3.1(a) shows an exemplary measurement on sample B1 at 1.5 K for a DC source-drain bias voltage of $V_{sd} = 1\,\text{mV}$. Corresponding data for samples of growth run A are given in Fig. 3.1(b). Two conductive ranges can be identified. First, at a gate voltage of about −4 V,

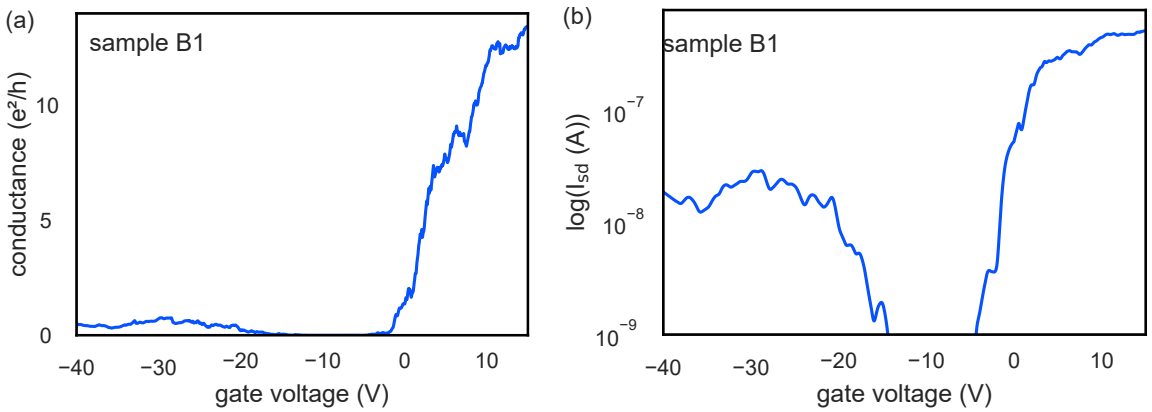

Figure 3.1 – *(a) Conductance G of sample B1 in units of e^2/h as a function of back-gate voltage V_g. The measurement was performed at T = 1.5 K. (b) Logarithmic plot of the corresponding source-drain current I_{sd} vs. V_g. Data taken from [70].*

the conductance increases with increasing V_g, thus indicating n-type conductance of the nanowire. Second, below a gate voltage of approximately −15 V the conductance increases as well towards more negative gate voltages, which corresponds to a p-type behaviour. Between these branches, the conductance is suppressed. We attribute this to an ambipolar behaviour, i.e. a switching between n- and p-type transport, induced by shifting the Fermi level E_F from the conduction band into the valence band with decreasing V_g. In between E_F is passing through the band gap, thus no carriers are available for transport. The ambipolar behavior occurs because of the very small band gap of InSb,

[1] Added to make sample naming consistent and provide more information about the selection of the growth runs.

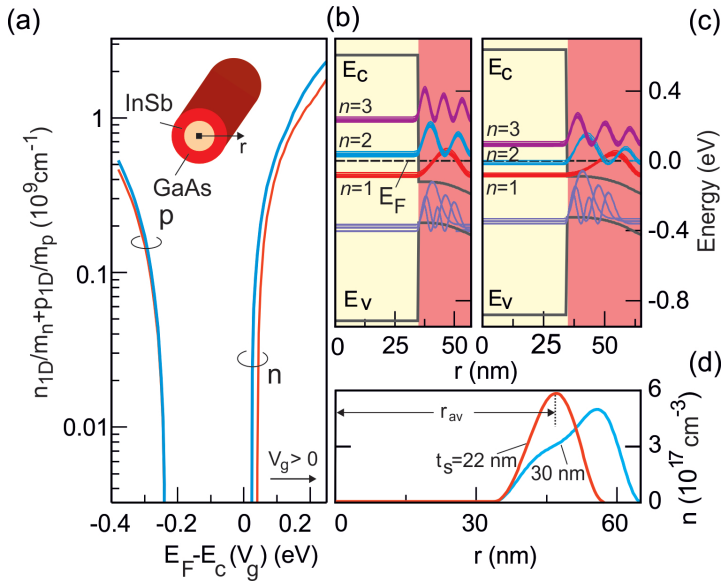

Figure 3.2 – *(a)* $G_t \propto n_{1D}/m_n + p_{1D}/m_p$ *as a function of the conduction band edge position with respect to* E_F *at the nanowire surface. The simulations correspond to nanowires of growth run B, assuming an InSb shell thickness of 22 nm (red) and 30 nm (blue), respectively. The Fermi level is set to zero energy. Inset: Sketch of the GaAs/InSb core-shell nanowire with a cylindrical cross section. (b) and (c) Band diagram and squared eigenfunctions for a GaAs/InSb nanowire corresponding to the second growth run with the shell thickness set to 22 nm (b) and 30 nm (c) and* $E_F - E_c = 0.2$ *eV; (d) Three-dimensional electron density as a function of the radial coordinate r for a nanowire corresponding to growth run B with the shell thickness set to 22 nm (red) and 30 nm (blue) and* $E_F - E_c = 0.2$ *eV. Image taken from [70].*

i.e. 235 meV at 1.5 K, compared to other III-V semiconductors. In order to point out the rapid decrease of the conductance when the band gap region is approached, we also plotted the source-drain current in a logarithmic scale in Fig. 3.1(b). Such an ambipolar transfer characteristic was observed before for InSb nanowire-based field-effect transistors [71, 443]. However, since these measurements were performed at room temperature, no complete pinch-off was achieved in the band-gap region because of thermal smearing. In our case at a temperature of 1.5 K a full pinch-off is achieved. As can be seen in figure 3.1(b), the conductance in the p-type region is lower than in the n-type region. We attribute this to the larger effective hole mass compared to the electron mass resulting in a lower mobility for holes. Furthermore, we cannot rule out that the contact resistance is increased for the p-type region, since the measurements are performed in a 2-terminal configuration. A closer look on the transfer characteristics reveals some superimposed modulations. At small conductance values, near the threshold to the gap region, the current-voltage characteristics reveal a non-linear behaviour with a plateau around zero source-drain bias, which we attribute to Coulomb blockade effects [458]. Owing to the low carrier concentration and potential fluctuations caused by disorder, charge islands separated by barriers are formed. In case of electron transport, a linear current-voltage characteristic was achieved at larger positive gate biases of $V_g > 5$ V for the sample shown in Fig. 3.1. In the p-type transport regime we did not succeed in observing linear characteristics. As a consequence, the following magneto-transport measurement were performed exclusively at a fixed positive gate bias in the *n*-type region, in order to prevent single electron transport contributions.

For the theoretical interpretation of the measurements shown in Fig. 3.1 we performed band structure calculations. Here, we approximated the hexagonal cross section a cylindrical one (cf. Fig. 3.2(a) (inset)) to simplify the simulations. The coupled Schrödinger and Poisson equations were solved self-consistently for the envelope function $\Phi_{nl}(r)e^{(il\varphi)}$ within the effective mass approximation and by assuming a lattice temperature of 4 K. Here, r and φ are the radial and angular coordinates, and n and l the radial and the orbital quantum numbers, respectively [459]. The measured source-drain current as a function of the gate voltage, as plotted in Fig. 3.1, does not show indications of quantized conductance due to ballistic transport. Instead, because of the numerous crystal lattice imperfections, the source-drain current undergoes random fluctuations. Thus, diffusive charge

transport can be assumed. The total electron and hole densities, n_{1D} and p_{1D}, were calculated by integrating the three-dimensional electron and hole densities, i.e. n(r) and p(r), over the nanowire cross section. The total conductance is defined as $G_t = e(n_{1D}\mu_n + p_{1D}\mu_p)$. Here, μ_p and μ_n correspond to the electron and hole mobilities, respectively. Following the relaxation time approximation and neglecting the origin of the charge carrier scattering, we can assume, that $G_t \propto n_{1D}/m_n + p_{1D}/m_p$, where m_n and m_p are the effective mass of electrons and holes, correspondingly. In order to simulate the effect of the back-gate voltage on the nanowire conductance we vary the boundary condition for the electrostatic potential at the nanowire surface, assuming that the electric field of the back-gate voltage does not break the axial symmetry. If the nanowire is subject to an applied gate voltage V_g, the position of the conduction band edge at the nanowire surface reads $E_c(V_g) = E_c(0) - \kappa e V_g$, where $E_c(0)$ is the unbiased position of the conduction band edge at the nanowire surface and κ is a coefficient which determines the ratio between the position of the conduction band with respect to the Fermi level E_F used for the calculations and the applied gate voltage. The latter will be discussed below.

Figure 3.2(a) shows $G_t \propto n_{1D}/m_n + p_{1D}/m_p$ as a function of conduction band edge position $E_c(V_g)$ with respect to E_F at the nanowire surface. The calculations were performed based on the minimum and maximum shell thickness of 22 and 30 nm, respectively, according to the geometry of nanowires of growth run B. The right part of the curve corresponds to a positive applied gate voltage and an n-type conductance of the nanowire. Obviously, the large positive gate voltage causes a downward band bending with E_F positioned inside the conduction band of the InSb shell. This case is demonstrated in Fig. 3.2(b) for $t_s = 22$ nm. The electron states of the first subband ($n = 1$) are below E_F and populated by electrons, thus electrons accumulate at the nanowire surface and the shell shows an n-type conductivity (cf. Fig. 3.2(a)). The electron density distribution shown in Figure 3.2(d) has a maximum near the center of the InSb shell. The intrinsic GaAs core of the nanowire is depleted, i.e. all the transport is restricted to the InSb shell. This assumption is based on the previous findings presented in [71], which showed a linear dependency between shell thickness and measured conductance for wires of different growth runs, which was independent from the corresponding core diameter. The change in the gate voltage towards the negative value leads to an upward bending of the energy bands at the surface. At a certain gate voltage the Fermi level is positioned inside the band gap which causes a depletion of the nanowire at low temperatures. A further upward band bending causes the Fermi level to shift into the valence band leading to a p-type conductance of the nanowire (cf. Fig. 3.1 and Fig. 3.2(a)). The p-type conductance is smaller than the corresponding n-type conductance due to the larger hole effective mass which agrees well with the experimental data shown in Fig. 3.1.

As mentioned above, the nanowires of growth run B have a shell of non-uniform width along the nanowire axis, varying between 22 and 30 nm. Thus, in Fig. 3.2(c) we also show the band diagram for an InSb shell thickness of 30 nm in the n-type conductivity regime. Due to the thicker shell, the energy eigenvalues are formed at lower values compared to the case of $t_s = 22$ nm depicted in Fig. 3.2(b). As a consequence, n-type conductance is found at smaller positive gate voltages. The energy states in the wider shell are also more densely packed. In addition, not only the first but also the second energy subband is occupied by electrons, which gives rise to a higher electron density (cf. Fig. 3.2(a)) and a rather broad electron density distribution within the shell. As shown in Fig. 3.2(d), the density distribution also has a weak second maximum located closer to the nanowire center. An important conclusion from this result is that in these nanowires tubular-like regions might exist which have a lower or higher electron density owing to the varying shell thickness.

In order to reveal the correspondence between the simulated and measured values of the conductance, one should find the ratio κ between $E_F - E_c$ and the gate voltage V_g at the nanowire surface. We apply the simplest method and compare the interval of the voltages/energies corresponding to the depleted regime of the nanowire, i.e. the regime when the conductance is equal to zero. According to Fig. 3.1, the gate voltage range in which the depletion occurs is about 10 V which corresponds to an energy range of about 0.25 eV in the simulation and $\kappa = 0.025$.

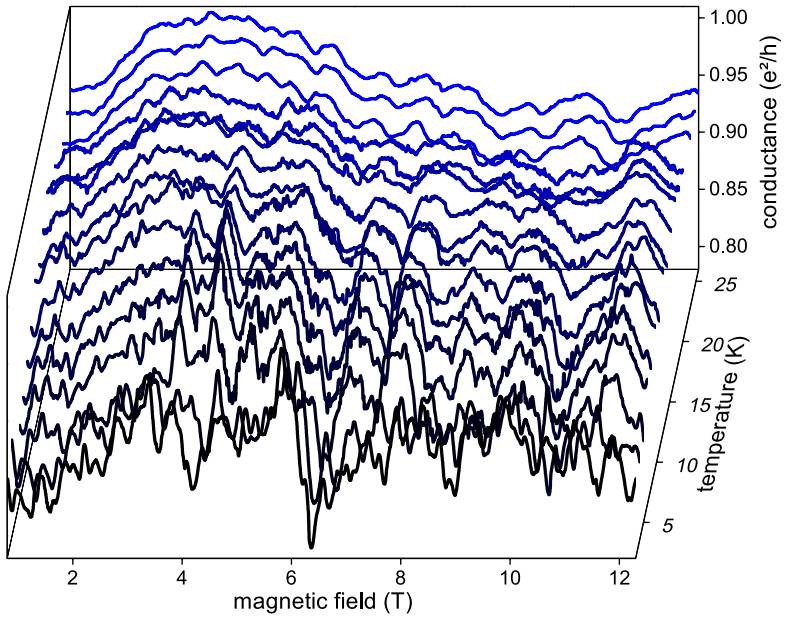

Figure 3.3 – *Conductance fluctuations in units of e^2/h of sample B1 as a function of a perpendicular magnetic field at temperatures between 2 and 25 K. Data taken from [70].*

3.2. UNIVERSAL CONDUCTANCE FLUCTUATIONS

After clarifying the general transport behaviour of our core/shell nanowires, we move on to the transport in the presence of a magnetic field. Figure 3.3 shows a typical conductance measurement of sample B1 as a function of a perpendicular magnetic field at temperatures between 2 and 25 K. In order to bring the nanowire into the n-type regime a back-gate voltage of 30 V was applied. The observed fluctuating pattern of the magnetoconductance can be assigned to universal conductance fluctuations, which originate from a superposition of several phase-coherent scattering loops of electron waves within the sample [97, 460–462]. The rich composition of both high and low frequency contributions is an indication for the coexistence of coherent loops with various sizes. If the temperature is increased, the rapidly oscillating components, which are related to larger loops, start to vanish. For temperatures above 17 K all pronounced fluctuations are suppressed, leaving the sample in a state in which the phase-coherence is lost.

On top of a qualitative description of the spectrum, it is possible to directly gain information on the characteristic parameters like the phase-coherence length l_φ. The phase-coherence length l_φ at different temperatures can be calculated using the expression [97, 460, 462]

$$l_\varphi = \gamma \frac{\Phi_0}{2 r_t B_c}, \tag{3.1}$$

with, the magnetic flux quantum Φ_0, a sample specific pre-factor γ, the total nanowire radius $r_t = r_c + t_s$, and the correlation field B_c. The latter is obtained by calculating the autocorrelation function of each single UCF trace. The correlation field acts as a figure of merit for the maximum area A encircled by a closed loop in which the electron partial waves interfere coherently. Following the relation $\Phi_0 = B_c \cdot A$, a larger correlation field is related to a smaller loop size and vice versa. Due to the fact that this model was initially developed for the characterization of two-dimensional samples, additional geometric and thermal corrections have to be considered. These are accounted for via the pre-factor $\gamma = 0.42 \ldots 1.3$ [90, 97].

In Fig. 3.4 l_φ, determined according to equation (3.1), is shown as a function of temperature for samples A and B1. To calculate l_φ we have chosen the minimum value for $\gamma = 0.42$, which means that the obtained values for l_φ represent the lower limits of the phase-coherence length.

Table 3.1 gives an overview about the most import parameters regarding the phase coherent transport for sample A and B1. Here, $l_{\varphi,max}$ refers to the maximum value of the phase-coherence

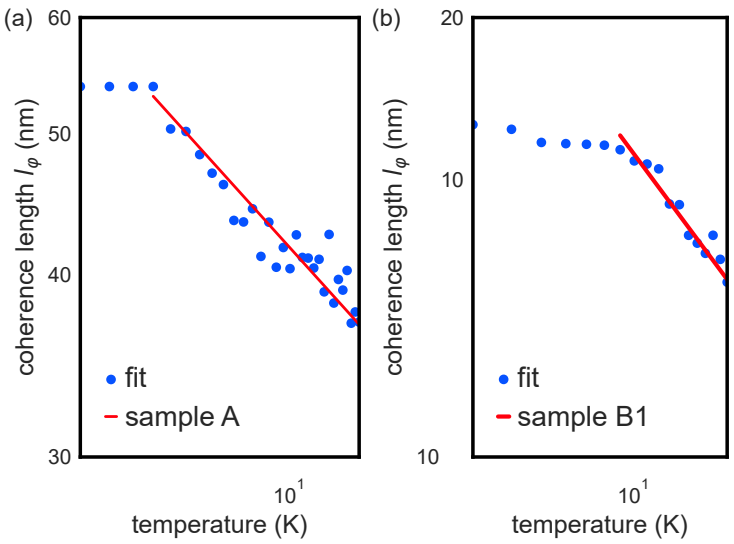

Figure 3.4 – *Temperature-dependent phase-coherence length for sample A (a) and B1 (b), based on the analysis of the correlation field B_c. The linear fit function (red) is used to extract ϵ as the damping rate of $l_\varphi(T)$. Data taken from [70].*

sample	r_t (nm)	L (nm)	$l_{\varphi,\max}$ (nm)	ϵ
A	75	500	23	-0.45
B1	69	500	55	-0.23

Table 3.1 – *Comparison of the two investigated devices with respect to the sample geometry and characteristic parameters: Total radius r_t, contact separation L, and $l_{\varphi,\max}$ as the maximum phase-coherence length l_φ extracted from the correlation field. The fit parameter ϵ corresponds to the temperature-dependent damping rate of l_φ.*

length obtained from the analysis of B_c. We attribute the comparably small phase-coherence length to a mismatch between the measured devices and the used model, which assumes a one-dimensional system. In our case, the diameter of the sample is in the same range as the contact separation and the exact sample geometry becomes more important [90]. Therefore, the pre-factor γ and thus l_φ might differ. However, due to the limited number of datasets, we restrict our further analysis to a qualitative comparison of the individual samples A and B1. The latter one shows a much larger phase-coherence length, which is in good agreement to the comparatively high conductance and gate tunability and could be an indication for better crystal quality and less defects.

Another important parameter is the temperature-dependent damping ϵ of the phase-coherence length. Our values of -0.45 and -0.23, respectively, are thereby in good agreement with previous works on nanowires [90, 463].

VII

3.3. WEAK ANTILOCALIZATION

Apart from universal conductance fluctuations, weak localization phenomena can also provide information about phase-coherence [88, 109]. Here, depending on whether spin-orbit coupling is involved or not, a magnetoconductance peak or dip is expected at zero magnetic field. Figure 3.5 (a) gives an overview of the conductance of sample B1 for low magnetic fields after the gate averaging procedure is performed for a voltage range of 14.2 V up to 21.8 V [98, 463]. The averaging was necessary to suppress conductance fluctuations.

In order to avoid any influence of the change in electron concentration, which is directly translated into a change of the background conductance, the whole gate measurement is cut into three segments which consist out of 25 individual magnetic field sweeps at different gate positions: 14.2 – 16.7 V, 16.8 – 19.3 V and 19.4 – 21.8 V. All three traces show a clear peak in conductance at $B = 0$ indicating weak antilocalization due to the presence of spin-orbit coupling [108, 109]. This is in contrast to previously measured GaAs/InAs core/shell nanowires, where a minimum in conductance around zero magnetic field, i.e. weak localization, was observed [80, 81]. Weak antilocalization and

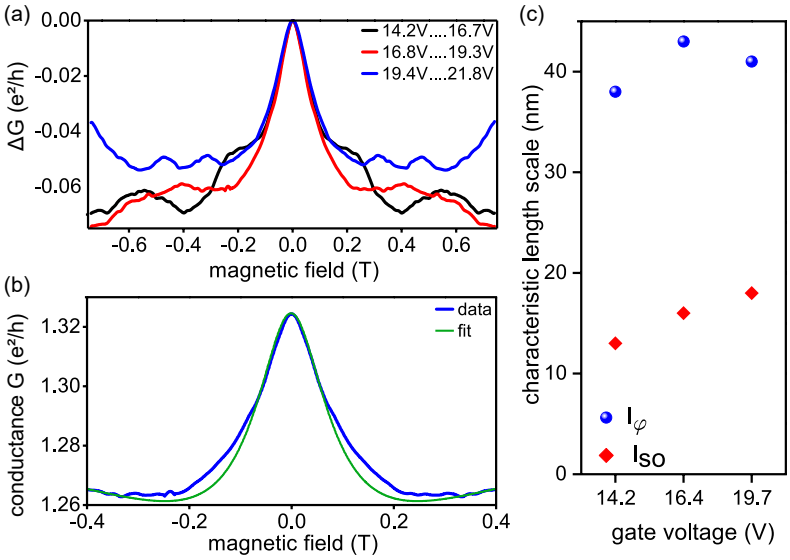

Figure 3.5 – *(a) Weak antilocalization features of sample B1 after the gate averaging procedure was performed. Every trace is a combination of 25 individual magnetic field sweeps at different gate voltages in the range of 14.2 up to 21.8 V. The sections were chosen such that the gate-induced increase of the background conductance was much smaller than all corrections related to interference effects. Additionally, in order to obtain a better comparability, the maximum conductance value of every WAL peak was subtracted from its corresponding trace, i.e.* $\Delta G = G(0) - G(B)$. *(b) Zoom-in of the second WAL trace for* 16.8 – 19.3 *V, and the resulting fit based on equation (3.2) with* $l_\varphi = 43$ *nm and* $l_{SO} = 16$ *nm. (c) Phase-coherence length* l_φ *and spin-orbit scattering length* l_{SO} *obtained from the fits according to equation (3.2) for the three different gate voltage sections. Data taken from [70].*

localization, as electron self-interference effects, both require a sufficiently large phase-coherence length relative to the system geometry. By sharing the same origin, the difference arises due to the influence of the electron spin, expressed by the spin-orbit scattering length l_{SO}. For a fit of the experimental data to a theoretical model we assume that our wires are in the quasi-one dimensional limit with $L \gg l_\varphi \gg w$, with L as the contact separation and w as the two-dimensional projection of the nanowire width [95]. For an average carrier concentration and mobility of $n = 3\times10^{18}\,\mathrm{cm}^{-3}$ and $\mu = 100\,\mathrm{cm}^2/\mathrm{Vs}$, which have been obtained by means of transistor and transconductance measurements for wires of this specific growth run at room temperature [71], we get an elastic scattering length of $l_e = v_F\tau_e = 10\,\mathrm{nm}$, which sets our system into the dirty metal regime ($l_e \ll w$) [96]. Thus we can use [95]

$$\Delta G(B) = -\frac{2e^2}{hL}\left[\frac{3}{2}\left(\frac{1}{l_\varphi^2}+\frac{4}{3l_{SO}^2}+\frac{1}{\mathscr{D}\tau_B}\right)^{-1/2} - \frac{1}{2}\left(\frac{1}{l_\varphi^2}+\frac{1}{\mathscr{D}\tau_B}\right)^{-1/2}\right] \tag{3.2}$$

for the conductance correction, with the diffusion constant $\mathscr{D}$ and the magnetic relaxation time τ_B.

For the latter one, we use

$$\tau_B = \frac{l_B^4}{K_1 w^3 v_F} + \frac{l_B^2 \tau_e}{K_2 w^2}\,, \tag{3.3}$$

with the magnetic length $l_B = \sqrt{\hbar/eB}$. Under the assumption of diffusive scattering and by including flux-cancellation effects, we take $K_1 = \frac{1}{4\pi}$ and $K_2 = \frac{1}{3}$ [95, 96]. Additionally, due to the special wire geometry, which restricts the transport to the conductive InSb shell and forbids all electron trajectories across the nanowire diameter, we make the assumption that $w = 45\,\text{nm}$, which is equal to the width of the top facet.

Figure 3.5(b) exemplarly shows a zoom-in of the second WAL trace, i.e. for 16.8 – 19.3 V, and the resulting fit based on equation (3.2), giving $l_\varphi = 43\,\text{nm}$ and $l_{SO} = 16\,\text{nm}$. The length of l_{SO} is rather small. We mainly attribute this to the small diffusion constant. In Fig. 3.5(c) the phase-coherence length l_φ and spin-orbit scattering length l_{SO} extracted from the fit are given for the three different gate voltage sections. While l_φ is basically constant, we find a small but clear increase of l_{SO} with increasing gate voltage. We mainly attribute the presence of spin-orbit coupling to the Rashba effect [105], even though the Dresselhaus contribution in InSb can be rather large [464]. Indeed, it was shown that, in spite of the fact that the nanowires are grown along the [111] direction, some Dresselhaus contribution might be relevant [115]. For weak antilocalization in InAs nanowires Rashba as well as Dresselhaus contributions were considered [113, 114]. The phase-coherence length extracted here is comparable to the value obtained from the universal conductance fluctuations.

VII

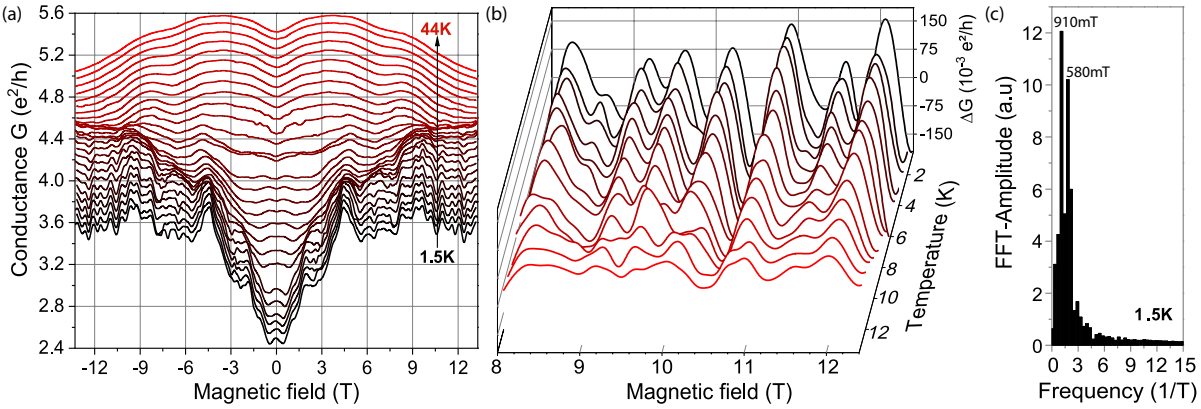

Figure 3.6 – *(a) Temperature-dependent magneto-conductance traces for sample A as a function of an in-plane magnetic field $B_{||}$.(b) Extracted conductance oscillations ΔG in units of e^2/h for sample A. The temperature range was restricted to 1.5 K up to 12 K. The slowly varying background conductance was subtracted.(c) Fast-Fourier-Transform (FFT) spectrum of the flux-periodic oscillations at T = 1.5 K. Image taken from [70].*

3.4. FLUX-PERIODIC OSCILLATIONS

In addition to measurements in a perpendicular magnetic field we also performed transport measurements in a magnetic field aligned parallel to the nanowire axis. Figure 3.6(a) shows the magneto-conductance of sample A at temperatures ranging from 1.5 to 44 K. Due to symmetry reasons, i.e. $G(B) = G(-B)$, we can conclude that the Onsager reciprocity is fulfilled [465]. It can be clearly seen, that all traces up to approx. 25 K are modulated by slowly varying background fluctuations, which can be attributed to universal conductance fluctuations. The latter ones originate from scattering loops with small areas, which are cooped within the InSb section of the wire and therefore limited by the thickness of the shell. However, for temperatures up to 12 K, the slowly fluctuating background is superimposed by flux-periodic oscillations. In order to analyze these regular oscillations, the low-frequency contribution of the universal conductance fluctuations was subtracted by means of a Savitzky-Golay fitting routine (see Supplementary Material). Furthermore, we only considered a range at larger magnetic fields in order to avoid the effect of weak antilocalization. The resulting magneto-conductance traces, depicted in Fig. 3.6(b), show a clear Aharonov–Bohm type oscillatory behaviour. Upon increasing the temperature, the oscillation amplitude is decreasing. The oscillations can be attributed to flux-periodic oscillations, as previously observed in nanowires with a conductive InAs shell around a GaAs core [79–81, 466]. These oscillations are attributed to closed-loop quantized states located within the InSb shell which shift their energetic position periodically with the encircled magnetic flux. The oscillation period is determined by the magnetic flux quantum and the cross section of the loop

$$\Delta B = \Phi_0/(\pi r^2)\,. \tag{3.4}$$

Here, we assumed a circular area encircled by the phase-coherent loop state. The Fourier transform of the magneto-conductance reveals peaks at $1.1\,\mathrm{T}^{-1}$ and $1.6\,\mathrm{T}^{-1}$, as shown in Fig. 3.6(c), which correspond to a radius of 38 and 45 nm, respectively. Since sample A has a core radius of 25 nm and a shell thickness of 50 nm, we can conclude, that the closed-loop states are located within the InSb shell, but slightly shifted towards the center. The presence of two peaks in the Fourier transform, i.e. two different cross sectional areas, can have two reasons. Either, there might be some potential fluctuations in the shell due to defects or the large g-factor of InSb might lead to an additional splitting of the energy spectrum [467].

In order to get a deeper insight into the origin of a certain oscillation pattern we performed magneto-conductance measurements in an axial magnetic field as a function of back-gate voltage. In Fig. 3.7(a) corresponding measurements of ΔG(B) are shown for sample B2.

Once again, regular conductance oscillations as a function of the magnetic field are observed. However, upon varying the gate voltage, the phase of the oscillations and the oscillation pattern

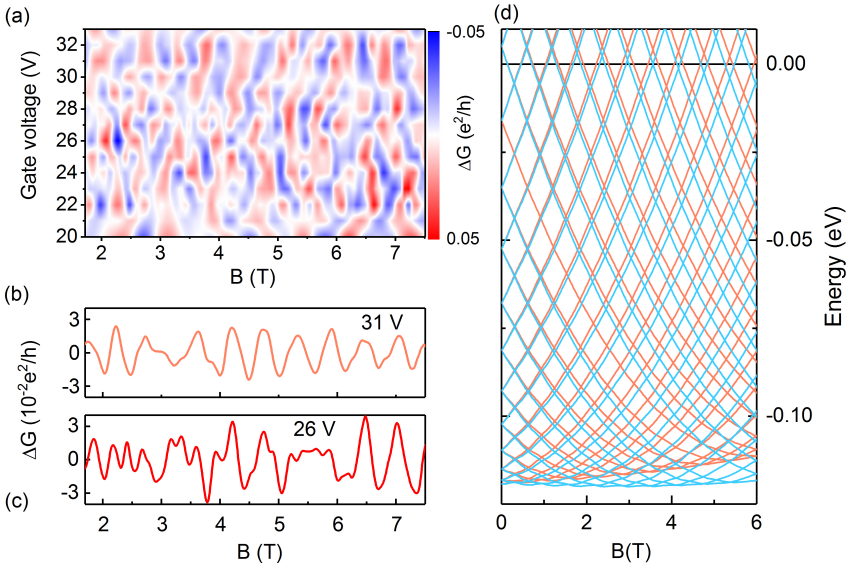

Figure 3.7 – *(a) Two-dimensional color-scale plot of the oscillating fraction of the magneto-conductance ΔG vs. the applied gate voltage and the parallel magnetic field for sample B2. The slowly varying background conductance was subtracted from the total conductance. (b), (c) Measured $\Delta G(B)$ traces as a function of B for $V_g = 31$ V and 26 V, respectively. (d) Calculated energy levels for spin up and down states for a nanowire corresponding to growth run B with $r_c = 35$ nm, $t_s = 22$ nm, and $(E_F - E_c) = 0.225$ eV. Image taken from [70].*

changes. In order to see this more clearly single traces of $\Delta G(B)$ are shown in Figures 3.7(b) and (c) for a gate voltage of 31 V and 26 V, correspondingly. Obviously, in the first case the magneto-conductance oscillates more slowly and regularly than in the second case.

The measured magneto-conductance oscillations are analyzed in more detail by calculating the energy spectrum as a function of magnetic field. In the same vein as the analysis presented in Sec. 3.1, the carrier density at the Fermi level $n_F(B)$ is assumed to be proportional to the conductance variations $\Delta G(B)$. Figure 3.7(d) shows the calculated energy spectrum as a function of an axial magnetic field for a nanowire structure corresponding to growth run B, i.e. assuming a shell thickness $t_s = 22$ nm. The magnetic field lifts the degeneracy of the orbital momentum quantum number l and the energy corresponding to each orbital momentum quantum number is almost parabolic with respect to the magnetic field. Thus, without spin effects, the energy spectrum is quasi-periodic in the magnetic field with a period $\Phi_0/(\pi r_{av}^2)$. Here, r_{av} is the average electronic radius which approximately corresponds to the distance from the maximum of the electron density distribution to the nanowire center (cf. Fig. 3.2(d)). The effect of the electron spin is modeled by introducing the Zeeman potential into the Schrödinger equation using a bulk InSb g-factor of $g_{InSb} = -51$ [449]. The Zeeman effect breaks spin degeneracy, increasing (decreasing) the energy of the states with spin down (up). The energy spectrum becomes modulated and more complex. We neglected the effect of spin-orbit coupling.

We assumed, that the wire is in the diffusive regime and only small bias voltages, i.e. $V_{sd} < 0.1$ mV, are applied. Thus, only electrons in close vicinity to E_F can participate in the transport. In that case the magneto-conductance is proportional to the number of carriers at the Fermi level

$$G(B) \sim n_F(B) = \int_{E_F-\Delta}^{\infty} D_{1D}(E,B) \frac{dE}{1+\exp[(E-E_F)/k_B T]}, \tag{3.5}$$

where $D_{1D}(E,B)$ is the one-dimensional density of states at a given magnetic field B, and k_B is the Boltzmann constant. The assumed energy spreading Δ is about several $k_B T$, with $T = 4$ K. As the magnetic field increases, the number of orbital momentum states in the vicinity of the Fermi level varies quasi-periodically, which ultimately leads to the oscillations in $G(B)$. In order to analyze the frequency components of the magneto-conductance oscillations we performed Fourier transforms

VII

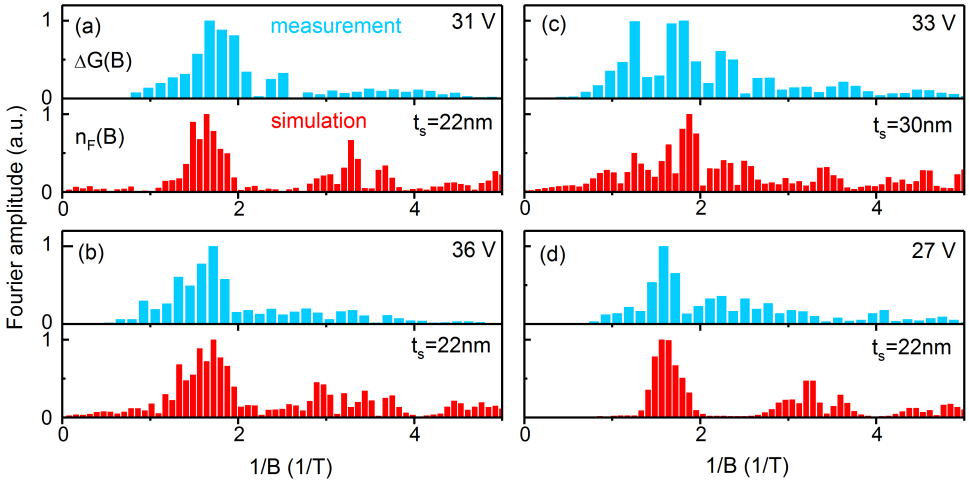

Figure 3.8 – *Normalized Fourier transform of the oscillating measured magneto-conductance $\Delta G(B)$ (blue) and the calculated electron density $n_F(B)$ (red), the gate voltage is set to 31 V (a), 36 V (b), 33 V (c), and 27 V (d), respectively. Image taken from [70].*

of the experimentally obtained traces of $\Delta G(B)$ and of the simulated densities $n_F(B)$. Some representative spectra are displayed in Fig. 3.8.

The frequency analysis of the experimental data reveals three dominant types of spectra. The first type (cf. Fig. 3.8(a) and (b), upper panels) is the most frequently observed one over the measured gate voltage range and has a peak at a frequency of about $1.7\,T^{-1}$. According to equation (3.4), we can conclude, that the oscillations are caused by the electron ensemble with average radius of $r_{av} \sim 47$ nm. Note that the nanowires of growth run B have a core with the radius of about 35 nm and a varying shell width along the nanowire axis. The calculation of the spatial electron distribution in the nanowire with varying shell thickness shows that r_{av} of 47 nm fits to the electron ensemble in the nanowire with the shell thickness of about 22 nm. The corresponding electron distribution is shown in Fig. 3.2(d). With this knowledge we calculated the oscillations of $n_F(B)$ with the magnetic field for a shell thickness of 22 nm and performed the corresponding Fourier transform. They are presented in figure 3.8(a) and (b), lower panels, and agree well with the experimental data. We would like to stress that, in accordance with the calculations for the higher gate voltage of 36 V, electrons of not only the first ($n = 1$), but also the second subband ($n = 2$) already contribute to the magneto-conductance. However, the frequency of the peak in the Fourier transforms of $\Delta G(B)$ and $n_F(B)$ (cf. Fig. 3.8(b)) remains at about $1.7\,T^{-1}$ and does not change with the gate voltage. The second type of the spectra taken form the experimental data shown in Fig. 3.8(c) has a much broader frequency range than the first type and basically no distinct sharp peak. It rather shows some distribution of frequencies which might be attributed to the electron ensemble with a wider space distribution than in the case of the stronger confinement we discussed above. This kind of distribution is typical for the electron ensemble in a nanowire with the wider shell, i.e. for a shell thickness of 30 nm, as shown in Fig. 3.2(d). The calculated Fourier transform of $n_F(B)$ for this shell thickness is displayed in Fig. 3.8(c) and has certain similarities with the experimental data. The third type of the spectra (cf. Fig. 3.8(d)) has a distinct peak at the frequency of about $1.7\,T^{-1}$ and also some frequency components forming a long tail. We attribute the pronounced peak to an electron ensemble confined within the narrow shell with the width of 22 nm. The corresponding calculated Fourier transform of $n_F(B)$ is shown in Fig. 3.8(d). The position of the peak fits to the experimental data. The additional frequency components might be related to electrons in shell sections having a bigger radius. The analysis of the Fourier spectra of the oscillating magneto-conductance suggest that, depending on the applied gate voltage, the oscillations are driven by electron fractions located in different regions of the nanowire. This may be expected due to the fact that the phase-coherence length ($l_\varphi \approx 50$ nm) is smaller than the distance between the drain and source contacts (350 nm), i.e. the coherent orbital momentum states relevant for a particular oscillation pattern are formed in a region of the nanowire shifting along

the nanowire axis with the gate voltage. Probably, this might also occur during the measurements of the magneto-conductance in GaAs/InAs core/shell nanowires performed during the previous study [81, 468]. However, as the shell thickness has been uniform along the nanowire axis, there was no clear evidence of this unlike now. We did not find a clear evidence of Zeeman splitting in our experiments, although this was observed in the simulations at some specific gate voltages by showing a split peak in the Fourier spectrum. We suspect, that the impact of the Zeeman effect is masked by other effects, like the varying shell thicknesses which results in a broadening of the Fourier spectrum.

3.5. DISCLAIMER

VII

All parts of this section, including figures and captions, have been already published by the author in [70] and [71]. All additional segments or those who have been altered are indicated with footnotes. For images, the phrase"...has been taken from..." was added to clarify their origin.The nanowire growth was performed by Torsten Rieger and Mihail Lepsa. The fabrication of the devices was evenly split between Johanna Janßen, Pujitha Perla and Patrick Zellekens. The transport measurements at room temperature were carried out by Patrick Zellekens and Franz-Josef Hackemüller. At low temperatures, the measurements were performed by Patrick Zellekens, with additional support from Johanna Janßen and Pujitha Perla. The manuscripts [70] and [71] have been written by Patrick Zellekens, with scientific supervision and advisory from Thomas Schäpers, Hans Lüth and Mihail Lepsa. All simulations and the corresponding interpretation in the manuscript were prepared by Natalia Demarina.

SUMMARY AND OUTLOOK

SUMMARY

In this work, III-V semiconductor nanowires were investigated with respect to their potential usability for superconductor-semiconductor hybrid devices and applications such as quantum bits, topological systems and spintronics. In the major part of this thesis, InAs nanowires were chosen to act as a tunable alternative to conventional and passive dielectric-based Josephson junctions. In order to do so, a number of challenges had to be overcome to combine the intrinsic coherence of superconductivity with the beneficial properties of these III-V nanowires.

Shapiro and emission measurements are the state-of-the-art technique to map out the current-phase relation. However, the common antenna-based approach suffers from a broad series of detrimental side effects such as the coupling to parasitic modes, which puts serious limitations to the exploitable power-frequency space. Thus, one of the major challenges in this project was the development of a highly integrated superconducting circuit based on a coplanar waveguide layout for more advanced AC measurements. For the electrostatic tuning, an improved version of the bottom gate structures introduced in the thesis of PhD F. Haas was designed. For the application of the DC and AC signal to the nanowire Josephson junction an **on-chip bias tee** was developed and optimized. Additionally, a normal conducting **shunt resistor** has been introduced to the measurement platform and subsequently optimized with respect to absolute resistance and resistance variation as well as thermal dissipation. This, allowed the investigation of the nanowire Josephson junction dynamics over the whole current and voltage range. Lastly, the gate design was further optimized to provide more options regarding the electrostatic manipulation of the device, e.g. the formation of tunnel barriers or the possibility to set the level of conductance in the area below the superconducting contacts. Doing so, it was possible to create a novel kind of gate structure based on an ultrathin stack of Ti/Pt with gate line widths of 10-15 nm and separations of only 15-20 nm. Keeping the general chip dimensions unchanged, it is possible to use a total of nine independent gate electrodes to tune the nanowire Josephson junction.

The presented thesis has been one of the first ones to exploit a novel type of semiconductor/superconductor hybrid nanowires for which the surrounding metal shell is formed under in-situ and ultra-high vacuum conditions. Following the timeline of the nanowire growth evolution, the first structures to be examined were InAs/Al core/half shell nanowires. Here, the junction had to be formed by wet chemical etching. In total, three types of wires with significantly different Tellurium doping levels have been studied. All of them had in common that they can host a gate tunable supercurrent. On the other hand, none of them showed signs of a clear hard gap and **OBTK transparencies** of only $T=0.5-0.65$. In the case of InAs/Al core/half shell nanowires with shadow mask defined junctions, it was possible to proof the existence of a **hard gap** without any sub-gap states, which is an important prerequisite for topological- or two-level-system-based applications. The gate tunability of the supercurrent also provided access to the quantum dot regime. Here, evidence for the existence of Yu-Shiba-Rusinov states was found. Additionally, at certain gate values, signatures of a quantum phase transition from a *singlett* into a *doublett* state, a so-called π-junction, could be measured. Following theoretical predictions, the latter might be a more simple way to create Majorana fermions and should definitely be a topic for further investigation.

However, it turned out that the half shell geometry also included some drawbacks. The most important one is the fact, that the built-in asymmetry of the system, i.e. the coverage of only half of the nanowire, gave rise to multiple *trajectories* with significantly different lengths $L_i > \xi$. Thus, to enforce a radial symmetry of the system, a full shell geometry was chosen. Here, the topological non-trivial geometry made it possible to get access to the so-called **Little-Parks regime**. Recent theoretical predictions have suggested that this could be used as a platform to create and manipulate parafermionic

excitations, e.g. Majorana zero modes. In contrast to prior measurements on core/shell systems, it turned out that the requirements for a successful investigation of the Little-Parks effect are much more strict. Extensive studies on the influence of the applied gate voltage, the strength of the parallel and perpendicular magnetic field as well as the maximum misalignment with respect to the ideal in-plane orientation were performed. In addition, it was possible to observe conductance features whose magnetic field dependent evolution was, in contrast to multiple Andreev reflections, not tied to the shrinking of the superconducting gap edge. Even though those states could just be observed within the central lobe, they were clearly not related to conventional Andreev bound states. The investigation of the junction dynamics by means of the Shapiro effect revealed a complex mode spectrum, which included the occurrence of missing as well as subharmonic steps for certain microwave power ranges. However, the reversed measurement showed no additional photon emissions at energies above the Josephson frequency. Based on those results, an alternative method to probe the state space was implemented. Here, the full shell nanowire was connected in parallel to another nanowire Josephson junction. This **SQUID** approach was inspired by the concept of Majorana-Transmons and is based on the fact that the entering and leaving of the topological phase space is associated with a significant and sudden change of the parity of the system. By using two independent gate electrodes, it was possible to tune the combined system into the regime in which both nanowires carry a clear supercurrent. The resulting interference pattern was then investigated at various magnetic field strengths, tilt angles and gate voltages. The latter revealed reproducible, symmetric and cosine-dependent phase jumps of π within the conventional interference pattern. The observed behavior was interpreted in terms of pronounced modifications of the underlying state spectrum and current-phase relation as they might occur for Landau-Zener transitions or emerging 4π modes.

The state-of-the-art technique to set, manipulate and probe individual Josephson-junction-type qubits is based on superconducting microwave circuits realized in an extended coplanar waveguide geometry. At the cost of a comparably large footprint, this layout has the advantage of an excellent control of the applied mode spectrum, the possibility to address multiple qubits independently as well as a stable potential landscape. Thus, a 2D circuit layout was developed. In order to minimize the dielectric losses within the substrate, a highly resistive silicon wafer was chosen as the carrier material. After first tests with aluminium, the superconductor for the microwave structures was changed to titanium nitride because of the simpler structuring process. The actual circuit was designed in a way that it can support four different qubit structures independently. Consequently, it also required four dedicated gate lines, which were realized in a bottom gate layout. However, in contrast to the former DC+AC measurements, the resonator-based measurements were much more sensitive to parasitic two-level states in the dielectric. Thus, a novel low-temperature dry etching process based was developed. Using this approach, it was possible to locally remove the dielectric in a controlled way without introducing a significant degree of roughness to the silicon surface underneath. The formation of the superconducting microwave structures was identified as another key challenge. Here, a combined lift-off and etching procedure was applied in order to suppress the formation of sidewalls and to keep the geometric component of the inductance constant and well-defined.

However, in case of the sputtered TiN, which was used for the major part of the structures in this thesis, even a thorough optimization of all process steps led to a maximum achievable internal quality factor of 40000. While this did not cause any issues for conventional Josephson junction characterization techniques, including Shapiro and emission, or the dispersive readout of qubits in the strong coupling regime, it set some severe limitations for microwave spectroscopy measurements. Thus, at some point the decision was made to completely redesign the manufacturing process. Instead of using a single substrate that has to host all kinds of different structures and materials, the design was changed to consist of two independent chips that were then mechanically coupled in a **flip-chip approach**. For the microwave structures, a sapphire wafer was chosen as the new carrier material. In addition, a MBE-grown layer of Niobium was used for the fabrication of the ground plane and the resonator due to the improved stickiness. However, the insulating nature of the sapphire substrate made it impossible to fabricate gate structures or the device itself directly on the circuit chip. Thus, a second, silicon-based sample has been designed, which was then fabricated in a similar fashion

as the earlier iterations of the Shapiro chips. The transition to the new sample layout improved the average internal quality factor by a factor of 50, with maximum values of $Q_i \approx 0.4 \cdot 10^6$ in the single photon limit and highly overcoupled case.

The described microwave circuits were used to investigate two different types of systems. In case of the Gatemon, it was possible to proof a gate-tunable and reproducible resonator-qubit coupling. The induced Rabi oscillations revealed an average lifetime of $T_1 \approx 150\,\text{ns}$. For the detuning-dependent device response, it turned out that the Gatemon indeed showed the expected behavior. However, the weak dependency of the **chevron-pattern** to changes in the drive frequency indicated that the current anharmonicity of the device was not large enough to suppress all transitions into higher levels. The latter was also identified as the most likely reason for the limited lifetime of the qubit system. For the Andreev devices, on the other hand, the microwave-driven measurement revealed a complex spectrum of Andreev bound states. In case of in-situ grown InAs/Al nanowire Josephson junctions with shadow mask formed junctions, it was possible to tune the system electrostatically into a condition where the channel contains only two, or even less, bound states. For such a configuration, a phase-sensitive dispersive readout revealed state lifetimes in the range of 40 ns. Here, the conclusion was drawn that those preliminary devices were mostly limited by the comparably poor internal quality factor of the used microwave circuit. Using the previously mentioned flip-Chip approach, it was possible to improve the stability and robustness of the devices significantly. Using two-tone spectroscopy, clear signatures of a spin-orbit interaction induced splitting of the normally spin-degenerate Andreev states were discovered. The displacement in momentum space, caused by the Rashba effect present in the InAs nanowire, induced a spin-polarization of the current and also allowed single quasiparticle transitions between adjacent Andreev bound states. This poisoning of the system was revealed by additional spectroscopy measurements that exhibited line shapes beyond the conventional phase dispersion of unpolarized bound states. With the help of an additional in-plane magnetic field, it was possible to also successfully shift the states in energy space by means of the Zeeman effect. This, together with a reduction of the number of channels to only one, is one of the most important requirements for the formation of a helical gap. In addition, the spectra revealed signatures of higher-order cavity-qubit photon interactions, which are typical for systems with large transparency and a non-sinusoidal current-phase relationship.

Even though InAs-based nanowire structures were used for the major part of this thesis, they are generally not the ideal candidate if it comes to spin-related phenomena. Thus, besides the optimization of the superconducting contacts and the Josephson junctions associated with them, one goal of the project was to exploit other, more complex III/V structures. In contrast to earlier works, which were focused on GaAs/InAs structures, the shell material was changed to InSb due to the much larger spin-orbit coupling. For positive gate voltages, i.e. electron transport, the gate and magnetic field dependent investigation of universal conductance fluctuations made characteristic length scales of the system such as the mean free path or the phase coherence length accessible. In contrast to prior studies of GaAs/InAs structures, it was also possible to observe signatures of weak antilocalization. Using gate averaging over a large voltage range, the extracted conductance peak was then used to extract the spin-orbit scattering length l_{SO}. The strong spin-orbit interaction also affected other quantum phenomena. Similar to prior measurements on GaAs/InAs, the radial symmetry and topologically non-trivial geometry gave rise to angular momentum states and flux periodic oscillations. It was found that the latter were modulated in terms of the superposition of two different frequency components which could be related to the presence of different energy levels for the two spin orientations. Using a modified Schrödinger-Poisson solver, the best fit between experiment and simulations was found for a g-factor of 51. This is in very good agreement with previous experiments, proving that GaAs/InSb core/shell nanowires could potentially provide a better access to the topological regime if used as building blocks for nanowire Josephson junctions.

OUTLOOK

The much higher quality of the sapphire-based microwave circuits has shifted seemingly solved problems back into focus. One of them is the stability of the superconductor with respect to the applied magnetic field. The improved internal quality factor gives now access to a regime in which even small instabilities of the vortex lattice, which were previously overwhelmed by material-related losses, manifest themselves as fluctuations of the resonator properties. Thus, the already established flux management approach has to be adjusted for Nb as the new superconductor. In addition, future iterations of the resonator circuit might require other lattice geometries beyond the conventional Abrikosov layout such as Ratchet structures.

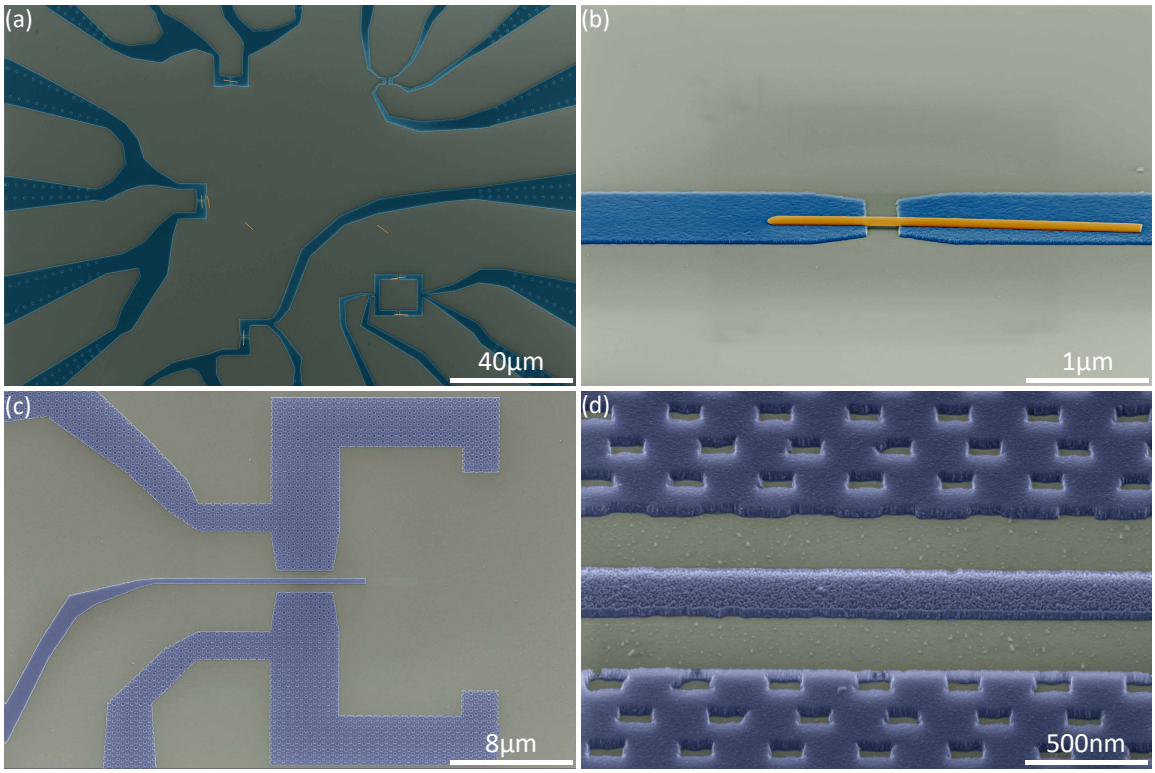

Figure 3.9 – *False-colored SEM micrograph of various Nb-based suspended junction structures. (a) Overview image of SQUIDs, four-terminal and butterfly structures. (b) Zoomed-in image of a single InAs nanowire bridging a 450 nm wide gap between two adjacent Nb electrodes. (c) Zoomed-in image of a second generation structure with additional electrodes for an on-chip bias tee, a dedicated gate electrode as well as flux traps. (d) Zoomed-in sideview of the gate electrode after the second etching step. The different degrees of roughness caused by the SF_6-based dry etch are clearly visible.*

However, a more urgent issue is related to the lifetime of the microscopic excitations within the nanowire channel. After the optimizations of the circuit properties and a thorough investigation of the DC characteristics of the nanowire Josephson junctions, which revealed high transparencies and a well resolved state spectrum, the used gate architecture was identified as the most likely cause for the limited performance of the **two-level system**. Other groups, such as the Quantronics team in Saclay, usually use a gate electrode that is only weakly coupled to the junction by means of a vacuum gap. However, the downside of this approach, which was also used for the first iterations of our Gatemon structures, is the extremely small and barely controllable lever arm that is caused by the almost random separation between the pre-patterned gate contact and the nanowire Josephson junction. An attempt to improve this by using a subsequently fabricated top gate electrode has also proven to be disadvantageous due to the comparably large number of traps in the required dielectric, which has to be deposited under unfavorable growth conditions. Thus, a prototype for a novel device layout based on pre-patterned superconductor structures was developed. Figure 3.9 (a) provides an overview of different structures that have been formed out of 40 nm thick Nb by means of dry etching. Doing so, it is not only possible to realize devices in four-terminal geometry and with channel lenghts

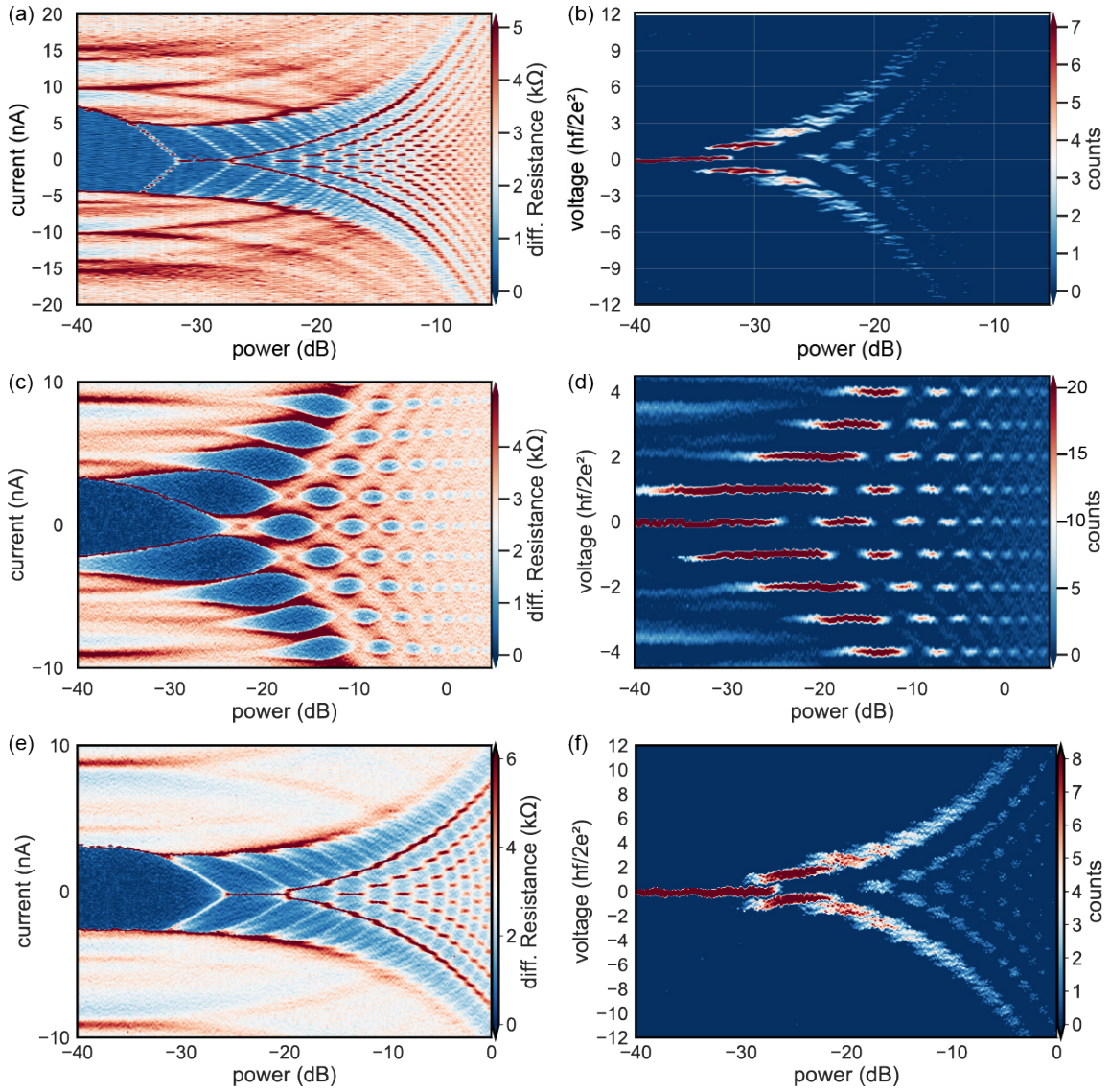

Figure 3.10 – *Shapiro spectrum of an InAs/Nb halfshell nanowire Josephson junction exposed to an in-plane magnetic field of 1.4 T. The blue areas, which correspond to the supercurrent regions between two* ***integer*** *Shapiro steps are interrupted in the center by additional dissipative features. Voltage-calibrated histogram of the same measurement. The features now manifest themselves as an* ***energetic splitting*** *of the integer steps. It should be pointed out that this effect, in contrast to missing or subharmonic steps, can not be attributed to the presence of higher harmonics caused by a strongly* ***non-sinusoidal*** *current-phase relation. The most likely explanation is based on Landau-Zener-Stückelberg transitions across an avoided crossing-induced (topological) minigap between the upper and lower branch of an Andreev bound state.*

of less than 20 nm, but also conventional SQUIDs as well as "butterfly" structures, in which a single nanowire is connected to four independent superconducting contacts in total. The advantage of this method is a full suspension of the nanowire segment with respect to the substrate underneath, as depicted in Fig. 3.9 (b). Regarding trap states on the silicon surface, the formed vacuum gap limits the surface-induced losses significantly. In order to make this approach applicable for qubit- and other microwave-applications, large scale arrays of flux traps can be formed in the very same etching step (cf. Fig. 3.9 (c)). Lastly, it is also possible to partly combine the advantage of a local gate electrode with the controlled decoupling of the suspended junction layout. Using a second, precisely tailored and short etching step, it is possible to thin down the central gate electrode by 5-10 nm. It should be noted that the introduced roughness, shown in Fig. 3.9 (d) is, is not detrimental to the device properties as it is not in direct contact with the nanowire channel anymore. First DC studies on similar devices have already proven that the described design allows the formation of high quality nanowire Josephson junction. The next step would be to adapt this approach to the special requirements of

microwave circuits and use it for the formation of actual qubit structures.

Another phenomenon, which, to our knowledge, has not been experimentally observed yet is a **splitting** of integer Shapiro steps, which can be seen in Fig. 3.10 for a InAs/Nb core/half shell nanowire with a junction defined using a shadow mask. The histogram shown in Fig. 3.10 (a) has been normalized to the *characteristic voltage* associated with the given measurement frequency and clearly shows a *double feature* for all integer values instead of a single, well-defined maximum. This is different from [subharmonic or **fractional** Shapiro steps in the sense that both effects just add additional constant voltage plateaus but do not interfere with the conventional integer features. In the Shapiro spectrum itself, which is shown in Fig. 3.10 (b), the observed effect corresponds to the additional, less pronounced *white lines* in the center of every more conductive region (blue). First theoretical predictions by F. Dominguez et al. in Braunschweig attribute those split steps to the **coexistence** of a 2π and a 4π mode. In terms of the **resistively shunted junction** model, it can be understood as a high probability for the *particle* in the *washboard potential* to receive an additional phase jump. In the **state space**, however, it is associated with *Landau-Zener-Stückelberg transitions* [229, 230] across a topological or trivial gap between the lower and upper branch of an Andreev bound state that would otherwise reach zero energy. After a careful investigation of the parameter space, including different combinations of *frequency*, *microwave power* and *magnetic field*. most of the correlations seem to fit to the expectations raised by the work of F. Dominguez et al. [267]. However, it should be pointed out, that in the original theoretical work the system consisted of a single bound state, which resulted in a linear increase of the LZS-transition rate for higher frequencies and a constant magnetic field. This effect is not observed in the experiment (cf. Fig. 3.10 (c) and (d)), which only shows the split steps for specific frequency-field combinations. Here, a smaller field requires a larger microwave drive and vice versa, as can be seen in Fig. 3.10 (e) and (f). First qualitative simulations performed by F. Dominguez and R. Deacon indicate that this behavior would fit to a scenario in which, above a certain energy, the Landau-Zener transitions are suppressed by transitions into higher levels and thus set an upper limit for the valid frequency at a given magnetic field. As this effect would, in principle, allow the creation and characterization of parafermionic excitations in systems with a significantly reduced level of complexity and *ideality*, it should definitely be considered as a topic for a future and much more detailed theoretical and experimental investigation.

ACKNOWLEDGEMENTS

I would like to express my sincere gratefulness to all the people who made this work possible.

First of all, I am especially thankful to Prof. Dr. Thomas Schäpers, who offered me the position and gave me the possibility to prepare this thesis at the PGI-9. I had the pleasure to benefit from his great experience in numerous different areas of the fabrication and characterization of superconducting and semiconducting devices. During countless discussions on all kind of topics I was able to learn a lot not only about physics but rather about science as a whole. Thanks to him, not only the problems related to my PhD study but also any problem I had during these three years were solved immediately. Further, my special thanks go to Prof. Markus Morgenstern who kindly agreed to be the second examiner of this thesis. No less thankful I am to Prof. Dr. Koji Ishibashi and Dr. Russell Deacon who provided me the unique chance to perform experiments in their lab in Tokyo, broaden and deepen my knowledge about microwave equipment, HF measurement techniques and superconductivity in general and get unique insights into the Japanese culture. Due to all persons mentioned above, my supervision has been the best a PhD student could wish for on both a scientific as well as on a personal level. Furthermore, I would like to thank Prof. Dr. Detlev Grützmacher for giving me the opportunity to work in his institute. Especially the joint collaboration with Japan would not have been possible without his continuous support. I thank also Prof. Dr. Hans Lüth for his ideas and fruitful discussions about nanowire structures and semiconductors in general. Lastly, I would like to thank Prof. Dr. Arno Förster for his continuous support during all stages of my studies, including the very beginning when I was still looking for the "right path to take" and when he spend a whole afternoon to provide me a first glimpse into the daily work of a true scientist. Without his engagement, nothing of this thesis would have been possible.

Many thanks go to all former Bachelor and Master students that worked within this project, namely Arthur Leis, Johanna Janßen, Naveen Shetty, Tobias Ziegler, P. Liebisch, Anna Linkenheil, Fredrik Marx and Qingzhen Wang. All of them made an essential contribution to the success of this project.

In addition, I thank all current and former group and institute members, including Sebastian Heedt, Fabian Haas, Karl Weis, Thorsten Wierzkowski, Daniel Rosenbach, Franz-Josef Hackemüller, Yulieth Arango and Alfred Fox. It has always been a pleasure to spend my time in a well-functioning and efficient workgroup. Furthermore, I could always find someone who cheered me up and helped out when something did not work out as planned. In this context I am particularly indebted to Herbert Kertz, as he always took care that everything worked out as planned in the lab. I would also like to thank my former officemate Christian Weyrich for making our working environment full of smiles and laughter and for the critical reading of the manuscript. Lastly, I am grateful to Dr. Natalia Demarina for many valuable discussions about the surface properties of InAs and InSb-based nanowires and for her insightful Schrödinger–Poisson solver calculations.

Aside from the helpful people in Jülich, I thank Steffen Schlör and Dr. Martin Weides for their huge contribution to the Gatemon project, including the design of the microwave circuit and the conduct of the experiments. Lastly, I would like to thank all the amazing people that I have met on conferences, meetings and all other kinds of scientific events, of whom quite a few became friends rather than just colleagues. In particular, I would like to mention Neill Lambert, Jorge Nunez, Ken Funo and Tarun Raheja for making my whole time in Japan a truely unique and special experience. I hope that we will manage to finish our Warhammer PnP session one day! Additionally, I would like to thank Andrei Manolescu, Sigurdur Erlingson, Anna Sitek and Kristján Klausen for all their help regarding the theoretical description of the transport phenomena in our nanowires and the opportunity to spend two amazing weeks at the quite cold and snowy coast of Iceland.

In addition, I would like to thank the growers of the nanowires, Torsten Rieger, Pujitha Perla and

Dr. Mihail Ion Lepsa in Jülich. They provided the wires that were subject to all the experiments in this thesis and have been always highly motivated to further optimize the nanowires for to enable new and more advanced transport studies.

I would like to express my gratitude to Dr. Florian Lentz and Dr. Stefan Trellenkamp for the excellent electron beam lithography results as well as continuous support during the implementation of complex design layouts. In addition, many thanks go to Rainer Benczek, Matthias Geitner, Dr. B. Bennemann and Stephanie Bunte who helped me a lot with the deposition and optimization of the different superconducting materials and the final processing steps of all samples. Lastly, I am very thankful to the whole clean room team which always ensured a perfect and trouble-free operation of the clean room facilities.

Finally, special acknowledgments are devoted to my family and my friends for all the non-scientific support. Without this, all the years of PhD studies and my stays in Japan would not have been possible. Thank you for being very supportive for what I do. Even though we don't see each other that often, you have always been a part of my life.

List of Publications

2022 P. Zellekens, R. Deacon, P. Perla, D. Grützmacher, M. I. Lepsa, T. Schäpers, K. Ishibashi,
Microwave Spectroscopy of Andreev states in InAs Nanowire-Based Hybrid Junctions using a flip-chip Layout
Comm. Phys. **5**, 267

2022 P. Perla, A. Faustmann, S. Koelling, P. Zellekens, R. Deacon, H. A. Fonseka, J. Kölzer, Y. Sato, A. M. Sanchez, O. Moutanabbir, K. Ishibashi, D. Grützmacher, M. I. Lepsa, T. Schäpers
Te-doped selective-area grown InAs nanowires for superconducting hybrid devices
Phys. Rev. Materials **6**, 024602

2021 P. Perla, H. A. Fonseka, P. Zellekens, R. Deacon, Y. Han, J. Kölzer, T. Mörstedt, B. Bennemann, A. Espiari, K. Ishibashi, D. Grützmacher, A. M. Sanchez, M. I. Lepsa, T. Schäpers
Fully in-situ Nb/InAs-nanowire Josephson junctions by selective-area growth and shadow evaporation
Nanoscale Advances **3**, 1413-1421

2020 P. Zellekens, R. Deacon, P. Perla, H. A. Fonseka, T. Mörstedt, S. A. Hindmarsh, B. Bennemann, F. Lentz, M. I. Lepsa, A. M. Sanchez, D. Grützmacher, K. Ishibashi, T. Schäpers
Hard-Gap Spectroscopy in a Self-Defined Mesoscopic InAs/Al Nanowire Josephson Junction
Phys. Rev. Applied **14**, 054019

2020 P. Zellekens, N. Demarina, Johanna Janßen, T. Rieger, M. Ion Lepsa, P. Perla, G. Panaitov, H. Lüth, D. Grützmacher, T. Schäpers
Phase coherent transport and spin-orbit interaction in GaAs/InSb core/shell nanowires,
Semicond. Sci. Technol **35**, 085003

2018 F. Haas, S. Dickheuer, P. Zellekens, T. Rieger, M. Lepsa, H. Lüth, D. Grützmacher, T. Schäpers
Quantum interferometer based on GaAs/InAs core/shell nanowires connected to superconducting contacts
Semicond. Sci. Technol., **33**, 064001

2017 P. Zellekens, T.Rieger, N. Demarina, A. A. Hassan, F. Hackemüller, H. Lüth, U. Pietsch, D. Grützmacher, T. Schäpers, M. Ion Lepsa
Strain relaxation and ambipolar electrical transport in GaAs/InSb core–shell nanowires
Nanoscale, **9**, 18392-18401

2017 F. Haas, P. Zellekens, T. Wenz, N. Demarina, T. Rieger, M. Lepsa, D. Grützmacher, H. Lüth, T. Schäpers
Anisotropic phase coherence in GaAs/InAs core/shell nanowires
Nanotechnology, **28**, 445202

2017 N. Güsken, T. Rieger, P. Zellekens, B. Bennemann, E. Neumann, M. Ion Lepsa, T. Schäpers, D. Grützmacher
MBE growth of Al/InAs and Nb/InAs superconducting hybrid nanowire structures
Nanoscale, **9**, 16735-16741

2017 G. Signorello, M. Schraff, P. Zellekens, U. Drechsler, M. Buerge, H. Steinauer, R. Heller, M. Tschudy, H. Riel
An open-source platform to study uniaxial stress effects on nanoscale devices
Review of Scientific Instruments **88**, 053906

2016 P. Zellekens, F. Haas, M. Lepsa, T. Rieger, D. Grützmacher, H. Lüth, T. Schäpers
Electron Interference in Hall Effect Measurements on GaAs/InAs Core/Shell Nanowires
Nano Lett., **17**, 1, 128–135

2016 F. Haas, Tobias Wenz, P. Zellekens, N. Demarina, T. Rieger, M. Lepsa, D. Grützmacher, H. Lüth, T. Schäpers
Angle-dependent magnetotransport in GaAs/InAs core/shell nanowires
Scientific Reports, **6**, 24573

2012 C. Blömers, T. Rieger, P. Zellekens, F. Haas, M. Ion Lepsa, Hilde Hardtdegen, Ö. Gül, N. Demarina, D. Grützmacher, H. Lüth, T. Schäpers
Realization of nanoscaled tubular conductors by means of GaAs/InAs core/shell nanowires
Nanotechnology **24**, 035203

DECLARATION/EIDESSTATTLICHE ERKLÄRUNG

I, Patrick Zellekens, hereby declare that this dissertation and the contents presented therein are my own and have been generated independently as a result of my own original research.

I hereby declare under oath

1. This work was done completely or mostly in the phase as a doctoral student of this faculty and university;

2. If any part of this dissertation was previously used for an academic degree or other qualification at this or another institution, this was clearly indicated;

3. Whenever other own or third – party publications were used, this was clearly stated;

4. . When quoting from other own or third – party publications, the source is always indicated. This dissertation is entirely my own work, with the exception of such quotations;

5. All major sources of support have been identified;

6. Whenever a part of this dissertation is based on collaboration with others, I have clearly identified what was done by others and what was done by myself;

7. Parts of this work were previously published in the publications listed in the LIST OF PUBLICATIONS

Tokyo, 01.06.2023

Patrick Zellekens

Eidesstattliche Erklärung

Ich, Patrick Zellekens erkläre hiermit, dass diese Dissertation und die darin dargelegten Inhalte meine eigenen sind und selbstständig, als Ergebnis meiner eigenen originären Forschung, generiert wurden.

Hiermit erkläre ich an Eides statt

1. Diese Arbeit wurde vollständig oder größtenteils in der Phase als Doktorand dieser Fakultät und Universität angefertigt;

2. Sofern irgendein Bestandteil dieser Dissertation zuvor für einen akademischen Abschluss oder eine andere Qualifikation an dieser oder einer anderen Institution verwendet wurde, wurde dies klar angezeigt;

3. Wenn immer andere eigene- oder Veröffentlichungen Dritter herangezogen wurden, wurden diese klar benannt;

4. Wenn aus anderen eigenen- oder Veröffentlichungen Dritter zitiert wurde, wurde stets die Quelle hierfür angegeben.

   Diese Dissertation ist vollständig meine eigene Arbeit, mit der Ausnahme solcher Zitate;

5. Alle wesentlichen Quellen von Unterstützung wurden benannt;

6. Wenn immer ein Teil dieser Dissertation auf der Zusammenarbeit mit anderen basiert, wurde von mir klar gekennzeichnet, was von anderen und was von mir selbst erarbeitet wurde;

7. Ein Teil oder Teile dieser Arbeit wurden zuvor veröffentlicht und zwar in den Publikationen, die in der LIST OF PUBLICATIONS verzeichnet sind.

Tokyo, 01.06.2023

Patrick Zellekens

VIII

Appendix

A

FABRICATION OF SUPERCONDUCTING MICROWAVE QUANTUM CIRCUITS: RECIPES

Fabrication chain for 1st gen. Shapiro chips				
	Process	**Parameters**		
0	**Substrate**	Si <100>, ρ >80 kΩcm (specified), ρ >180 kΩcm (measured), double-side polished, prime-grade, floating zone, t=525 μm		
1	**Spin coating**	HMDS Program 3, 130°C	UV 6.06 4000 rpm, 60s	
		baking procedure: 80°C for 30s, 130°C for 60s, 80°C for 30s		
2	**E-beam Lithography**	Patterning of E-beam and dicing marks (negative)		
3	**Development**	Post-exposure bake 140 °C for 5 min	Development in CD-26 60s, continuous movement	Rinse for 10 min DI water
4	**Dry etching**	Recipe CHF_3+ O_2	CHF_3: 55 O_2: 5 Etching time: 13 min	
5	**Cleaning**	Aceton + IPA + Gigabatch oxygen plasma + Aceton + IPA		
6	**ALD**	Thin dielectric layer of Al_2O_3/HfO_2 for electrical isolation		
7	**Spin coating**	HMDS Program 3, 130°C	PMMA 950K 4000 rpm, 60s	
		baking procedure: 100°C for 60s, 180°C for 10m		
8	**E-beam Lithography**	Patterning of thin bottom gate electrodes and leads		
9	**Development**	Development in pure IPA 110s, continuous movement	Post-development bake 100°C for 10min	
10	**Metal deposition**	Gigabatch Oxygen plasma, 200W 200sccm for 15s PLS 500 or Univex: 10nm Ti, 10nm Pt		
11	**Lift-off**	Hot DMSO:Cyclopentanon 2:1, 90°C for at least 6 hours Rinse in flowing DI water for 20m Aceton+IPA		
12	**Spin coating**	HMDS Program 3, 130°C	UV 6.06:Ethyllactat 2:1 4000 rpm, 60s	
		baking procedure: 80°C for 30s, 130°C for 60s, 80°C for 30s		
13	**E-beam Lithography**	Patterning of gate bonding pads and thick gate leads		
10	**Metal deposition**	Gigabatch Oxygen plasma, 200W 200sccm for 15s PLS 500 or Univex: 30nm Ti, 120nm Pt		
15	**Lift-off**	Hot DMSO:Cyclopentanon 2:1, 90°C for at least 6 hours Rinse in flowing DI water for 20m Aceton+IPA		
16	**ALD**	Deposition of Gate dielectric 3 nm/12 nm of Al_2O_3/HfO_2		
17	**Spin coating**	HMDS Program 3, 130°C	UV 6.06:Ethyllactat 2:1 4000 rpm, 60s	
		baking procedure: 80°C for 30s, 130°C for 60s, 80°C for 30s		
18	**E-beam Lithography**	Patterning of Shapiro circuit and bias tee		
19	**Metal deposition**	Gigabatch Oxygen plasma, 200W 200sccm for 15s LLS Evo for 80nm sputtered TiN		
20	**Lift-off**	Hot DMSO:Cyclopentanon 2:1, 90°C for at least 6 hours Rinse in flowing DI water for 20m Aceton+IPA		

Table 1 – *Overview of the required processing steps for the fabrication of Shapiro chips with single bottom gate electrodes.*

Fabrication chain for silicon-based 1st gen. Andreev circuits				
	Process	**Parameters**		
0	**Substrate**	Si <100>, ρ >80 kΩcm (specified), ρ >180 kΩcm (measured), double-side polished, prime-grade, floating zone, t=525 μm		
1	**Spin coating**	HMDS Program 3, 130°C	UV 6.06 4000 rpm, 60s	
		baking procedure: 80°C for 30s, 130°C for 60s, 80°C for 30s		
2	**E-beam Lithography**	Patterning of E-beam and dicing marks (negative)		
3	**Development**	Post-exposure bake 140 °C for 5 min	Development in CD-26 80s, continuous movement	Rinse for 10 min DI water
4	**Dry etching**	Recipe CHF_3+ O_2 Etching time: 13 min	CHF_3: 55 O_2: 5	
5	**Cleaning**	Aceton + IPA + Gigabatch oxygen plasma + Aceton + IPA		
6	**ALD**	Thin dielectric layer of Al_2O_3/HfO_2 for electrical isolation		
7	**Spin coating**	HMDS Program 3, 130°C	PMMA 950K 4000 rpm, 60s	
		baking procedure: 100°C for 60s, 180°C for 10m		
8	**E-beam Lithography**	Patterning of thin bottom gate electrodes and leads		
9	**Development**	Development in pure IPA 110s, continuous movement	Post-development bake 100°C for 10min	
10	**Metal deposition**	Gigabatch Oxygen plasma, 200W 200sccm for 15s PLS 500 or Univex: 10nm Ti, 10nm Pt		
11	**Lift-off**	Hot DMSO:Cyclopentanon 2:1, 90°C for at least 6 hours Rinse in flowing DI water for 20m Aceton+IPA		
12	**Spin coating**	HMDS Program 3, 130°C	UV 6.06:Ethyllactat 2:1 4000 rpm, 60s	
		baking procedure: 80°C for 30s, 130°C for 60s, 80°C for 30s		
13	**E-beam Lithography**	Patterning of gate bonding pads and thick gate leads		
10	**Metal deposition**	Gigabatch Oxygen plasma, 200W 200sccm for 15s PLS 500 or Univex: 30nm Ti, 120nm Pt		
15	**Lift-off**	Hot DMSO:Cyclopentanon 2:1, 90°C for at least 6 hours Rinse in flowing DI water for 20m Aceton+IPA		
16	**ALD**	Deposition of Gate dielectric 3 nm/12 nm of Al_2O_3/HfO_2		
17	**Spin coating**	HMDS Program 3, 130°C	UV 6.06:Ethyllactat 2:1 4000 rpm, 60s	
		baking procedure: 80°C for 30s, 130°C for 60s, 80°C for 30s		
18	**E-beam Lithography**	Patterning of gate protection masks for global dielectric removal		
19	**Development**	Post-exposure bake 140 °C for 5 min	Development in CD-26 80s, continuous movement	Rinse for 10 min DI water
20	**Cleaning**	Aceton + IPA + Gigabatch oxygen plasma + Aceton + IPA		
21	**Dry etching**	Recipe PZ_CHF_3_20C Etching time: 105 s	CHF_3: 35 ICP: 0 W RF: 200 W	
22	**Spin coating**	HMDS Program 3, 130°C	UV 6.06 4000 rpm, 60s	
		baking procedure: 80°C for 30s, 130°C for 60s, 80°C for 30s		
23	**E-beam Lithography**	Patterning of gate protection masks for global superconductor deposition		
24	**Development**	Post-exposure bake 140 °C for 5 min	Development in CD-26 80s, continuous movement	Rinse for 10 min DI water
25	**Metal deposition**	Gigabatch Oxygen plasma, 200W 200sccm for 15s LLS Evo for 80nm sputtered TiN		
26	**Lift-off**	Hot DMSO:Cyclopentanon 2:1, 90°C for at least 6 hours Rinse in flowing DI water for 20m Aceton+IPA		
27	**Spin coating**	HMDS Program 3, 130°C	UV 6.06:Ethyllactat 2:1 4000 rpm, 60s	
		baking procedure: 80°C for 30s, 130°C for 60s, 80°C for 30s		
28	**E-beam Lithography**	Patterning of etch mask for microwave structures (resonator, transmission line etc.)		
29	**Development**	Post-exposure bake 140 °C for 5 min	Development in CD-26 80s, continuous movement	Rinse for 10 min DI water
30	**Dry etching**	Recipe PZ_TiN_etch Etching time: 18 s	Cl_2: 12 SF_6: 2 Ar: 60 ICP: 700 W RF: 50 W	
31	**Cleaning**	Aceton + IPA + Gigabatch oxygen plasma + Aceton + IPA		

Table 2 – *Overview of the required processing steps for the fabrication of silicon-based multi-qubit Andreev circuits.*

BIBLIOGRAPHY

[1] S. Vaitiekėnas, et al. "Flux-induced topological superconductivity in full-shell nanowires." *Science*, 367(6485): eaav3392, **2020**. doi:10.1126/science.aav3392. 1, 3, 183, 184

[2] Benjamin D. Woods, et al. "Electronic structure of full-shell InAs/Al hybrid semiconductor-superconductor nanowires: Spin-orbit coupling and topological phase space." *Physical Review B*, 99(16), **2019**. doi:10.1103/PhysRevB.99.161118. 1, 3, 18, 195

[3] W. A. Little and R. D. Parks. "Observation of Quantum Periodicity in the Transition Temperature of a Superconducting Cylinder." *Physical Review Letters*, 9(1):9–12, **1962**. doi:10.1103/PhysRevLett.9.9. 1, 3

[4] Frank Arute, et al. "Quantum supremacy using a programmable superconducting processor." *Nature*, 574(7779): 505–510, **2019**. doi:10.1038/s41586-019-1666-5. 5

[5] Giuseppe E Santoro and Erio Tosatti. "Optimization using quantum mechanics: quantum annealing through adiabatic evolution." *Journal of Physics A: Mathematical and General*, 39(36):R393–R431, **2006**. doi:10.1088/0305-4470/39/36/R01. 5

[6] Dorit Aharonov, et al. "Adiabatic Quantum Computation is Equivalent to Standard Quantum Computation." *SIAM Journal on Computing*, 37(1):166–194, **2007**. doi:10.1137/S0097539705447323.

[7] Arnab Das and Bikas K. Chakrabarti. "Colloquium: Quantum annealing and analog quantum computation." *Reviews of Modern Physics*, 80(3):1061–1081, **2008**. doi:10.1103/RevModPhys.80.1061.

[8] Nicola Jones. "Computing: The quantum company." *Nature*, 498(7454):286–288, **2013**. doi:10.1038/498286a. 5

[9] R. Barends, et al. "Superconducting quantum circuits at the surface code threshold for fault tolerance." *Nature*, 508 (7497):500–503, **2014**. doi:10.1038/nature13171. 5, 116

[10] Christopher A. Fuchs and Carlton M. Caves. "Ensemble-Dependent Bounds for Accessible Information in Quantum Mechanics." *Physical Review Letters*, 73(23):3047–3050, **1994**. doi:10.1103/PhysRevLett.73.3047.

[11] Richard Jozsa. "Fidelity for Mixed Quantum States." *Journal of Modern Optics*, 41(12):2315–2323, **1994**. doi:10.1080/09500349414552171.

[12] Michael A. Nielsen and Isaac L. Chuang. "Quantum Computation and Quantum Information." Cambridge University Press, **2009**. doi:10.1017/CBO9780511976667. 5

[13] M. Konig, et al. "Quantum Spin Hall Insulator State in HgTe Quantum Wells." *Science*, 318(5851):766–770, **2007**. doi:10.1126/science.1148047. 5

[14] V. Mourik, et al. "Signatures of Majorana Fermions in Hybrid Superconductor-Semiconductor Nanowire Devices." *Science*, 336(6084):1003–1007, **2012**. doi:10.1126/science.1222360. 5

[15] Aaron Chew, et al. "Fermionized parafermions and symmetry-enriched Majorana modes." *Physical Review B*, 98(8), **2018**. doi:10.1103/PhysRevB.98.085143. 5

[16] Jason Alicea and Paul Fendley. "Topological Phases with Parafermions: Theory and Blueprints." *Annual Review of Condensed Matter Physics*, 7(1):119–139, **2016**. doi:10.1146/annurev-conmatphys-031115-011336. 5

[17] Ettore Majorana. "Atomi orientati in campo magnetico variabile." *Il Nuovo Cimento*, 9(2):43–50, **1932**. doi:10.1007/BF02960953. 5, 65

[18] Louis H. Kauffman and Samuel J. Lomonaco. "Braiding with Majorana fermions." *Quantum Information and Computation IX*, 98730E(98730E), **2016**. doi:10.1117/12.2228510. 5

[19] X. Ma, et al. "Braiding Majorana fermions and creating quantum logic gates with vortices on a periodic pinning structure." *Physical Review B*, 101(2), **2020**. doi:10.1103/PhysRevB.101.024514.

[20] Adrian Hutter and Daniel Loss. "Quantum computing with parafermions." *Physical Review B*, 93(12), **2016**. doi:10.1103/PhysRevB.93.125105. 5

[21] Stefano Longhi and Giuseppe Della Valle. "Anyons in one-dimensional lattices: a photonic realization." *Optics Letters*, 37(11):2160, **2012**. doi:10.1364/OL.37.002160. 5

[22] Mingsen Pan, et al. "Photonic zero mode in a non-Hermitian photonic lattice." *Nature Communications*, 9(1), **2018**. doi:10.1038/s41467-018-03822-8. 5

[23] Zhongbo Yan, et al. "Vortex End Majorana Zero Modes in Superconducting Dirac and Weyl Semimetals." *Physical Review Letters*, 124(25), **2020**. doi:10.1103/PhysRevLett.124.257001. 5

[24] Ming-Xun Deng, et al. "Superconducting states and Majorana modes in transition-metal dichalcogenides under inhomogeneous strain." *Physical Review B*, 99(8), **2019**. doi:10.1103/PhysRevB.99.085106. 5

[25] Alexandra C. Ford, et al. "Diameter-Dependent Electron Mobility of InAs Nanowires." *Nano Letters*, 9(1):360–365, **2009**. doi:10.1021/nl803154m. 11

[26] K. Takase, et al. "Highly gate-tuneable Rashba spin-orbit interaction in a gate-all-around InAs nanowire metal-oxide-semiconductor field-effect transistor." *Scientific Reports*, 7(1), **2017**. doi:10.1038/s41598-017-01080-0. 11

[27] Jiyin Wang, et al. "Measurements of the spin-orbit interaction and Landé g factor in a pure-phase InAs nanowire double quantum dot in the Pauli spin-blockade regime." *Applied Physics Letters*, 109(5):053106, **2016**. doi:10.1063/1.4960464. 11

[28] Samuel d'Hollosy, et al. "g-factor anisotropy in nanowire-based InAs quantum dots." *AIP Conference Proceedings*, **2013**. doi:10.1063/1.4848434.

[29] M. T. Björk, et al. "Tunable effective gfactor in InAs nanowire quantum dots." *Physical Review B*, 72(20), **2005**. doi:10.1103/PhysRevB.72.201307. 11, 18

[30] Morten Kjaergaard. "Proximity Induced Superconducting Properties in One and Two Dimensional Semiconductors: Towards Topological States of Matter." PhD thesis, University of Copenhagen, **2015**. 11

[31] P. Krogstrup, et al. "Epitaxy of semiconductor–superconductor nanowires." *Nature Materials*, 14(4):400–406, **2015**. doi:10.1038/nmat4176. 11, 13, 129, 145, 151

[32] Nicholas A. Güsken. "MBE growth and characterization of Te-doped InAs nanowires and InAs/superconductor hybrid structures." Master's thesis, RWTH Aachen, **2016**. 12, 135

[33] Nicholas A. Güsken, et al. "MBE growth of Al/InAs and Nb/InAs superconducting hybrid nanowire structures." *Nanoscale*, 9(43):16735–16741, **2017**. doi:10.1039/C7NR03982D. 11, 13, 129, 131, 145

[34] A Kelrich, et al. "Shadowing and mask opening effects during selective-area vapor–liquid–solid growth of InP nanowires by metalorganic molecular beam epitaxy." *Nanotechnology*, 24(47):475302, **2013**. doi:10.1088/0957-4484/24/47/475302. 11

[35] Bernhard Mandl, et al. "Growth Mechanism of Self-Catalyzed Group III-V Nanowires." *Nano Letters*, 10(11):4443–4449, **2010**. doi:10.1021/nl1022699.

[36] Pratyush Das Kanungo, et al. "Selective area growth of III–V nanowires and their heterostructures on silicon in a nanotube template: towards monolithic integration of nano-devices." *Nanotechnology*, 24(22):225304, **2013**. doi:10.1088/0957-4484/24/22/225304.

[37] D Bahrami, et al. "High yield of self-catalyzed GaAs nanowire growth on silicon (111) substrate templated by focused ion beam patterning." *Nanotechnology*, 31(18):185302, **2020**. doi:10.1088/1361-6528/ab6d99. 11

[38] Torsten Rieger. "Growth and structural characterization of III-V semiconductor nanowires." PhD thesis, RWTH Aachen, **2015**. 12, 197

[39] Pujitha Perla. "Growth and characterization of InAs nanowire-based Josephson junctions." PhD thesis, RWTH Aachen, **2020**. 12, 14, 136

[40] Richard C. Tolman. "The Effect of Droplet Size on Surface Tension." *The Journal of Chemical Physics*, 17(3):333–337, **1949**. doi:10.1063/1.1747247. 13

[41] Arthur Leis. "InAs/Al nanowire Josephson junctions for transmon qubits: Realization and electrical characterization." Master's thesis, RWTH Aachen, **2016**. 14, 130, 160, 161

[42] Filip Krizek, et al. "Growth of InAs Wurtzite Nanocrosses from Hexagonal and Cubic Basis." *Nano Letters*, 17(10):6090–6096, **2017**. doi:10.1021/acs.nanolett.7b02604. 14

[43] Alessandro Enrico, et al. "Scalable Manufacturing of Single Nanowire Devices Using Crack-Defined Shadow Mask Lithography." *ACS Applied Materials & Interfaces*, 11(8):8217–8226, **2019**. doi:10.1021/acsami.8b19410.

[44] Damon J. Carrad, et al. "Shadow Epitaxy for In Situ Growth of Generic Semiconductor/Superconductor Hybrids." *Advanced Materials*, page 1908411, **2020**. doi:10.1002/adma.201908411. 129, 145

[45] Sasa Gazibegovic, et al. "Epitaxy of Advanced Nanowire Quantum Devices." *Nature*, 548:434–438, **2017**. doi:doi:10.1038/nature23468. 148, 195

[46] Peter Schüffelgen, et al. "Selective area growth and stencil lithography for in situ fabricated quantum devices." *Nature Nanotechnology*, 14(9):825–831, **2019**. doi:10.1038/s41565-019-0506-y. 14

[47] H. Seidel. "Anisotropic Etching of Crystalline Silicon in Alkaline Solutions." *Journal of The Electrochemical Society*, 137(11):3612, **1990**. doi:10.1149/1.2086277. 14

[48] Avvaru Venkata Narasimha Rao, et al. "Determination of precise crystallographic directions on Si{111} wafers using self-aligning pre-etched pattern." *Micro and Nano Systems Letters*, 6(1), **2018**. doi:10.1186/s40486-018-0066-1.

[49] Akarapu Ashok and Prem Pal. "Silicon micromachining in 25surfactant concentrations ranging from ppb to ppm." *Microsystem Technologies*, 23(1):47–54, **2015**. doi:10.1007/s00542-015-2699-9. 14

[50] Pujitha Perla, et al. "Fully in situ Nb/InAs-nanowire Josephson junctions by selective-area growth and shadow evaporation." *Nanoscale Adv.*, 3(5):1413–1421, **2021**. doi:10.1039/D0NA00999G. 15

[51] R. De L. Kronig, et al. "Quantum mechanics of electrons in crystal lattices." *Proceedings of the Royal Society of London. Series A, Containing Papers of a Mathematical and Physical Character*, 130(814):499–513, **1931**. doi:10.1098/rspa.1931.0019. 16

[52] Felix Bloch. "Über die Quantenmechanik der Elektronen in Kristallgittern." *Zeitschrift für Physik*, 52(7-8):555–600, **1929**. doi:10.1007/BF01339455. 16

[53] P. D. C. King, et al. "Determination of the branch-point energy of InN: Chemical trends in common-cation and common-anion semiconductors." *Physical Review B*, 77(4), **2008**. doi:10.1103/PhysRevB.77.045316. 16

[54] Yoyo Hinuma, et al. "Band alignment of semiconductors from density-functional theory and many-body perturbation theory." *Physical Review B*, 90(15), **2014**. doi:10.1103/PhysRevB.90.155405.

[55] Sergej Schuwalow, et al. "Band bending profile and band offset extraction at semiconductor-metal interfaces." *arxiv*, **2019**. doi:arXiv:1910.02735. 16, 17

[56] L. Ö. Olsson, et al. "Charge Accumulation at InAs Surfaces." *Physical Review Letters*, 76(19):3626–3629, **1996**. doi:10.1103/PhysRevLett.76.3626. 16

[57] V. E. Degtyarev, et al. "Features of electron gas in InAs nanowires imposed by interplay between nanowire geometry, doping and surface states." *Scientific Reports*, 7(1), **2017**. doi:10.1038/s41598-017-03415-3.

[58] James L. Webb, et al. "Electrical and Surface Properties of InAs/InSb Nanowires Cleaned by Atomic Hydrogen." *Nano Letters*, 15(8):4865–4875, **2015**. doi:10.1021/acs.nanolett.5b00282. 16

[59] Hans Lüth. "Solid Surfaces, Interfaces and Thin Films." Springer Berlin Heidelberg, **2010**. doi:10.1007/978-3-642-13592-7. 16

[60] C. Gutsche, et al. "Ohmic contacts to n-GaAs nanowires." *Journal of Applied Physics*, 110(1):014305, **2011**. doi:10.1063/1.3603041. 16

[61] Marcelo Rizzo Piton, et al. "Optimization of Ohmic Contacts to p-GaAs Nanowires." *Nanoscale Research Letters*, 14 (1), **2019**. doi:10.1186/s11671-019-3175-8. 16

[62] T.D. Veal, et al. "Surface Preparation of InAs (110) Using Atomic Hydrogen." *Sultan Qaboos University Journal for Science [SQUJS]*, 7(2):303, **2002**. doi:10.24200/squjs.vol7iss2pp303-310. 16

[63] D B Suyatin, et al. "Sulfur passivation for ohmic contact formation to InAs nanowires." *Nanotechnology*, 18(10): 105307, **2007**. doi:10.1088/0957-4484/18/10/105307. 16

[64] D.Y. Petrovykh, et al. "Chemical and electronic properties of sulfur-passivated InAs surfaces." *Surface Science*, 523 (3):231–240, **2003**. doi:10.1016/S0039-6028(02)02411-1. 16

[65] M J L Sourribes, et al. "Minimization of the contact resistance between InAs nanowires and metallic contacts." *Nanotechnology*, 24(4):045703, **2013**. doi:10.1088/0957-4484/24/4/045703. 16

[66] Thomas Heinzel. "Mesoscopic Electronics in Solid State Nanostructures." Wiley, **2006**. doi:10.1002/9783527618910. 16, 43, 44

[67] H Hasegawa and T Sawada. "On the electrical properties of compound semiconductor interfaces in metal/insulator/semiconductor structures and the possible origin of interface states." *Thin Solid Films*, 103(1-3):119–140, **1983**. doi:10.1016/0040-6090(83)90430-3. 17

[68] F. Luthi, et al. "Evolution of Nanowire Transmon Qubits and Their Coherence in a Magnetic Field." *Physical Review Letters*, 120(10), **2018**. doi:10.1103/physrevlett.120.100502. 17

[69] Torsten Rieger, et al. "Molecular Beam Epitaxy Growth of GaAs/InAs Core–Shell Nanowires and Fabrication of InAs Nanotubes." *Nano Letters*, 12(11):5559–5564, **2012**. doi:10.1021/nl302502b. 17

[70] Patrick Zellekens, et al. "Phase coherent transport and spin-orbit interaction in GaAs/InSb core/shell nanowires." *Semiconductor Science and Technology*, **2020**. doi:10.1088/1361-6641/ab8396. 18, 203, 204, 206, 207, 208, 210, 211, 212, 214

[71] Patrick Zellekens, et al. "Strain relaxation and ambipolar electrical transport in GaAs/InSb core–shell nanowires." *Nanoscale*, 9(46):18392–18401, **2017**. doi:10.1039/C7NR05201D. 18, 19, 195, 199, 200, 204, 205, 208, 214

[72] Andrei Manolescu, et al. "Majorana states in prismatic core-shell nanowires." *Physical Review B*, 96(12), **2017**. doi:10.1103/PhysRevB.96.125435. 18

[73] Anna Sitek, et al. "In-gap corner states in core-shell polygonal quantum rings." *Scientific Reports*, 7(1), **2017**. doi:10.1038/srep40197.

[74] Miguel Urbaneja Torres, et al. "Conductance features of core-shell nanowires determined by their internal geometry." *Physical Review B*, 98(8), **2018**. doi:10.1103/PhysRevB.98.085419.

[75] Anna Sitek, et al. "Corner and side localization of electrons in irregular hexagonal semiconductor shells." *Nanotechnology*, 30(45):454001, **2019**. doi:10.1088/1361-6528/ab37a1.

[76] Kristján Óttar Klausen, et al. "Majorana Zero Modes in Nanowires with Combined Triangular and Hexagonal Geometry." *Nanotechnology*, **2020**. doi:10.1088/1361-6528/ab932e. 18

[77] Stefan Birner, et al. "Ballistic quantum transport using the contact block reduction (CBR) method." *Journal of Computational Electronics*, 8(3-4):267–286, **2009**. doi:10.1007/s10825-009-0293-z. 18, 19

[78] S. Birner, et al. "nextnano: General Purpose 3-D Simulations." *IEEE Transactions on Electron Devices*, 54(9):2137–2142, **2007**. doi:10.1109/TED.2007.902871. 18, 19

[79] Fabian Haas, et al. "Angle-dependent magnetotransport in GaAs/InAs core/shell nanowires." *Scientific Reports*, 6(1), **2016**. doi:10.1038/srep24573. 18, 195, 210

[80] Fabian Haas, et al. "Anisotropic phase coherence in GaAs/InAs core/shell nanowires." *Nanotechnology*, 28(44):445202, **2017**. doi:10.1088/1361-6528/aa887d. 208

[81] Ö. Gül, et al. "Flux periodic magnetoconductance oscillations in GaAs/InAs core/shell nanowires." *Physical Review B*, 89(4), **2014**. doi:10.1103/PhysRevB.89.045417. 18, 129, 195, 198, 208, 210, 213

[82] F Haas, et al. "Quantum interferometer based on GaAs/InAs core/shell nanowires connected to superconducting contacts." *Semiconductor Science and Technology*, 33(6):064001, **2018**. doi:10.1088/1361-6641/aabc6d. 18, 129

[83] M.-E. Pistol and C. E. Pryor. "Band structure of core-shell semiconductor nanowires." *Physical Review B*, 78(11), **2008**. doi:10.1103/PhysRevB.78.115319. 19

[84] Ivan Knez and Rui-Rui Du. "Quantum spin Hall effect in inverted InAs/GaSb quantum wells." *Frontiers of Physics*, 7(2):200–207, **2011**. doi:10.1007/s11467-011-0204-1. 19

[85] Ivan Knez, et al. "Evidence for Helical Edge Modes in InvertedInAs/GaSbQuantum Wells." *Physical Review Letters*, 107(13), **2011**. doi:10.1103/PhysRevLett.107.136603.

[86] Y. Naveh and B. Laikhtman. "Band-structure tailoring by electric field in a weakly coupled electron-hole system." *Applied Physics Letters*, 66(15):1980–1982, **1995**. doi:10.1063/1.113297. 19

[87] Y. Aharonov and A. Casher. "Topological Quantum Effects for Neutral Particles." *Physical Review Letters*, 53(4):319–321, **1984**. doi:10.1103/PhysRevLett.53.319. 21

[88] C.W.J. Beenakker and H. van Houten. "Quantum Transport in Semiconductor Nanostructures." Elsevier, **1991**. doi:10.1016/S0081-1947(08)60091-0. 23, 24, 25, 26, 208

[89] Christian Blömers. "Electronic Transport in Narrow-Gap Semiconductor Nanowires." PhD thesis, RWTH Aachen, **2012**.

[90] Ch. Blomers, et al. "Electronic Phase Coherence in InAs Nanowires." *Nano Letters*, 11(9):3550–3556, **2011**. doi:10.1021/nl201102a. 24, 206, 207

[91] P. W. Anderson. "Absence of Diffusion in Certain Random Lattices." *Physical Review*, 109(5):1492–1505, **1958**. doi:10.1103/PhysRev.109.1492. 25

[92] P. W. Anderson, et al. "Possible Explanation of Nonlinear Conductivity in Thin-Film Metal Wires." *Physical Review Letters*, 43(10):718–720, **1979**. doi:10.1103/PhysRevLett.43.718. 25

[93] Y.V. Nazarov and Y.M. Blanter. "Quantum Transport: Introduction to Nanoscience," volume 51. Informa UK Limited, **2010**. doi:10.1080/00107510903282549. 25

[94] Sudip Chakravarty and Albert Schmid. "Weak localization: The quasiclassical theory of electrons in a random potential." *Physics Reports*, 140(4):193–236, **1986**. doi:10.1016/0370-1573(86)90027-X. 26

[95] Ç. Kurdak, et al. "Quantum interference effects and spin-orbit interaction in quasi-one-dimensional wires and rings." *Physical Review B*, 46(11):6846–6856, **1992**. doi:10.1103/PhysRevB.46.6846. 26, 27, 208, 209

[96] C. W. J. Beenakker and H. van Houten. "Boundary scattering and weak localization of electrons in a magnetic field." *Physical Review B*, 38(5):3232–3240, **1988**. doi:10.1103/PhysRevB.38.3232. 26, 208, 209

[97] C. W. J. Beenakker and H. van Houten. "Flux-cancellation effect on narrow-channel magnetoresistance fluctuations." *Phys. Rev. B*, 37(11):6544–6546, **1988**. doi:10.1103/PhysRevB.37.6544. 27, 206

[98] P. Roulleau, et al. "Suppression of weak antilocalization in InAs nanowires." *Phys. Rev. B*, 81(15):155449, **2010**. doi:10.1103/PhysRevB.81.155449. 27, 208

[99] Minhao Liu, et al. "Crossover between Weak Antilocalization and Weak Localization in a Magnetically Doped Topological Insulator." *Physical Review Letters*, 108(3), **2012**. doi:10.1103/PhysRevLett.108.036805. 26

[100] Guolin Zheng, et al. "Weak localization effect in topological insulator micro flakes grown on insulating ferrimagnet BaFe12O19." *Scientific Reports*, 6(1), **2016**. doi:10.1038/srep21334. 26

[101] Vladimir I. Fal'ko, et al. "Weak localization in graphene." *Solid State Communications*, 143(1-2):33–38, **2007**. doi:10.1016/j.ssc.2007.03.049. 26

[102] Dong Liang, et al. "One-Dimensional Weak Localization of Electrons in a Single InAs Nanowire." *Nano Letters*, 9(4): 1709–1712, **2009**. doi:10.1021/nl900424k. 26

[103] Yu A Bychkov and E I Rashba. "Oscillatory effects and the magnetic susceptibility of carriers in inversion layers." *Journal of Physics C: Solid State Physics*, 17(33):6039–6045, **1984**. doi:10.1088/0022-3719/17/33/015. 26

[104] Emmanuel Rashba and V Sheka. "Symmetry of energy bands in crystals of wurtzite type II. Symmetry of bands with spin-orbit interaction included." *New. J. Phys.*, 17:050202, **2015**. doi:nrs.harvard.edu/urn-3:HUL.InstRepos:29426010.

[105] Yu A Bychkov and É I Rashba. "Properties of a 2D electron gas with lifted spectral degeneracy." *JETP lett*, 39(2):78, **1984**. 26, 209

[106] G. Dresselhaus. "Spin-Orbit Coupling Effects in Zinc Blende Structures." *Physical Review*, 100(2):580–586, **1955**. doi:10.1103/PhysRev.100.580. 26

[107] G. Bergmann. "Weak anti-localization—An experimental proof for the destructive interference of rotated spin." *Solid State Communications*, 42(11):815–817, **1982**. doi:10.1016/0038-1098(82)90013-8. 26, 27

[108] S. Hikami, et al. "Spin-orbit interaction and magnetoresistance in the two dimensional random system." *Progress of Theoretical Physics*, 63(2):707–10, **1980**. doi:10.1143/PTP.63.707. 208

[109] G. Bergmann. "Weak localization in thin films, a time-of-flight experiment with conduction electrons." *Physics Reports*, 107:1–58, **1984**. 26, 208

[110] M.I. Dyakonov and V.I. Perel. "Current-induced spin orientation of electrons in semiconductors." *Physics Letters A*, 35(6):459–460, **1971**. doi:10.1016/0375-9601(71)90196-4. 26

[111] R. J. Elliott. "Theory of the Effect of Spin-Orbit Coupling on Magnetic Resonance in Some Semiconductors." *Physical Review*, 96(2):266–279, **1954**. doi:10.1103/PhysRev.96.266. 26

[112] Y. Yafet. "g Factors and Spin-Lattice Relaxation of Conduction Electrons." *Solid State Physics*, 14:1–98, **1963**. doi:10.1016/S0081-1947(08)60259-3. 26

[113] Michael Kammermeier, et al. "Weak (anti)localization in tubular semiconductor nanowires with spin-orbit coupling." *Phys. Rev. B*, 93:205306, **2016**. doi:10.1103/PhysRevB.93.205306. 27, 209

[114] Michael Kammermeier, et al. "Magnetoconductance correction in zinc-blende semiconductor nanowires with spin-orbit coupling." *Phys. Rev. B*, 96:235302, **2017**. doi:10.1103/PhysRevB.96.235302. 209

[115] A. Bringer, et al. "Dresselhaus spin-orbit coupling in [111]-oriented semiconductor nanowires." *Phys. Rev. B*, 99: 085437, **2019**. doi:10.1103/PhysRevB.99.085437. 209

[116] Sebastian Heedt. "Spin Coherence and Quantum Transport in Semiconductor Nanowires." PhD thesis, RWTH Aachen, **2019**. 27, 119

[117] Prof. Dr. Sigurdur I. Erlingsson. School of science and engineering, reykjavik university, reykjavík, iceland. private communication, **2018**. 27

[118] Dr. Paul Wenk. Institute i - theoretical physics, university of regensburg, regensburg, germany. private communication, **2018**.

[119] Prof. Dr. José Carlos Egues de Menezes. Institute of physics, university of são paulo, são paulo, brazil. private communication, **2018**. 27

[120] Vinay Ambegaokar and Alexis Baratoff. "Tunneling Between Superconductors." *Phys. Rev. Lett.*, 10:486–489, **1963**. doi:10.1103/PhysRevLett.10.486. 30

[121] K. K. Likharev. "Superconducting weak links." *Reviews of Modern Physics*, 51(1):101–159, **1979**. doi:10.1103/RevModPhys.51.101. 30

[122] B.D. Josephson. "Supercurrents through barriers." *Advances in Physics*, 14(56):419–451, **1965**. doi:10.1080/00018736500101091. 30, 35

[123] W. C. Stewart. "Current-Voltage Characteristics of Josephson Junctions." *Applied Physics Letters*, 12(8):277–280, **1968**. doi:10.1063/1.1651991. 31

[124] D. E. McCumber. "Effect of ac Impedance on dc VoltageâCurrent Characteristics of Superconductor WeakâLink Junctions." *Journal of Applied Physics*, 39(7):3113–3118, **1968**. doi:10.1063/1.1656743. 31

[125] James A. Blackburn, et al. "A survey of classical and quantum interpretations of experiments on Josephson junctions at very low temperatures." *Physics Reports*, 611:1–33, **2016**. doi:10.1016/j.physrep.2015.10.010. 32

[126] R De Luca, et al. "Mechanical analog of an over-damped Josephson junction." *European Journal of Physics*, 36(5): 055042, **2015**. doi:10.1088/0143-0807/36/5/055042. 32

[127] Kaveh Gharavi, et al. "Nb/InAs nanowire proximity junctions from Josephson to quantum dot regimes." *Nanotechnology*, 28(8):085202, **2017**. doi:10.1088/1361-6528/aa5643. 34

[128] Sean Hart, et al. "Current-phase relations of InAs nanowire Josephson junctions: From interacting to multimode regimes." *Physical Review B*, 100(6), **2019**. doi:10.1103/PhysRevB.100.064523. 34, 40

[129] A. Buzdin and A. E. Koshelev. "Periodic alternating 0- and -junction structures as realization of-Josephson junctions." *Physical Review B*, 67(22), **2003**. doi:10.1103/PhysRevB.67.220504. 35

[130] H. Sickinger, et al. "Experimental Evidence of aJosephson Junction." *Physical Review Letters*, 109(10), **2012**. doi:10.1103/PhysRevLett.109.107002.

[131] D. B. Szombati, et al. "Josephson 0-junction in nanowire quantum dots." *Nature Physics*, 12(6):568–572, **2016**. doi:10.1038/nphys3742. 35, 37

[132] Sidney Shapiro. "Josephson Currents in Superconducting Tunneling: The Effect of Microwaves and Other Observations." *Physical Review Letters*, 11(2):80–82, **1963**. doi:10.1103/PhysRevLett.11.80. 35

[133] J. Wiedenmann, et al. "4-periodic Josephson supercurrent in HgTe-based topological Josephson junctions." *Nature Communications*, 7(1), **2016**. doi:10.1038/ncomms10303. 36, 91, 139, 143

[134] A Valizadeh, et al. "On the Origin of Fractional Shapiro Steps in Systems of Josephson Junctions with Few Degrees of Freedom." *Journal of Nonlinear Mathematical Physics*, 15(sup3):407–416, **2008**. doi:10.2991/jnmp.2008.15.s3.39. 36

[135] P. Dubos, et al. "Coherent Low-Energy Charge Transport in a Diffusive S-N-S Junction." *Physical Review Letters*, 87 (20), **2001**. doi:10.1103/PhysRevLett.87.206801. 36

[136] M. Chauvin, et al. "Superconducting Atomic Contacts under Microwave Irradiation." *Physical Review Letters*, 97(6), **2006**. doi:10.1103/PhysRevLett.97.067006. 37, 133, 140, 141, 142, 172, 175

[137] J. C. Cuevas, et al. "Subharmonic Shapiro Steps and Assisted Tunneling in Superconducting Point Contacts." *Physical Review Letters*, 88(15), **2002**. doi:10.1103/PhysRevLett.88.157001.

[138] M. J. Renne and D. Polder. "Some analytical results for the resistively shunted Josephson junction." *Revue de Physique Appliquée*, 9(1):25–28, **1974**. doi:10.1051/rphysap:019740090102500. 36

[139] R. S. Deacon, et al. "Josephson Radiation from Gapless Andreev Bound States in HgTe-Based Topological Junctions." *Physical Review X*, 7(2), **2017**. doi:10.1103/PhysRevX.7.021011. 36

[140] Martin Chauvin. "The Josephson Effect in Atomic Contacts." Theses, Université Pierre et Marie Curie - Paris VI, **2005**. 37, 133, 134, 140, 141, 142, 172, 175

[141] L. A. Ivanchenko, Yu. M. ; Zil'Berman. "The Josephson effect in small tunnel contacts." *Soviet Phys. JETP*, 28, **1969**. 37, 41, 142

[142] Vinay Ambegaokar and B. I. Halperin. "Voltage Due to Thermal Noise in the dc Josephson Effect." *Physical Review Letters*, 22(25):1364–1366, **1969**. doi:10.1103/PhysRevLett.22.1364. 37, 141, 142

[143] J. Kurkijärvi and V. Ambegaokar. "Numerical calculation of thermal noise-voltage in a Josephson junction of finite capacitance." *Physics Letters A*, 31(6):314–315, **1970**. doi:10.1016/0375-9601(70)90876-5. 37, 141, 142

[144] N. N. Bogoljubov, et al. "A New Method in the Theory of Superconductivity." *Fortschritte der Physik*, 6(11-12):605–682, **1958**. doi:10.1002/prop.19580061102. 38

[145] P. G. De Gennes. "Superconductivity of Metals and Alloys." CRC Press, **2018**. doi:10.1201/9780429497032. 38

[146] P.G. de Gennes and D. Saint-James. "Elementary excitations in the vicinity of a normal metal-superconducting metal contact." *Physics Letters*, 4(2):151–152, **1963**. doi:10.1016/0031-9163(63)90148-3. 38

[147] D. Saint-James. "Excitations élémentaires au voisinage de la surface de séparation d'un métal normal et d'un métal supraconducteur." *Journal de Physique*, 25(10):899–905, **1964**. doi:10.1051/jphys:019640025010089900.

[148] Aleksandr F. Andreev. "Electron spectrum of the intermediate state of superconductors." *Soviet Physics JETP*, 22:455, **1965**. 38, 39

[149] A F Andreev. "Thermal conductivity of the intermediate state of superconductors." *Soviet Physics-JETP*, 19(6):1228–1232, **1964**. 38, 39

[150] C. W. J. Beenakker and H. van Houten. "Josephson current through a superconducting quantum point contact shorter than the coherence length." *Physical Review Letters*, 66(23):3056–3059, **1991**. doi:10.1103/PhysRevLett.66.3056. 39

[151] Akira Furusaki and Masaru Tsukada. "Dc Josephson effect and Andreev reflection." *Solid State Communications*, 78 (4):299–302, **1991**. doi:10.1016/0038-1098(91)90201-6. 40

[152] Philip F. Bagwell. "Suppression of the Josephson current through a narrow, mesoscopic, semiconductor channel by a single impurity." *Physical Review B*, 46(19):12573–12586, **1992**. doi:10.1103/PhysRevB.46.12573. 39

[153] I O Kulik and A N Omel'yanchuk. "Contribution to the microscopic theory of the Josephson effect in superconducting bridges." *JETP Lett. (USSR) (Engl. Transl.), v. 21, no. 4, pp. 96-97*, **1975**. 39

[154] Rolf Landauer. "Electrical resistance of disordered one-dimensional lattices." *Philosophical Magazine*, 21(172):863–867, **1970**. doi:10.1080/14786437008238472. 39

[155] Horacio M. Pastawski. "Classical and quantum transport from generalized Landauer-Büttiker equations." *Physical Review B*, 44(12):6329–6339, **1991**. doi:10.1103/PhysRevB.44.6329. 39

[156] J. A. Sauls. "Andreev bound states and their signatures." *Philosophical Transactions of the Royal Society A: Mathematical, Physical and Engineering Sciences*, 376(2125):20180140, **2018**. doi:10.1098/rsta.2018.0140. 39, 40

[157] A. Zazunov, et al. "Andreev Level Qubit." *Physical Review Letters*, 90(8), **2003**. doi:10.1103/PhysRevLett.90.087003. 39, 56, 57

[158] Nikolai M. Chtchelkatchev and Yu. V. Nazarov. "Andreev Quantum Dots for Spin Manipulation." *Physical Review Letters*, 90(22), **2003**. doi:10.1103/PhysRevLett.90.226806. 39

[159] A. A. Golubov, et al. "The current-phase relation in Josephson junctions." *Reviews of Modern Physics*, 76(2):411–469, **2004**. doi:10.1103/RevModPhys.76.411. 40

[160] Carlo Beenakker. "Transport Phenomena in Mesoscopic Systems." Springer Berlin Heidelberg, **1992**. doi:10.1007/978-3-642-84818-6. 40

[161] Akira Furusaki, et al. "Josephson effect of the superconducting quantum point contact." *Physical Review B*, 45(18): 10563–10575, **1992**. doi:10.1103/PhysRevB.45.10563. 40

[162] Eric M. Spanton, et al. "Current–phase relations of few-mode InAs nanowire Josephson junctions." *Nature Physics*, 13(12):1177–1181, **2017**. doi:10.1038/nphys4224. 40

[163] G. de Lange, et al. "Realization of Microwave Quantum Circuits Using Hybrid Superconducting-Semiconducting Nanowire Josephson Elements." *Physical Review Letters*, 115(12), **2015**. doi:10.1103/PhysRevLett.115.127002. 40

[164] M. Octavio, et al. "Subharmonic energy-gap structure in superconducting constrictions." *Physical Review B*, 27(11): 6739–6746, **1983**. doi:10.1103/PhysRevB.27.6739. 41, 131, 140, 147, 148, 152

[165] C. W. J. Beenakker and H. van Houten. "Semiconductor Heterostructures and Nanostructures." In *Solid State Physics*, volume 44, pages 1–228. Academic, New York, **1991**. 43

[166] Thomas Ihn. "Semiconductor Nanostructures." Oxford University Press, **2009**. doi:10.1093/acprof:oso/9780199534425.001.0001. 43, 44

[167] P.L. McEuen, et al. "Coulomb interactions and energy-level spectrum of a small electron gas." *Physica B: Condensed Matter*, 189(1-4):70–79, **1993**. doi:10.1016/0921-4526(93)90147-X. 43

[168] I Shorubalko, et al. "Tunable few-electron quantum dots in InAs nanowires." *Nanotechnology*, 18(4):044014, **2006**. doi:10.1088/0957-4484/18/4/044014. 45

[169] S. Tarucha, et al. "Shell Filling and Spin Effects in a Few Electron Quantum Dot." *Physical Review Letters*, 77(17): 3613–3616, **1996**. doi:10.1103/PhysRevLett.77.3613.

[170] Damaz de Jong, et al. "Rapid Detection of Coherent Tunneling in an InAs Nanowire Quantum Dot through Dispersive Gate Sensing." *Physical Review Applied*, 11(4), **2019**. doi:10.1103/PhysRevApplied.11.044061. 45

[171] L Yu. "Bound state in superconductors with paramagnetic impurities." *Wu Li Hsueh Pao (China) Supersedes Chung-Kuo Wu Li Hsueh For English translation see Chin. J. Phys. (Peking) (Engl. Transl.)*, Vol:21, **1965**. 46, 149, 176

[172] Hiroyuki Shiba. "Classical Spins in Superconductors." *Progress of Theoretical Physics*, 40(3):435–451, **1968**. doi:https://doi.org/10.1143/PTP.40.435.

[173] A I Rusinov. "Theory of gapless superconductivity in alloys with paramagnetic impurities." *Zh. Eksp. Theor. Fiz., 56: 2047-56(June 1969).*, **1969**. 46, 149, 176

[174] J. Kondo. "Resistance Minimum in Dilute Magnetic Alloys." *Progress of Theoretical Physics*, 32(1):37–49, **1964**. doi:10.1143/PTP.32.37. 46

[175] P. W. Anderson. "Localized Magnetic States in Metals." *Physical Review*, 124(1):41–53, **1961**. doi:10.1103/PhysRev.124.41. 46

[176] Thomas Vojta. "Quantum phase transitions in electronic systems." *Annalen der Physik*, 9(6):403–440, **2000**. doi:10.1002/1521-3889(200006)9:6<403::AID-ANDP403>3.0.CO;2-R. 46

[177] A. Kadlecová, et al. "Practical Guide to Quantum Phase Transitions in Quantum-Dot-Based Tunable Josephson Junctions." *Physical Review Applied*, 11(4), **2019**. doi:10.1103/PhysRevApplied.11.044094.

[178] H. Ingerslev Jørgensen, et al. "Critical Current 0- Transition in Designed Josephson Quantum Dot Junctions." *Nano Letters*, 7(8):2441–2445, **2007**. doi:10.1021/nl071152w.

[179] Romain Maurand, et al. "First-Order 0--Quantum Phase Transition in the Kondo Regime of a Superconducting Carbon-Nanotube Quantum Dot." *Physical Review X*, 2(1), **2012**. doi:10.1103/PHYSREVX.2.011009. 46

[180] L N Bulaevskii, et al. "Superconducting system with weak coupling to the current in the ground state." *JETP Lett. (USSR) (Engl. Transl.); (United States)*, 25:7, **1977**. 46

[181] D. J. Van Harlingen. "Phase-sensitive tests of the symmetry of the pairing state in the high-temperature superconductors—Evidence fordx2-y2symmetry." *Reviews of Modern Physics*, 67(2):515–535, **1995**. doi:10.1103/RevModPhys.67.515.

[182] J.-P. Cleuziou, et al. "Carbon nanotube superconducting quantum interference device." *Nature Nanotechnology*, 1 (1):53–59, **2006**. doi:10.1038/nnano.2006.54. 46, 47

[183] V. V. Ryazanov, et al. "Coupling of Two Superconductors through a Ferromagnet: Evidence for aJunction." *Physical Review Letters*, 86(11):2427–2430, **2001**. doi:10.1103/PhysRevLett.86.2427. 47

[184] J. W. A. Robinson, et al. "Critical Current Oscillations in Strong Ferromagnetic Junctions." *Physical Review Letters*, 97(17), **2006** . doi:10.1103/PhysRevLett.97.177003.

[185] O. Vávra, et al. "0 and phase Josephson coupling through an insulating barrier with magnetic impurities." *Physical Review B*, 74(2), **2006**. doi:10.1103/PhysRevB.74.020502. 47

[186] Boris Chesca. "Magnetic field dependencies of the critical current and of the resonant modes of dc SQUIDs fabricated from superconductors withs idx2—y2 order-parameter symmetries." *Annalen der Physik*, 8(6):511–522, **1999**. doi:10.1002/(SICI)1521-3889(199909)8:6<511::AID-ANDP511>3.0.CO;2-K. 47

[187] R. R. Schulz, et al. "Design and realization of an all d-wave dc -superconducting quantum interference device." *Applied Physics Letters*, 76(7):912–914, **2000**. doi:10.1063/1.125627. 47

[188] Chenrong Liu, et al. "Temperature-dependent spectral function of a Kondo impurity in an s -wave superconductor." *Physical Review B*, 99(17), **2019**. doi:10.1103/PhysRevB.99.174502. 47

[189] A. Kamlapure, et al. "Investigation of the Yu-Shiba-Rusinov states of a multi-impurity Kondo system." *arxiv*, **2019**. doi:arXiv:1911.03794.

[190] Juan Carlos Estrada Saldaña, et al. "Temperature induced shifts of Yu–Shiba–Rusinov resonances in nanowire-based hybrid quantum dots." *Communications Physics*, 3(1), **2020**. doi:10.1038/s42005-020-0392-5. 47

[191] Nino Hatter, et al. "Scaling of Yu-Shiba-Rusinov energies in the weak-coupling Kondo regime." *Nature Communications*, 8(1), **2017**. doi:10.1038/s41467-017-02277-7. 47

[192] Shawulienu Kezilebieke, et al. "Observation of Coexistence of Yu-Shiba-Rusinov States and Spin-Flip Excitations." *Nano Letters*, 19(7):4614–4619, **2019**. doi:10.1021/acs.nanolett.9b01583. 47

[193] J L Lado and J Fernández-Rossier. "Unconventional Yu–Shiba–Rusinov states in hydrogenated graphene." *2D Materials*, 3(2):025001, **2016**. doi:10.1088/2053-1583/3/2/025001. 47

[194] Alejandro Lopez-Bezanilla and J. L. Lado. "Defect-induced magnetism and Yu-Shiba-Rusinov states in twisted bilayer graphene." *Physical Review Materials*, 3(8), **2019**. doi:10.1103/PhysRevMaterials.3.084003.

[195] E. Cortés del Río, et al. "Observation of Yu-Shiba-Rusinov states in superconducting graphene." *arxiv*, **2020**. doi:arXiv:2010.10377. 47

[196] Claude Cohen-Tannoudji, et al. "Atom-Photon Interactions: Basic Processes and Applications." VCH PUBN, **1998**. ISBN 0471293369. 51

[197] Ying Wu and Xiaoxue Yang. "Strong-Coupling Theory of Periodically Driven Two-Level Systems." *Physical Review Letters*, 98(1), **2007**. doi:10.1103/PhysRevLett.98.013601.

[198] Kazuyuki Fujii. "Introduction to the Rotating Wave Approximation (RWA) : Two Coherent Oscillations." *Journal of Modern Physics*, 8(12):2042–2058, **2017**. doi:10.4236/jmp.2017.812124. 51

[199] C.P. Wen. "Coplanar Waveguide, a Surface Strip Transmission Line Suitable for Nonreciprocal Gyromagnetic Device Applications." *1969 G-MTT International Microwave Symposium*, 17(12):1087–1090, **1969**. doi:10.1109/TMTT.1969.1127105. 52

[200] Rainee N. Simons. "Coplanar Waveguide Circuits, Components, and Systems." John Wiley Sons, **2004**. ISBN 9780471463931. 52

[201] Martin Caulton. "Lumped Elements in Microwave Integrated Circuits." Advances in Microwaves, **1974**. doi:10.1016/B978-0-12-027908-1.50009-8. 53

[202] Inder Bahl. "Lumped Elements for RF and Microwave Circuits." Artech House Publishers, **2003**. ISBN 1580533094. 53

[203] William Hayt. "Engineering circuit analysis." McGraw-Hill, New York, **1971**. ISBN 0070273820. 53

[204] Christopher Donaghy-Spargo. "On Heaviside's contributions to transmission line theory: waves, diffusion and energy flux." *Philosophical Transactions of the Royal Society A: Mathematical, Physical and Engineering Sciences*, 376 (2134):20170457, **2018**. doi:10.1098/rsta.2017.0457.

[205] Oliver Heaviside. "Electrical Papers." Cambridge University Press, **2009**. doi:10.1017/cbo9780511983139. 53

[206] Arthur Anderson. "Transmission Lines: From Lumped Element to Distributed Element Regimes." *All About Circuits*, **2015**. 53

[207] H.J. Carlin. "Distributed circuit design with transmisssion line elements." *Proceedings of the IEEE*, 59(7):1059–1081, **1971**. doi:10.1109/PROC.1971.8334. 53

[208] A. E. Guile. "Electrical power systems." Pergamon Press, Oxford New York, **1977**. ISBN 008021729X. 54

[209] Peter Wilson. "The Circuit Designer's Companion." Elsevier LTD, Oxford, **2017**. ISBN 0081017642. 54

[210] Gary Breed. "There's Nothing Magic About 50 Ohms." *High Frequency Electronics*, **2007**. 54

[211] John Golio. "The RF and microwave handbook." CRC Press, Boca Raton, FL, **2001**. ISBN 084938592X. 54

[212] R. H. Dicke. "A Computational Method Applicable to Microwave Networks." *Journal of Applied Physics*, 18(10):873–878, **1947**. doi:10.1063/1.1697561. 55

[213] Stefan Lindenmeier and Robert Weigel. "Electromagnetics and Network Theory and their Microwave Technology Applications." Springer-Verlag GmbH, **2011**. ISBN 9783642183751. 55

[214] V. Belevitch. "Summary of the History of Circuit Theory." *Proceedings of the IRE*, 50(5):848–855, **1962**. doi:10.1109/JRPROC.1962.288301. 55

[215] M. E. Valkenburg. "Circuit theory: foundations and classical contributions." Dowden, Hutchinson & Ross, Stroudsburg, Pa, **1974**. ISBN 9780879330842. 55

[216] K. Kurokawa. "Power Waves and the Scattering Matrix." *IEEE Transactions on Microwave Theory and Techniques*, 13 (2):194–202, **1965**. doi:10.1109/TMTT.1965.1125964. 55

[217] S. Mahashabde, et al. "Fast tunable high Q-factor superconducting microwave resonators." *Phys. Rev. Applied*, 14(4), **2020**. doi:10.1103/PhysRevApplied.14.044040. 55

[218] M. R. Vissers, et al. "Low loss superconducting titanium nitride coplanar waveguide resonators." *Applied Physics Letters*, 97(23):232509, **2010**. doi:10.1063/1.3517252.

[219] R. Barends, et al. "Niobium and Tantalum High Q Resonators for Photon Detectors." *IEEE Transactions on Applied Superconductivity*, 17(2):263–266, **2007**. doi:10.1109/TASC.2007.898541. 55

[220] Jens Koch, et al. "Charge-insensitive qubit design derived from the Cooper pair box." *Physical Review A*, 76(4), **2007**. doi:10.1103/PhysRevA.76.042319. 56, 60, 62, 158

[221] Sunghun Park and A. Levy Yeyati. "Andreev spin qubits in multichannel Rashba nanowires." *Phys. Rev. B*, 96:125416, **2017**. doi:10.1103/PhysRevB.96.125416. 57, 178, 180

[222] Y. Nakamura, et al. "Coherent control of macroscopic quantum states in a single-Cooper-pair box." *Nature*, 398 (6730):786–788, **1999**. doi:10.1038/19718. 58

[223] Jonathan R. Friedman, et al. "Quantum superposition of distinct macroscopic states." *Nature*, 406(6791):43–46, **2000**. doi:10.1038/35017505. 58

[224] I. Siddiqi, et al. "Dispersive measurements of superconducting qubit coherence with a fast latching readout." *Physical Review B*, 73(5), **2006**. doi:10.1103/PhysRevB.73.054510. 61

[225] Sigmund Kohler. "Dispersive readout: Universal theory beyond the rotating-wave approximation." *Physical Review A*, 98(2), **2018**. doi:10.1103/PhysRevA.98.023849. 61

[226] D. A. Ivanov and M. V. Feigel'man. "Two-level Hamiltonian of a superconducting quantum point contact." *Physical Review B*, 59(13):8444–8446, **1999**. doi:10.1103/PhysRevB.59.8444. 64

[227] Landry Bretheau. "Localized Excitations in Superconducting Atomic Contacts: PROBING THE ANDREEV DOUBLET." PhD thesis, Ecole Polytechnique X Univ., **2013**. 64

[228] W. Pauli. "Zur Quantenmechanik des magnetischen Elektrons." *Zeitschrift für Physik*, 43(9-10):601–623, **1927**. doi:10.1007/BF01397326. 64

[229] L. D. Landau. "Collected papers of L.D. Landau." Pergamon Press, Oxford,New York, **1965**. ISBN 9781483152707. 65, 99, 220

[230] Clarence Zener. "Non-adiabatic crossing of energy levels." *Proceedings of the Royal Society of London. Series A, Containing Papers of a Mathematical and Physical Character*, 137(833):696–702, **1932**. doi:10.1098/rspa.1932.0165. 220

[231] Ernst Carl Gerlach Stueckelberg. "Theorie der unelastischen Stösse zwischen Atomen." *An Unconventional Figure of Twentieth Century Physics*, pages 117–171, **2009**. doi:10.1007/978-3-7643-8878-2$_9$. 65

[232] Diego Rainis and Daniel Loss. "Majorana qubit decoherence by quasiparticle poisoning." *Physical Review B*, 85(17), **2012**. doi:10.1103/PhysRevB.85.174533. 65

[233] L. Bretheau, et al. "Supercurrent Spectroscopy of Andreev States." *Physical Review X*, 3(4), **2013**. doi:10.1103/PhysRevX.3.041034.

[234] D. G. Olivares, et al. "Dynamics of quasiparticle trapping in Andreev levels." *Physical Review B*, 89(10), **2014**. doi:10.1103/PhysRevB.89.104504. 65

[235] Christian Weyrich. "Electrical Transport and Magnetoresistance in MBE–grown 3D Topological Insulator Thin Films and Nanostructures." PhD thesis, RWTH Aachen, **2018**. 76, 119

[236] Johanna Janßen. "Transport measurements on GaAs/InSb core/shell nanowires." Master's thesis, Rwth Aachen, **2016**. 78, 79

[237] Patrick Zellekens. "Transportmessungen an GaAs/InAs, GaAs/InSb und InAs/GaSb Core/Shell Nanodrähten." Master's thesis, TU Ilmenau, **2015**. 78

[238] Jens Schwenderling. "Electronic Transport Through Quantum Dots in Semiconductor Nanowires." Master's thesis, RWTH Aachen, **2015**. 78

[239] Shazia Yasin, et al. "Comparison of MIBK/IPA and water/IPA as PMMA developers for electron beam nanolithography." *Microelectronic Engineering*, 61-62:745–753, **2002**. doi:10.1016/S0167-9317(02)00468-9. 79

[240] Jung-Sub Wi, et al. "Enhanced development properties of IPA (isopropyl alcohol) on the PMMA electron beam resist." *Electronic Materials Letters*, 3:1–5, **2007**. 79

[241] Mark C. Rosamond and Edmund H. Linfield. "Contrast-sensitivity behaviour of PMMA in 7:3 IPA:water develor." In *MNE 2015*, **2015**. 79

[242] John Robertson and Robert M. Wallace. "High-K materials and metal gates for CMOS applications." *Materials Science and Engineering: R: Reports*, 88:1–41, **2015**. doi:10.1016/j.mser.2014.11.001. 81

[243] T. Heeg, et al. "Growth and properties of epitaxial rare-earth scandate thin films." *Applied Physics A*, 83(1):103–106, **2006**. doi:10.1007/s00339-005-3463-2. 81

[244] T Rieger, et al. "Crystallization of HfO2 in InAs/HfO2 core-shell nanowires." *Nanotechnology*, 25(40):405701, **2014**. doi:10.1088/0957-4484/25/40/405701. 81

[245] Mikko Ritala, et al. "Development of crystallinity and morphology in hafnium dioxide thin films grown by atomic layer epitaxy." *Thin Solid Films*, 250(1):72 – 80, **1994**. doi:https://doi.org/10.1016/0040-6090(94)90168-6.

[246] Kaupo Kukli, et al. "Properties of HfO2 Thin Films Grown by ALD from Hafnium tetrakis(ethylmethylamide) and Water." *Journal of The Electrochemical Society*, 151(8):F189–F193, **2004**. doi:10.1149/1.1770934. 81

[247] Frederik Marx. "Elektrische Charakterisierung von Dielektrischen Schichten für Qubit-Schaltkreise." Master's thesis, FH Aachen, **2018**. 82

[248] M von Schickfus and S Hunklinger. "The dielectric coupling of low-energy excitations in vitreous silica to electromagnetic waves." *Journal of Physics C: Solid State Physics*, 9(16):L439–L442, **1976**. doi:10.1088/0022-3719/9/16/006. 82

[249] Brage Golding, et al. "Intrinsic Electric Dipole Moment of Tunneling Systems in Silica Glasses." *Phys. Rev. Lett.*, 43: 1817–1821, **1979**. doi:10.1103/PhysRevLett.43.1817. 82

[250] Jiansong Gao, et al. "Experimental evidence for a surface distribution of two-level systems in superconducting lithographed microwave resonators." *Applied Physics Letters*, 92(15):152505, **2008**. doi:10.1063/1.2906373. 83

[251] R. Barends, et al. "Contribution of dielectrics to frequency and noise of NbTiN superconducting resonators." *Applied Physics Letters*, 92(22):223502, **2008**. doi:10.1063/1.2937837. 84

[252] R. Barends, et al. "Reduced frequency noise in superconducting resonators." *Applied Physics Letters*, 97(3):033507, **2010**. doi:10.1063/1.3467052. 84

[253] William D. Oliver and Paul B. Welander. "Materials in superconducting quantum bits." *MRS Bulletin*, 38(10):816â825, **2013**. doi:10.1557/mrs.2013.229. 84

[254] Jeremy M. Sage, et al. "Study of loss in superconducting coplanar waveguide resonators." *Journal of Applied Physics*, 109(6):063915, **2011**. doi:10.1063/1.3552890. 84

[255] M. S. Khalil, et al. "Loss Dependence on Geometry and Applied Power in Superconducting Coplanar Resonators." *IEEE Transactions on Applied Superconductivity*, 21(3):879–882, **2011**. doi:10.1109/TASC.2010.2090330. 85

[256] C J K Richardson, et al. "Fabrication artifacts and parallel loss channels in metamorphic epitaxial aluminum superconducting resonators." *Superconductor Science and Technology*, 29(6):064003, **2016**. doi:10.1088/0953-2048/29/6/064003. 85

[257] Shinobu Ohya, et al. "Sputtered TiN films for superconducting coplanar waveguide resonators." *arXiv*, **2013**. doi:arxiv.org/abs/1306.2966. 87, 104

[258] Thomas Welton Christian Reichardt. "Solvents and Solvent Effects in Organic Chemistry." Wiley-VCH GmbH, **2010**. ISBN 3527324739. 88

[259] Pearton S. J., et al. "Hybrid electron cyclotron resonance-RF plasma etching of TiNxthin films grown by low pressure rapid thermal metalorganic chemical vapour deposition." *Semicond. Sci. Technol.*, 6(8):830, **1991**. doi:10.1088/0268-1242/6/8/022. 88

[260] Fracassi F., et al. "Dry etching of titanium nitride thin films in CF4–O2 plasmas." *J. Vac. Sci. Technol. A*, 13(2):335, **1994**. doi:10.1116/1.579419.

[261] Jong-Chang Woo, et al. "The Dry Etching of TiN Thin Films Using Inductively Coupled CF4/Ar Plasma." *Transactions on Electrical and Electronic Materials*, 14(2):67–70, **2013**. doi:10.4313/TEEM.2013.14.2.67. 88

[262] Young-Hee Joo, et al. "Dry etching characteristics of TiN thin films in CF4/BCl3/N2 plasma." *Thin Solid Films*, 520 (6):2339 – 2342, **2012**. doi:https://doi.org/10.1016/j.tsf.2011.10.013. 88

[263] Bruno Lee Sang, et al. "Selective dry etching of TiN nanostructures over SiO2 nanotrenches using a Cl2/Ar/N2 inductively coupled plasma." *Journal of Vacuum Science & Technology B, Nanotechnology and Microelectronics: Materials, Processing, Measurement, and Phenomena*, 34(2):02M102, **2016**. doi:10.1116/1.4936885. 88

[264] J. Tonotani, et al. "Dry etching characteristics of TiN film using Ar/CHF3, Ar/Cl2, and Ar/BCl3 gas chemistries in an inductively coupled plasma." *Journal of Vacuum Science & Technology B: Microelectronics and Nanometer Structures Processing, Measurement, and Phenomena*, 21(5):2163–2168, **2003**. doi:10.1116/1.1612517. 88

[265] Martin Sandberg, et al. "Etch induced microwave losses in titanium nitride superconducting resonators." *Applied Physics Letters*, 100(26):262605, **2012**. doi:10.1063/1.4729623. 88

[266] Fernando Domínguez, et al. "Dynamical detection of Majorana fermions in current-biased nanowires." *Physical Review B*, 86(14), **2012**. doi:10.1103/PhysRevB.86.140503. 91

[267] F. Domínguez, et al. "Josephson junction dynamics in the presence of 2 - and 4 -periodic supercurrents." *Physical Review B*, 95(19), **2017**. doi:10.1103/PhysRevB.95.195430. 91, 220

[268] Chun-Xiao Liu, et al. "Andreev bound states versus Majorana bound states in quantum dot-nanowire-superconductor hybrid structures: Trivial versus topological zero-bias conductance peaks." *Physical Review B*, 96 (7), **2017**. doi:10.1103/PhysRevB.96.075161. 91, 191

[269] Fan Zhang and Wei Pan. "A missing step is a key step." *Nature Materials*, 17(10):851–852, **2018**. doi:10.1038/s41563-018-0179-1. 139, 143

[270] Leonid P. Rokhinson, et al. "The fractional a.c. Josephson effect in a semiconductor–superconductor nanowire as a signature of Majorana particles." *Nature Physics*, 8(11):795–799, **2012**. doi:10.1038/nphys2429. 143

[271] Erwann Bocquillon, et al. "Gapless Andreev bound states in the quantum spin Hall insulator HgTe." *Nature Nanotechnology*, 12(2):137–143, **2016**. doi:10.1038/nnano.2016.159. 91

[272] C. P. Yue, et al. "A physical model for planar spiral inductors on silicon." In *International Electron Devices Meeting. Technical Digest*, pages 155–158, **1996**. doi:10.1109/IEDM.1996.553144. 93

[273] A. M. Niknejad and R. G. Meyer. "Analysis, design, and optimization of spiral inductors and transformers for Si RF ICs." *IEEE Journal of Solid-State Circuits*, 33(10):1470–1481, **1998**. doi:10.1109/4.720393. 93

[274] H. A. Wheeler. "Simple Inductance Formulas for Radio Coils." *Proceedings of the Institute of Radio Engineers*, 16(10): 1398–1400, **1928**. doi:10.1109/JRPROC.1928.221309. 93

[275] S. S. Mohan, et al. "Simple accurate expressions for planar spiral inductances." *IEEE Journal of Solid-State Circuits*, 34(10):1419–1424, **1999**. doi:10.1109/4.792620. 93

[276] Nihad Dib, et al. "CAD modeling of coplanar waveguide interdigital capacitor." *International Journal of RF and Microwave Computer-Aided Engineering*, 15(6):551–559, **2005**. doi:10.1002/mmce.20099. 94

[277] N. Dib. "Comprehensive study of CAD models of several coplanar waveguide (CPW) discontinuities." *IEE Proceedings - Microwaves, Antennas and Propagation*, 152(2):69–76, **2005**. doi:10.1049/ip-map:20045039.

[278] KR Ajayan and KJ Vinoy. "Planar inter digital capacitors on printed circuit board." *IEEE Trans. Microw. Theory Tech*, 41(9):191–194, **1993**. 94

[279] Haining Pan, et al. "Quantized and unquantized zero-bias tunneling conductance peaks in Majorana nanowires: Conductance below and above 2e2/h." *Physical Review B*, 103(21), **2021**. doi:10.1103/PhysRevB.103.214502. 96

[280] M. Büttiker. "Absence of backscattering in the quantum Hall effect in multiprobe conductors." *Physical Review B*, 38 (14):9375–9389, **1988**. doi:10.1103/PhysRevB.38.9375. 96

[281] J. Bardeen, et al. "Theory of Superconductivity." *Physical Review*, 108(5):1175–1204, **1957**. doi:10.1103/PhysRev.108.1175. 99

[282] A A Abrikosov. "Magnetic properties of superconductors of the second group." *Sov. Phys. - JETP (Engl. Transl.); (United States)*, 5:6, **1957**. 99

[283] L P Gor'kov. "Microscopic derivation of the Ginzburg–Landau equations in the theory of superconductivity." *Sov. Phys. - JETP (Engl. Transl.); (United States)*, 9:6, **1959**. 99

[284] F. London and H. London. "The electromagnetic equations of the supraconductor." *Proceedings of the Royal Society of London. Series A - Mathematical and Physical Sciences*, 149(866):71–88, **1935**. doi:10.1098/rspa.1935.0048. 99

[285] A.A. Abrikosov. "The magnetic properties of superconducting alloys." *Journal of Physics and Chemistry of Solids*, 2 (3):199–208, **1957**. doi:10.1016/0022-3697(57)90083-5. 99, 100

[286] Francisco Estellés-Duart, et al. "Current-driven production of vortex-antivortex pairs in planar Josephson junction arrays and phase cracks in long-range order." *Scientific Reports*, 8(1), **2018**. doi:10.1038/s41598-018-33467-y. 99

[287] N. D. Mermin. "The topological theory of defects in ordered media." *Reviews of Modern Physics*, 51(3):591–648, **1979**. doi:10.1103/RevModPhys.51.591.

[288] Pedro Leopoldo e Silva Lopes. "Vortex Bound States in Superconducting Topological Matter." PhD thesis, Universidade Estadual de Campinas, **2016**. 99

[289] H Suderow, et al. "Imaging superconducting vortex cores and lattices with a scanning tunneling microscope." *Superconductor Science and Technology*, 27(6):063001, **2014**. doi:10.1088/0953-2048/27/6/063001. 100

[290] E. H. Brandt. "The flux-line lattice in superconductors." *Rep. Prog. Phys.*, 58(11):1465–1594, **1995**. doi:10.1088/0034-4885/58/11/003. 100, 103, 104

[291] Laurent-Patrick Lévy. "Vortices in Type II Superconductors," pages 337–353. Springer Berlin Heidelberg, Berlin, Heidelberg, **2000**. ISBN 978-3-662-04271-7. doi:10.1007/978-3-662-04271-7$_1$5. 101

[292] A. Wallraff, et al. "Quantum Dynamics of Vortices and Vortex Qubits." Wiley-VCH Verlag GmbH & Co. KGaA, **2005**. doi:10.1002/3527606009.ch13. 101

[293] Gaia Grimaldi, et al. "Inhomogeneous magnetic flux focusing in superconducting Josephson networks." *Physical Review B*, 59(21):13608–13611, **1999**. doi:10.1103/PhysRevB.59.13608. 101

[294] Ali A Babaei Brojeny and John R Clem. "Four coplanar superconducting strips: flux-focusing effects and inductance." *Superconductor Science and Technology*, 17(11):1275–1282, **2004**. doi:10.1088/0953-2048/17/11/007. 101

[295] Enrico Silva, et al. "Vortices at Microwave Frequencies." *Physical Sciences Reviews*, 2(10), **2017**. doi:10.1515/psr-2017-8004. 101

[296] C. Caroli, et al. "Bound Fermion states on a vortex line in a type II superconductor." *Physics Letters*, 9(4):307–309, **1964**. doi:10.1016/0031-9163(64)90375-0. 101

[297] M. J. Stephen and J. Bardeen. "Viscosity of Type-II Superconductors." *Physical Review Letters*, 14(4):112–113, **1965**. doi:10.1103/PhysRevLett.14.112.

[298] M Golosovsky, et al. "High-frequency vortex dynamics in." *Superconductor Science and Technology*, 9(1):1–15, **1996**. doi:10.1088/0953-2048/9/1/001. 101

[299] A M Campbell. "The response of pinned flux vortices to low-frequency fields." *Journal of Physics C: Solid State Physics*, 2(8):1492–1501, **1969**. doi:10.1088/0022-3719/2/8/318. 101

[300] A M Campbell. "The interaction distance between flux lines and pinning centres." *Journal of Physics C: Solid State Physics*, 4(18):3186–3198, **1971**. doi:10.1088/0022-3719/4/18/023.

[301] R. Willa, et al. "Campbell Response in Type-II Superconductors under Strong Pinning Conditions." *Physical Review Letters*, 115(20), **2015**. doi:10.1103/PhysRevLett.115.207001. 101

[302] D. Bothner, et al. "Improving the performance of superconducting microwave resonators in magnetic fields." *Applied Physics Letters*, 98(10):102504, **2011**. doi:10.1063/1.3560480. 102

[303] D. Bothner, et al. "Reducing vortex losses in superconducting microwave resonators with microsphere patterned antidot arrays." *Applied Physics Letters*, 100(1):012601, **2012**. doi:10.1063/1.3673869.

[304] J.G. Kroll, et al. "Magnetic-Field-Resilient Superconducting Coplanar-Waveguide Resonators for Hybrid Circuit Quantum Electrodynamics Experiments." *Physical Review Applied*, 11(6), **2019**. doi:10.1103/PhysRevApplied.11.064053. 102, 104, 108

[305] B.B. Goodman and M. Wertheimer. "Observation of the speed of flux jumps in superconducting niobium." *Physics Letters*, 18(3):236–238, **1965**. doi:10.1016/0031-9163(65)90308-2. 103

[306] Yukikazu Iwasa. "Case Studies in Superconducting Magnets," volume 48. Springer US, **2009**. doi:10.1007/b112047. 103

[307] C. P. Bean. "Magnetization of Hard Superconductors." *Physical Review Letters*, 8(6):250–253, **1962**. doi:10.1103/PhysRevLett.8.250. 103

[308] Charles P. Bean. "Magnetization of High-Field Superconductors." *Reviews of Modern Physics*, 36(1):31–39, **1964**. doi:10.1103/RevModPhys.36.31. 103

[309] Y. B. Kim, et al. "Magnetization and Critical Supercurrents." *Physical Review*, 129(2):528–535, **1963**. doi:10.1103/PhysRev.129.528. 103

[310] C. P. Bean and J. D. Livingston. "Surface Barrier in Type-II Superconductors." *Physical Review Letters*, 12(1):14–16, **1964**. doi:10.1103/PhysRevLett.12.14. 103

[311] M. Zehetmayer. "How the vortex lattice of a superconductor becomes disordered: a study by scanning tunneling spectroscopy." *Scientific Reports*, 5(1), **2015**. doi:10.1038/srep09244. 103

[312] H. J. Fink. "Stability Limit of the Superheated Meissner State due to Three-Dimensional Fluctuations of the Order Parameter and Vector Potential." *Physical Review*, 182(2):498–503, **1969**. doi:10.1103/PhysRev.182.498. 103

[313] Lorenz Kramer. "Breakdown of the superheated Meissner state and spontaneous vortex nucleation in type II superconductors." *Zeitschrift für Physik A Hadrons and nuclei*, 259(4):333–346, **1973**. doi:10.1007/BF01395939.

[314] Andrew J. Dolgert, et al. "Superheating fields of superconductors: Asymptotic analysis and numerical results." *Physical Review B*, 53(9):5650–5660, **1996**. doi:10.1103/PhysRevB.53.5650. 103

[315] Horaiu Năstase. "Classical Field Theory." Cambridge University Press, **2019**. doi:10.1017/9781108569392. 104

[316] Andrea Benfenati, et al. "Vortex nucleation barrier in superconductors beyond the Bean-Livingston approximation: A numerical approach for the sphaleron problem in a gauge theory." *Physical Review B*, 101(22), **2020**. doi:10.1103/PhysRevB.101.220505. 104

[317] P.G. de Gennes. "Vortex nucleation in type II superconductors." *Solid State Communications*, 3(6):127–130, **1965**. doi:10.1016/0038-1098(65)90387-X. 104

[318] G. Stejic, et al. "Effect of geometry on the critical currents of thin films." *Physical Review B*, 49(2):1274–1288, **1994**. doi:10.1103/PhysRevB.49.1274. 104

[319] Jennifer Deang, et al. "Vortices in superconductors: modelling and computer simulations." *Philosophical Transactions of the Royal Society of London. Series A: Mathematical, Physical and Engineering Sciences*, 355(1731):1957–1968, **1997**. doi:10.1098/rsta.1997.0098. 104

[320] H. M. Iftekhar Jaim, et al. "Superconducting TiN Films Sputtered Over a Large Range of Substrate DC Bias." *IEEE Transactions on Applied Superconductivity*, 25(3):1–5, **2015**. doi:10.1109/TASC.2014.2366036. 104

[321] A Torgovkin, et al. "High quality superconducting titanium nitride thin film growth using infrared pulsed laser deposition." *Superconductor Science and Technology*, 31(5):055017, **2018**. doi:10.1088/1361-6668/aab7d6. 104

[322] C.-S. Lee, et al. "Reducing vortex density in superconductors using the 'ratchet effect'." *Nature*, 400(6742):337–340, **1999**. doi:10.1038/22485. 104

[323] G. Berdiyorov. "Vortex Structure and Critical Parameters in Superconducting Thin Films with Arrays of Pinning Centers." Proefschriften UA-WET. Universiteit Antwerpen.,Faculteit Wetenschappen, Departement Fysica, **2007**. 104

[324] M. A. Washington and T. A. Fulton. "Observation of flux trapping threshold in narrow superconducting thin films." *Applied Physics Letters*, 40(9):848–850, **1982**. doi:10.1063/1.93252. 106

[325] O. M. Chumak, et al. "Threshold Field for Runaway Instability of Bilayer Hard Type-II Superconductor." *Journal of Low Temperature Physics*, 179(1-2):75–82, **2014**. doi:10.1007/s10909-014-1230-5. 106

[326] A. G. Zaitsev, et al. "Effect of a dc magnetic field on the microwave losses inMgB2thin films." *Physical Review B*, 75 (21), **2007**. doi:10.1103/PhysRevB.75.212505. 106

[327] N. Pompeo and E. Silva. "Reliable determination of vortex parameters from measurements of the microwave complex resistivity." *Physical Review B*, 78(9), **2008**. doi:10.1103/PhysRevB.78.094503. 106

[328] C. Song, et al. "Microwave response of vortices in superconducting thin films of Re and Al." *Physical Review B*, 79 (17), **2009**. doi:10.1103/PhysRevB.79.174512. 106

[329] B. L. Brandt, et al. "Intermediate state of thin superconductors." *Journal of Low Temperature Physics*, 4(1):41–63, **1971**. doi:10.1007/BF00628436. 108

[330] V N Gladilin, et al. "Vortices in a wedge made of a type-I superconductor." *New Journal of Physics*, 17(6):063032, **2015**. doi:10.1088/1367-2630/17/6/063032. 108

[331] S. E. de Graaf, et al. "Magnetic field resilient superconducting fractal resonators for coupling to free spins." *Journal of Applied Physics*, 112(12):123905, **2012**. doi:10.1063/1.4769208. 108

[332] J. G. Kroll, et al. "Magnetic field compatible circuit quantum electrodynamics with graphene Josephson junctions." *Nature Communications*, 9(1), **2018**. doi:10.1038/s41467-018-07124-x. 108

[333] F. Laermer. "Method of anisotropically etching silicon." *USA Patent No 5501893*, **1996**. 112

[334] Reza Abdolvand and Farrokh Ayazi. "An advanced reactive ion etching process for very high aspect-ratio sub-micron wide trenches in silicon." *Sensors and Actuators A: Physical*, 144(1):109 – 116, **2008**. doi:https://doi.org/10.1016/j.sna.2007.12.026. 112

[335] A. Bruno, et al. "Reducing intrinsic loss in superconducting resonators by surface treatment and deep etching of silicon substrates." *Applied Physics Letters*, 106(18):182601, **2015**. doi:10.1063/1.4919761. 112, 116

[336] G. Calusine, et al. "Analysis and mitigation of interface losses in trenched superconducting coplanar waveguide resonators." *Applied Physics Letters*, 112(6):062601, **2018**. doi:10.1063/1.5006888. 112

[337] A. Megrant, et al. "Planar superconducting resonators with internal quality factors above one million." *Applied Physics Letters*, 100(11):113510, **2012**. doi:10.1063/1.3693409. 112, 116

[338] Hanhee Paik and Kevin D. Osborn. "Reducing quantum-regime dielectric loss of silicon nitride for superconducting quantum circuits." *Applied Physics Letters*, 96(7):072505, **2010**. doi:10.1063/1.3309703. 114, 115

[339] Aaron D. O'Connell, et al. "Microwave dielectric loss at single photon energies and millikelvin temperatures." *Applied Physics Letters*, 92(11):112903, **2008**. doi:10.1063/1.2898887.

[340] David S. Wisbey, et al. "Effect of metal/substrate interfaces on radio-frequency loss in superconducting coplanar waveguides." *Journal of Applied Physics*, 108(9):093918, **2010**. doi:10.1063/1.3499608. 114, 115

[341] Jordi Naqui, et al. "Symmetry-Related Electromagnetic Properties of Resonator-Loaded Transmission Lines and Applications." *Applied Sciences*, 5(2):88–113, **2015**. doi:10.3390/app5020088. 114, 115

[342] M. S. Khalil, et al. "An analysis method for asymmetric resonator transmission applied to superconducting devices." *Journal of Applied Physics*, 111(5):054510, **2012**. doi:10.1063/1.3692073.

[343] Moe S. Khalil, et al. "Loss Dependence on Geometry and Applied Power in Superconducting Coplanar Resonators." *IEEE Transactions on Applied Superconductivity*, 21(3):879–882, **2011**. doi:10.1109/TASC.2010.2090330. 114, 115

[344] S. Probst, et al. "Efficient and robust analysis of complex scattering data under noise in microwave resonators." *Review of Scientific Instruments*, 86(2):024706, **2015**. doi:10.1063/1.4907935. 115

[345] H.T. Friis. "Noise Figures of Radio Receivers." *Proceedings of the IRE*, 32(7):419–422, **1944**. doi:10.1109/JRPROC.1944.232049. 123

[346] B. Yurke, et al. "Observation of parametric amplification and deamplification in a Josephson parametric amplifier." *Physical Review A*, 39(5):2519–2533, **1989**. doi:10.1103/physreva.39.2519. 123

[347] Ananda Roy and Michel Devoret. "Introduction to parametric amplification of quantum signals with Josephson circuits." *Comptes Rendus Physique*, 17(7):740–755, **2016**. doi:10.1016/j.crhy.2016.07.012. 123

[348] T. Mimura. "The early history of the high electron mobility transistor (HEMT)." *IEEE Transactions on Microwave Theory and Techniques*, 50(3):780–782, **2002**. doi:10.1109/22.989961. 123

[349] John L. B. Walker. "Handbook of RF and Microwave Power Amplifiers." CAMBRIDGE, **2011**. ISBN 0521760100.

[350] Yutaro Yamaguchi, et al. "GaN HEMT high efficiency amplifier for Microwave Wireless Power Transmission." *2015 IEEE International Symposium on Radio-Frequency Integration Technology (RFIT)*, **2015**. doi:10.1109/RFIT.2015.7377932. 123

[351] Christopher Cooper. "Physics." Fitzroy Dearborn, Chicago, **2001**. ISBN 9781579583583. 123

[352] M. Cohn and W. King. "A Sideband-Mixing Superheterodyne Receiver." *Proceedings of the IRE*, 44(11):1595–1599, **1956**. doi:10.1109/JRPROC.1956.274878.

[353] Rudolf Graf. "Modern dictionary of electronics." Newnes, Boston, **1999**. ISBN 9780750698665. 123

[354] R. Vijay, et al. "Dispersive microwave readout for quantum electrical circuits." *2011 IEEE MTT-S International Microwave Symposium*, **2011**. doi:10.1109/MWSYM.2011.5972726. 124

[355] Oñder Gül, et al. "Hard Superconducting Gap in InSb Nanowires." *Nano Letters*, 17(4):2690–2696, **2017**. doi:10.1021/acs.nanolett.7b00540. PMID: 28355877. 129, 148

[356] Francesco Giazotto, et al. "A Josephson quantum electron pump." *Nature Physics*, 7(11):857–861, **2011**. doi:10.1038/nphys2053. 129

[357] H. Y. Günel, et al. "Supercurrent in Nb/InAs-nanowire/Nb Josephson junctions." *Journal of Applied Physics*, 112(3):034316, **2012**. doi:10.1063/1.4745024. 129

[358] Y.-J. Doh. "Tunable Supercurrent Through Semiconductor Nanowires." *Science*, 309(5732):272–275, **2005**. doi:10.1126/science.1113523. 129, 147, 178

[359] Stefano Roddaro, et al. "Hot-electron effects in InAs nanowire Josephson junctions." *Nano Research*, 4(3):259–265, **2010**. doi:10.1007/s12274-010-0077-6. 129

[360] Sasa Gazibegovic, et al. "Epitaxy of advanced nanowire quantum devices." *Nature*, 548(7668):434–438, **2017**. doi:10.1038/nature23468. 129, 145

[361] T. W. Larsen, et al. "Semiconductor-Nanowire-Based Superconducting Qubit." *Phys. Rev. Lett.*, 115:127001, **2015**. doi:10.1103/PhysRevLett.115.127001. 130

[362] Naveen Shetty. "Fabrication and Transport measurement in Semiconductor-Superconductor Hybrid structures." Master's thesis, Technische Universität Dresden, **2018**. 130

[363] Charles Kittel. "Introduction to Solid State Physics." John Wiley Sons Inc, **2004**. ISBN 047141526X. 130

[364] Katrin Steinberg, et al. "Quasiparticle response of superconducting aluminum to electromagnetic radiation." *Physical Review B*, 77(21), **2008**. doi:10.1103/PhysRevB.77.214517. 130

[365] K. Flensberg, et al. "Subharmonic energy-gap structure in superconducting weak links." *Phys. Rev. B*, 38:8707–8711, **1988**. doi:10.1103/PhysRevB.38.8707. 131, 140, 147, 148, 152

[366] Gabriel Niebler, et al. "Analytical calculation of the excess current in the Octavio–Tinkham–Blonder–Klapwijk theory." *Superconductor Science and Technology*, 22(8):085016, **2009**. 131, 148, 152

[367] H. Courtois, et al. "Origin of Hysteresis in a Proximity Josephson Junction." *Physical Review Letters*, 101(6), **2008**. doi:10.1103/PhysRevLett.101.067002. 134

[368] P. Joyez, et al. "The Josephson Effect in Nanoscale Tunnel Junctions." *Journal of Superconductivity*, 12(6):757–766, **1999**. doi:10.1023/A:1007733009637. 134

[369] Pujitha Perla, et al. "Te-doped selective-area grown InAs nanowires for superconducting hybrid devices." *arxiv*, **2021**. doi:arXiv:2110.09352. 135, 136, 137, 138, 139

[370] Kamil Sladek, et al. "Influence of Silicon Doping on the SA-MOVPE of InAs Nanowires." *MRS Proceedings*, 1258, **2010**. doi:10.1557/PROC-1258-P02-05. 135

[371] S. Wirths, et al. "Effect of Si-doping on InAs nanowire transport and morphology." *Journal of Applied Physics*, 110(5): 053709, **2011**. doi:10.1063/1.3631026.

[372] Dong Woo Park, et al. "Structural and electrical properties of catalyst-free Si-doped InAs nanowires formed on Si(111)." *Scientific Reports*, 5(1), **2015**. doi:10.1038/srep16652.

[373] Jesper Wallentin and Magnus T. Borgström. "Doping of semiconductor nanowires." *Journal of Materials Research*, 26(17):2142–2156, **2011**. doi:10.1557/jmr.2011.214. 135

[374] R. Sankaran. "Te doping of vapor phase epitaxial GaAs." *Journal of Crystal Growth*, 50(4):859–864, **1980**. doi:10.1016/0022-0248(80)90148-7. 135

[375] Marta Orrù, et al. "A Roadmap for Controlled and Efficient n-Type Doping of Self-Assisted GaAs Nanowires Grown by Molecular Beam Epitaxy." *Advanced Functional Materials*, 26(17):2836–2845, **2016**. doi:10.1002/adfm.201504853. 135

[376] Nicholas A. Güsken, et al. "Influence of Te-Doping on Catalyst-Free VS InAs Nanowires." *Nanoscale Research Letters*, 14(1), **2019**. doi:10.1186/s11671-019-3004-0. 135

[377] C. Janvier, et al. "Coherent manipulation of Andreev states in superconducting atomic contacts." *Science*, 349(6253): 1199–1202, **2015**. doi:10.1126/science.aab2179. 140, 172, 175

[378] L. Tosi, et al. "Spin-Orbit Splitting of Andreev States Revealed by Microwave Spectroscopy." *Physical Review X*, 9(1), **2019**. doi:10.1103/PhysRevX.9.011010. 140, 172, 175, 177, 178, 180

[379] Anindya Das, et al. "Zero-bias peaks and splitting in an Al–InAs nanowire topological superconductor as a signature of Majorana fermions." *Nature Physics*, 8(12):887–895, **2012**. doi:10.1038/nphys2479. 140

[380] Hao Zhang, et al. "Next steps of quantum transport in Majorana nanowire devices." *Nature Communications*, 10(1), **2019**. doi:10.1038/s41467-019-13133-1.

[381] M. T. Deng, et al. "Majorana bound state in a coupled quantum-dot hybrid-nanowire system." *Science*, 354(6319): 1557–1562, **2016**. doi:10.1126/science.aaf3961. 140

[382] Sigurdur I. Erlingsson. School of science and engineering, reykjavik university, reykjavík, iceland. Private Communication, **2018**. 142

[383] J.R. Johansson, et al. "QuTiP 2: A Python framework for the dynamics of open quantum systems." *Computer Physics Communications*, 184(4):1234–1240, **2013**. doi:10.1016/j.cpc.2012.11.019. 142, 172

[384] J.R. Johansson, et al. "QuTiP: An open-source Python framework for the dynamics of open quantum systems." *Computer Physics Communications*, 183(8):1760–1772, **2012**. doi:10.1016/j.cpc.2012.02.021. 142, 172

[385] Christoph W Groth, et al. "Kwant: a software package for quantum transport." *New Journal of Physics*, 16(6):063065, **2014**. doi:10.1088/1367-2630/16/6/063065. 142

[386] Neill Lambert. Riken center for emergent matter science, wako, japan. Private Communication, **2020**. 142

[387] Sen Li, et al. "0–π phase transition in hybrid superconductor–InSb nanowire quantum dot devices." *Phys. Rev. B*, 95: 014515, **2017**. doi:10.1103/PhysRevB.95.014515. 145, 150

[388] Patrick Zellekens, et al. "Hard-Gap Spectroscopy in a Self-Defined Mesoscopic InAs / Al Nanowire Josephson Junction." *Physical Review Applied*, 14(5), **2020**. doi:10.1103/PhysRevApplied.14.054019. 146, 147, 148, 149, 150, 151, 153

[389] H. Y. Günel, et al. "Supercurrent in Nb/InAs-nanowire/Nb Josephson junctions." *Journal of Applied Physics*, 112: 034316, **2012**. doi:http://dx.doi.org/10.1063/1.4745024. 147, 178

[390] Hao Zhang, et al. "Ballistic superconductivity in semiconductor nanowires." *Nature Communications*, 8:16025, **2017**. doi:doi:10.1038/ncomms16025. 148, 195

[391] W. Chang, et al. "Hard gap in epitaxial semiconductor-superconductor nanowires." *Nature Nanotechnology*, 10:232, **2015**. doi:10.1038/NNANO.2014.306. 148

[392] R. S. Deacon, et al. "Tunneling Spectroscopy of Andreev Energy Levels in a Quantum Dot Coupled to a Superconductor." *Physical Review Letters*, 104(7), **2010**. doi:10.1103/PhysRevLett.104.076805. 150

[393] J. A. van Dam, et al. "Supercurrent reversal in quantum dots." *Nature*, 442:667–670, **2006**. doi:http://dx.doi.org/10.1038/nature05018. 150

[394] R. Meservey and P. M. Tedrow. "Properties of Very Thin Aluminum Films." *Journal of Applied Physics*, 42(1):51–53, **1971**. doi:10.1063/1.1659648. 151

[395] S. Nadj-Perge, et al. "Spectroscopy of Spin-Orbit Quantum Bits in Indium Antimonide Nanowires." *Physical Review Letters*, 108(16), **2012**. doi:10.1103/PhysRevLett.108.166801. 152

[396] Hanhee Paik, et al. "Observation of High Coherence in Josephson Junction Qubits Measured in a Three-Dimensional Circuit QED Architecture." *Physical Review Letters*, 107(24), **2011**. doi:10.1103/PhysRevLett.107.240501. 158

[397] Adam Patrick Sears. "Extending Coherence in Superconducting Qubits: From microseconds to milliseconds." PhD thesis, Yale University, **2013**. 158

[398] G Wendin. "Quantum information processing with superconducting circuits: a review." *Reports on Progress in Physics*, 80(10):106001, **2017**. doi:10.1088/1361-6633/aa7e1a. 158

[399] Anna Schäfer, et al. "Hexagonal LaLuO3as high-dielectric." *Journal of Vacuum Science & Technology B, Nanotechnology and Microelectronics: Materials, Processing, Measurement, and Phenomena*, 33(1):01A104, **2015**. doi:10.1116/1.4904401. 159

[400] J. A. Schreier, et al. "Suppressing charge noise decoherence in superconducting charge qubits." *Physical Review B*, 77(18), **2008**. doi:10.1103/PhysRevB.77.180502. 158

[401] Samuel James Bader. "Higher levels of the transmon qubit." PhD thesis, Massachusetts Institute of Technology, **2014**. 159, 160

[402] Gustav Andersson. "Circuit quantum electrodynamics with a transmon qubit in a 3D cavity." Master's thesis, Technische Universität München, **2015**. 159, 160

[403] Serge Haroche and Daniel Kleppner. "Cavity Quantum Electrodynamics." *Physics Today*, 42(1):24–30, **1989**. doi:10.1063/1.881201. 159

[404] Ileana-Cristina Benea-Chelmus, et al. "Electric field correlation measurements on the electromagnetic vacuum state." *Nature*, 568(7751):202–206, **2019**. doi:10.1038/s41586-019-1083-9. 159

[405] Steffen Schlör. Private communication with steffen schlör and martin weides. KIT Karlsruhe Institute of Technology, Karlsruhe, Germany, **2018**. 160

[406] Steffen Schlör. "Intrinsic decoherence in superconducting quantum circuits." PhD thesis, Karlsruher Institut für Technologie, **2019**. 161, 162, 164

[407] Jochen Braumüller, et al. "Concentric transmon qubit featuring fast tunability and an anisotropic magnetic dipole moment." *Applied Physics Letters*, 108(3):032601, **2016**. doi:10.1063/1.4940230. 162

[408] Andre Schneider, et al. "Transmon qubit in a magnetic field: Evolution of coherence and transition frequency." *Physical Review Research*, 1(2), **2019**. doi:10.1103/PhysRevResearch.1.023003. 162

[409] E.H. Lenzing and J.C. Rautio. "A model for discretization error in electromagnetic analysis of capacitors." *IEEE Transactions on Microwave Theory and Techniques*, 46(2):162–166, **1998**. doi:10.1109/22.660982. 162

[410] James C. Rautio. "Perfectly calibrated internal ports in EM analysis of planar circuits." *2008 IEEE MTT-S International Microwave Symposium Digest*, **2008**. doi:10.1109/MWSYM.2008.4633033.

[411] Allen F. Horn, et al. "Conductor profile effects on the propagation constant of microstrip transmission lines." *2010 IEEE MTT-S International Microwave Symposium*, **2010**. doi:10.1109/MWSYM.2010.5515933. 162

[412] Kilian Flöhr, et al. "Manipulating InAs nanowires with submicrometer precision." *Review of Scientific Instruments*, 82(11):113705, **2011**. doi:10.1063/1.3657135. 162, 168

[413] Patrick Liebisch. "Optimization of semiconductor-superconductor hybrid Qubits based on InAs Nanowires." Master's thesis, RWTH Aachen, **2019**. 162

[414] Sung Un Cho, et al. "Tunable superconducting qudit mediated by microwave photons." *AIP Advances*, 5(8):087186, **2015**. doi:10.1063/1.4930103. 165

[415] P. Scarlino, et al. "Coherent microwave-photon-mediated coupling between a semiconductor and a superconducting qubit." *Nature Communications*, 10(1), **2019**. doi:10.1038/s41467-019-10798-6.

[416] Mahdi Naghiloo. "Introduction to Experimental Quantum Measurement with Superconducting Qubits." *arxiv*, **2019**. doi:arXiv:1904.09291. 165

[417] Michael Mück, et al. "Radio Frequency SQUIDs and their Applications." Springer Netherlands, **2001**. doi:10.1007/978-94-010-0450-$3_1$9. 168

[418] John Clarke and Alex I. Braginski. "The SQUID Handbook." Wiley, **2004**. doi:10.1002/3527603646. 168

[419] J. E. Mooij. "Josephson Persistent-Current Qubit." *Science*, 285(5430):1036–1039, **1999**. doi:10.1126/science.285.5430.1036. 169

[420] T. P. Orlando, et al. "Superconducting persistent-current qubit." *Physical Review B*, 60(22):15398–15413, **1999**. doi:10.1103/PhysRevB.60.15398.

[421] V. T. Petrashov, et al. "Andreev Probe of Persistent Current States in Superconducting Quantum Circuits." *Physical Review Letters*, 95(14), **2005**. doi:10.1103/PhysRevLett.95.147001. 169

[422] P. Drude. "Zur Elektronentheorie der Metalle." *Annalen der Physik*, 306(3):566–613, **1900**. doi:https://doi.org/10.1002/andp.19003060312. 170

[423] Harald Ibach and Hans Lüth. ""Free" Electrons in Solids." Springer Berlin Heidelberg, **2009**. doi:https://doi.org/10.1007/978-3-540-93804-0_6.

[424] P. L. Taylor. "The Relaxation Time of Conduction Electrons in the Noble Metals." *Proceedings of the Royal Society of London. Series A, Mathematical and Physical Sciences*, 275(1361):209–217, **1963**. 170

[425] C. Metzger, et al. "Circuit-QED with phase-biased Josephson weak links." *Physical Review Research*, 3(1), **2021**. doi:10.1103/PhysRevResearch.3.013036. 175, 178, 180

[426] Patrick Zellekens, et al. "Microwave spectroscopy of Andreev states in InAs nanowire-based hybrid junctions using a flip-chip layout." *Communications Physics*, 5(1):267, **2022**. doi:10.1038/s42005-022-01035-6. 112, 178, 179

[427] Manuel Houzet and Mikhail A. Skvortsov. "Mesoscopic fluctuations of the supercurrent in diffusive Josephson junctions." *Physical Review B*, 77(2), **2008**. doi:10.1103/PhysRevB.77.024525. 178

[428] Yuval Oreg, et al. "Helical Liquids and Majorana Bound States in Quantum Wires." *Physical Review Letters*, 105(17), **2010**. doi:10.1103/PhysRevLett.105.177002. 183

[429] Roman M. Lutchyn, et al. "Majorana Fermions and a Topological Phase Transition in Semiconductor-Superconductor Heterostructures." *Physical Review Letters*, 105(7), **2010**. doi:10.1103/PhysRevLett.105.077001. 183

[430] Fernando Peñaranda, et al. "Even-odd effect and Majorana states in full-shell nanowires." *Physical Review Research*, 2(2), **2020**. doi:10.1103/PhysRevResearch.2.023171. 183, 184

[431] Eran Ginossar and Eytan Grosfeld. "Microwave transitions as a signature of coherent parity mixing effects in the Majorana-transmon qubit." *Nature Communications*, 5(1), **2014**. doi:10.1038/ncomms5772. 190

[432] J. Q. You, et al. "Encoding a qubit with Majorana modes in superconducting circuits." *Scientific Reports*, 4(1), **2014**. doi:10.1038/srep05535.

[433] Daniel Litinski. "Large-Scale Topological Quantum Computing with and without Majorana Fermions." PhD thesis, Freie Universität Berlin, **2019**.

[434] F Hassler, et al. "The top-transmon: a hybrid superconducting qubit for parity-protected quantum computation." *New Journal of Physics*, 13(9):095004, **2011**. doi:10.1088/1367-2630/13/9/095004. 190

[435] Konstantin Yavilberg, et al. "Fermion parity measurement and control in Majorana circuit quantum electrodynamics." *Physical Review B*, 92(7), **2015**. doi:10.1103/PhysRevB.92.075143. 190

[436] Tong Zhou, et al. "Phase Control of Majorana Bound States in a Topological X Junction." *Physical Review Letters*, 124 (13), **2020**. doi:10.1103/PhysRevLett.124.137001.

[437] Benedikt Scharf, et al. "Tuning topological superconductivity in phase-controlled Josephson junctions with Rashba and Dresselhaus spin-orbit coupling." *Physical Review B*, 99(21), **2019**. doi:10.1103/PhysRevB.99.214503.

[438] Matthieu C. Dartiailh, et al. "Phase Signature of Topological Transition in Josephson Junctions." *Physical Review Letters*, 126(3), **2021**. doi:10.1103/PhysRevLett.126.036802. 190

[439] Chun-Xiao Liu, et al. "Distinguishing topological Majorana bound states from trivial Andreev bound states: Proposed tests through differential tunneling conductance spectroscopy." *Physical Review B*, 97(21), **2018**. doi:10.1103/PhysRevB.97.214502. 191

[440] L. S. Ricco, et al. "Spin-dependent zero-bias peak in a hybrid nanowire-quantum dot system: Distinguishing isolated Majorana fermions from Andreev bound states." *Physical Review B*, 99(15), **2019**. doi:10.1103/PhysRevB.99.155159.

[441] Marco Valentini, et al. "Flux-tunable Andreev bound states in hybrid full-shell nanowires." *arXiv preprint arXiv:2008.02348*, **2020**.

[442] Hao Zhang, et al. "Retraction Note: Quantized Majorana conductance." *Nature*, 591(7851):E30–E30, **2021**. doi:10.1038/s41586-021-03373-x. 191

[443] D. Candebat, et al. "InSb nanowire field-effect transistors - electrical characterization and material analysis." *2009 67th Annual Device Research Conference (DRC). University Park, PA, USA, 20090622*, pages 13–14, **2009**. 195, 204

[444] Henrik A. Nilsson, et al. "Temperature dependent properties of InSb and InAs nanowire field-effect transistors." *Applied Physics Letters*, 96(15):153505, **2010**. doi:10.1063/1.3402760.

[445] Yennai Wang, et al. "Field effect transistor based on single crystalline InSb nanowire." *J. Mater. Chem.*, pages 2459–2462, **2011**. doi:10.1039/C0JM03855E.

[446] Claes Thelander, et al. "Electrical properties of $InAs_{1-x}Sb_x$ and InSb nanowires grown by molecular beam epitaxy." *Applied Physics Letters*, 100(23):232105, **2012**. doi:http://dx.doi.org/10.1063/1.4726037.

[447] Önder Gül, et al. "Towards high mobility InSb nanowire devices." *Nanotechnology*, 26(21):215202, **2015**. 195

[448] Henrik A. Nilsson, et al. "Giant, Level-Dependent g Factors in InSb Nanowire Quantum Dots." *Nano Letters*, 9(9): 3151–3156, **2009**. doi:10.1021/nl901333a. 195

[449] Ilse van Weperen, et al. "Quantized Conductance in an InSb Nanowire." *Nano Letters*, 13(2):387–391, **2013**. doi:10.1021/nl3035256. 211

[450] I. van Weperen, et al. "Spin-orbit interaction in InSb nanowires." *Phys. Rev. B*, 91:201413, **2015**. doi:10.1103/PhysRevB.91.201413. 195

[451] V. Mourik, et al. "Signatures of Majorana Fermions in Hybrid Superconductor-Semiconductor Nanowire Devices." *Science*, 336(6084):1003–1007, **2012**. doi:10.1126/science.1222360. 195

[452] Su-Huai Wei and Alex Zunger. "Calculated natural band offsets of all II–VI and III–V semiconductors: Chemical trends and the role of cation d orbitals." *Applied Physics Letters*, 72(16):2011–2013, **1998**. doi:https://doi.org/10.1063/1.121249. 198

[453] Rita Magri, et al. "Evolution of the band-gap and band-edge energies of the lattice-matched GaInAsSb-GaSb and GaInAsSbInAs alloys as a function of composition." *Journal of Applied Physics*, 98(4):043701, **2005**. doi:https://doi.org/10.1063/1.2010621. 198

[454] Serge Luryi, et al. "Future Trends in Microelectronics: Journey Into the Unknown." WILEY, **2016**. ISBN 1119069114. doi:10.1002/9781119069225. 198

[455] Yoon-Suk Kim, et al. "Towards efficient band structure and effective mass calculations for III-V direct band-gap semiconductors." *Physical Review B*, 82(20), **2010**. doi:10.1103/PhysRevB.82.205212. 198

[456] Marius Grundmann. "The Physics of Semiconductors." Springer-Verlag GmbH, **2006**. ISBN 9783540346616. 200

[457] Gérald Bastard and Joel Schulman. "Wave Mechanics Applied to Semiconductor Heterostructures." *Physics Today*, 45(2):103–105, **1992**. doi:10.1063/1.2809545. 201

[458] Karl Weis, et al. "Quantum dots in InAs nanowires induced by surface potential fluctuations." *Nanotechnology*, 25 (13):135203, **2014**. doi:10.1088/0957-4484/25/13/135203. 204

[459] N. V. Demarina, et al. "InAs Nanowires with Surface States as Building Blocks for Tube-Like Electrical Sensing Devices." In *Future Trends in Microelectronics: Frontiers and Innovations*. John Wiley & Sons, Inc., Hoboken, NJ,, **2013**. 204

[460] P. A. Lee and A. D. Stone. "Universal conductance fluctuations in metals." *Phys. Rev. Lett.*, 55(15):1622–1625, **1985**. doi:10.1103/PhysRevLett.55.1622. 206

[461] B. L. Al'tshuler. "Fluctuations in the extrinsic conductivity of disordered conductors." *JETP Lett.*, 41:648–651, **1985**.

[462] P. A. Lee, et al. "Universal conductance fluctuations in metals: Effects of finite temperature, interactions, and magnetic field." *Phys. Rev. B*, 35(3):1039–1070, **1987**. doi:10.1103/PhysRevB.35.1039. 206

[463] S. Estévez Hernández, et al. "Spin-orbit coupling and phase coherence in InAs nanowires." *Phys. Rev. B*, 82:235303, **2010**. doi:10.1103/PhysRevB.82.235303. 207, 208

[464] R. Winkler. "Spin orbit coupling effects in two-dimensional electron and hole systems." Springer–Verlag, Berlin, Heidelberg, New York, **2003**. 209

[465] M. Büttiker. "Four-Terminal Phase-Coherent Conductance." *Phys. Rev. Lett.*, 57:1761–1764, **1986**. doi:10.1103/PhysRevLett.57.1761. 210

[466] Fabian Haas, et al. "Electron Interference in Hall Effect Measurements on GaAs/InAs Core/Shell Nanowires." *Nano Letters*, 17(1):128–135, **2016**. doi:10.1021/acs.nanolett.6b03611. 210

[467] Tomas Orn Rosdahl, et al. "Spin and impurity effects on flux-periodic oscillations in core-shell nanowires." *Phys. Rev. B*, 90:035421, **2014**. doi:10.1103/PhysRevB.90.035421. 210

[468] Fabian Haas, et al. "Anisotropic phase coherence in GaAs/InAs core/shell nanowires." *Nanotechnology*, 28(44): 445202, **2017**. doi:https://doi.org/10.1088/1361-6528/aa887d. 213